Investigating Cardiomyocyte Dysfunction in Dilated Cardiomyopathy Associated with Duchenne Muscular Dystrophy

Darren Graham Samuel Wilson

180155648

Submitted in partial fulfilment of the requirements of the Degree of Doctor of Philosophy

This work was supported by the British Heart Foundation Grant Code FS/18/64/34185

Declaration

I, Darren Graham Samuel Wilson, confirm that the research included within this thesis is my own work or that where it has been carried out in collaboration with, or supported by others, that this is duly acknowledged below, and my contribution indicated.

Previously published material is also acknowledged below. I attest that I have exercised reasonable care to ensure that the work is original and does not to the best of my knowledge break any UK law, infringe any third party's copyright or other Intellectual Property Right, or contain any confidential material. I accept that Queen Mary University of London has the right to use plagiarism detection software to check the electronic version of the thesis. I confirm that this thesis has not been previously submitted for the award of a degree by this or any other university.

Signature: Darren Graham Samuel Wilson

Date: 26/09/2023

Publications

Wilson, D. G. S. & Iskratch, T. Factoring in the Force: A Novel Role of eIF6. *Journal of Cell Biology doi: 10.1083/jcb.202201002* (2022)

Wilson, D. G. S., Tinker, A., & Iskratch, T., The Role of the Dystrophin Glycoprotein Complex in Muscle Cell Mechanotransduction. *Nature Communications Biology doi: 10.1038/s42003-022-03980-y* (2022)

Battey, E., Hoang, A., Ross, J. A., Pollock, R. D., Kalakoutis, M., **Wilson, D. G. S.,** Pugh, J. N., Lazarus, N. R., Close, G. L., Iskratsch, T., Harridge, S. D. R., Ochala, J., Stroud, M. J., Myonuclear Alterations Associated with Exercise are Independent of Age in Humans. *Journal of Physiology, doi: 10.1113/JP284128* (2023)

Hawkes, W., Marhuenda, E., Reynolds, P., O'Neill, C., Pandey, P., **Wilson, D. G. S.,** Freeley, M., Huang, D., Hu, J., Gondarenko, S., Hone, J., Gadegaard, N., Palma, M. Regulation of Cardiomyocyte Adhesion and Mechanosignalling Through Distinct Nanoscale Behaviour of Integrin Ligands Mimicking Healthy or Fibrotic ECM. Philosophical Transactions B, doi: 10.1098/rstb.2022.0021 (2022)

Presentations

49th European Muscle Conference, Prague - *20 minute talk*

International Society For Heart Research, Berlin, - *poster*

British Heart Foundation 4-Year PhD Conference, Leeds, - *20 minute talk*

5th Russell Binions PhD Symposium, London, - *20 minute talk*

Triangle Cytoskeleton Meeting, Online - *poster*

Abstract

Mutations within the *DMD* gene are responsible for the severe, X-linked inherited disease Duchenne muscular dystrophy (DMD). DMD is characterised by the absence of the costameric protein, dystrophin, from striated muscle tissue. Dystrophin has a multitude of roles, but vitally, prevents contraction-induced sarcolemmal damage by functioning as a molecular spring. Dilated cardiomyopathy (DCM) is pathognomonic of DMD, with patients typically succumbing to cardiac failure by 30 years.

Here, I hypothesised that dystrophin is central to mechanotransduction and is a significant contributor to the viscoelasticity of cardiomyocytes. Moreover, that dystrophin has a strong interaction with the underlying cytoskeleton necessary to fulfil these roles. Further, I hypothesise that the absence of dystrophin, as is the case in DMD, is a primary driver of the DMD associated DCM pathology observed. I differentiated and characterised wild-type (WT) and DMD mutant human induced pluripotent stem cell derived cardiomyocytes (hiPSC-CMs), that acted as a physiologically relevant platform to model DMD associated DCM at the single-cell resolution.

Absence of dystrophin resulted in severely altered cellular and nuclear morphology alongside significantly decreased localisation of the mechanosensitive transcriptional co-activator, Yes-associated protein (YAP). Moreover, the Young's modulus and viscoelasticity in DMD hiPSC-CMs was significantly decreased compared to WT. These changes were further exacerbated by alterations to the extracellular matrix (ECM) from a healthy (6 kPa) to fibrotic (130 kPa) elasticity. Lastly, DMD hiPSC-CMs had an altered response to physiological stimuli, including cyclic stretch mimicking

myocardial contraction, and healthy cyclic cardiac pressure application, notably in YAP localisation and cell and nuclear morphology. Together, these data support the role of dystrophin as a vital mechanotransducing protein that makes significant contributions to the underpinning mechanical behaviour, and mechanoresponse of, cardiomyocytes. These data provide avenues that may be exploited in the future for use therapeutically.

Acknowledgements

First, I should like to thank my supervisors. Each has helped to shape, in their own way, the project and myself as a scientist. I'd like to extend thanks to Professor Andrew Tinker. To work with someone as insightful and talented as Andy has been a real pleasure. I have enjoyed the chats through the years and the guidance that you have offered. Secondly, I want to thank Professor (recently elected to, congratulations!) Thomas Iskratsch. Thomas is an inspirational scientist with a tremendous amount of generosity. He has wisdom and scientific *nous* beyond his years, and I am extremely privileged to have worked with, and learned from, such a talented scientist. Without Thomas' help I doubt I would have made it to the end of my PhD, and I am truly grateful to have experienced such wonderful support and optimism that helped to keep me focused and on track. And…of course, the occasional pub visit didn't hurt either. To have someone who truly believes in you and is willing to push you; someone to stimulate the scientific discussion, is a true gift. I learned the value of this as well as having a supportive, generous, insightful, and wise, supervisor. For this lesson, I would like to thank Dr Yung-Yao Lin.

Of course, with great supervisors, come great lab members. Each lab has been very welcoming, and I would like to thank everyone that I have worked with over the years. In particular, I want to thank Dr Emilie Marhuenda and Dr Pamela Swiatlowksa. We've been through the wars together, but we are better and tougher for it. Without your help in the lab, I would have failed a long, long time ago, so thank you! And thanks for putting up with my endless "And…where is that?" without killing me. I also wish to thank Caoimhe O'Neil, Dr Will Hawkes, Dr Matt Ward, Nivethitha Lakshminaraaisimulu, Dr Soraya Lopategui, Dr Brian Sit, Dr Ioannis Xanthus,

Holly Bachas-Brook, and Saba Qureshi, all of whom have helped to keep me sane in the lab!

My foray into the world of stem cells would have been a cataclysmic nightmare if not for the expertise of Cristina Morera (who put in so much time and effort, for which I am truly, truly grateful), Dr Amaia Paredes, Dr Anna Kowala, Dr Adam Denny, and Dr Matthew Cook. Each of you has helped keep me sane and put up with my endless complaints, for which I am truly grateful. Other Blizard crew I should like to thank include Dr Juan Labora, Dr Paula Carpintero, Dr Olga Eleftheriadou, and Dr Jihee Kim. I will always treasure the happy, and I must say, very long lunches filled with laughter- a true balm for the daily grind of the lab. I also want to thank our, somewhat honorary, lab member Rachel Wilson. Rachel successfully blended scientific discussion, amazing lab skills, and banter into a new level. I will miss our time together.

My time spent at the William Harvey Institute within Andy's lab was limited, but I was supported by many generous individuals. I should particularly like to thank Dr Alison Thomas, Dr Aled Jones, Yaqob Taleb, and Fahad Al Hattali. I would also like to thank everyone that I started my BHF journey with, whom I am only a tad envious for all finishing before me, Dr Hannah Nicholls, Dr Silvia Fanti, and Dr Kaya Olczak. Congratulations to each of you and thank you for kind words and support throughout.

I could never have embarked on such a venture without the support, guidance, and honest advice, such as "don't do a PhD…everyone hates it", from my friends. For this I would like to thank Dr John McGonigle and Dr Laura Burzynski. I particularly owe both of you so much for your heart felt kindness and introduction to so many fun board games. I'd like to thank Calum and Jenny McCune, Mike Beattie, Andrew McCune, and Louise

Allardice. Lockdown was difficult on everyone, but you guys made life so much better by regularly hanging out over Discord. Playing games, drinking, chatting, laughing, and crying, I can honestly say I had some of my best moments with you all. Thank you all for your unwavering support. I'd also like to thank Dr Stefan Noons and Megan Bell, who I have known for…nearly all of my life, so many chats to help keep me going! I also want to thank Holly Whyatt for unwavering support and checking in on me. I'd also like to thank Diane Mitchell and Dr Eleni Athanasakos for endless banter and drinks! I'd like to thank the 'Cambridges', Dr Ed O'Reilly and Sangik, Violette Giang and Will, and Jason Tun. I also want to extend thanks to the 'Sheffields' David Souter, Matt Ingham for their hospitality, booze, and games over the years.

To everyone else, I love you all and thank you for being there- there are too many to individually name!

I also want to thank my family, who have been absolutely unwavering throughout the duration of my PhD and beyond. To my mum, Karina, thank you so much for endless support and guidance, and kindness. To my dad, Robert, thank you for always being there and making sure mum answers the phone! And to my brother, Jamie, thank you for reminding me that life can indeed be stressful outside of a PhD. I would also like to take a moment to appreciate the love and support that I had from my grandmother, Mina. Unfortunately, at the very beginning of my PhD, my gran passed away. She was forever supportive and loving, and I am certain she would have been chuffed to bits to see me finish up. I would also like to thank my husbands' parents, Angie and Lindsay Barber. Angie and Lindsay have been real sweethearts over the years and their support has meant so much to me.

Lastly, to my partner in crime, my husband, Jeremy - I caught up, and we can be Dr together! You have been an absolute rock, love of my life, and best friend. I have no idea where I'd even be today if not for you. You have always been there for me and the amount we have endured and experienced together, really, is incredible. Thank you for being there and for putting up with me in the darkest of times. For being my biggest cheerleader. I love you with all of my heart. Last, but by no means least, to Kiki- our wee woolly fluff. We couldn't have asked for a better little cat. The cuddles and purrs over the years have certainly kept me going more than you will realise.

Table of Contents

Table of Figures

Table of Tables

Table of Abbreviations

A	Area
A.U.	Arbitrary units
AAV	Adeno associated virus
ABD	Actin binding domain
ACEi	Angiotensin converting enzyme inhibitor
AFM	Atomic force microscopy
AMPK	Adenosine monophosphate activated protein kinase
ANOVA	Analysis of variance
AON	Antisense oligonucleotide
AR	Aspect ratio
ARB	Angiotensin receptor blocking
ARP 2/3	Actin related protein 2/3
ATAC-seq	Assay for transposase-accessible chromatin with sequencing
atm	Atmospheres
BMD	Becker's muscular dystrophy
Bpm	Beats per minute
Ca^{2+}	Calcium ion
cDNA	Complementary DNA
CH domain	Calponin homology domain
CICR	Calcium induced calcium release
CPAP	Continuous positive airway pressure
CR	Cysteine rich
CRISPR	Clustered regularly interspace short palindromic repeats
CRISPRi	Clustered regularly interspaced small palindromic repeats interference
CT	Cysteine terminal
Ct	Cycle threshold
DAPI	4',6-diamidino-2-phenylindole
DCM	Dilated cardiomyopathy
Dex	Dexamethasone
DGC	Dystrophin glycoprotein complex
DMD	Duchenne muscular dystrophy
DMD	Dystrophin (gene)
DMSO	Dimethlysulphoxide
E	Young's modulus
E'	Elastic/storage modulus
E"	Viscous/loss modulus
ECM	Extracellular matrix
EHT	Engineered heart tissue
EMA	European medicines agency
ERK 1/2	Extracellular signal related kinase 1/2
F	Force
FA	Focal adhesion
F-actin	Filamentous actin
FAK	Focal adhesion kinase
FDA	Food and drug administration
FKRP	Fukutin related protein
G-actin	Globular actin

gDNA	Genomic DNA
GiWi	GSK3β inhibition-Wnt inhibition
Grb2	Growth factor receptor bound protein 2
GRMD	Golden retriever muscular dystrophy
GSK3β	Glycogen synthase kinase 3-β
HDAC8	Histone deacetylase 8
HF	Heart failure
hiPSC	Human induced pluripotent stem cell
hiPSC-CM	Human induced pluripotent stem cell derived cardiomyocyte
Hr	Hour
Hz	Hertz (frequency)
ICC	Immunocytochemistry
JNK	Jun N-terminal kinase
kb	kilobase
kPa	kiloPascals
L	Length
L-AA	L-ascorbic acid
LGMD	Limb Girdle muscular dystrophy
LINC	Linker of nucleoskeleton and cytoskeleton
LMNA	Lamin A/C (gene)
LOX	Lysyl oxidase
LTCC	Long type calcium channel
LV	Left ventricle
mdx	Muscular dystrophy X (DMD murine mutant)
MEF	Mouse embryonic fibroblast
Min	Minute
MLC2A	Myosin light chain 2 Atrial
MLC2V	Myosin light chain 2 ventricular
mM	Millimolar
mmHg	Millimetres of Mercury
MPa	MegaPascals
mRNA	Messenger ribonucleic acid
MT	Microtubules
mV	Millivolt
MYH6	Myosin heavy chain 6
MYH7	Myosin heavy chain 7
N	Biological replicates
n	Number of cells/nuclei
NF-κB	Nuclear factor κB
ng	Nanogram
nm	nanometre
nNOS	Neuronal nitric oxide
NOX2	NADPH oxidase 2
NUP 153	Nucleoporin 153
P/S	Penicillin/Streptomycin
P188	Poloxamer 188
PBS	Phosphate buffered saline
PCR	Polymerase chain reaction
PDMS	Polydimethylsiloxane
pN	PicoNewton

POMT 1/2	Protein O-mannosyltransferase
rHA	Recombinant human albumin
RI	Rock inhibitor (Y-27632)
RIPK	Receptor intercalating kinase 3
ROS	Reactive oxygen species
Rpm	Rotations per minute
RT	Room temperature
RT-qPCR	Real-time quantitative polymerase chain reaction
RyR2	Ryanodine receptor 2
s	Second
S.D.	Standard deviation
S.E.M	Standard error of the mean
SG	Sarcoglycan
siRNA	Small interfering ribonucleic acid
SNP	Single nucleotide polymorphism
SR	Spectrin repeat domain
SR	Sarcoplasmic reticulum
SSPN	Sarcospan
STAT3	Signal transducer and activator of transcription 3
T3	Triiodothyronine
TAE	Tris acetate EDTA buffer
TGF-β	Transforming growth factor β
TnC	Troponin C
TnI	Troponin I
TnT	Troponin T
TRPC	Transient receptor potential channel
TTN	Titin (gene)
T-tubule	Transverse tubule
v/v	Volume by volume
VEGF	Vascular endothelial growth factor (gene)
WT	Wild-type
WWS	Walker-Warburg syndrome
YAP	Yes-associated protein
α-DG	Alpha dystroglycan
β-DG	Beta dystroglycan
ΔEx	Deleted exon
ε	Strain
µL	Microlitre
µM	micromolar
σ	Stress

1 General Introduction

To see a world in a grain of sand

And a heaven in a wild flower,

Hold infinity in the palm of your hand

And eternity in an hour.

William Blake

Never confuse education with intelligence, you can have a PhD and still be an idiot-

Richard Feynman

1.1 Introduction to the Cardiomyocyte

Cells are in continual communication with their microenvironment, namely the extracellular matrix (ECM), which is essential to their homeostatic and regulatory functions, allowing the perception of physicochemical signals. Physicochemical information is exchanged between cells and the ECM with integration of these signals manifesting in cellular alterations including activation of mechanosensitive proteins such as focal adhesion kinase (FAK), activation of G protein coupled receptors, rearrangement of the cytoskeleton, and lastly regulation of the (epi)genome.

Cells can distinguish between types of force including substrate sensing, pressure, and stretch[1]. Adaptability in the face of such forces requires the complex integration of all physicochemical information, a process termed mechanotransduction. Crucial to mechanotransduction in cardiomyocytes are the costameric regions where myofibrils connect to the ECM, which are comprised of integrin adhesions and the dystrophin-glycoprotein complex (DGC) [2]. In addition to the integrins and DGC, the sarcomere is connected via proteins, such as obscurin and ankyrin. These discrete adhesions lead to a cascade of physicochemical induced signalling within cells including the upregulation of mechanosensitive transcription factors (*e.g.* Yes-associated protein and FAK) that underpin differentiation, proliferation, organogenesis, migration, and disease progression [3,4].

The integrin adhesions and DGC are so crucial within the context of mechanotransduction that more detail on them is provided. The integrins are a superfamily of transmembrane heterodimers comprised of alpha and beta subunits, giving rise to 24 unique combinations in mammals. This allows tissue specific integrin expression patterns to form, suited to the specificities of the ECM required[5]. Integrins have been long recognised as

anchoring cells to the ECM as well as mediating both 'inside-out' and 'outside-in' signalling. In parallel to the integrins, the DGC directly bridges the ECM to the actin and microtubule cytoskeleton thereby establishing the critical connection between the exterior and the interior of the cell[6]. Of particular importance to the DGC is dystrophin. Dystrophin is a cytoskeletal protein encoded by *DMD* (Xp21.1-Xp22) acting to localise and maintain the overall DGC. In addition to this, dystrophin has many other critical functions including maintaining structural integrity of the sarcolemma by protecting against contraction-induced injury and acting as a signalling nexus[7,8].

Accessory proteins have been shown to localise to dystrophin including *bona fide* mechanotransducers, such as neuronal nitric oxide synthase (nNOS), Yes-associated protein (YAP), and caveolin-3 [3,9,10]. Full length dystrophin is 427 kDa, however, multiple internal promoters within *DMD* undergo transcription to produce several naturally truncated isoforms, including the 71 kDa isoform, Dp71m[11]. Full length dystrophin (Dp427m) is expressed predominantly in cardiac and skeletal muscle, however, it has been observed in central nervous system tissues including the retina and Purkinje tissue[12].

In addition to the adhesome, the cellular machinery associated with cell-matrix interactions, formed by the integrins and their downstream targets and the DGC, these two complexes represent the critical interface between the 'inside' and 'outside' of the cell. It is essential for cellular behaviour and survival that these focal adhesions are not abnormally disrupted. Moreover, evidence supports dystrophin as a regulator of mechanosensitive ion channels including stretch-activated channels, particularly L-type Ca^{2+} channels and TRPC channels[13].

Underpinning the importance of the ECM-cell connection and mechanotransduction are the genetically and phenotypically heterogenous diseases, the muscular dystrophies. Muscular dystrophies are frequently the result of disruption between the sarcolemma and the ECM[14] or the nuclear membrane and the cytoskeleton[15]. Mutations in either the integrin adhesion proteins or components within the DGC have revealed themselves to be causes for muscular dystrophies, often culminating in progressive dilated cardiomyopathy (DCM) (Table 1.1 and Figure 1.1)[16,17]. Specifically, mutations within the *DMD* gene, that encodes dystrophin, are the cause of Duchenne muscular dystrophy (DMD), and its milder, allelic variant Becker muscular dystrophy (BMD)[18]. The DGC is comprised of several subcomplexes including α-, and β-dystroglycan (α/β-DG), sarcoglycan-sarcospan, syntrophin, as well as dystrophin[2]. Each of which, if mutated, result in some form of muscular dystrophy.

Table 1.1: Overview of mutations in DGC components and integrins that cause distinct forms of muscular dystrophy. *DCM = dilated cardiomyopathy. LGMD = Limb-Girdle muscular dystrophy. WWS = Walker-Warburg syndrome. XLCM = X-Linked cardiomyopathy*

Disease	Gene	Location	Mutation	Phenotype	Ref
Dystrophinopathy	*Deletions*				
	DMD	Xp21.1	ΔEx 1 (muscle promoter region)	XLCM with fibrosis; Fatal DCM	[19] [20]
			ΔEx 48-50	DCM and aberrant Ca^{2+} handling	[21]
			ΔEx 4	DCM with severe fibrosis	[22]
			ΔEx 48-54	Left ventricular dysfunction with	[23]

				abnormal ECG. Pre-mature death	
	Duplications				
			Ex 2 dup.	Decreased left ventricular function, hypokinesia, and DCM	[24]
			Ex 8-11 dup.	Cardiomyopathy present	[25]
	Point Mutations				
			c.1043 A>G (p.T279A)	Mutation in hinge 1 region of dystrophin. XLCM	[26]
			c.4996 C>T (p.Arg1666X)	Premature stop codon. Arrhythmia and aberrant Ca^{2+} handling. Increased ROS production	[27]
			c.10801 C>T (p.Gln3601X)	Premature stop codon. Exon 76 absent. Cardiomyopathy.	[28]
Dystroglycanopathy	*Deletions*				
	LARGE	22q12.3	ΔEx9-10	WWS present, hypotonia and severe neurological pathology. Premature death at age 6 months	[29]
	Point Mutations				
	FKRP	19q13.3	c.296 A>G (p.Y309C)	Congenital muscular dystrophy with severe	[30]

				hypotonia. Cardiac phenotype not reported by Brockington.	
			c.826 C>A	Mutations in *FKRP* caused LGMD2I with cardiomyopathy reported. Abnormal ECG and respiratory distress.	[31]
	FCMD	19q31	c.859 T>G (p.C250G)	Range of severity. Can be fatal by 1yr as in WWS or relatively mild. Cardiac involvement has been reported.	[32]
	DAG1	3p21	c.575 C>T (p.T192M)	LGMD with neurocognitive difficulties. No cardiac pathology was found.	[33]
	POMT 1	9q34.1	c.430 A>G (p.N144D)	DCM onset at 12yrs with ejection fraction of 36%.	[34]
Sarcoglycanopathy	*Insertions*				
	SGCB	4q12	(Ex 3) 383^384ins37 6-383	LGMD with severe DCM	[35]
	Point Mutations				
	SGCA	17q21	c.218 C>T (p. P73L)	LGMD2D	[36]

Integrins	*Duplications*				
	ITGA7	12q13.2	c.1088dupG (p. H363Sfs*15)	Congenital muscular dystrophy with limb atrophy. Cardiac function was reportedly normal.	[37]
	Point Mutations				
			c.1506-2A>G	Congenital muscular dystrophy with severe neurocognitive difficulties	[38]

Whilst dystrophin is important to the homeostatic function of striated muscle cells, the exact underpinning mechanisms are less obvious, particularly in its capacity to mediate several downstream cellular events such as regulation of mechanosensitive ion channels. Several outstanding questions in relation to the absence of dystrophin have arisen, including: Does dystrophin regulate cytoskeletal architecture, if so, how? If acting as a regulator of the cytoskeleton, to what extent does dystrophin dictate cellular viscoelasticity and how does this compare to the integrins? Does the DGC cross-talk with the integrin adhesions and, if so, how and to what extent? Fully understanding and answering these questions will contribute to better comprehension of the disease phenotype observed in DMD.

1.2 The Cardiomyocyte: The Contractile Cell of the Myocardium

The mammalian heart is the first organ to fully develop during embryogenesis and is comprised of two atria and two ventricles. The

primary function of the heart is to pump blood throughout the body via contraction-relaxation cycles to overcome the inherent limitations imposed by diffusion based nutrient delivery[39]. Central to this is the contractile cell within the heart, termed the cardiomyocyte. Adult cardiomyocytes are approximately 50-100 µm in length and 10-20 µm in diameter[40].

Despite the clearly vital contractile function of the heart, it may be surprising that cardiomyocytes account for only 25-35% of the total cell count within the heart (although they do account for some 70% of the total volume)[41]. The remaining cell types within the heart include endothelial cells (approximately 50%) lining the endocardial surface creating a non-thrombogenic layer; fibroblasts (15-20%) that regulate the composition of the ECM thus acting as major determinants towards myocardial viscoelasticity; and smaller cell populations have been described, including leukocytes[41]. Cardiomyocytes within distinct regions of the heart have subtly different structures. For example, atrial cardiomyocytes typically do not contain transverse (T) tubules. Other structures, such as the venous and arterial vasculature, and lymphatics are comprised of specific cell populations, including vascular smooth muscle cells and macrophages. Interestingly, embryonic sub-populations of macrophages, delineated as CCR2-, may be contribute towards cardiac regeneration in neonatal murine model[42].

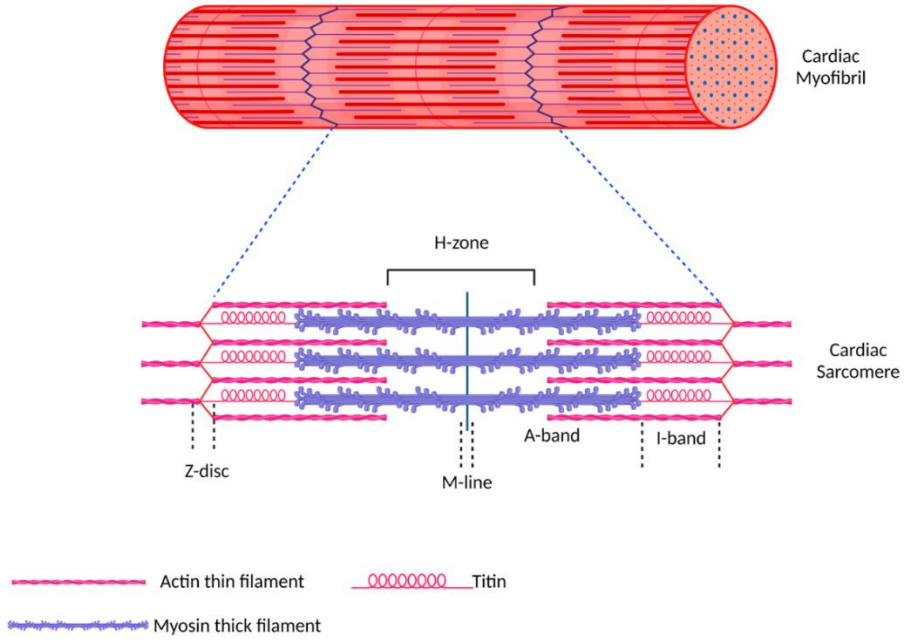

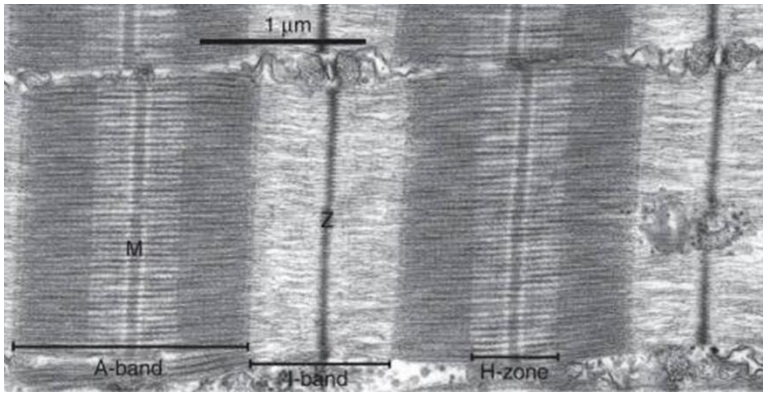

Figure 1.1: Overview of Sarcomeric Cytoarchitecture. *The cardiac sarcomere is comprised of thin filaments (actin) and thick filaments (myosin). These interdigitate to form the physical basis for cross-bridge cycling resulting in cardiac contraction. The Z-disc acts to anchor the sarcomere and is a substantial mechanosensing nexus. Titin is anchored at the Z-disc and confers passive stiffness to the cardiomyocyte. Below the schematic is an electron micrograph highlighting the major sarcomeric regions. Figure created using Biorender.com and EM image adapted* [43]

1.3 The Cardiomyocyte: Form Determines Function

1.3.1 Gap Junctions and Desmosomes

The intercalated disc regions of the cardiomyocyte are comprised of three distinct sub-regions: gap junctions, desmosomes, and adherens junctions[44]. Intercalated discs function to physically connect cardiomyocytes to one another permitting rapid movement of ionic current as well as conferring structural stability. Desmosomes connect to the intermediate filaments within the cardiomyocyte via armadillo proteins, such as plakoglobin and plakophilin, and desmoplakin which connects to desmin in the intermediate filaments[44]. Here, desmosomes can then provide mechanical stability throughout the cardiomyocyte.

Adherens junctions are comprised largely of N-cadherin that is an anchorage site for myofibrils and actin[44]. N-cadherin connects the actin cytoskeleton of adjacent cardiomyocytes together and can interlink to neighbouring N-cadherin proteins of cardiomyocytes. Together, this confers mechanical stability across the myocardial network. Moreover, N-cadherin can act as a mechanosensor and can regulate downstream proteins, including JNK[44].

Gap junctions are large hexameric channels termed connexons that are in close proximity to neighbouring cardiomyocytes (approximately 4 nm). Each connexon is comprised of six connexin 43 proteins and allow molecules of up to 1 kDa to readily pass[44](Figure 1.2). Connexin 43 is the predominantly expressed connexin within the heart and is highly expressed in the ventricles. Gap junctions mediate rapid electrical throughput between cardiomyocytes, allowing the myocardium to function as a syncytium.

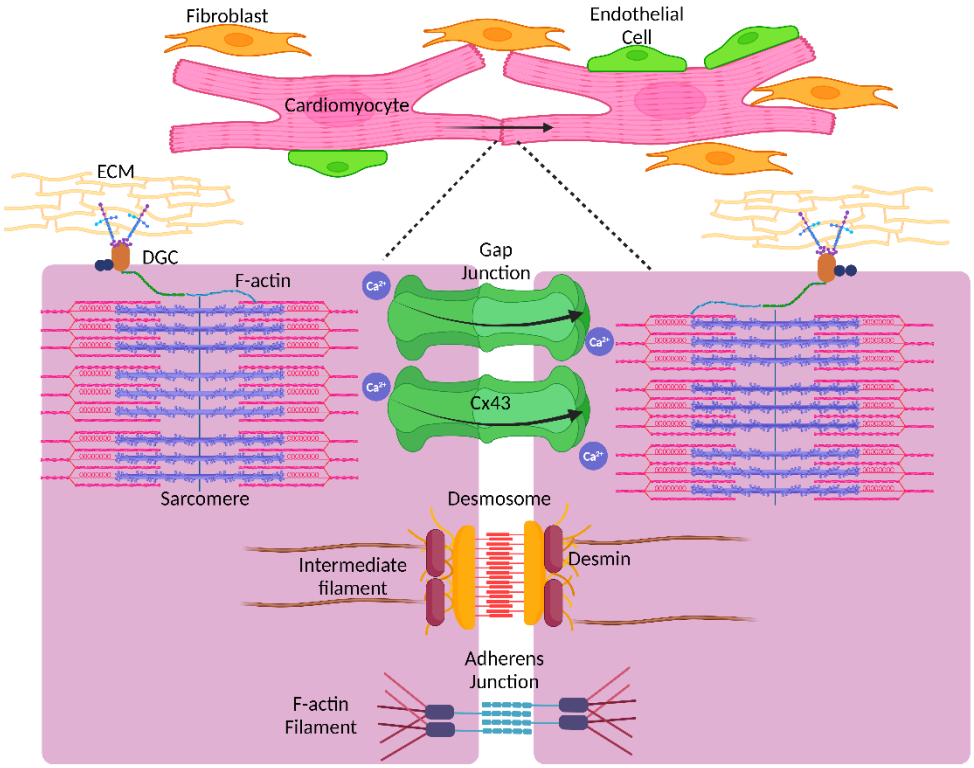

Figure 1.2: The Cardiomyocyte Intercalated Disc. *The intercalated disc between two cardiomyocytes depicting gap junctions, desmosomes, and adherens junction. Gap junctions, comprised of connexin 43, facilitates rapid flux of Ca^{2+} ions required for syncytial contraction of the myocardium. The desmosome confers structural stability. Desmin is bound via plakoglobins and plackophilins, connecting to intermediate filaments. Adherens junctions comprised of cadherins provide tensile stability and anchorage between cardiomyocytes. Adherens junctions also connect to F-actin filaments. Image created using Biorender.*

1.3.2 The Costamere

The costamere is located on the lateral aspect of the cardiomyocyte and is the major site for the ECM-cell interface. Two macromolecular complexes establish the connection to the ECM: integrin-vinculin-talin adhesions[1] and the dystrophin-glycoprotein complex (DGC)[45]. Functionally, the costamere

enables lateral force transmission and the dissipation of contraction-induced forces, in addition to bidirectional signalling, although it is important to note that not all signalling is bidirectional. Focal adhesions are pivotal hubs for mechanotransduction and allow both 'outside-in' and 'inside-out' signalling. The DGC is the focus of the work here and more detail is provided later.

Integrins connect to talin and vinculin, both of which reinforce the stability of the complex as well as connecting to the cytoskeleton[46]. Integrin activation depends on RIAM and VASP proteins as well as sufficient force. The heart contains two isoforms of talin, talin-1 and -2, that share 80% homology but are functionally distinct [47]. These are developmentally regulated within the myocardium with talin-2 having increased affinity for β1D binding. Talin and vinculin act as mechanosensors where their assembly is contingent upon a minimal force threshold, such that soft substrates generate insufficient forces to activate talin and vinculin localisation to the integrins[46].

1.3.3 The Sarcomere

Myofibrils are roughly 1 µm in length and composed of multiple sarcomere units[48]. The sarcomere is the fundamental unit of contractility within the cardiomyocyte with a hexagonal lattice of actin thin filaments that interdigitate to myosin thick filaments[48]. The diastolic resting length of the sarcomere approximates 2 µm with thick filaments being 1.6 µm long and 11 nm wide alongside thin filaments that are 1.05 µm in length and 6 nm wide[48].

Thick filaments are chiefly comprised of class II contractile myosins, of which MYH6 and MYH7 are cardiac specific[49]. Cardiac maturation sees

isoform switching between MYH6 and MYH7 from the embryonic-like MYH6 to MYH7 that is primarily expressed within adult cardiomyocytes. The adult ventricle contains 95% MYH7 to 5% MYH6, and this is considered a biomarker of maturity[49]. Additionally, upregulation of *GATA4* and triiodothyronine 3 expression regulates sarcomere maturation[50]. Structurally, the globin heads of myosin bind to actin, and the coiled-coil domains form α-helices to give the thick filaments typical appearance[49]. Thick filaments also contain a sarcomeric stabilisation protein, cardiac myosin binding protein C [51].

Thin filaments are comprised of F-actin, two forms of tropomyosin, and three troponins: troponin I (TnI), troponin C (TnC), and troponin T (TnT)[52]. Together, the troponin-tropomyosin complex forms the Ca^{2+} regulatory complex, vital to excitation-contraction coupling. The heart contains several isoforms of actin, but α-cardiac actin encoded by *ACTC* accounts for some 80% of all isoforms[49]. Actin and myosin interdigitate and slide during excitation-contraction coupling causing sarcomere shortening.

Titin is the largest protein within the human genome formed by 363 exons and spans from the Z-disc to the M-band of sarcomeres[49]. Functionally, titin primarily acts as a molecular spring, dictating passive diastolic stiffness (smaller contributions to passive stiffness come from other proteins, including microtubules)[4]. Three isoforms of titin have been described, including the compliant foetal titin, and two adult isoforms, N2B and N2BA, that share more than 90% homology[49]. Isoform switching occurs during cardiogenesis and further regulation of titin is achieved by posttranslational modifications. The portion of titin within the I-band of the sarcomere houses the highly extensible regions, including the PEVK and N2B(A) domains[47]. N2BA is more extensible and compliant than N2B, however both

isoforms are expressed. The ratio between isoforms determines the overall passive stiffness for the heart (30:70; N2BA: N2B)[53]. Increased expression of the more compliant N2BA isoform has been described in patients with dilated cardiomyopathy (DCM), accounting for increased stretching and dilatation observed in these patients[53]. The portion of titin within the A-band is inextensible.

1.4 The Cytoskeleton

The multitudinous functions of the cytoskeleton include cellular migration, polarity, mitosis, nutrient delivery, and mechanotransduction to name a few[54,55]. Overall, the cytoskeleton is distinguished into three major subtypes: actin filaments, microtubules, and the intermediate filaments[54,55]. The cytoskeleton is highly dynamic and adaptable, necessary for responding to stimuli and enacting cellular alterations. Moreover, the cytoskeleton governs the viscoelastic properties of the cardiomyocyte, an important determinant for cell homeostasis. The cytoskeleton is a prestressed structure that maintains morphology of the cell[56]. This is largely achieved by the tension generating actomyosin filaments against the compressive, resistant microtubules. Together, actin and microtubules maintain an equilibrium of force distribution throughout the cell. The crosslinked nature of the cytoskeleton is largely responsible for the viscoelastic properties observed[56].

1.4.1 The Actin Cytoskeleton

Free globular actin monomers (G-actin) assemble to form filamentous actin (F-actin), a highly dynamic structure. Three actin isoforms are present within vertebrates, α-, β-, and γ-actin. Only α-actin is specific to striated muscle, with β- and γ-actin ubiquitously expressed amongst tissues. Actin

filaments, approximately 8 nm in diameter and 6-7 µm in length, have polarity with barbed ends being inserted at the Z-disc of the sarcomere and pointed ends face towards the M-band[55]. Whilst individual actin filaments have variable mechanical properties, such as stiffness, larger order structures can be formed in conjunction with accessory proteins, increasing overall actin stability[57]. Nucleation of actin monomers is the main rate-determining stage of actin assembly.

A suite of accessory proteins regulates the formation of higher order structures. In cardiomyocytes, α-actinin is an important crosslinker of F-actin, with cardiac specific isoform encoded by *ACTA2*[55]. An α-actinin 2 homodimer cross-links two adjacent anti-parallel F-actin filaments forming a structurally stable lattice, essential for Z-disc stability. Moreover, α-actinin is a binding partner to numerous other proteins at the Z-disc, for example titin and muscle LIM domain proteins[55].

1.4.2 The Microtubule Cytoskeleton

Microtubules are structurally larger compared to actin filaments and are rigid, cylindrical hollow tubes approximately 25 nm in diameter[58]. Microtubules are highly dynamic, and nucleation is GTP dependent, in contrast to the ATP dependency of actin filaments (Figure 1.3). α- and β-tubulin dimers form a protofilament and the assembly of thirteen such protofilaments forms the microtubule polymer[58]. This confers a large degree of physical stiffness to the macromolecule.

The minus-end of the microtubule is stabilised by the microtubule-organising centre and is slow growing and chiefly comprised of α-tubulin, whereas the plus-end of the microtubule undergoes a series of rapid polymerisation and depolymerisation, comprised of β-tubulin monomers[58].

Tubulin monomers may also undergo various posttranslational modifications, such as detyrosination or acetylation[59,60], that modulate the biomechanical properties of the final structure.

Microtubules organise subcellular domains within the cardiomyocyte, for example, anchoring the nucleus to the Z-disc. Detyrosinated microtubules underpin this process via the A-kinase anchor proteins that bind to the linker of nucleo- and cytoskeleton (LINC) complex[61]. Moreover, microtubules are responsible for trafficking and localising proteins to the intercalated disc. Importantly, microtubules govern the transport of connexin 43 to the intercalated discs[62].

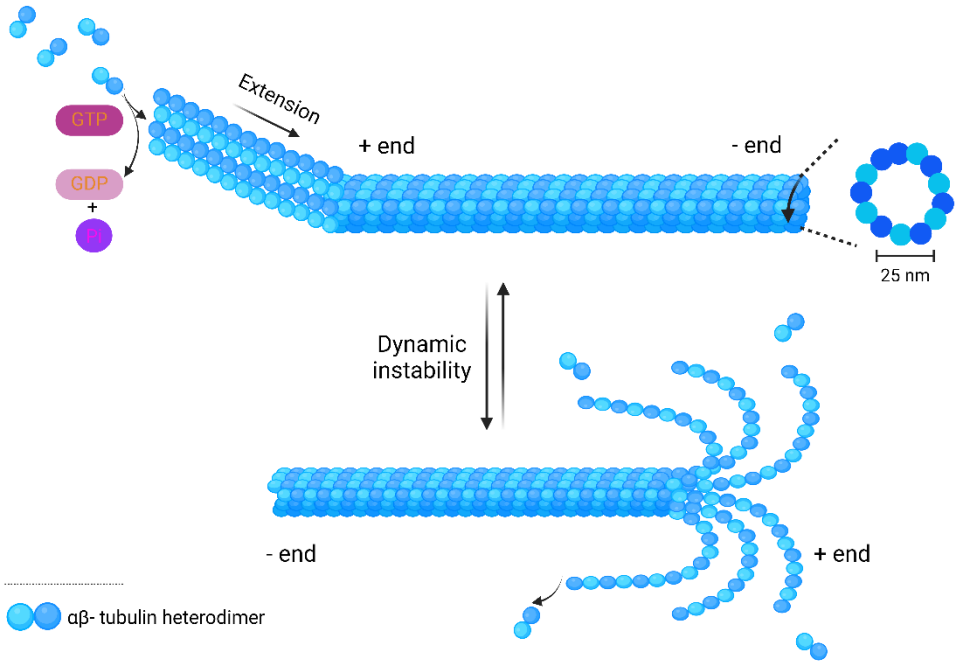

Figure 1.3 Assembly and Disassembly of Microtubules. *Microtubules form a protofilament and extend at the + end in a GTP dependent manner. A microtubule organising centre (not shown) anchors the growing microtubule. Actin undergoes similar formation but is ATP dependent. Image created using Biorender.*

1.5 The Cardiac Extracellular Matrix is Critical to Cardiac (Patho)physiology

1.5.1 The Healthy Cardiac Extracellular Matrix (ECM)

The cardiac ECM is a diverse, plastic, three-dimensional structural meshwork maintaining the geometry of the heart[63]. Embedded within this network are cardiomyocytes, cardiac fibroblasts, endothelial cells, and resident macrophages, each contributing to myocardial homeostasis. Far from being an inert and passive entity, the ECM is intimately involved with regulating cardiomyocyte functions including force transmission, cytoskeleton dynamics, proliferation, as well as acting as a reservoir of cytokines, metalloproteinases, and other signalling proteins[63,64]. The ECM responds to cardiomyocyte biochemical and biomechanical actions and, in tandem, promotes a spatiotemporally regulated matrix optimised to housing cardiomyocytes. At the organ scale, this translates to a functional heart able to perform its diastolic and systolic functions that are essential for life.

The physicochemical profile of the cardiac ECM alters throughout development and disease[64]. The embryonic cardiac ECM expresses collagen I, chondroitin sulphate, fibulin, and fibronectin, amongst other constituents[63]. In particular, fibronectin is instrumental in orchestrating the initial myocardial developmental steps by promoting cell migration, adhesion, and polarity[64], notably via the expression of the embryonic isoforms EIIIA and EIIIB[65,66]. Expression of fibronectin is critical to the development of the nascent heart and mutations have been shown to be embryonically lethal, underpinning its crucial role within the cardiac ECM[67,68].

As cardiac maturation proceeds, a phenotypic switch of the proteoglycans occurs in the myocardial ECM, with glycosylation of α-DG marking the transition from nascent/embryonic fibronectin rich cardiac ECM towards the adult-like laminin-211 binding[69]. Establishing the DGC-ECM axis signals maturation of the costameric and focal adhesion regions necessary for mechanotransduction[69].

The interaction between the DGC and laminin is so essential to the discussion that further detail on laminin is warranted here. The laminins are a large family of heterotrimeric proteins composed of three peptide chains (α, β, and γ) located in the basement membrane compartment of the cardiac ECM, with key functions in cell adhesion, mechanotransduction, and cross-linking other proteins[70,71]. Foremost, in the context of muscular dystrophies, including DMD, laminin occupies a particularly important role as it is the direct binding partner to α-DG and α7β1D[72]. Disrupting the interaction between the DGC and laminin α2 causes the phenotypes observed in DMD/BMD and Limb Girdle Muscular Dystrophy Type 2I (LGMD2I)[2,73,74]. Moreover, mutations in the *ITGA7* gene, encoding for α7 integrin, are a cause of congenital muscular dystrophy that is phenotypically similar to DMD[16,75].

In addition to laminin, the adult heart expresses collagen I (80%) and collagen III (10%) and the ratio between the two is particularly important to myocardial elasticity[71]. Type I collagen is a determinant of tensile strength and stiffness, whilst type III collagen confers elasticity to the ECM. Overexpression of collagen I increases passive stiffness in the diseased myocardium. Both collagens contribute to the overall viscoelasticity of the ECM to give a Young's modulus (a measure of stiffness) of approximately 10 kPa[76]. The remainder of the cardiac ECM is comprised of several other

distinct glycosaminoglycans and proteoglycans, for example agrin[77] and pikachurin[64,78].

Although the exact mutations disrupting the ECM-cell interface may vary, the underlying concept remains clear. That is to say, a compromise in the connection of ECM-cell interface is a driver for the cardiac phenotype associated with muscular dystrophy. Once the linkage to the ECM is lost, the cardiomyocyte's capacity for mechanosensing is diminished. This subsequently impacts the ability of the myocardium to respond to, or govern, alterations within its environment[79].

1.5.2 The Cardiac ECM in DMD Associated DCM

The ECM in DMD undergoes significant alterations including fibrosis, elevated inflammatory infiltrate, and, as a result, cardiomyocyte necrosis. As the cardiac ECM has a critical role in transmission of physiological force at the cellular level, and regulating diastolic and systolic function, any alterations to the biomechanical profile can distort mechanotransduction[63].

Further, the capacity for adult cardiomyocyte proliferation is extremely limited occurring at a rate of approximately 1% *per annum*. This rate of proliferation is incapable of maintaining pace with lost cardiomyocytes in DCM and fulminant heart failure[80]. DCM and heart failure commonly result in the premature death of DMD/BMD patients, therefore consideration of the cardiac ECM and cardiomyocyte renewal in the context of DMD is prudent[81].

In response to injurious stimuli, ageing, or disease, the cardiac ECM undergoes expansion in a process termed remodelling[4,64]. Remodelling alters the physicochemical composition of the ECM, often exacerbating the underlying pathology[82]. In this manner, the cardiomyocyte-ECM interaction

results in a positive feedback axis pushing further towards heart failure. It should be noted here that heart failure is a heterogenous disease with distinct aetiologies that may all have some unique underpinning aspect. For example, consider the distinction between dilated and hypertrophic cardiomyopathies.

Viscoelasticity of healthy myocardium is reported as 10 kPa[83] increasing to as much as 50-130 kPa in the fibrotic myocardium[4,76]. This is a direct consequence of the increased deposition of collagen type I and fibronectin[63,66,84], with several groups reporting increased stiffness in diseased hearts[85–90]. More specifically, the initial phases of remodelling include the activation of proinflammatory and profibrogenic cytokines, such as Transforming Growth Factor (TGF) β and lysyl oxidases (LOX), that reside within the cardiac ECM[91]. TGF-β has been reported to decrease the activity of matrix metalloproteinases whilst concomitantly increasing the expression of profibrotic enzymes, such as tissue inhibitors of metalloproteinases[92]. Additionally, TGFβ/LOX promote the deposition of collagen type I, thus tilting the ratio in favour of collagen I thereby increasing the myocardial stiffness[63,93].

Increased collagen type I promotes diastolic dysfunction due to decreased compliance of the heart[85], as well as promoting arrhythmias by disrupting re-entry circuits[94]. Elevated myocardial stiffness leads to altered cell morphology, disrupted sarcomeric architecture, abnormal electromechanical coupling, aberrant mechanotransduction, posttranslational modifications of the cytoskeleton, and altered gene expression[85,86,89,90,95]. Groups[86] have reported disorganised myofibril striations when cardiomyocytes were cultured on fibrotic elasticity (34 kPa) which were associated with decreased beating rates. This strongly supports

the notion that ECM-cell relationship is well optimised and attuned in a tissue specific manner.

Moreover, expression of alternatively spliced isoforms of fibronectin increases, such as type III repeat extra domain A (EDA), which promotes cardiac inflammation via recruitment of myofibroblasts and monocytes. Proinflammation leads to increased cardiac fibrosis[84,96,97]. Inhibiting fibronectin overexpression was shown to attenuate fibrosis associated with heart failure and improved cardiac function for 4 weeks post-ischaemia[84]. Lastly, fibronectin EDA III promoted activation of nuclear factor κB (NF-κB), further exacerbating adverse cardiac remodelling[98]. Cumulatively, these data highlight the important and dynamic role that the cardiac ECM plays in maintaining appropriate biomechanics of the heart. It also indicates how the disrupted ECM in muscular dystrophies is a significant driver towards the disease phenotype.

Finally, the interplay between fibrosis and altered mechanotransduction caused by mutations in the DGC that disrupt the ECM-cell interface is not clearly defined. What is clear, however, is that it does alter mechanotransduction which can be a signifier of cell death[99]. Myocardial remodelling has shown itself to be a cause for necroptosis via activation of receptor-interacting kinase 3 (RIPK3) in DMD[100,101]. Recently it was shown that myocardial fibrosis activated a RIPK1-RIPK3 complex that promoted cardiac dysfunction and decreased autophagy, leading to increased cell death[102]. Moreover, fibrotic stiffness can have a deleterious impact on the genome of DMD cardiomyocytes, where increased stiffness can drive shortening of telomeres as well as promoting activation of p53 and p21[103].

Therefore, the ECM-DGC axis of cardiomyocytes is vital, especially given that fibrosis is a hallmark in the myocardium of DMD. A positive correlation

between the extent of fibrosis and poor clinical outcomes has been reported for DMD[91,104].

The mechanosensing apparatus of cardiomyocytes at costameric regions allows bidirectional communication via a cytoskeleton-DGC-ECM axis alongside the integrins, influencing substrate rigidity[4,95]. Cardiac passive stiffness is determined by the interaction of titin and microtubule network to the sarcomere[4] with de-tyrosination mediating this interaction[105,106]. De-tyrosinated microtubules are increased in DMD and is a driver of cardiac pathogenesis by promoting reactive oxygen species (ROS), altered cell stiffness, and dysregulated Ca^{2+} handling[59,60,99]. Decreasing de-tyrosination of microtubules in *mdx* model improved the overall cardiac function, as determined by decreased contraction-induced injury and incidence of arrhythmias, highlighting the importance of the cytoskeleton in this context[99].

1.6 The Dystrophin Glycoprotein Complex (DGC) is a Large Sub-Sarcolemmal Complex Connecting the Intracellular Cytoskeleton to the Cardiac Extracellular Matrix

1.6.1 Overview of the DGC

The DGC is a multiprotein complex located at the costameric region of cardiomyocytes with several important functions including, providing structural stability to the sarcolemma and thus protecting against contraction-induced injury; acting as a molecular scaffold for multiple proteins thereby functioning as a signalling nexus; regulating mechanosensitive ion channels, such as the TRPC channels, and lateral force transmission at the costameres (Figure 1.4).

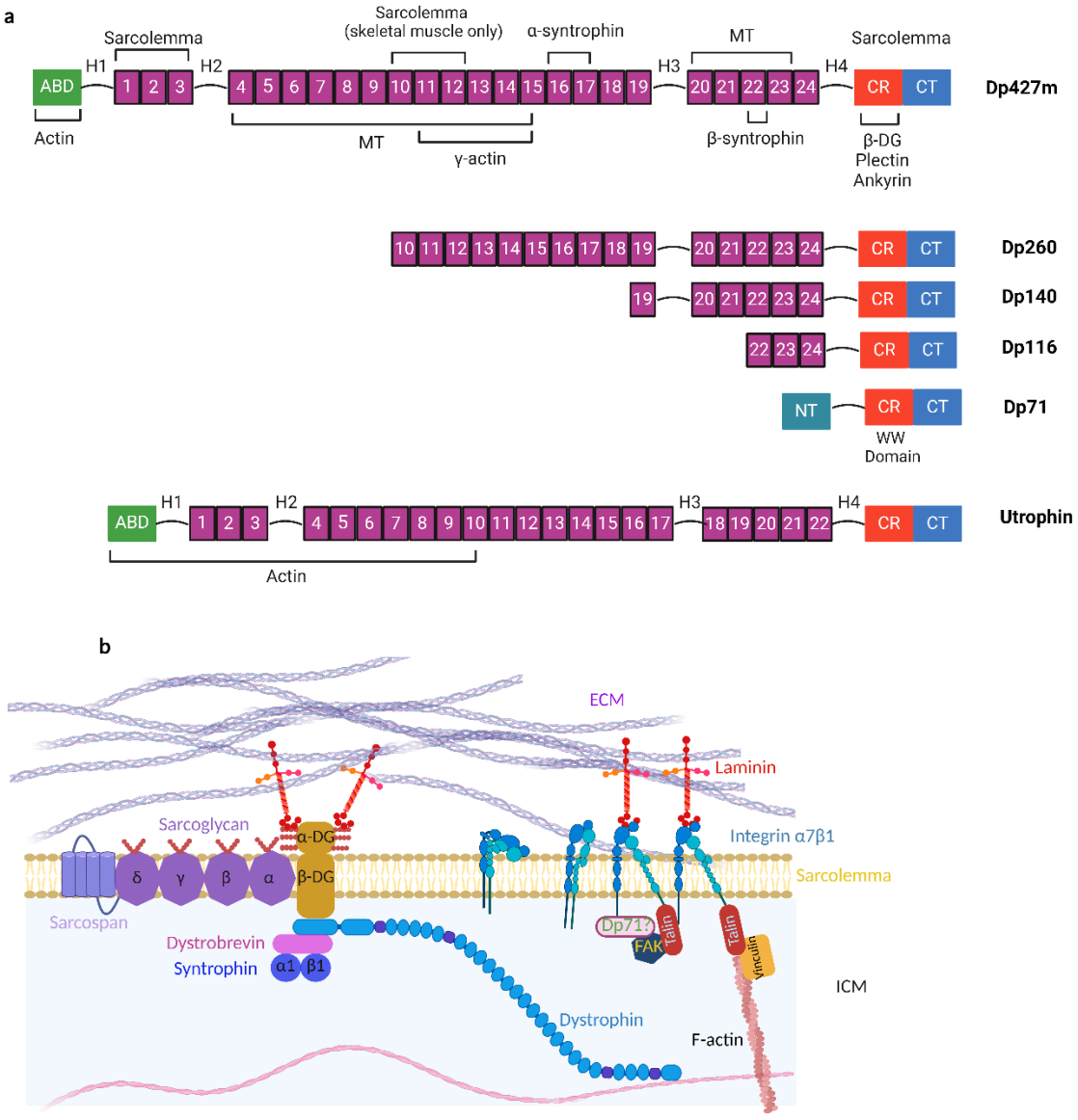

Figure 1.4: Overview of the Dystrophin Glycoprotein Complex with a Focus on Dystrophin and its Isoforms. A) *Schematic depicting several key dystrophin isoforms and important binding regions. Utrophin localises at the sarcolemma of embryonic cardiomyocytes and is replaced by full length dystrophin over time. Note the similarity between utrophin and Dp427. However, utrophin is shorter and unable to bind to microtubules. Dystrophin has 24 spectrin repeats separated by four hinges, as well as having an actin binding domain (ABD), cysteine rich (CR) domain, and c-terminus (CT). Key binding partners are highlighted, including microtubules (MT) and the sarcolemma.* ***B)*** *The dystrophin glycoprotein complex*

(DGC) as a whole, situated at the sarcolemma. Biomechanical forces are transduced between the ECM to F-actin. Note the potential crosstalk between the DGC and integrin adhesions, with Dp71 potentially having a role at focal adhesions. Image adapted from: [45]

The cornerstone of the DGC is the protein dystrophin, which is necessary for the localisation and maintenance of the entire complex. Multiple isoforms of dystrophin have been described and expression of these isoforms can be unique within tissues. For example, cardiac tissue expresses full length (Dp427m) as well as a shorter dystrophin isoform, Dp71m, whilst skeletal tissue expresses only the former[11]. Looking at the roles that each isoform has may reveal novel insights into not only its physiological function but also the pathogenesis in muscular dystrophies. Elucidation of the shorter isoforms may also confer some therapeutic advantage as a mini- or micro- dystrophin.

Mutations within the dystrophin gene (*DMD*) result in the severe muscular dystrophy, DMD/BMD, as well as the downregulation, and in cases complete absence, of the other DGC constituents. Therefore, an appreciation for the entire DGC complex is required to understand how the loss of these proteins contributes towards the disease phenotype.

The composition of the DGC was unravelled during the late 1980s with a particular focus on dystrophin. Seminal discoveries towards identification of dystrophin were carried out by Koenig[107,108], Hoffman[109], and Ervasti[110] revealing dystrophin to be a 427 kDa protein in striated muscle tissue[111].

Subsequent work revealed the presence of additional subcomplexes associated with dystrophin including, sarcoglycans, sarcospans, dystroglycans, dystrobrevin, and asyntrophins[2], together forming the current model of the DGC. This section will first disseminate the evidence

for a role of the DGC in mechanosensing whilst looking at the individual components in detail.

1.6.2 Dystrophin

The full-length isoform of dystrophin present in striated muscle tissue is Dp427m ('m' indicates muscle isoform to distinguish from others, *e.g.* brain) and is a large rod protein comprising four functional domains localised at the sub-sarcolemma in cardiomyocytes, specifically at costameric regions[109,112]. Dp427m is encoded at Xp21.1 by the *DMD* gene, comprised of 79 exons from 2.2 megabases and is the largest gene within the human genome[2].

The presence of the DGC at costameres immediately suggests its role in mechanotransduction and it has been shown to co-localise with integrin adhesions and the cytoskeleton[113]. Moreover, given that costameres are focal points for lateral mechanical force transduction, the localisation of Dp427m here highlights its role in protecting cells against contraction-induced injury. Downstream, Dp427m interacts with the actin and microtubule cytoskeleton thereby completing the connection of the intracellular *milieu* to the ECM.

Several internal promoters within *DMD* produce a variety of functional truncated isoforms of dystrophin, some of which display tissue specificity. One such case is the small isoform, Dp71m. Dp71m lacks the spectrin repeat domains and N-terminal actin binding domain (ABD), whilst retaining a CR/CT domain, enabling Dp71m to interact with the sarcolemma.

In cardiomyocytes, the role of Dp71m is unclear, but evidence suggests that it localises at T-tubules suggesting a role in excitation-contraction

coupling[114–116]. To the best of my knowledge, examination of Dp71m in cardiac tissue has not recently attracted significant attention, but previous groups have shown it to be involved in stretch-activated ion channels and the regulation of nNOS[114,117]. In contrast to cardiac research, Dp71 has been the subject of extensive research in both neuroscience and platelet research fields. Reviewing the findings from these works may further our understanding, or hint at, a role for Dp71 in cardiomyocytes[118–120].

Within neural tissue, Dp71b is the predominantly expressed isoform of dystrophin, with some 14 sub-variants reported[119]. Dp71b is an important regulator of aquaporin-4 and Kir4.1 potassium ion channels, and its absence has been shown to cause alterations in the permeability of the blood-brain-barrier[121]. Given the role of Dp71b in regulating ion channels, we can speculate that Dp71m may be acting similarly in cardiomyocytes.

A more in-depth examination of the protein structure of dystrophin now follows. Structurally, Dp427m is a filamentous rod protein comprised of four regions (Figure 1.4).

An N-terminal ABD1, composed of two calponin homology (CH) domains, is crucial for interacting with F-actin and for securing γ-actin to the sub-sarcolemma[122,123]. The connection between the ECM and cytoskeleton is mediated by dystrophin and this suggests that dystrophin contributes to the viscoelasticity of the cell, as described by tensegrity model (this is discussed in further detail[124,125] in §1.8).

The central rod domain is comprised of 24 spectrin-like repeat proteins (SR), each approximately 100 amino acid residues in length[2]. The SRs are interspersed by four hinge domains conferring flexibility and extensibility to dystrophin, hinting at a mechanoprotective function. Evidence for

dystrophin's putative mechanoprotective role was provided by Le[8] where the extensibility of the SR domains was demonstrated. Using magnetic tweezers it was shown that the SR domain could extend over 800 nm within physiological force range (15-30 pN); forces achieved by actomyosin contraction[126]. Here, the authors suggested that this was a plausible property of dystrophin allowing it to 'buffer' against contraction-induced injury, enabling dystrophin to act as a molecular shock absorber[8].

Additionally, the central rod of Dp427m secures the protein to the sarcolemma via hydrophobic and electrostatic interactions with phosphatidylserine[127,128]. Interestingly, dystrophin's central rod interacts with sarcolemmal phospholipids differently between skeletal and cardiac tissue, perhaps reflecting tissue specific requirements for spring-like activity (compare continual cardiac contractility to voluntary skeletal muscle contractility)[129]. Specifically, in cardiomyocytes, SR domain R1-R3 and CT/CR domains are crucial to sarcolemmal binding, whilst skeletal muscle additionally binds via SR domain R10-R12[129].

Dystrophin's interaction to the cytoskeleton is partially mediated by the SR domains. Connection to γ-actin requires SR 11-17 of ABD2, composed of basic amino acid residues, and is distinct from CH domains. Microtubules directly interact with dystrophin's rod-domain via SR 4-15 and 20-23[130–132]. Disruptions between microtubules and dystrophin have been shown to increase ROS, exacerbating the DMD phenotype[99].

The CR region contains a WW domain binding directly to the PPxY motif of β-DG[2]. The connection between dystrophin and the dystroglycan complex establishes the ECM-cell axis[133]. This connection is vital for striated muscle as evidenced by the fact that disrupting the link between the ECM and cell interior causes life-limiting muscular dystrophies.

A secondary attachment point sarcolemmal phospholipids comes from the CR domain. This interaction is mediated by the presence of ankyrin-B[131]. Ankyrin-B and ankyrin-G are required for the costameric localisation of dystrophin and the DGC as a whole, as their absence leads to diffuse sarcolemmal patterning of the DGC[131].

Lastly, the CT domain is highly conserved region that forms coiled-coils, crucial to binding with α-dystrobrevin and α1-, β1-syntrophins[134,135]. α-dystrobrevin binds to the CT domain of dystrophin providing additional sarcolemmal stabilisation of dystrophin[136].

1.6.3 Utrophin

Utrophin is the autologous homologue of dystrophin, expressed by *UTRN* located on chromosome 6q, sharing 80% protein homology. Utrophin is widely expressed in various tissues including endothelial cells, neuronal tissues, and striated muscle tissue during embryonic and foetal development[137]. Embryonically, utrophin localises at the sarcolemma and is subsequently downregulated postnatally in striated muscle tissues, being replaced by dystrophin[135]. Postnatally, utrophin localisation is limited to myotendinous and neuromuscular junctions of skeletal muscle[137,138].

The binding partners of utrophin are generally similar to that of dystrophin, although some key differences have been described. For example, dystrophin interacts with β-DG specifically via its WW domain, stabilised by the ZZ domain within its CT region (specifically mediated via cysteine residues 3307-3354)[139,140]. Utrophin also binds to β-DG via WW/ZZ domains, but the exact residues underpinning this interaction are distinct to that of dystrophin (3064-3102 in utrophin)[139,140]. Importantly, binding of utrophin to β-DG was approximately 2-fold lower compared to that of

dystrophin, suggesting some distinction in its function[140]. It was reported that dystrophin bound to F-actin via SR 11-17 whilst the comparable region in utrophin was unable to bind to F-actin, regardless of large F-actin concentrations[141–143]. Lastly, utrophin cannot bind to microtubules, unlike dystrophin[132].

Biomechanically, the SR of utrophin have a distinct unfolding pattern compared to dystrophin[144]. Utrophin SR unfold at larger forces, similar to that of titin and not dystrophin[144]. This is appropriate in its capacity for localising and transducing force at stiff elastic myotendinous junctions but may render utrophin less suitable buffering against contraction-induced forces[144]. Together, these data suggest altered mechanotransduction and mechanical buffering in the instance of utrophin overexpression, especially in light of its differential binding partners and mechanisms, however this requires further validation.

Despite these distinctions, utrophin is considered to perform similarly to dystrophin, leading to its consideration as a potential therapeutic strategy for DMD/BMD[145,146]. In fact, some patients with DMD re-express utrophin, presumably as a compensatory mechanism, a notion supported by phenotypic rescue in murine models with utrophin overexpression[147]. Whilst upregulation of utrophin is a plausible therapeutic strategy, long-term utrophin strategies are unclear at present due to its distinct form and function compared to dystrophin. Moreover, implementation and localisation of utrophin over a long time-frame will require some degree of consideration, as this is not straightforward. Of special interest are female carriers harbouring *DMD* mutations. Here, a mosaic pattern of dystrophin expression has been reported and it is interesting to note that this is also reflected by the expression of utrophin. The ratio between dystrophin and

utrophin may potentiate the extent of DCM in this cohort of patients[148], although murine carrier models have shown comparable cardiac compliance to that of WT[149] suggesting that female mosaics are less affected compared to DMD patients.

1.6.4 The Dystroglycan Sub-Complex

The dystroglycan complex is comprised of both α- and β-dystroglycan (α-, β-DG), transcribed from the *DAG1* gene. *DAG1* undergoes posttranslational cleavage into the two constituent proteins[150]. α-DG is heavily glycosylated on the extracellular aspect of the DGC and directly interacts with laminin-211, agrin[151], pikachurin[78], and the proline residues of dystrophin's CT/CR region[77,78,152,153]. The *O*-linked glycosylation, particularly that of serine residues, is essential for its interaction with the ECM and is carried out by the glycosyltransferase fukutin related protein encoded by *FKRP.* It is also involved in the development and maintenance of the ECM, as indicated by decreased expression of laminin α2 and α-DG when *FKRP* is mutated[30,154]. Moreover, FKRP may also direct basal lamina formation and cardiac ECM modification by glycosylating fibronectin[69]. Other proteins associated with the functional glycosylation of α-DG include POMT2 which has *O*-mannosyltransferase activity as well as the protein LARGE1[155].

β-DG contains a PPxY binding motif that directly localises and sequesters the mechanosensitive transcriptional co-activator YAP[3], implicating the DGC towards regulation of the cardiomyocyte cell cycle. α-DG in neonatal cardiomyocytes interacts with agrin thereby promoting cardiac regeneration at the expense of cell maturation as well as causing dissolution of the DGC[77]. As maturation of cardiomyocytes proceeds, agrin expression decreases and is replaced by laminin, thought to promote cell-cycle arrest[77]. Morikawa[3] showed that double knockouts of dystrophin and

Salvador (a negative regulator of YAP) lead to over proliferation of cardiomyocytes at a scar region generated by myocardial infarction. This has led to the exciting notion that manipulation of YAP could be clinically valuable against tissue loss for heart failure. Dissolution of the DGC induced by agrin may therefore represent an axis that permits the activation of YAP, thus making it a potential avenue for cardiac regeneration. Although, the long-term impact of YAP re-expression or agrin in the myocardium remains unclear.

Mechanically, α- and β-DG are required to maintain the interaction between the sarcolemma and the basal lamina[156]. Both α-DG and α7 integrin contribute to force production and transmission at costameres. Absence of α-DG causes dissociation of the sarcolemma from the basal lamina[156], rendering muscle tissue susceptible to contraction-induced injury. As mentioned previously, the dystroglycan complex regulates the overall turnover of the DGC when engaged to its cognate ligand, laminin. This results in phosphorylation of tyrosine 892 of PPxY binding motif in β-DG [157], leading to detachment from dystrophin. Physiologically, this process is highly regulated and is absent in muscular dystrophies[157].

Cyclic stretch has been shown to activate ERK1/2 and AMPK pathways via the dystroglycan complex and plectin[158]. Together, plectin and dystroglycan were required to act not only as a scaffold, but involved in mechanotransduction as well, with the knockdown of plectin decreasing ERK1/2 and AMPK activity[158]. The binding of plectin to the cytoskeletal protein, desmin, was shown to ameliorate the disease phenotype observed in a *mdx:desmin* and *mdx* mice[159]. In this way, plectin acts to link β-DG to the intermediate filament cytoskeleton. Moreover, dystroglycan interacts with the growth factor receptor-bound protein 2 (Grb2) known to be

involved with cytoskeletal rearrangement[160]. Integrin activation of Ras was shown to be mediated via Grb2 and this may represent a potential avenue for cross-talk between integrins and the DGC[161].

Mutations of the genes involved in the glycosylation of α-DG result in dystroglycanopathies. Phenotypically, dystroglycanopathies display great diversity. Underpinning each, however, is the disruption of the ECM-DGC interaction[30]. Primary dystroglycanopathies caused by mutations in *DAG1* are extremely rare due to the embryonic lethality[162]. This further underpins the necessity for the ECM-cell axis.

The majority of dystroglycanopathies are caused by mutations of proteins associated with the glycosylation stages. Glycosylation of α-DG is mediated by over a sequential series of steps, each dependent on the successful glycosylation of the preceding step. Therefore, a hierarchy presents itself, where mutations nearer the initial steps of glycosylation cause increasingly severe disease phenotypes. For example, mutations in *POMT1* give rise to the extremely severe Walker-Warburg Syndrome, characterised by lissencephaly and significantly reduced lifespan of less than 3 years[163]. However, mutations in *FKRP* largely manifest as Limb Girdle Muscular Dystrophy (LGMDs) which are often, though not always, relatively mild. Mutations in *FKRP* have, however, been shown to be a rare cause for WWS[164]. Numerous mutations have been identified in *FKRP* with the founder mutation (c.826>A) most commonly causing LGMD2I[165].

1.6.5 The Sarcospan-Sarcoglycan Sub-Complex

The sarcospan-sarcoglycan complex contributes to the formation of the DGC and directly interacts with β-DG. In cardiac tissue, four single-pass sarcoglycans are present: α, β, γ, and δ[166]. Recently, a missense mutation

c.218C>T in exon 3 as well as a partial heterozygous deletion in exons 7-8 within the *SGCA* gene was shown to be causative of LGMD2D[36]. However, the authors did not assess the cardiac phenotype in this case.

Other groups have identified *SGCD* in both porcine[167] and murine[168] models that led to decreased expression of proteins in the sarcoglycan complex thereby disrupting the overall structure of the DGC and resulted in DCM. Moreover, it has been reported that 19% of all patients containing a mutation of *SGCA, SGCB,* or *SGCG* display DCM, with 25% of all patients requiring respiratory support[169].

Recessive mutations in sarcoglycan (SG) δ lead to the reduction or complete absence of the sarcoglycan complex, and subsequently the DGC, in myocardial tissue and are a cause for LGMD and DCM[170]. Interestingly, dominant negative mutations in SG-δ are cardiac specific resulting in familial dilated cardiomyopathy[171]. The SG-δ dominant negative mutations R97Q and R71T were shown to be stably expressed in rat cardiomyocytes without causing significant disruption to the overall DGC[172]. However, under mechanical stress cardiac cells harbouring these mutations were more susceptible to sarcolemmal damage and permeability as well as mechanical dysfunction, consistent with a DCM phenotype[172].

Sarcospan (SSPN) is a 25 kDa tetraspanin localising with the sarcoglycan sub-complex, thought to act as a protein scaffold[173,174]. As a protein scaffold, SSPN stabilises the localisation and glycosylation of α-DG [173,175]. Overexpression of SSPN in murine models revealed increased binding between striated muscle and laminin[176]. Recently, overexpression of SSPN enhanced both the maturation and glycosylation of α-DG in cardiac tissue independently from galactosaminyltransferase 2 (*Galgt2)* knockdown in an *mdx* model, thereby alleviating the disease phenotype[175]. Increased

glycosylation of the dystroglycan complex strengthens the interaction to the ECM and therefore mitigate the disease phenotype. Moreover, SSPN overexpression decreased the interaction of integrin β1D with the DGC, highlighting the possibility that SSPN may regulate crosstalk between integrins and the DGC[175]. In support of this notion, SSPN interacts with integrin adhesions evidencing a degree of crosstalk between the DGC and integrins[174–176]. Indeed, knockdown of SSPN led to increased expression of α7β1 in murine skeletal muscle.

1.6.6 The Syntrophins

The Syntrophins are a family of proteins, approximately 58 kDa in mass. Syntrophins have no intrinsic enzymatic activity of their own acting as molecular adaptors[177,178]. Five isoforms have been identified (α-1, β-1, β-2, γ-1, and γ-2) displaying tissue-specific expression, for example α-1 is predominantly expressed in striated muscle tissue[179]. Syntrophins are important adaptors promoting association between dystrophin and signalling molecules, including nNOS in skeletal muscle[180]. α-syntrophin directly interacts with the SR 16-17 domain of dystrophin that, binds to the PDZ binding motif of nNOS[180,181].

Syntrophins also interact with dystrobrevin via PH2 and SU binding domains, and these also interact with the actin cytoskeleton[182]. Indeed, the syntrophins appear to have a particularly pivotal role in modulating cytoskeletal dynamics with the α and β isoforms directly interacting with F-actin[182], perhaps contributing to the viscoelasticity and biomechanics of the cell. Furthermore, syntrophins have been shown to modulate the cytoskeleton via Rac1[183].

Modulation of syntrophin restored functionality in DMD *mdx* model as demonstrated by introducing a micro-dystrophin construct (ΔR4-R23/ΔCT) that promoted α-syntrophin, as well as other DGC proteins, comparable to that of the WT[184].

Additionally, the syntrophins are well documented regulators of ion channels[185–187]. The PDZ binding-motif of syntrophins regulates the cardiac sodium voltage-gated channel, $Na_v1.5$[185], essential to cardiac excitability and conduction. Interestingly, in *mdx* murine models $Na_v1.5$ channel was downregulated, with animals displaying arrhythmias[185]. Moreover, the mechanosensitive ion channel family, the transient receptor potential channels (TRPC), are also under regulation of α1-syntrophin in cardiac tissue[187] with TRPC6 inhibition ameliorating arrhythmia in a murine model of DMD[187]. Increased activity of TRPC6 was found to be proarrhythmic in DMD and could be reversed by the addition of protein kinase G. Mechanistically, the absence of dystrophin promotes stretch-induced [Ca^{2+}] influx acting upstream of TRPC6. Activation of TRPC6 in cardiomyocytes and smooth muscle cells promoted Ca^{2+} overload, a hallmark of DMD[186,188].

1.6.7 The Entire DGC Complex Functions Synergistically: The Sum is Greater than the Individual Components

In the absence of dystrophin, the entire DGC complex undergoes substantial downregulation or, in some cases, complete dissolution. The mechanoprotection and mechanotransduction afforded by the presence of dystrophin and the DGC are thus lost, and this is the cause of DMD/BMD. This aspect is not unique to dystrophin and mutations in other DGC constituents can promote similar downregulation of the DGC as well as cause other forms of muscular dystrophy. As such, it is crucial to consider the DGC as a whole, considering that it appears to function synergistically.

Each of the protein constituents contributes to the overall localisation and stabilisation of the DGC and are important determinants for accessory proteins, cytoskeletal interactions, ion channel regulation, and gene expression.

1.6.8 The DGC is Well Positioned to Act as a *Bona Fide* Mechanotransducer and is Critical to Cardiomyocyte Homeostasis

As shown above, many of the proteins of the DGC are involved in mechanotransduction and signalling, with dystrophin being particularly important for this role. Given that the DGC is located at costameres supports the notion that it is involved in mechanotransduction along with the integrins. Therefore, the DGC is physically receptive to force transmission and is responsible for mechanosensing the microenvironment and cytoskeletal rearrangement, consistent with the tensegrity model[189].

Moreover, Dp427m acts as a mechanoprotector buffering against biomechanical forces by extending SR domains within its central rod, maintaining unravelling forces at 25 pN over an 800 nm extension[8]. By unravelling its central rod domain, dystrophin acts as a molecular spring and protects against contraction-induced forces generated by cardiomyocytes[8]. Given the diversity of proteins and phospholipids that interact with the SR domain, it is interesting to speculate whether unravelling of the SR domain alters the binding kinetics of mechanosensitive proteins, in a manner analogous to that of talin[190–192]. However, this is currently not established and requires further examination.

Transmission of physical force occurs via the N-terminus of dystrophin as this directly interacts with both F- and γ-actin[123,193]. Conducting forces to and from the sarcolemma permits the cell to perceive alterations to the

environment and react accordingly, for example restructuring cytoskeletal architecture.

Force can then be transmitted by actin to the LINC complex (Figure 1.5), which communicates mechanical force to the nucleus[194]. Studies have shown that mechanotransduction can be more than 40 times more rapid compared to soluble signalling and can regulate chromatin and gene expression apparatus[194–198]. Dystrophin also interacts with microtubules, and it is the interaction with both aspects of the cytoskeleton that makes dystrophin well poised to regulate the viscoelasticity of cardiomyocytes[132,199]. Indeed, it has been shown that dystrophin is essential to the maintenance of γ-actin and microtubule lattice formation at the sub-sarcolemma[123,199].

There is tentative evidence to suggest a link between cytoskeletal dynamics and nuclear mechanotransduction in DMD. Recently, a study revealed a link between gene regulation and the cytoskeleton in DMD[200]. Here, deleterious upregulation of histone deacetylase 8 (HDAC8) was observed in DMD and selective inhibition improved skeletal muscle function. Specifically, inhibition of HDAC8 increased acetylation of α-tubulin, restoring cytoskeletal architecture in the myotubes isolated from DMD patients[200].

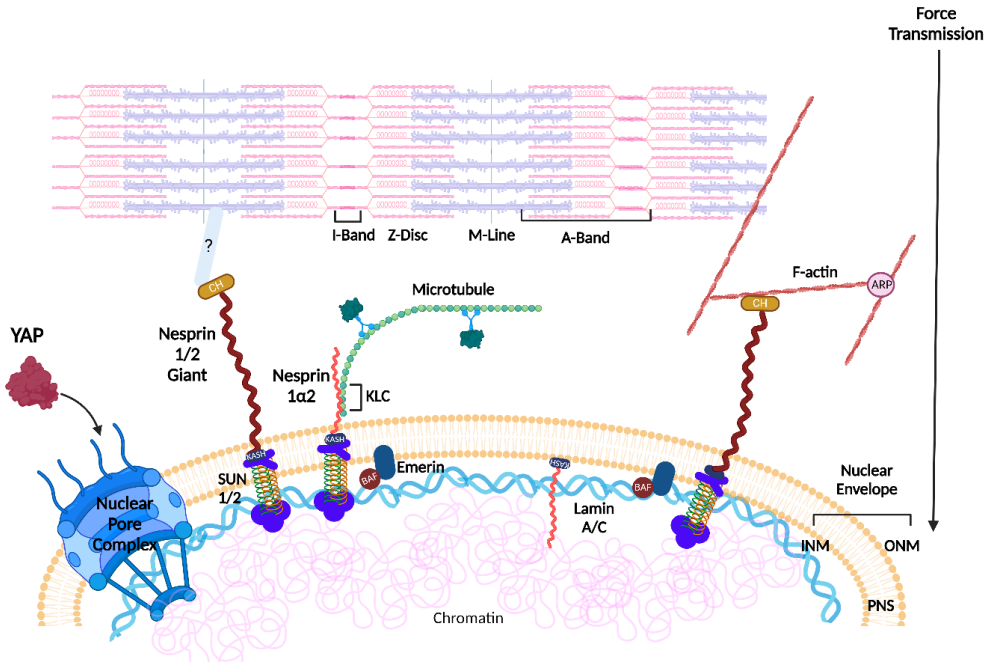

Figure 1.5: Overview of the LINC Complex in Striated Muscle. *The LINC complex connects the cytoskeleton to the nucleoskeleton and genome. Nesprin 1/2 giant have a KASH domain that is a nuclear envelope targeting domain that binds to SUN 1/2 proteins. SUN 1/2 binds to emerin and lamin A/C and the genome. At the N-terminus, Nesprin 1/2 giant have a calponin homology domain that binds to F-actin, facilitating mechanotransduction. The spectrin repeat domains of nesprins can bind to multiple proteins, including microtubules. This is specifically mediated by the highly conserved 'LEWD' binding domain of nesprins to the KLC of microtubules. Nesprins are thought to bind to, and may localise at, the sarcomere but the connecting proteins are not known. INM= inner nuclear membrane; ONM= outer nuclear membrane; PNS= perinuclear space. Image created using Biorender.*

Finally, mechanosensitive accessory proteins localise at the DGC, including ERK1/2, Grb, nNOS, and AMPK[9]. Dystrophin interacts with AMPK via intermediate proteins, including sarcolemmal-associated dysferlin[201]. Interestingly, unlike skeletal muscle, nNOS does not directly localise with the DGC in cardiac tissue, although nNOS is phosphorylated in response to AMPK mechanical activation. This occurs in response to stretch to form a

dystrophin-AMPK-nNOS axis[9]. In the *mdx* model, the dystrophin-AMPK-nNOS axis was disrupted but could be restored pharmacologically, indicating that force was the primary driver for nNOS activation in cardiomyocytes as the drug bypassed the requirement for force.

1.7 The Case for Crosstalk Between Integrins and the DGC

Integrins are a superfamily of transmembrane proteins responsible for focal adhesion formation, mechanosensing of the ECM, and mechanotransduction[1]. There are 24 distinct integrins formed as heterodimers from 18 α- and 8 β-subunits displaying tissue specificity[202,203]. Moreover, integrin expression within the same tissue is subject to spatiotemporal changes, notably during cardiogenesis. Such an example is the shift from fibronectin α5β1 integrins (present in embryonic cardiomyocytes) towards expression of laminin binding α7β1D integrins, indicative of cardiac maturation[204,205].

In cardiomyocytes, integrins localise at costameric regions and are central to mechanotransduction, regulation of cytoskeletal architecture and dynamics, and cellular processes including migration. Importantly, integrins contribute to the overall viscoelasticity of the cell by directing cytoskeletal dynamics[206–208]. Whether forces directed by integrin adhesions converge with those directed via dystrophin is currently unknown. It is beyond the scope here to detail integrin activation and specific downstream targets, although a short overview is provided. (The following references permit further exploration of this area[1,202,209,210]).

In brief, the integrins facilitate rigidity sensing where increased force across the ECM-integrin interface strengthens the bond between the integrin (as well as recruitment of additional integrin units) and the ECM, a behaviour

called a catch-bond[211]. Activation of integrins in this manner promotes a signalling cascade and recruitment of multiple proteins, such as FAK and the Src family kinases. Recruitment of talin and vinculin allows the integrin to interact with F-actin. If the force is sufficiently large, segregation of multiple integrins occurs to form nanoclusters that can induce formation of more actin cables and thus increase force generation[212].

Integrins have been widely described in the context of focal adhesion formation and maturation, allowing cells to sense their microenvironment and assess ECM rigidity and communicating this biomechanical 'information' along prestressed actin cables[196,213,214].

A small degree of evidence supports crosstalk between the DGC and the integrins, which may not be particularly surprising given their similar locale and synergistic function[215–217]. Mainly, these insights derive from studies where either the DGC constituents or integrin proteins are mutated, causing various muscular dystrophies. Double knockout studies (dystrophin and integrin α7) reveal a more severe disease phenotype than individual knockouts *i.e.* accelerated myopathy and premature lethality. This is perhaps unsurprising given that near complete loss of anchorage can result in anoikis. Intriguingly, expression of α7β1D integrins in the absence of dystrophin is increased, hinting towards a compensatory mechanism[16,218,219]. Together, these data suggest crosstalk between DGC and integrin adhesions.

Previous work has shown that mutations in the integrin α7 (*ITGA7)* are a cause of congenital muscular dystrophy with a disease phenotype similar to DMD[17,75]. Mayer[75] showed that the absence of α7 caused necrosis of myofibres, centralised nuclei, and disrupted the sarcomeric architecture, features consistent with a later finding in humans harbouring primary

mutations in *ITGA7* [38]. The DGC did not appear to compensate for the loss of α7[75].

The absence of dystrophin, as in DMD or the *mdx* murine model, has consistently revealed an upregulation in the α7 integrin. This is thought to be a compensatory mechanism although this compensation appears insufficient in the long-term for DMD patients[38,75,220,221]. Overexpression of α7 pharmacologically or via adeno-associated viruses (AAV) delivery has shown attenuation of the DMD disease phenotype in both skeletal and cardiac tissue[222].

Of particular promise is sunitinib, a Food and Drug Association (FDA) approved tyrosine kinase inhibitor. Sunitinib functions to increase expression of α7β1D promoting attachment to the ECM basement membrane. Moreover, sunitinib downregulated signal transducer and activator of transcription 3 (STAT3), a known promoter of fibrosis. Overall, this acted to attenuate cardiac fibrosis. Another compound, SU9516, led to similar cardiac improvements in C2C12 and *mdx* models[223]. SU9516 acted to downregulate NF-κB activity whilst increasing expression of α7β1D[223]. Interestingly, a mainstay treatment in DMD, the glucocorticosteroid prednisone, also increases α7β1 in skeletal muscle of patients with DMD as well as in the golden retriever model, GRMD[224]. Overexpression of SSPN upregulated cardiac β1D expression in a dystrophin-utrophin double knockout, *mdx:utn*$^{+/-}$ model. Sarcolemmal stability was improved further supporting crosstalk between the DGC and integrins [225]. Lastly, a *dag1* knockout modelling dystroglycanopathy showed elevated α7 expression that attenuated, but did not fully rescue, the disease phenotype[226]. The authors suggested that α7 integrin compensation was beneficial in attenuating the disease phenotype but was insufficient for long-term

disease prevention. This observation aligns with disease progression observed in DMD patients[226].

Truncated isoforms of dystrophin may offer unique insights into potential crosstalk mechanisms. Dp71f directly interacts with β1 integrin in neuronal tissue and interacts with downstream mechanosensitive proteins, such as FAK[227]. Moreover, Dp71f localised at focal adhesions in astrocytes and co-immunoprecipitated with β1 integrin as well as vinculin and actinin[228]. To the best of my knowledge this has not been demonstrated in cardiomyocytes, but these studies offer a glimpse into a putative role for Dp71-integrin crosstalk in cardiomyocytes.

Further studies have shown that double knockout of integrins and DGC components result in an exacerbated, rapidly advancing disease phenotype than either knockout alone, suggesting that the compensation by one or other group does not fully attenuate disease phenotype[176,222,225]. For example, the *mdx:β1* double knockout showed worsening cardiac dysfunction that progressed more rapidly towards heart failure compared to knockout of *DMD* or *β1* alone[218].

Overall, these data indicate that not only do the DGC and integrin complexes co-localise, but that there is complementary, synergistic compensation occurring when either is disrupted. Compensation by either complex, in the absence of the other, attempts to maintain the ECM-cell interaction necessary for subsequent mechanotransduction events to occur. Whilst initial compensation appears to improve the disease phenotype, over time this begins to fail. What drives this failure is not well understood but it is responsible for the deterioration of muscle tissue displayed by patients. Further work into this research area, with a view to

long-term phenotypic rescue, is urgently required for patients living with muscular dystrophy.

1.8 The Role of the DGC in Cardiomyocyte Mechanotransduction

1.8.1 Overview of Mechanotransduction

Cells are responsive to mechanical force that governs a multitude of processes, including differentiation, embryogenesis, focal adhesion formation, cell migration, proliferation, survival, cell morphology, and gene regulation[1,229–231]. The cytoskeleton is central to establishing and maintaining the viscoelasticity of the cell and for communicating mechanical force between the ECM and ICM of the cell. Perception of mechanical forces across focal adhesions and the DGC induces cytoskeletal rearrangements and activation of mechanosensitive proteins involved in signalling or genetic regulation. Disruption between the ECM-cell interface can negatively affect the cell's ability to respond to physicochemical alterations of the ECM (Figure 1.6).

1.8.2 The DGC Plays a Role in Maintaining the Viscoelasticity of Cardiomyocytes as Described by the Tensegrity Model

Tensegrity is a model describing how prestressed structures physically support themselves using a connected system of compressive and tensile elements[56]. Forces on the compressive and tensile elements are in equilibrium during external force application, meaning that changes in external forces cause remodelling of the structural components in order to maintain internal equilibrium.

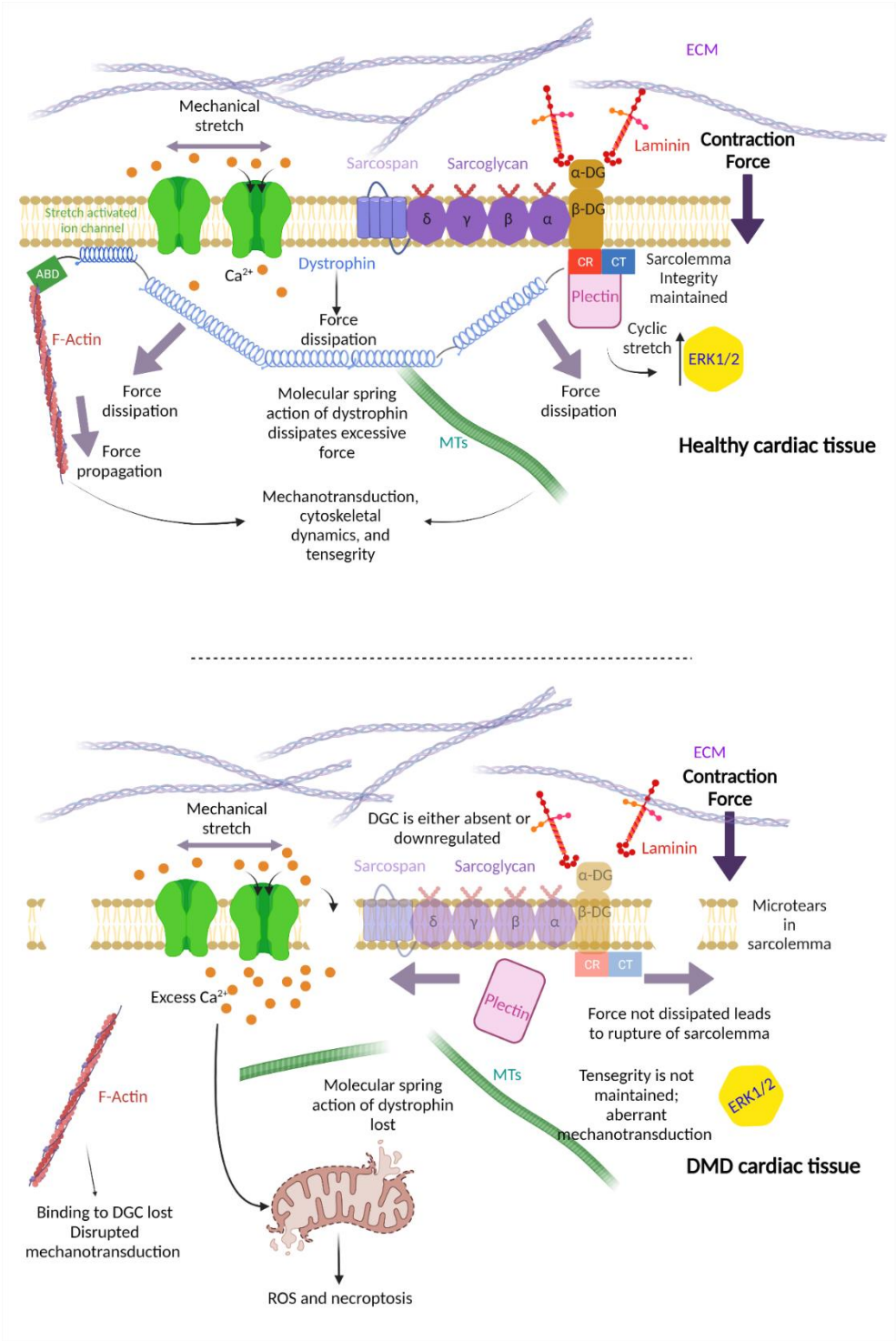

Figure 1.6: The Dystrophin Glycoprotein Complex has a Central Role in Biomechanics:

Dystrophin is central to mechanotransduction in healthy cardiac tissue. Biomechanical

force is propagated along pre-tensed actin and microtubule (MT) cables which can then be transmitted to the nucleus. Moreover, this mechanism allows the cardiomyocyte to maintain tensegrity and respond to changes in the ECM and is perhaps involved in rigidity sensing. Stretch activated ion channels are regulated by dystrophin mediating Ca^{2+} ion entry, important for excitation-contraction coupling as well as signaling. Plectin is associated with β-DG and regulates ERK1/2 activity. In DMD, the absence of dystrophin leads to contraction-induced microtears of the sarcolemma, allowing excess entry of Ca^{2+} ions, leading to mitochondrial dysfunction and cell death. Moreover, biomechanical signals fail to propagate along actin and MT cables causing aberrant mechanotransduction. In the absence of dystrophin, the whole DGC can be absent or downregulated, further disrupting downstream signaling. Image adapted from: [45].

For cardiomyocytes, tensegrity describes how a prestressed cytoskeleton is well poised for mechanical force transduction and propagation. Tension is generated by the actin cytoskeleton, specifically via actomyosin contraction, whilst microtubules form the compressive elements[56,189]. Equilibrium between tensile and compressive forces produces the overall prestressed state of the cell, determining the overall viscoelasticity. As such, alterations of the cytoskeleton, particularly cortical actin which is a key regulator of cell surface tension, can be assessed by measuring Young's modulus of the cell[232]. The prestressed state of the cytoskeleton mediates its own mechanoresponsivity. In other words, force causes rearrangement and redistribution of cytoskeletal components.

Adapting to changes in force involves the formation of new actin cables and microtubule buckling and reformation[189]. Propagation of forces along prestressed actin cables has been shown to act more than 40-fold more rapidly than soluble ligand interactions[194,196], indicating that mechanical force acutely regulates cell behaviour. Moreover, forces influence cell behaviour across various time-scales from the rapid induction of integrin activation to long-term (epi)genetic changes. Therefore, this mechanism

allows cardiomyocytes to sense changes in the ECM in real-time and adapt to long-term alterations, such as changes to ECM elasticity.

Recent work showed that dystrophin deficient C2C12 myoblasts displayed significantly disrupted focal adhesions and altered YAP localisation, indicating that dystrophin has a vital role in mechanotransduction[233]. Focal adhesion disruption renders the cytoskeleton-DGC-ECM axis dysfunctional causing cardiac dilatation and increased compliance in *mdx* models[149]. Interestingly, female carrier *mdx*, where only approximately 50% of the cardiomyocytes expresses a functional DGC, did not show this increased compliance in response to mechanical stretch[149]. The authors demonstrated that this effect was distinct from sarcolemmal damage and related to the disruption of ECM-cell interface by using knockouts of other costameric region proteins, including β-SG[149].

The DGC is a key focal point for lateral force transmission in striated muscle tissue across the costameres, connecting sarcomeres downstream via Z-discs[113]. The sarcomere-ECM connection allows communication and transduction of mechanical forces into biochemical and genetic alterations, ultimately governing striated muscle behaviour. Magnetic micromanipulation showed that disruption of the actin cytoskeleton led to decreased cell stiffness when α-DG was stimulated compared to untreated cells with an intact actin cytoskeleton[234]. This suggests that the DGC is a regulator of cellular viscoelasticity.

1.9 Duchenne Muscular Dystrophy

The central focus of this thesis is how the loss of dystrophin affects cardiomyocyte functionality. The loss of dystrophin causes Duchenne muscular dystrophy (DMD) and the milder, allelic variant Becker muscular dystrophy (BMD). Here, more detail is provided on the disease, reviewing the underlying molecular mechanisms to gross pathology.

DMD/BMD is a catastrophic X-linked recessive muscular dystrophy caused by mutations in the *DMD* gene, located on chromosome Xp21[235]. Causative mutations in *DMD* are highly diverse but insertions and deletions are the most prevalent type accounting for 72% of all mutations in *DMD*[236]. DMD is characterised by the functional absence of dystrophin, defined as less than 3% protein by mass. DMD has an incidence of 1:3500-5000 males and is characterised by the early loss of ambulation (< 5yrs), skeletal muscle atrophy, neuropsychological impairment, respiratory insufficiency, and progressive DCM, that carries a significantly poorer prognosis compared to DCM of other aetiologies[81,235,237]. Historically, respiratory insufficiency due to diaphragmatic atrophy and pneumonia was the leading cause of premature death of patients, typically occurring by their early twenties[14]. However, improved therapeutic strategies such as the introduction of glucocorticosteroids and continuous positive airway pressure (CPAP) have extended the lifespan of these patients to a median age of 28.1 years as recorded in DMD patients born after 1990[238]. Improvement of supportive respiratory care precipitated progressive DCM as a novel cause for premature death with DCM and heart failure are now attributable for approximately 50% of all deaths in DMD patients[81,237], typically occurring during the third decade[14].

The milder BMD is also caused by mutations in *DMD.* However, multiple internal promoters within *DMD* can produce truncated, but functional isoforms, of dystrophin, such as Dp71. Synthesis of some portion of dystrophin is superior to no expression this accounts for the milder phenotype displayed in BMD.

However, the relationship between disease progression and the presence or absence of specific regions of dystrophin has become apparent. For example, the ABD1 has been revealed as being particularly important. Patients with BMD have a comparatively better prognosis compared to DMD and may retain ambulation into adulthood, with a lifespan of up to 60 yrs[239]. That being said, cardiac involvement develops in up to 75% of BMD patients manifesting, on average, by 28.7 yrs[239]. Patients harbouring deletions between exons 12-17 or 31-49 are particularly susceptible to developing DCM, leading to a poorer prognosis[239].

1.9.1 Progressive Dilated Cardiomyopathy in the Context of DMD

Clinically, DCM is a highly heterogenous disease that can be the result of several distinct aetiologies, distinguished into either primary or secondary causes[240]. Primary causes of DCM are often the result of mutations within genes (very often sarcomeric or cytoskeletal) such as *DMD*[104]*, LMNA*[241]*,* or *TTN*[242]. Secondary causes are often attributed to environmental factors and can range from viral infection induced myocarditis to alcohol[243]. Irrespective of the underlying cause, DCM is characterised by left ventricular dilatation with increased compliance, ventricular wall thinning, proinflammatory and fibrofatty infiltrate, decreased systolic output (*i.e.* ejection fraction < 50%), hypocontractility, and propensity for arrhythmia[2]. The extent of DCM in DMD (Figure 1.7) patients is essentially ubiquitous by late teens (90% by 18 years) but can be detected in approximately 59% of

patients by 10 years[2,104,244]. It is critically important to address this issue as left ventricular ejection fraction steadily declines annually at a rate of 1.6% *per annum*[245].

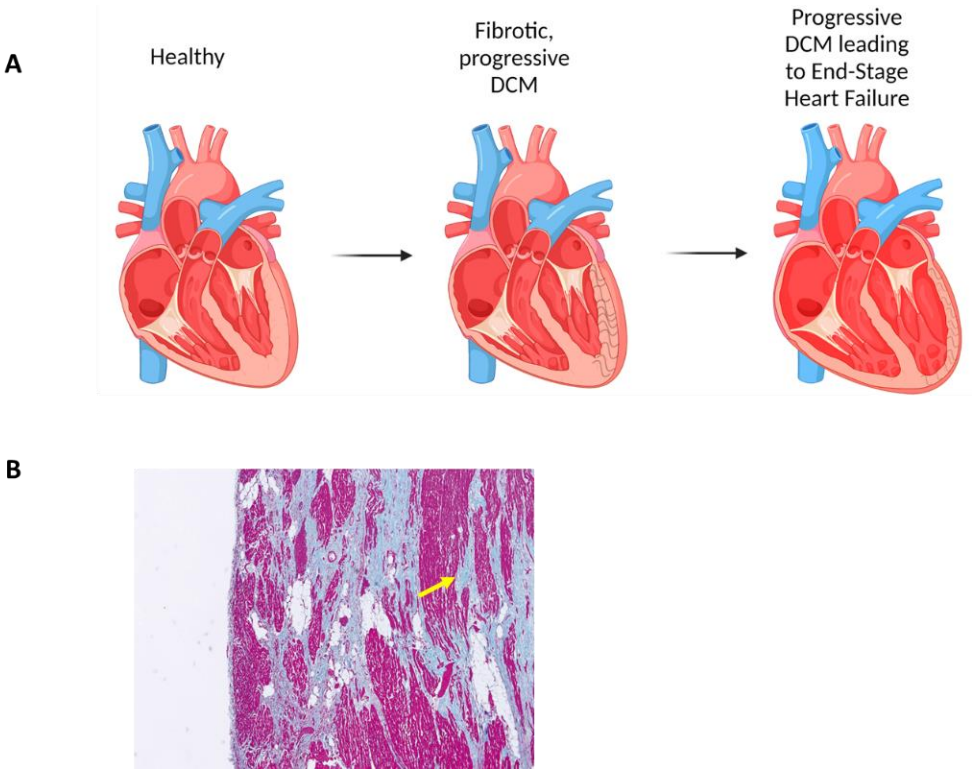

Figure 1.7: DMD Associated DCM A) *Progression of DMD associated DCM. The heart becomes fibrotic with high levels of proinflammatory infiltrate during childhood. By teen-years, 90% of all DMD patients have clinically overt DCM, described by thinning of the left ventricular wall and extensive fibrosis. Cardiac physiology declines, as described, for example, by the ejection fraction.* ***B)*** *Histological microphotograph stained with Masson's trichrome demonstrating extensive fibrosis within cardiac tissue in DMD. Fibrosis alters the extracellular milieu, exacerbating the underlying pathology and is a cause for arrhythmias in DMD. (A created using BioRender; B is adapted from [104]).*

Treatment of cardiac dysfunction, adjacent to skeletal muscle therapeutics, is critical to overall DMD patient quality of life. This fact was reinforced by a study that sought to improve skeletal muscle function, without consideration to cardiac tissue, utilising the *mdx* murine model[246].

Transfection of a mini-dystrophin construct led to improvements in skeletal muscle function but unexpectedly exacerbated underlying cardiac function. Improved skeletal muscle function facilitated additional exercise that led to a 5-fold increase in cardiac dysfunction[246].

Arrhythmias are commonplace in DMD patients, particularly sinus and ventricular tachycardia, and are a cause of sudden cardiac death in the DMD population[104]. Arrhythmias arise as a result of fibrofatty infiltration and altered ECM, such as increased deposition of collagen type I. The inferobasal aspect of the left ventricle is particularly susceptible to arrhythmia due to disrupted re-entry circuits in conjunction with dysfunctional $[Ca^{2+}]_i$ handling and dysregulated ion channel function[247,248]. Recognition of the clinical cardiac picture is paramount as earlier implementation of therapeutic strategies may delay onset of severe DCM.

1.10 Female Dystrophinopathy

The inheritance pattern of DMD is X-linked and as such overwhelmingly effects males. However, in exceptionally rare cases (<1:1,000,000) females may display fulminant DMD (Figure 1.8) due, in part, to i) Turner syndrome (45, X) whereby the X chromosome harbours a *DMD* mutation, ii) Unbalanced mosaic predominantly expressing mutated X chromosome due to X-inactivation, iii) both X chromosomes harbouring *DMD* mutations- which is possible in theory but not, to the authors knowledge, been reported in the literature[249–251].

More commonly are females displaying mosaicism, *i.e.* approximately 50% of cells expressing unmutated X chromosome whilst the remainder express the mutated form. Female mosaics tend not to have an elevated risk of DCM compared to the general population however, approximately 20% do

display a phenotype comparable to the milder allelic variant, BMD. In cases such as these, up to 17% of patients subsequently develop DCM and heart failure, even in the absence of skeletal muscle pathology[250]. Current therapeutic strategies are non-distinct to male DMD counterparts focusing mainly on treating under standard heart failure algorithms.

In light of this, more research into the female specific effects of *DMD* mutations should be performed to better understand and treat the female demographic.

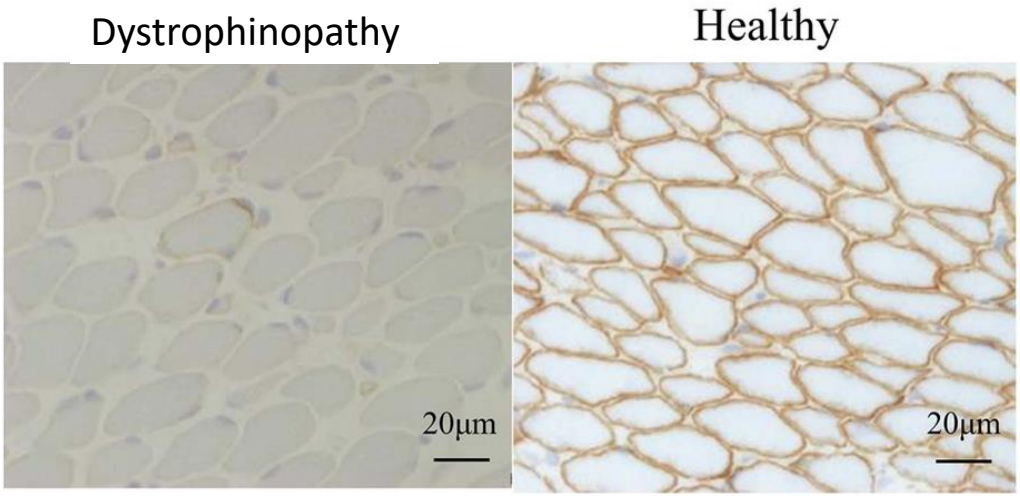

Figure 1.8: Female Dystrophinopathy in Striated Muscle*. The almost complete absence of dystrophin in skeletal muscle biopsy from a female dystrophinopathy patient. In rare cases such as these, female patients can develop signs and symptoms comparable to male DMD patients, including DCM and heart failure. Image adapted from* [252]

1.11 Current Therapeutic Strategies for DMD

Cardiorespiratory complications limit survival in patients with DMD and current therapeutic strategies are palliative, not curative. The mainstays within the therapeutic algorithms centre around delaying the onset of pathophysiological 'milestones', for example loss of ambulation[253]. Adding to the difficulty in treating DMD is that alignment between genotype and phenotype is not always clear in DMD/BMD, with some unexpectedly severe phenotypes being reported for what were predicted to be minor mutations. Approximately 10% of DMD/BMD patients do not align with the 'reading frame' rule and correlating genotype to phenotype is challenging[254]. Additionally, discordance between respiratory and cardiac function can increase the complexity for implementing personalised healthcare[255,256]. In general, two therapeutic branches for DMD/BMD can be described. The first and most regularly utilised approach is to delay the onset and progression of DCM and skeletal muscle dysfunction while maintaining respiration. The second branch is more experimental with the aim to cure the fundamental disease, primarily by attempting the restoration of dystrophin.

1.11.1 Therapeutics Used to Stave Off Disease Progression

DMD associated DCM is amenable to traditional heart failure (HF) treatments including angiotensin converting enzyme (ACEi) inhibitors[257], β-blockers, Ca^{2+} channel blockers, and mineralocorticoids[258,259]. HF therapy is utilised in conjunction with glucocorticosteroids, *e.g.* deflazacort, to reduce inflammation. There is debate within the cardiology community as to when HF treatments should be implemented, with some advocating for before the onset of DCM is detected versus post-detection of DCM. Addressing this issue, a randomised clinical trial assessed the effect of an ACEi,

perindopril versus placebo in DMD patients (with ejection fraction > 55%). After 60 months, the trial showed delayed onset of DCM with improved LV function in the perindopril group compared to the placebo group, leading to the use of perindopril and ACEi generally as standard treatments in DMD/BMD[257]. Other trials have assessed the efficacy between ACEi and angiotensin receptor blockers (ARBs), for example losartan compared to lisinopril[260]. After 12 months, the trial concluded that there was no significant difference losartan and lisinopril with both successfully increasing ejection fraction in their respective patient cohorts, on average by 6.9 %[260].

In addition to ACEi/ARB therapy, mineralocorticoid antagonists can significantly delay progression of LV dysfunction and preserve ejection fraction in DMD. Eplerenone significantly decreased cardiac strain compared to placebo and improved ejection fraction[259]. This effect was particularly enhanced in combination with an ACEi. Other trials have assessed various mineralocorticoid antagonists including spironolactone, reporting findings comparable to eplerenone[258]. The addition of mineralocorticoids, in combination with ACEi/ARBs, is beneficial in delaying declining cardiac function in DMD associated DCM.

Overall, the onset and progression of DMD associated DCM can be delayed utilising standard HF therapeutic strategies. Treatments are reportedly well tolerated by patients and are shown to improve ejection fraction and attenuate LV remodelling. However, the implementation of HF drugs does not prevent ensuing heart failure and patients continue to decompensate. Nor do these therapies act to cure DMD/BMD or act to restore dystrophin. Therefore, the second branch aiming to address these concerns is considered next.

1.11.2 Experimental Treatment Stratagems Used to Improve Cardiac Function

Experimental therapies aim to restore functional dystrophin to striated muscle tissue to cease disease progression. A variety of methods have been considered including exon skipping, AAV transfection, and clustered regularly inter-spaced short palindromic repeats (CRISPR). Of these, exon skipping has had moderate success and was approved by the FDA and European Medicines Agency (EMA). Discussion of some of the more relevant strategies is provided.

1.11.3 Exon Skipping

The reading frame rule states that adjacent exons that maintain an open reading frame, despite deletion of other exons, should result in a phenotype comparable to the milder BMD phenotype due to truncated, but functional, dystrophin isoforms[261]. This motivated the advent of exon skipping therapy for use in DMD.

In essence, exon skipping mediates the production of truncated, yet functional, dystrophin isoforms that can partially restore function (Figure 1.9). Currently, FDA approved antisense oligonucleotides (AON) are available including the phosphorodiamidate morpholino oligomers eteplirsen (targets exon 51) and golodirsen (targets exon 53). Despite moderate success with eteplirsen and golodirsen, they are of benefit to only a limited number of patients. Specifically, only 14%[262] and 8%[263] of DMD patients are candidates for eteplirsen or golodirsen respectively. Whilst dystrophin production and 6-minute time walk were both increased in patients after 180 weeks when treated using eteplirsen, protein quantification revealed very modest increases of dystrophin[264].

Western blot analysis revealed the increase of dystrophin here to be only 0.28% compared to untreated patients, a finding supported by another trial using golodirsen where dystrophin expression was increased by 0.92%[265]. These findings raised some initial debate as to the efficacy of the AONs but ultimately, due to the perceived benefits such as the improved walk time, the FDA continued approval and indeed accelerated wider access to these drugs.

Further confounding factors in restoring open reading frames is the vast diversity of mutations, each requiring development of a unique AON. Some 83% of DMD patients are eligible for exon skipping therapy but the aforementioned restriction has delayed treatment. Nonetheless, several clinical trials are currently underway and will be reporting results in 2024 and may expand the pharmaceutical arsenal that can be used for exon skipping in DMD/BMD patients[266].

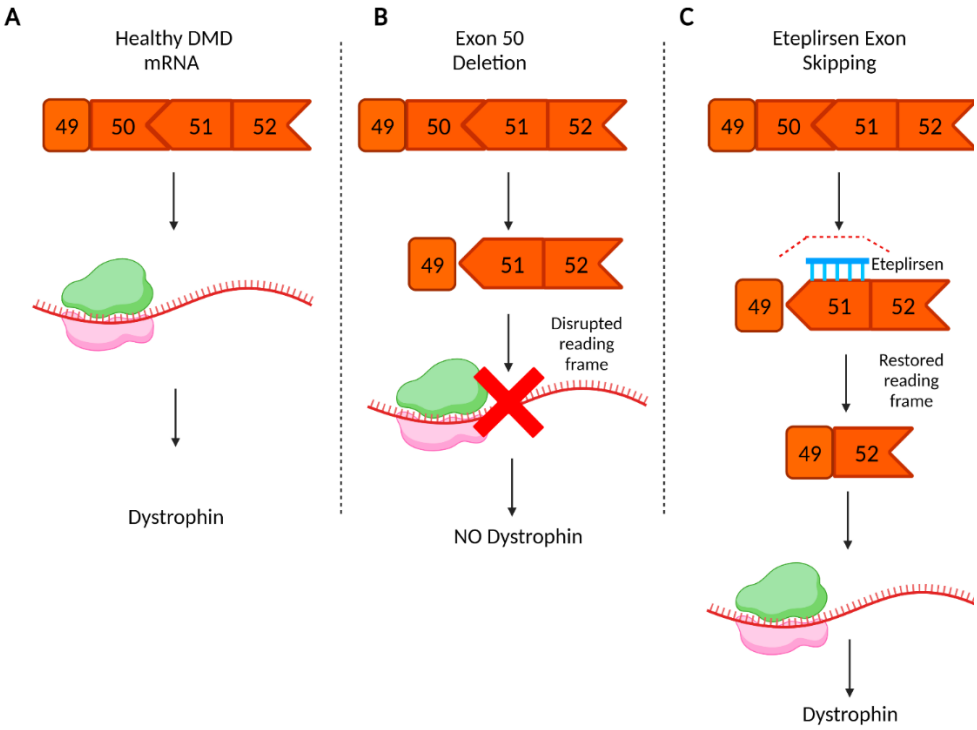

Figure 1.9: Exon Skipping as a Method to Restore Dystrophin Expression. A) *The healthy scenario whereby mRNA is transcirbed from DMD and translated to dystrophin, localising at the sarcolemma in striated muscle.* ***B)*** *An example of an exon deletion in DMD causing the loss of functional dystrophin. The absence of exon 50 results in a premature stop codon causing mRNA to undergo nonsense mediated decay. This prevents the translation of functional dystrophin, resulting in DMD.* ***C)*** *Eteplirsen (shown in blue) restores the the open reading frame of mRNA by skipping exon 51. This results in a truncated, yet importantly, functional isoform of dystrophin shown to improve patient outcomes. However, eteplirsen is only suitable for 14% of DMD patients. (Figure created using BioRender).*

1.11.4 Mini/Micro-Dystrophin Expression using Adeno-Associated Viruses

Another approach seeking to restore dystrophin in cardiomyocytes is the use of AAV vectors[267]. The primary limitation to this approach is the small carrying capacity of AAV, which is approximately 5 kb. The cDNA of dystrophin is substantially larger than 5 kb, being approximately 11.5 kb, motivating development of the so-called mini- or micro-dystrophins (Figure

1.10). The presence of some dystrophin is far superior to complete absence of dystrophin and currently some AAV are at the clinical trial stage[265,268].

A natural question arising in the face of this limitation is which sections of the dystrophin protein should be included within an AAV vector. Thus far, preclinical trials have identified four essential components necessary for a mini/micro-dystrophin. First, the N-terminal ABD is required for functional mini/micro-dystrophin constructs to support localisation to the sarcolemma, which is interesting as not all naturally occurring isoforms contain this feature, such as Dp71 (although Dp71 does not strictly always localise to the sarcolemma). Second, the WW domain within the CT region is required for binding to β-DG. Third, hinge regions 1 and 4 as well as SR domains 4-5 are required. Finally, it needs variable remaining SR domains[265].

Despite the limited carrying capacity of AAV, the vector does display a natural tropism for striated muscle tissue and is not highly immunogenic, making them attractive therapeutic strategies[264]. However, within the human population it is common to have neutralising antibodies targeted against AAV that may render the therapy ineffective[264]. Moreover, AAV has been scrutinised due to complications arising during a Pfizer trial that resulted in the death of a patient[264]. Therefore, careful consideration and wider research is necessary to evaluate the utility of this mode of treatment.

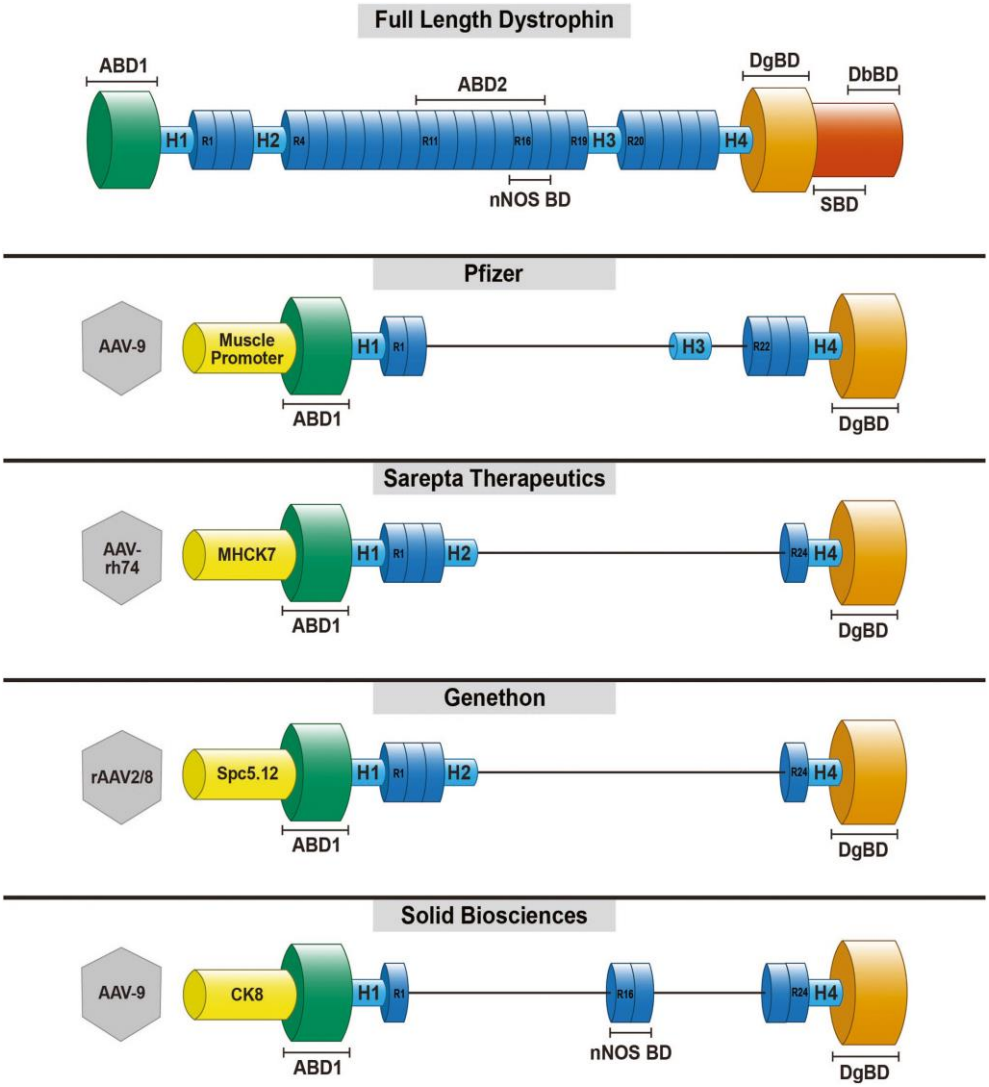

Figure 1.10: Current Mini/Micro-Dystrophins at Clinical Trial Stage for DMD *Several mini/micro-dystrophins have been developed for AAV delivery into striated muscle tissue. High dose transfection is more effective but may be more toxic to patients. AAV has been shown to increase dystrophin expression within skeletal muscle tissue as well as increasing the 6-minute time walk in patients. Figure adapted from Boehler*[269].

Overall, experimental therapies have shown moderate success towards restoring dystrophin as well as improving the quality of life for patients. However, significant challenges and unanswered questions remain, primarily directed towards patient safety and treatment efficacy. Many of

the clinical trials mentioned have end-points of less than 5 years, meaning that the results may not translate or extend to decades-long improvements for patients. Nonetheless, despite these concerns, continued investment into advancing these areas has generated tangible improvements to patient quality of life, which is a substantial achievement alone. Furthering these areas over the following years will hopefully continue this trend and yield continued benefits.

1.11.5 Can Mechanobiology Reveal Novel Therapeutic Targets?

Many of the therapies discussed are based on classic genetic and cell signalling pathways. The genetic revolution has been notably vital towards the development of clinically relevant therapies as well as furthering the understanding of basic biology. The relevant question now is to ask if there is a role for mechanotherapies. In essence, there are two aspects to be considered for mechanotherapy. Firstly, the elucidation of biomechanical pathways and how these interact and alter throughout disease progression. Second, the implementation of mechano-centric therapeutics.

The first aspect is easier to comprehend and to implement. Indeed, the work of this thesis is within the remit of this first consideration of mechanotherapy. Revealing and disentangling mechanical pathways will be essential to better grasp the overall biology and is necessary at all levels from individual molecules to the whole organ.

The second consideration is somewhat more difficult, and clarification may be required here when considering what may be considered a ‘mechanotherapy’. Do we simply mean a drug, or intervention, that modulates the activity of a known mechanosensor? For example, should we consider the promotion or inhibition of, say, integrins to be

mechanotherapy? Or do we mean the advent and implementation of bioengineered and mechanical devices that can regulate tissues, such examples include ventricular assist devices and the development of cardiac patches[270].

In any case, the furthering and development of this aspect of medicine may yield great revelations similar to the genetic revolution. Attention should be focused on the integration of 'higher order' biomechanics and how changes at molecular level can translate to cellular and long-term changes[271]. Consideration towards (epi)genetic regulation and the integration between mechanics and genetics will likely be of significant clinical benefit.

1.12 The Molecular Mechanisms Underpinning Cardiac Dysfunction in the DMD Patient

Having discussed the gross pathology and cardiac specific effect of DMD, consideration to the underlying molecular and cellular mechanisms is now provided. The molecular pathomechanisms underpinning DMD associated DCM are attributable to several stages: i) structural integrity of the sarcolemma is compromised[7], ii) dysregulation of Ca^{2+} handling caused by influx via sarcolemmal microtears and dysregulated ion channels[272], iii) disruption to both the actin and microtubule cytoskeleton, resulting in aberrant mechanotransduction[199], iv) generation of ROS[99], and v) mitochondrial dysfunction leading to necrosis[273].

1.12.1 The Cardiac Sarcolemma Is Compromised in DMD

One of the primary roles of dystrophin is to protect against contraction-induced injury and other mechanical forces. The high extensibility of the SR domains allows dystrophin to function as a molecular spring[8]. This was evidenced by Le[8] where it was shown that the central rod domain of

dystrophin acts as a molecular spring maintaining forces below 25 pN over an 800 nm length, falling within physiologically normal parameters[8]. This provided strong evidence that dystrophin buffers against excessive forces to maintain the integrity of the sarcolemma as well as supporting its role in mechanotransduction.

Sarcolemmal fragility in DMD was demonstrated using dyes that are usually impermeable to intact membranes. Porcion orange was detectable in the skeletal muscle of *mdx* mice, but not in WT, after a diaphragmatic stress test[7]. Similarly, *ex vivo* mechanical stress in dystrophin-deficient myocardium showed increased uptake of Evan's blue dye which is unable to penetrate an intact sarcolemma[274]. Together, these data provide evidence of sarcolemmal fragility in dystrophin deficient myocardium making it less resistant to contraction forces, with comparable observations being made for human DMD patients[8,275]. Further, decreased afterload *in vivo* improved the cardiomyocyte sarcolemma in DMD patients, as evidenced by the diminished uptake of Evan's blue dye[274].

The use of the artificial membrane sealants, poloxamers, provides further evidence that dystrophin is required for maintaining sarcolemmal integrity. The use of poloxamer 188 (P188) in both a canine[276] and murine[277] model of DMD substantially reduced myocardial fibrosis and prevented uptake of Evan's dye. Further, a reduction in LV remodelling was reported alongside decreased serum biomarkers of cardiac injury, cardiac troponin I and brain natriuretic peptide[278]. These studies highlight the susceptibility of the cardiac sarcolemma to contraction-induced injury in the absence of dystrophin. P188 is FDA approved for short-term use but clinical trials examining its efficacy in treating progressive DCM and skeletal muscle dysfunction in DMD patients are still underway. However, it may be a

promising adjunct to the more conventionally utilised therapies discussed earlier[279].

In addition to sarcolemmal fragility, mounting evidence is showing dysregulated sarcolemmal repair mechanisms in muscular dystrophies[273,280]. Elevated Ca^{2+} flux due to microtears of the sarcolemma may further weaken the ability of cells to repair the damage[281]. Mitochondria have been reported to respond to sarcolemmal injury by binding to microtears and initiating repair[282]. One hypothesis accounting for this phenomenon is that mitochondria act to absorb excess Ca^{2+} ions[282]. Indeed, it has been shown in muscular dystrophies that sustained Ca^{2+} overload promotes mitochondrial dysfunction, resulting in poor sarcolemmal injury-repair mechanisms[282].

Sustained Ca^{2+} overload promotes a transition in permeability of mitochondria causing development of a large pore complex, promoting autophagy of mitochondria and cell death[273]. Elevated Ca^{2+} promotes the activation of cyclophilin D. Cyclophilin D is implicated as increasing mitochondrial permeability culminating in rupture if not rapidly reversed. Pharmacological and genetic ablation of cyclophilin D prevented mitochondrial sensitivity to Ca^{2+} overload, concomitant mitochondrial swelling, and mitochondrial driven necrosis and may thus be a valid therapeutic option[273].

1.12.2 Ca^{2+} Is a Potent Secondary Mechanism Contributing to the Pathogenesis in DMD

The dysregulation of Ca^{2+} handling is a hallmark of DMD/BMD[272,283]. Not only is Ca^{2+} pivotal for excitation-contraction coupling of cardiomyocytes but it is also a significant secondary signalling ion. Therefore, it is no

surprise that $[Ca^{2+}]_i$ is tightly controlled in cardiomyocytes. Groups have reported that increased Ca^{2+} entry into cardiomyocytes leads to the activation of proteases[284], mitochondrial dysfunction[285,286], generation of ROS[99,287], cellular necrosis[101,288], and aberrant mechanotransduction[79]. Dysregulated Ca^{2+} entry is considered to occur via two non-mutually exclusive mechanisms. First, Ca^{2+} enters via microtears down its concentration gradient into the cardiomyocyte [289]. Second, the dysregulation of mechanosensitive Ca^{2+} ion channels (including TRPC, LTCC, and stretch-activated channels), may also permit the influx of excessive Ca^{2+} ions[13,99]. Evidently, excess Ca^{2+} entry leading to calcium overload actuates the DMD phenotype in cardiomyocytes[272,290,291].

Particular attention should be afforded to channels associated with calcium induced calcium release (CICR). CICR is the mechanism by which a cardiac action potential triggers activation of the L-type Ca^{2+} ion channels. In turn, Ca^{2+} entry via L-type Ca^{2+} channels stimulate the opening of ryanodine (RyR2) receptors that then release additional Ca^{2+} from the sarcoplasmic reticulum (SR) to the cytosol, generating localised Ca^{2+} sparks. Cumulatively, the synchronised, cell-wide generation of Ca^{2+} sparks produce the Ca^{2+} flux required for exciotation-contraction[292]. Hypernitrosylation of RyR1/2 channels in *mdx* and human cardiomyocytes increased the frequency of Ca^{2+} sparks leading to arrhythmia[293]. Because hypernitrosylation is a ROS induced posttranslational modification, this relates Ca^{2+} dysregulation to ROS activity[294]. Destabilisation of the RyR2 channel in cardiomyocytes causes them to become 'leaky', manifesting as arrhythmias as well as depleting the SR Ca^{2+} store, thus weakening contraction. Fauconnier[294] showed that stabilising the RyR2 receptor by preventing calstabin2 depletion was sufficient to prevent arrhythmia *in vivo*[294]. Lastly, P188 can

normalise Ca^{2+} flux into the cardiomyocyte, providing convincing evidence that sarcolemmal disruption is a *bona fide* Ca^{2+} entry mechanism and that this is a driver of aberrant CICR and fatal arrhythmias in DMD[277].

Mechanosensitive stretch-activated calcium channels, such as the TRPC family of cation channels, are hyperactive in DMD[290]. TRPC were shown to be hypersensitive to stress-stimulated contraction that augments the physiological systolic contraction within the DMD heart[186].

Specifically, the mechanosensitive TRPC6 channel is one such example of how stress-stimulated contraction results in excess Ca^{2+} flux leading to increased reports of sudden cardiac death in DMD patients. Moreover, excessive activation of TRPC6 is linked to hypernitrosylation of RyR2, reinforcing the connection between Ca^{2+} dysregulation, ROS production, and cardiac pathology. The administration of PKG decreases activity of TRPC6, improving the cardiac response to stress-stimulated contraction and arrhythmia generation[187]. Deletion of theTRPC6 gene in the double knockout murine model *mdx:utrn*$^{+/-}$ reversed the underlying cardiac pathology by decreasing hypernitrosylation, restoring homeostatic Ca^{2+}, and improving cardiac remodelling[187].

Pharmacological inhibition of TRPC6 and TRPC3 in DMD vascular smooth muscle cells using GsMTx-4, a highly specific mechanosensitive ion channel inhibitor, attenuated pathological $[Ca^{2+}]_i$[295]. GsMTx-4 downregulated NADPH oxidase 2 (NOX2) activity as well as ROS, although the underlying mechanism was not clearly delineated[296]. Furthermore, application of GsMTx-4 was reportedly cardioprotective and therefore this may represent a pharmacological strategy targeting mechanosensitive channels for DMD[297].

1.12.3 The Cytoskeleton is Dysfunctional in DMD and is a Key Contributor to the Mechanopathogenesis of Cardiomyocytes

Alterations in the architecture or dynamics of the cytoskeleton are prime candidates for overall cellular disruption, and this is indeed the case for DMD.

In particular, the microtubule cytoskeleton has garnered widespread interest in the context of DMD[99,199,298]. Dystrophin directly interacts with microtubules specifically at SR domain 24 and the WW domain[199]. Absence of dystrophin disrupts the microtubule lattice, with *mdx* mice demonstrating a 2.5-fold increase in α-, and β-tubulin monomers, suggesting disorganisation of microtubules[199]. Interestingly, elevated tubulin monomers in *mdx* did not correlate to a shift in the balance of tubulin-microtubule equilibrium, but rather the long-term stabilisation of microtubules was disrupted[199]. This contrasts with other evidence indicating a hyperdense microtubular network in DMD cardiomyocytes and may be the result of the underlying genetic heterogeneity of DMD[59].

In DMD, the microtubule cytoskeleton was reportedly stiffer compared to WT controls[99], indicating an alteration to the overall viscoelasticity of the cell. Increased stiffness of cardiomyocytes causes impaired sarcomeric contraction and time to peak due to cytoskeletal resistance, parameters that can be improved by the application of parthenolide, which decreases detyrosinated microtubules, thought to be responsible for the increased stiffness[99]. Moreover, parthenolide prevented aberrant Ca^{2+} waves in response to stress, underscoring the relationship between the cytoskeleton and Ca^{2+} regulation[99]. Overall, these findings implicate the disorganisation of the cytoskeleton as a determinant of DMD pathogenesis.

Functionally, it has been reported that mechanical stretch increases NOX2 generated ROS as well as elevated Ca^{2+} in *mdx* but not in WT muscles[299]. The role of the microtubule network in connecting axial stress with NOX2, and Ca^{2+} is particularly significant as it relates all of the core pathological features in DMD. The authors suggested that either Piezo 1/2 or TRPC1 stretch activated channels were responsible for the influx of Ca^{2+} observed and are significant contributors towards the DMD cardiac phenotype[299].

Disorganised costameric microtubules in DMD relates to the mislocalisation of organelles, including the Golgi complex[300]. The Golgi apparatus was shown to be mislocalised with an altered morphology in *mdx* compared to WT. Additionally, Golgi functionality was disrupted causing abnormal posttranslational modifications of proteins[300]. The authors successfully rescued the disease phenotype by transfecting *mdx* skeletal muscle cells with the micro-dystrophin, ΔR4-R23, containing binding motifs to actin and microtubules, indicating that it is the cytoskeletal regulation of the Golgi that has gone awry in DMD[300].

Furthermore, nuclear localisation was reportedly hypermobile in *mdx*. Interestingly, Iyer[298] demonstrated downregulation of integral LINC complex proteins in *mdx* mice that disrupted the connection between the nucleus and cytoskeleton. Disruption to the LINC complex is also a notable cause for muscular dystrophy and DCM[301–303]. Transcriptional activity of nesprin-1, a LINC complex protein connecting to the F-actin cytoskeleton, was also diminished, indicating not only disruption to the LINC complex proteome, but dysregulated gene expression. This may be caused by an inability to regulate chromosome nuclear localisation and epigenetic markers[298]. Together these findings suggest that disruption to the microtubule cytoskeleton is a significant factor contributing towards the DMD

phenotype. An overwhelming majority of studies have utilised skeletal muscle and the *mdx* model for elucidating the role of microtubule in DMD. Further work clarifying the role in cardiomyocytes should be performed.

The actin cytoskeleton also contributes to the viscoelasticity, force propagation, and overall mechanobiology of the cell[194]. Reports using hiPSC derived cardiomyocytes (hiPSC-CMs) showed that restoring the ABD1/2 binding sites of dystrophin significantly improved Ca^{2+} handling dynamics[304] suggesting that it is not only microtubules that govern Ca^{2+} dynamics. In support of this notion, mutations in cytoskeletal genes, including those of the DGC (*DMD, PDLIM3, FKTN, SGCG,* and *SSPN*), are a cause for atrial fibrillation in inherited DCM[305,306]. Fatal tachyarrhythmias are pathognomonic in DMD, and it is interesting that mutations of the cytoskeleton seem to be so strongly associated with this phenotype.

The γ-actin subsarcolemmal lattice directly interacts with dystrophin and is increased 10-fold in *mdx* mice compared to WT[307]. This is likely a compensatory mechanism to maintain the integrity of the subsarcolemmal lattice. Notably, the connection to F-actin is disrupted, thereby negatively impacting mechanotransduction along prestressed actin cables. Upregulation of γ-actin potentially complements the increased α7β1 expression discussed previously in relation to DMD.

Lastly, aberrant epigenetic regulation of the actin cytoskeleton has been reported in DMD human cardiac tissue[308]. Lysine acetylation of nucleoporin (NUP) 153 promoted its activation, allowing NUP 153 to subsequently localise and transcribe downstream targets. Multiple genes associated with regulation of the actin cytoskeleton (such as nexilin and p300) and cardiac remodelling were upregulated due to NUP 153 activity, exacerbating the underlying DMD phenotype. Moreover, overexpression of NUP 153 led to

increased $Ca_V1.2$ ion channel activity and Ca^{2+} overload. Accordingly, NUP 153 silencing reversed these findings, demonstrating that epigenetics makes an important contribution to the overall DMD phenotype[308].

1.13 The Use of Human Induced Pluripotent Stem Cell Derived Cardiomyocytes (hiPSC-CMs) in DMD

Conventional models for DMD research have typically centred on using animal models. Of these, the most popular has long been the *mdx* murine model[309]. Pilot studies utilising *mdx* found it particularly suited to recapitulating the skeletal muscle phenotype, which at the time was the primary research concern for DMD. Later work revealed that *mdx* was a poor proxy for mimicking the cardiac phenotype that is observed in DMD patients. This, coupled to the fundamental differences between murine and human cardiac physiology, have brought into question the usefulness of this model[310]. Alternative animal models for DMD are in use, such as canine[311] and porcine[312] models, however these are expensive to generate and maintain as they require more sophisticated facilities and expertise not widely available. Nevertheless, the golden retriever muscular dystrophy (GRMD) model does indeed display DCM comparable to that of the human and are therefore vital to preclinical trials. One such example is the use of GRMD in trialling mini/micro-dystrophin constructs for preclinical trials[311].

The advent of human induced pluripotent stem cells (hiPSCs) and downstream tissue differentiation have highlighted the shortcomings of the various animal models. Moreover, hiPSCs are human derived and thus physiologically relevant for modelling pathophysiology. Additionally, hiPSCs are capable of recapitulating disease phenotypes observed and have garnered widespread usage in the DMD field as well as cardiology in

general[313–316]. Originally hiPSCs were described and characterised by Yamanaka using mouse embryonic fibroblasts (MEFs)[317]. The elucidation and transfection of four governing transcription factors led to the dedifferentiation of the MEFs. These four factors are c-MYC, KLF4, OCT3/4, and SOX2, and are now dubbed the 'Yamanaka' factors. Subsequent work by Yamanaka[318] using human dermal fibroblasts demonstrated the conservation of the transcription factors by successfully dedifferentiating human dermal fibroblasts. It should be noted here that reprogramming of somatic cells can be achieved using either viral vectors, CRISPR, or the tetracycline inducible piggyBac transposon. The elegance of the hiPSC is multifactorial. hiPSCs can, in theory, provide an unlimited supply of stem cells and can undergo redirected differentiation, that is to say make any desired cell type.

The generation of hiPSC-CMs was finessed in work by Lian[319] and Burridge[320], amongst others, where pharmacological manipulation of Wnt/β-catenin pathway was shown to be sufficient to induce cardiogenesis in hiPSCs. Since then, significant effort has been made towards optimising hiPSC-CMs with the aim to as faithfully recapitulating the adult cardiomyocyte phenotype as possible[321,322]. Due to the importance of Wnt/β-catenin in hiPSC-CM differentiation, a brief overview is provided.

The highly evolutionarily conserved Wnt/β-catenin family of proteins are central to the cardiac differentiation utilised in this work. Wnt binds to the transmembrane ligand, G-protein couple receptor, frizzled. Activation of frizzled upregulates the activity of the transcriptional activator, β-catenin. In the absence of Wnt, glycogen synthase kinase-3β (GSK3β) forms a destruction complex targeting the N-terminus of β-catenin causing its ubiquitination and subsequent degradation[323]. However, binding of Wnt to

frizzled promotes the activity of dishevelled, which localises to GSK3β, interfering with its ability to ubiquitinate β-catenin. This enables β-catenin to translocate to the nucleus and activate downstream genes, for example *VEGF*. It is also important to note that Wnt undergoes a series of lipidation steps that are necessary for its secretion. A palmitoylation stage carried out by porcupine is particularly notable as this is one of the targets for inhibiting Wnt used here for cardiac differentiation[324].

The use of hiPSC-CMs in DMD has emerged as a revolutionary model with widespread applications such as the screening of pharmacological compounds, elucidating underlying (patho)mechanisms, and can be used to complement and further *in vivo* work. The emergence of several limitations in hiPSC-CM has hindered their use clinically, such as an immature phenotype where hiPSC-CMs are comparable to embryonic and foetal cardiomyocytes and not adult cardiomyocytes. This aspect has been extensively characterised at the (epi)genome, proteome, and metabolome levels.

1.14 Summary of General Introduction

The importance of the DGC in the maintenance of striated muscle tissue cannot be overstated. In its absence, patients suffer from a catastrophic, life-limiting muscular dystrophy (DMD) that impacts all aspects of their lives. In order to alleviate the disease phenotype, with the aim of curing patients with DMD, it is important to elucidate and examine the underpinning mechanisms. The myocardium leverages the spring-like action of dystrophin to protect against contraction-induced injury, and thus maintain the sarcolemma. Moreover, the DGC acts to scaffold additional mechanosensitive proteins, such as nNOS, YAP, and AMPK. Finally, maintaining the ECM-cell interface poises dystrophin as a governing body

of cellular viscoelasticity, a feature important for overall cardiomyocyte functionality. The absence of dystrophin or other DGC components impairs the integrity of the sarcolemma as well as preventing repair mechanisms from being carried out. In addition to this, several key aspects of cellular physiology undergo disruption including Ca^{2+}, cytoskeletal architecture, and epigenetic regulation.

Examination into biomechanics has revealed itself to be particularly important in governing cellular and molecular processes, dictating higher order phenotypes. In particular, I have highlighted and examined evidence showcasing the impact of disrupted biomechanics in DMD and how this may drive the underlying pathomechanisms. Overall, the absence of dystrophin and other constituents of the DGC, or disruption to their functional aspects *e.g.* glycosylation, results in a weakened and structurally fragile sarcolemma. This renders it susceptible to contraction-induced injury with a negative impact on cellular mechanotransduction, mitochondrial dysfunction, pro-inflammatory state, and necrotic cell death being characteristic. Moreover, faulty ion channel regulation, elevated Ca^{2+}, and ROS production further drive the disease phenotype accounting for arrhythmias and sudden cardiac death observed in patients. Communication to the nucleus is disrupted leading to aberrant mechanotransduction and altered gene expression.

In summary, disrupting the ECM-cell interface promotes aberrant mechanotransduction that may prevent adaptation and appropriate responsivity of cardiomyocytes to their microenvironment. Altogether, this contributes towards the overall DCM and end-stage heart failure observed in DMD.

1.15 Aims and Hypothesis of Thesis

The cause of death within the majority of DMD patients is now DCM and end-stage heart failure. Over 90% of the DMD population at 18 years have clinically overt signs of DCM[325], with heart function declining steadily, with death typically ensuing by the third decade of life. This severe disease is caused by the absence of the protein, dystrophin, which functions as a mechanoprotector of the sarcolemma.

My hypothesis is the requirement of dystrophin for maintaining the overall integrity and function of cardiomyocytes, with an essential role in mechanotransduction. I hypothesise that dystrophin enacts these features via its ability to interact and regulate the cytoskeleton, acting to bridge the extra- and intra-cellular components and actuating cellular viscoelasticity, overall facilitating cardiac adaptation to the microenvironment. Thus, the absence of dystrophin, as is the case for DMD/BMD, results in the loss of these vital functions and is the central driver of the DMD pathogenesis.

To validate my hypothesis, several aims have been devised for this thesis. First, I aimed to generate, maintain, and characterise a human DMD relevant cardiac model. Here, I used a 2-D monolayer culture to generate both WT and DMD mutant hiPSC-CM cell lines. Establishing the model is of critical importance as this determines all subsequent experiments.

Second, to characterise the cellular and nuclear morphology of hiPSC-CMs in response to a variety of physiologically relevant mechanical stimuli. These include altered substrate elasticity, hydrodynamic pressure application, and stretch. In addition to this, I aimed to characterise the overall cardiomyocyte viscoelasticity.

Finally, I aimed to determine whether downstream signalling events were affected in DMD compared to WT cardiomyocytes. hiPSC-CMs at baseline or subjected to the aforementioned mechanical experiments were examined. In particular, I want to examine the nuclear localisation of the mechanosensitive protein, YAP.

2 Methods and Materials

Do it or do not do it- you will regret both:

Søren Kierkegaard

Never work with animals or children...(I'd like to add 'or iPSCs'!)

W.C. Fields (modified by Darren Wilson)

2.1 Cell Culture Techniques

2.1.1 Overview of the Four Human Pluripotent Stem Cell (hiPSC) Cell Lines

This work utilised four human pluripotent stem cell (hiPSC) lines:

GM25256 'CRISPRi' termed **WT 1** throughout the work. This cell line was obtained from the Coriell Institute GM25256 and was derived from human dermal fibroblasts. The donor was a healthy 30-year-old male.

HPSI0214i-kucg_2 termed **WT 2** throughout the work. This cell line was obtained from European Collection of Authenticated Cell Cultures and was derived from human dermal fibroblasts. The donor was a healthy 65–69-year-old male.

CENSOi002-B termed **DMD 1** throughout the work. This cell line was obtained from the European Collection of Authenticated Cell Culture and was derived from fibroblasts. The donor was a confirmed DMD patient aged 5-9 year old male harbouring the mutation c.9691C>T (p.Gln3231*).

CENSOi007-A termed **DMD 2** throughout the work. This cell line was obtained from a collaborator at University College London, Great Ormond Street Hospital, from Professor Jennifer Morgan. The donor was a confirmed DMD patient aged 10–14-year-old male harbouring a deletion of exon 52 in *DMD*.

All of the above hiPSC cell line were verified via teratoma formation and pluripotency biomarkers (including SSEA-4, TRA-1-60, OCT3/4) prior to this body of work by either the company at source or by previous laboratory members within Dr Lin's laboratory.

2.1.2 Thawing and Plating of hiPSCs

Conventional hiPSCs were thawed from liquid nitrogen or -80^{o}C at 37^{o}C. 1 mL StemFlex medium (see §2.8) supplemented with 10 µM Y-27632 dihydrochloride ROCK inhibitor (RI; Tocris 1254) was added dropwise to the cryovial prior to transfer to a 15 mL falcon tube. Then, hiPSCs were centrifuged at 1200 rpm for 5 min at RT before being transferred to a 6 well plate. All experiments using hiPSCs were carried out in sterile conditions in a class II laminar flow biological safety cabinet.

6-well plates were coated with vitronectin recombinant human protein (Invitrogen, A14700) for 1 hr at room temperature (RT) at a concentration of 5 µg/mL in 1x phosphate buffered saline (PBS; ThermoFisher, 14190-169). Plates were washed with 1x PBS twice after coating with vitronectin prior to the seeding of hiPSCs. hiPSCs were thawed at 37^{o}C in StemFlex medium (Gibco, A3349401) supplemented with 1% penicillin-streptomycin (P/S; ThermoFisher, 15070063) and 10 µM RI before centrifuging at 1200 rpm for 5 min at RT. hiPSCs were then resuspended in Stemflex medium supplemented with 1% P/S and RI and plated for 24 hrs at 37^{o}C, 5% CO_2. Afterwards, the medium was changed to Stemflex plus 1% P/S and changed every other day until cells were 80-90% confluent. When confluent, hiPSCs were dissociated non-enzymatically using Versene solution (Gibco, 15040066) and incubated for 5 min at RT (0.5 mL/well). Versene was aspirated and cells were mechanically detached into clumps using a wide bore P1000 tip and replated in Stemflex medium supplemented with 1% P/S and 10 µM RI. Cells were then distributed as required (typical passage was 1:6). The passage number used for the hiPSC cell lines ranged between 4-80.

2.1.3 hiPSC Cell Cryopreservation

Cryopreservation of hiPSCs was carried out by passaging cells as described previously (§2.1.2). After the removal of Versene, 1 mL StemFlex supplemented with both 10 µM RI and 10% DMSO (Sigma, D2650) was added to each well, termed hiPSC freezing media. Cells were harvested as described before (§2.1.2) and then placed into a cryovial. hiPSCs were then transferred to -80^{o}C for 24 hrs and then transferred to -196^{o}C in liquid N_2 for long-term storage.

2.1.4 Cardiac Differentiation Protocol for hiPSC

Cardiac differentiation was carried out based on protocols developed by Lian[319], Burridge[320], Mandegar[326], and Parikh[327]. hiPSCs were dissociated using 0.5 mL of Trypsin-EDTA (0.05%) (Gibco, 11580626) for 5-7 min at 37^{o}C before being neutralised by Stemflex medium supplemented with 1% P/S and 10 µM RI. hiPSCs were counted and then seeded at a density of 4.5x10^{4} cm^{-2} in a 24-well plate coated using Matrigel® (Corning, 1543550) at a concentration of 0.3 mg/mL in DMEM/F-12 medium (Gibco, 11554546) for 1 hr at 37^{o}C and then rinsed once with 1x PBS before seeding hiPSCs. hiPSCs were seeded onto the Matrigel® coated plate using Stemflex medium supplemented with 1% P/S and 10 µM RI for 24 hrs, this was termed Day -3 (D-3) (Figure 2.1). After 24 hrs, the media was changed to Stemflex medium with only 1% P/S and hiPSCs were incubated for 48 hrs to recover.

Biphasic manipulation of the Wnt/β-catenin pathway is required to generate hiPSC-CMs and is generally referred to as the 'GiWi' protocol, wherein the initial step is to inhibit glycogen synthase kinase 3-β (GSK3-β; Gi) followed by the second step which is to inhibit Wnt activity (Wi).

Pharmacological modulation using CHIR99021 and C59 is sufficient for generating hiPSC-CMs by modulating Gi and Wi respectively.

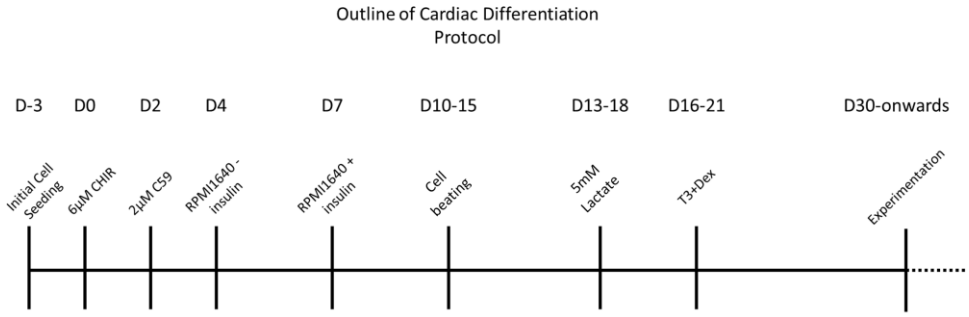

Figure 2.1: Timeline of pharmacological driven cardiac differentiation of hiPSCs to hiPSC-CMs *hiPSCs were seeded at 4.5x10^4 cm^{-2} at D-3. Pharmacological modulation of the Wnt/β-catenin was used to produce hiPSC-CMs. 6 μM CHIR was used to inhibit GSK-3β to allow expression of β-catenin thereby directing cells towards mesoderm lineage. Following this, 2 μM C59 was used to inhibit production of Wnt, thus committing cells to cardiac lineage. hiPSC-CMs were given RPMI 1640 supplemented with B27 without insulin until D7 where the media was supplemented with B27 with insulin. To purify hiPSC-CMs, 5 mM lactate was used in glucose free media for 6 days. Maturation was enhanced using 0.1 μM T3 and 1 μM dex was administered for 10 days prior to experimentation.*

At D0, the media was changed to RPMI-1640 medium (Sigma, R5886) supplemented with 1x B27 (-insulin) (ThermoFisher, A1895601) with 150 μL P/S and 213 μg/mL 2-Phospho-L-ascorbic acid (L-AA) (Sigma, 49752) and 500 μg/mL recombinant human albumin (rHA) (Sigma, A9731) and 6 μM CHIR99021 (Tocris, 4423) for 48 hrs at 37^{o}C, 5% CO_2. CHIR99021 enhances Wnt/β-catenin activation by inhibiting GSK3-β.

Following this, the media was changed to RPMI-1640 medium plus B27 (-insulin) with 1% P/S and L-AA and rHA supplemented with 2 μM C59 (abcam, ab142216) for 48 hrs at 37^{o}C, 5% CO_2 inhibiting Wnt activity. Afterwards, the media was changed to RPMI-1640 medium plus B27 (-

insulin) containing 150µL P/S, 213 µg/mL L-AA, and 500 µg/mL rHA and changed every other day until D7.

At D7, the media was changed to contain B27 (+insulin) and changed every other day until cells were observed beating (between D7-10). hiPSC-CMs then underwent metabolic selection to purify the hiPSC-CMs using RPMI-1640 medium (without glucose) (ThermoFisher, 11879020) plus 150 µL P/S, 213 µg/mL L-AA, 500 µg/mL rHA supplemented with 5 mM lactate (Sigma, 71718) for 6 days, with the media being refreshed on day 3.

Following metabolic selection, hiPSC-CMs were incubated with 0.5mL Accutase (Merck, SCR005) for 10-15 min at 37^{o}C before being neutralised using RPMI-1640 medium containing B27 (+insulin), 150 µL P/S, 213 µg/mL L-AA, 500 µg/mL rHA supplemented with 0.1 µM tri-iodothyronine (T3) (Sigma, T2877) and 1 µM dexamethasone (Dex) (Cayman, 11015) plus 10% knockout replacement serum (KSR) (ThermoFisher, 10828028) plus 2 µM thiazovivin (Selleck, S1459) for use in experiments.

T3 and Dex supplemented media was used for a minimum of 10 days to improve hiPSC-CM maturation before use in subsequent experiments. Brightfield images of hiPSC-CMs were obtained using the EVOSTM XL Core configured microscope at different time points documenting the progress of cardiac differentiation. These were namely D0, D2, D4, D7, post-T3/Dex (~D30). hiPSC-CMs were maintained at 37^{o}C with 5% CO_2 for the duration of their incubation.

2.2 Nucleotide Techniques

2.2.1 Genomic DNA Extraction

Genomic DNA (gDNA) was extracted from a minimum of $5x10^5$ cells using the QIAamp DNA Mini Kit (Qiagen, 51304) as per the manufacturer's instructions. In brief, cell pellets were thawed on ice. Following this, 180 µL of buffer ATL with 20 µL proteinase K were added, prior to 30 s vortex to homogenise cells. Following this, 200 µL buffer AL was added and cells underwent vortexing, prior to 10 min incubation at 70^{o}C. Afterwards, 200 µL 70% ethanol was added and the cells were vortexed again. The mixture was then added to a QIAamp Mini spin column within a 2 mL collection tube and centrifuged at 8000 rpm for 1 min. Flow through was discarded. 500 µL of buffer AW1 was added, followed by centrifugation at 8000 rpm for 1 min. After flow through was discarded 500 µL of buffer AW2 was added. The cells were then centrifuged at 14000 rpm for 3 min. The QIAamp mini spin column was then transferred to a fresh 2 mL collection tube and centrifuged at 14000 rpm for 1 min to reduce carry over of any buffer. 30 µL of ultrapure water (Invitrogen, 10977-035) was then added and incubated at RT for 5 min. Following this, cells were then centrifuged at 8000 rpm for 1 min, thereby eluting the DNA. 1 µL of DNA sample was taken and quantified using either nanodrop or Qubit™ Fluorometer (Life Technologies, Q32216.

gDNA was then eluted into a sterile collection column using 30 µL of nucleotide-free ultrapure water (Invitrogen, 10977-035) and the concentration of gDNA was determined using Qubit™ Fluorometer (Life Technologies, Q32216) with the Qubit™ dsDNA high sensitivity assay kit (Invitrogen, Q32854) as per the kit's instructions.

2.2.2 Polymerase Chain Reaction

Polymerase chain reaction (PCR) was used to amplify regions of interest prior to sequencing, notably over the mutation site c.9691 exon 67 of *DMD* (Table 2.10), to confirm the mutational status of the hiPSC cell lines. PCR was carried out using 60 ng total gDNA using the LongAmp Taq DNA Polymerase Amplification Kit (New England Biolabs, MO323S), with reaction set-up shown in Table 2.2 and cycling parameters in Table 2.3.

Table 2.1: Primers used to amplify and sequence exon 67 of DMD c.9691C>T Custom primers were produced by Integrated DNA Technologies, UK.

Primers	Sequence	Product Length (bp)
DMD c.9691C>T	F 5' GCACAAATTAGAAGTAACCCCA 3' R 5' AAATCTCCATCTGCAGCAGG 3'	1192

Table 2.2: LongAmp gDNA PCR Reaction Set-up

Reagent	Volume (µL)	Final Concentration
5X LongAmp *Taq* Reaction Buffer	5	1X
10 mM dNTPs	0.75	300 µM
DMSO	1.25	
Forward Primer (10 µM)	1	0.4 µL
Reverse Primer (10 µM)	1	0.4 µL
LongAmp *Taq* DNA Polymerase	1	2.5 units/ 25 µL
Nuclease-free Water	to 25 µL	
Template DNA	Variable	>60 ng
Total Reaction Volume	25	

Table 2.3: Thermocycling conditions for amplifying gDNA using PCR

Step	Temperature (^{o}C)	Time
Initial denaturation	94	30 s
30 Cycles	94	30 s
	45-65	1 min
	65	60 s/kb
Final Extension	65	10 min
Hold	4	indefinitely

2.2.3 Gel Electrophoresis

A 1% agarose gel was prepared by dissolving 0.5 g of agarose powder (Sigma, 9012-36-6) in 50 mL of 1x Tris acetate EDTA buffer (TAE) with 5 µL Sybr safe (ThermoFisher, S33100) and poured into the casting tray with comb (to form wells) and allowed to set at RT for a minimum of 20 min. Afterwards, the gel was placed into a gel electrophoresis tank with sufficient 1x TAE buffer added to submerge the gel and then the comb was removed. 5 µL of a DNA ladder (Thermo, 10488058) was added into the first well with 15 µL of PCR product added into the subsequent wells. Gel electrophoresis was set at a voltage of 100 mV for 30 min. After, the gel was visualised using a Chemidoc system.

2.2.4 Sequencing of Genomic DNA Fragments

Amplified gDNA was sequenced using the primers listed in Table 2.1 by Source BioScience (Cambridge) with results analysed in SnapGene® Viewer 5.0.7. First, the PCR products were purified using the MinElute PCR Purification Kit (Qiagen, 28004) as per kit instructions. In brief, 5 volumes of buffer PB was added to 1 volume of PCR reaction mix. The colour of the mixture was checked to ensure optimal pH (yellow indicated optimal pH.

Orange or violet colouring indicated pH was basic and required the addition of sodium acetate at pH 5.0). A MiniElute column was then placed into a 2 mL collection tube, and the PCR mixture was added to the MiniElute column. Following this, the MiniElute column was centrifuged at 13000 rpm for 1 min. Flow through was then discarded, and the MiniElute column was added back to the 2 mL collection tube. Subsequently, 750 µL buffer PE was then added to the sample and centrifuge, as before, for 1 min. Afterwards, the MiniElute column was then added to a fresh 2 mL collection tube. 10 µL of ultrapure water then added and the sample incubated at RT for 2 min prior to centrifugation, as before, for 1 min.

The principle behind the purification step centres around the pH and nucleic acid adsorption to the silica membrane within the MiniElute column. The buffer adds a high-salt environment to mediate this interaction. Impurities within the PCR mixture fail to adsorb and are subsequently washed away leaving a low-salt, purified PCR product.

Following purification of the PCR product, 10 ng/µL of PCR product and 3.2 pmol/µL/primer in 5 µL reactions were sent to Source BioScience for analysis. The result was then analysed using SnapGene® Viewer 5.0.7.

2.2.5 RNA Extraction

hiPSCs or hiPSC-CMs were harvested using 175 µL/well RLT buffer (Qiagen, 79216) supplemented with 10 µL β-2-mercaptoethanol (Gibco, 11528926). Samples were then snap frozen at -20^{o}C before being transferred to -80^{o}C for storage of up to 1 month.

When ready for use, the work surface and equipment were treated using RNaseZAP (Thermo, AM9780) to reduce risk of cross-contamination.

Samples were thawed on ice and total RNA was extracted using the RNeasy Plus Mini Kit (Qiagen, 74134) as per the manufacturer's instructions.

The principle of the RNeasy Plus Mini Kit is first to lyse and homogenise samples, in a buffer that inactivates and denatures RNases, thus protecting the RNA. Previously harvested cell samples were thawed on ice (contained within 350 µL of buffer RLT and 10 µL β-mercaptoethanol). The 350 µL of the cell mixture was then added to a genomic DNA (gDNA) collection tube that was contained within a 2 mL collection tube. Then, the sample was centrifuged at 10000 rpm for 2 min. The column was discarded and the flow through was retained. Following this, 350 µL of 70 % ethanol was added to the flow through and mixed via pipetting. The addition of ethanol optimises binding conditions for RNA to the membrane within the column. Subsequent washes result in the rinsing away of impurities. Then, 700 µL of the sample was added to an RNeasy spin column within a 2 mL collection tube and centrifuged at 10000 rpm for 15 s. Flow through was discarded and 700 µL of buffer RW 1 was added to the sample. The sample was centrifuged as before for 15 s. Afterwards, 500 µL buffer RPE was added to the sample followed by centrifugation, as before. Flow through was discarded and this step was repeated, except the sample was centrifuged for 2 min at 10000 rpm. The RNeasy column was then placed into a new 2 mL collection tube and 30 µL of RNase-free ultrapure water was added and incubated for 1 min at RT prior to centrifugation at 10000 rpm for 1 min.

30 µL was eluted into a sterile collection tube in nucleotide-free ultrapure water. The concentration of total RNA was determined using the Qubit™ Fluorometer with the Qubit™ RNA HS Assay Kit (Invitrogen, Q32852).

2.2.6 Reverse Transcription: cDNA Synthesis from mRNA Template

mRNA was converted to cDNA using the High-Capacity cDNA Reverse Transcription Kit (Applied Biosystems, 4368814). 300 ng of total mRNA was added up to a volume of 10 µL and mixed with the master mix outlined in Table 2.4. Thermocycling PCR conditions for synthesising cDNA are outlined in Table 2.5. cDNA templates were stored at -20^{o}C until required.

Table 2.4: High-capacity cDNA reverse transcription reaction master mix.

Reagent	Volume (µL)	Final concentration
10X RT Buffer	2	2X
25X dNTP Mix (100 mM)	0.8	8 mM
10X RT Random Primers	2	2X
Reverse Transcriptase	1	50 U/ µL
RNase Inhibitor	1	
Nucleotide-free Water	3.2	
mRNA 300 ng	10	
Total Volume	**20**	

Table 2.5: Thermocycling parameters for the conversion of mRNA to cDNA.

Step	Temperature (^{o}C)	Time
1	25	10 min
2	37	2 hrs
3	85	5 min
Hold	4	Indefinite

2.2.7 Real-Time Quantitative PCR (RT-qPCR)

Once mRNA was converted to cDNA, relative gene expression was measured by RT-qPCR using the PowerUp™ SYBR™ Green Master Mix (Applied Biosystems, A25742) in the so-called 2-step RT-qPCR process. The reaction set-up is detailed in Table 2.6 and thermocycling conditions are detailed in Table 2.7. Primers were sourced from the literature or were designed using NCBI Blast. Custom primers for RT-qPCR were purchased from Integrated DNA Technologies UK and the sequences are provided in Table 2.8.

Table 2.6: RT-qPCR reaction set-up

Reagent	Volume (µL)	Final Concentration
PowerUp™SYBR™ Green Master Mix (2X)	6	1X
Forward Primer (10 µM)	0.12	0.1 µM
Reverse Primer (10 µM)	0.12	0.1 µM
cDNA (diluted 1:10)	5	
Nucleotide-free Water	0.72	
Total Volume	12	

Table 2.7: Thermocycling conditions for RT-qPCR

	Step	Temperature (^{o}C)	Time
Holding Stage	1	50	2 min
	2	95	2 min
Cycling Stage (x40)	1	95	3 s
	2	60	30 s
Melt Curve Stage	1	95	15 s
	2	60	1 min
	3	95	15 s

Table 2.8: List of primers used for RT-qPCR.

Gene Type	Gene	Sequence
Cardiac Structural Genes	*ACTN2*	F 5' CTTCTACCACGCTTTTGCGG 3' R 5' AGGCACCAGCAATATCCGAC 3'
	MYH6	F 5' TTCAGGATTCTCCGTGAAGGG 3' R 5' GTCGAACTTGGGTGGGTTCT 3'
	MYH7	F 5' TTGGCACGAAGGGCTTGAA 3' R 5' TTCCTCCCAAGGAGCTGTTAC 3'
	TNNT2	F 5' GACAGAGCGGAAAAGTGGGA 3' R 5' CTCCTTGGCCTTCTCCCTCA 3'
Cardiac Developmental Genes	*ISL-1*	F 5' GGATTTGGAATGGCATGCGG 3' R 5' CATTTGATCCCGTACAACCTGA 3'
	NKX2.5	F 5' CAAGTGTGCGTCTGCCTTTC 3' R 5' CGCACAGCTCTTTCTTTTCGG 3'
	GATA 4	F 5' TCCTCCCACGCATATTATCG 3' R 5' AAGCTCTGATACATGGTCCC 3'

Integrin Expression Genes	*ITGA1*	F 5’ CCTGAGAAGAGGAGAGATGGTA 3’ R 5’ GCTGTCACTTGTTGCACTTAAA 3’
	ITGβ1A	F’ 5’ TGATCCTGTGTCCCATTGTAAG 3’ R 5’ TGACCTCGTTGTTCCCATTC 3’
	ITGβ1D	F 5’ TGATCCTGTGTCCCATTGTAAG 3’ R 5’ TGACCTCGTTGTTCCCATTC 3’
	ITGA7	F 5’ CTGTGAGATGAGAGTGGGTAAA 3’ R 5’ GAATGGGAGAGGAAGGGATTAG 3’
	ITGA6	F 5’ TTGGCGAGCAAGCTATGAA 3’ R 5’ CTGTGCCGAGGTTTGTAAGA 3’
	ITGA5	F 5’ GGTGGACCAGGAAGCTATTT 3’ R 5’ GAACCAGGTTGATCAGGTACTC 3’
	ITGA1	F 5’ CCTGAGAAGAGGAGAGATGGTA 3’ R 5’ GCTGTCACTTGTTGCACTTAAA 3’
Pluripotency Expression Gene	*NANOG*	F 5’ AGAAAAACAACTGGCCGAAGAAT 3’ R 5’ GTTGAATTGTTCCAGGTCTGGTT 3’
Dystrophin Expression Genes	*DMD (whole gene)*	F 5’ TGGGGGCAGTAACATTGAGC 3’ R 5’ CCGCTTCGATCTCTGGCTTA 3’
	DMD C-terminus	F 5’ TGACCACTATTTATGACCGCCTG 3’ R 5’ CTCCCTGTTCGTCCCGTATC 3’
	DMD N-terminus	F 5’ CACTGGCAGGTCAAAAATGTAATG 3’ R 5’ TGGCCTATGACTATGGATGAGAGC 3’
Transcriptional Co-activator	*YAP*	F 5’ GCGGCTGAAACAGCAAGAAC 3’ R 5’ TTGGTAACTGGCTACGCAGG 3’

Housekeeping Gene	*GAPDH*	F 5' CTCCTCCACCTTTGACGCTG 3' R 5' CATACCAGGAAATGAGCTTGACA 3'

The RT-qPCR reaction was carried out using the SteponePlus™ Real-Time PCR System and Thermal Cycling Block and data was analysed using the delta-delta Ct method ($2^{-\Delta\Delta Ct}$). GAPDH was used as the housekeeping gene for normalisation.

The $2^{-\Delta\Delta Ct}$ method is a relative quantification of mRNA gene transcripts to a reference gene, the so-called 'housekeeping gene', and is not an absolute quantification. The Ct is the point at which fluorescence breaches the defined threshold. The quantification steps are as follows.

The change in ΔCt is calculated by:

$$\Delta Ct = Ct_{Target\ gene} - Ct_{Housekeeping\ gene} \quad (Eq. 2.1)$$

Next, the ΔΔCt is calculated by:

$$\Delta\Delta Ct = \Delta Ct_{Target\ sample} - \Delta Ct_{Housekeeping\ sample} \quad (Eq. 2.2)$$

From this, the $2^{-\Delta\Delta Ct}$ can be determined directly. The normalisation value is set to 1, as $2^0 = 1$. The 2 is derived from the normalisation value plus the PCR amplification efficiency under the assumption of 100% (*i.e.* 1). Once the $2^{-\Delta\Delta Ct}$ has been calculated, normalisation to WT 1 can then take place and values are then in reference to this.

Melt curves for each primer pair were examined to ensure that only single peaks were produced, an indicator that primer-dimers were not produced indicative primers specificity. The Ct value was defined when the amplification curve passes the threshold which typically begins

approximately cycle 15 onwards, depending on the gene. The more cycles required to breach the threshold indicates a lower abundance detectable mRNA product and thus decreased gene expression. Maximum number of cycles was 40.

2.3 Immunocytochemistry Techniques

Immunocytochemistry was used to throughout to determine expression, localisation, and relative fluorescence intensity of proteins within hiPSCs or hiPSC-CMs, with primary and secondary antibodies listed in Table 2.9. Firstly, hiPSCs or hiPSC-CMs were washed using 1x PBS prior to fixation using 4% (v/v) paraformaldehyde (ThermoFisher, 28906) in 1x PBS for 10 min at RT. Cells were then washed three times in 1x PBS, 5 min per wash. Permeabilisation of cells was carried out using 0.1% Triton-X 100x (Sigma, T8787) in 1x PBS for 10 min at RT. Following three washes in 1x PBS, 5 min each, cells were blocked using 5% goat serum (Sigma, G9023) and 1% BSA (Fisher, BP9700-100) in 1x PBS for 1 hr at RT, termed blocking buffer. Then, the primary antibody in blocking buffer was added either overnight at 4^{o}C or 2 hr at RT. Following incubation with primary antibody, the cells were washed three times as before prior to the addition of the secondary antibody.

Secondary antibodies and 4',6-diamidino-2-phenylindole (DAPI) were made up in blocking buffer and incubated at RT for 1 hr hidden from light. Following incubation with secondary antibody, cells were washed as before, and stored in 1x PBS at 4^{o}C (in the dark) until imaged.

Imaging was carried out using either the Nikon CSU-W1 SoRa Spinning Disk Confocal or the Zeiss LSM710 Confocal and Elyra PS.1 Super-resolution microscopes. For image intensity data acquisition, the same imaging

parameters (laser intensity; exposure time) were maintained per experiment between cell lines to ensure consistency.

Table 2.9: Primary and secondary antibodies used for immunocytochemistry

	Biomarker	Species	Isotype	Dilution	Catalogue Number
	Primary Antibodies				
Pluripotency Biomarkers	Anti-NANOG	Mouse Monoclonal	IgG1	1:100	Abcam, ab80892
	Anti-OCT3/4	Mouse Monoclonal	IgG2b	1:100	Santa Cruz, sc-5279
	Anti-SSEA4	Mouse Monoclonal	IgG3	1:50	BD Bioscience, 560796
	Anti-TRA-1-60	Mouse Monoclonal	IgM	1:100	Santa Cruz, sc-21705
	Anti-SOX2	Mouse Monoclonal	IgG2a	1:100	R&D, MAB2018
Cardiac Structural and Developmental Biomarkers	Anti-NKX2.5	Mouse Monoclonal	IgG1	1:100	Santa Cruz, sc-376565
	Anti-TNNT2	Mouse Monoclonal	IgG1	1:300	Abcam, ab8295
	Anti-α-actinin (sarcomeric)	Mouse Monoclonal	IgM	1:100	Sigma, A2172
Focal Adhesion Related	Anti-Vinculin	Mouse Monoclonal	IgG1	1:100	Sigma, V9131
	Anti-Integrin β1	Mouse Monoclonal	IgG1	1:100	Abcam, ab30394

	Anti-Phospho Src (Tyr 416)	Rabbit Polyclonal	-	1:100	CST 2101
	Anti-Phospho-FAK (Y397)	Rabbit Monoclonal	IgG	1:100	CST 8556
Nuclear Envelope	Anti-Lamin A/C	Rabbit Monoclonal	IgG	1:200	ThermoFisher, 2Q2G6
Cytoskeleton and Related Proteins	Recombinant Anti-Dystrophin	Rabbit Monoclonal	IgG	1:50	Abcam, ab275391
	Anti-α-Tubulin	Rabbit Polyclonal	-	1:100	Abcam, ab4074
Nuclear Cell	Anti-YAP1	Mouse Monoclonal	IgG2a	1:100	Santa Cruz, sc-101199
	Secondary Antibodies				
	Alexa Fluor™ 488	Goat Anti-Mouse	IgG	1:100	ThermoFisher, A32723
	Alexa Fluor™ 594	Goat Anti-Mouse	IgG2a	1:100	ThermoFisher, A21135
	Alexa Fluor™ 546	Goat Anti-Mouse	IgM	1:100	ThermoFisher, A21045
	Alexa Fluor™ 546	Goat Anti-Mouse	IgG	1:100	ThermoFisher, A11035
	Phalloidin CruzFluor™ 647nm Conjugate	-	-	1:100	SantaCruz, sc-363797

2.4 Biomechanical Techniques

2.4.1 Fabrication of Polydimethylsiloxane (PDMS) of Different Elasticities

Polydimethylsiloxane (PDMS) is a silicone-based polymer widely used in microfluidics, organ-on-a-chip models, and in the manufacture of different substrate elasticities. PDMS is widely used as it is biocompatible, optically transparent, and the elastic moduli are easily tuneable.

Sylgard® 184 (Dow Corning, 101697) silicone elastomer base was added to Sylgard® silicone elastomer curing agent in a 1:10 ratio, being determined by mass. This was then mixed at RT until opaque white prior to centrifugation at 10,000 rpm for 5 min at 4^{o}C. Sylgard® 527 (Dow Corning, 101693) was made by mixing equal parts 'Part A' and 'Part B', again by measuring mass, and was centrifuged at 10,000 rpm for 5 min at 4^{o}C.

To produce coverslips mimicking the Young's modulus of a healthy cardiac environment (6 kPa) or a fibrotic cardiac environment (130 kPa), blending of Sylgard® 184 and Sylgard® 527 was carried out to produce graded PDMS. For 6 kPa PDMS the mixing ratio between Sylgard® 184 to Sylgard® 527 was 1:20 and for the 130 kPa PDMS the mixing ratio was 1:5. These ratios had been established within Dr Iskratsch's lab previously and reported in the literature[328]. Once the PDMS had been mixed according to the different ratios it was allowed to precure at RT for 1 hr.

2.4.2 Fabrication of PDMS Coated Glass Coverslips

18 x 18 mm round, glass coverslips (VWR, 631-153P) were oxygen plasma treated for 5 min (Harrick Plasma, room air, 18 W) to facilitate binding of PDMS to the glass coverslip and to sterilise and remove organic contaminants[329]. Specifically, oxygen plasma treatment introduces

functional polar groups, namely SiOH (silanol) to PDMS[329]. The introduction of the silanol group increases hydrophilicity which in turn facilitates the binding of PDMS to the glass and extracellular matrix constituent, laminin.

Following the initial round of oxygen plasma treatment, coverslips were coated with 150 µL of either 6 kPa or 130 kPa PDMS. Coverslips were then spin coated clockwise at 1000 rpm for 40 s using the WS-650 Spin 3000 (Laurell Technologies) to ensure an evenly distributed PDMS layer. Afterwards, spin coated coverslips were then cured at either 60^{o}C overnight or at 80^{o}C for 2 hrs prior to use. Coverslips were then plasma treated for 30 s and then sterilised for 10 min at RT using 70% ethanol. Excess ethanol was then removed, and coverslips were air-dried for 10 min prior to being washed using sterile 1x PBS, three times, 5 min per wash.

After sterilisation, the addition of 10 µg/mL laminin (Sigma, L2020) was added to the PDMS coated coverslips for 2 hr at 37^{o}C. Following this, coverslips were washed once with 1x PBS for 5 min before hiPSC-CMs were reseeded, as described §2.1.4, onto the coverslips. hiPSC-CMs were allowed to recover for 5 days on the coverslips before undergoing subsequent experiments. This also ensured that hiPSC-CMs could adapt to the respective substrate elasticity.

2.4.3 Nanoindentation as a means for determining Young's modulus of hiPSC-CMs

The mechanical properties of cells have emerged as a critical parameter for determining disease states, development, and for examining underlying structures- in particular the cytoskeleton. Importantly, alterations in cellular viscoelasticity are increasingly acknowledged disease biomarkers[330].

Two techniques have been developed to examine the underlying viscoelasticity, or more accurately, the Young's modulus of cells: atomic force spectroscopy (AFM) and nanoindentation. Both nanoindentation and AFM are based on similar principles, the central distinguishing characteristic being the scale of operation. AFM typically measures on a smaller scale compared to nanoindentation and can probe single molecules. Although there is considerable overlap between the two. Nanoindentation was used in this work to measure larger scale areas of hiPSC-CMs. Specifically, nanoindentation was performed over the cytoplasmic region of hiPSC-CMs to maintain consistency across experiments. Nuclear nanoindentation was not carried out in this work.

The Young's modulus is a characteristic quantifying the stiffness of materials in response to deformation; and in this case is largely determined by the cytoskeletal architecture and dynamics in cells. Mathematically, the Young's modulus (E) relates two properties tensile stress (σ) and tensile strain (ε) in response to a known force, measuring the capacity of the material to deform. Tensile stress is defined as the force (F) over the area (A) and tensile strain is defined as the change in length (dL) over the total original length (L_o). The relationships are defined as follows:

$$E = \frac{\sigma}{\varepsilon} = \frac{F/A}{dL/Lo} \quad (Eq. 2.3)$$

Further consideration for nanoindentation is to indent onto a cell by a given force. In other words, the load application should be optimised so as not to indent beyond 10% of the total cell height. In this way, the Hertzian model can be applied to interpret the data.

Loading the force onto the sample requires the deflection of a cantilever, of known spring constant, that can then generate a loading-unloading force

curve. Essentially, a force-displacement curve is obtained and then the Hertzian model (Figure 2.2) is applied to the loading region of this curve. Indentation force (F) is assumed to be linear to cantilever bending and can be related by Hooke's law: (*Eq. 2.4).*

$$F = \kappa\delta \ \ (Eq. 2.4)$$

Where κ is the spring constant of the cantilever and δ is the deflection of the cantilever. Importantly, Hooke's law can also be applied to cytoskeletal elements.

The Hertzian model is commonly used to obtain the Young's modulus from the loading-unloading force curve by relating depth, spring constant, the probe, and the cell. Due to the role that height plays in interpretation of the loading-unloading curve, it is vital to maintain across experiments for consistent and comparable data acquisition. With the Hertzian model, knowing the force and depth of indentation allows for calculation of the underlying stiffness. The Hertz model can be written as (*Eq. 2.5)*:

$$F = \frac{4}{3} E_{eff} \sqrt{R_i} \cdot h^{\frac{3}{2}} \ \ (Eq. 2.5)$$

Where E_{eff} is the effective Young's modulus, R_i is the radius of the spherical probe, and *h* is the indentation height. The Hertzian model predicts a linear load-unload curve where load and unload curves are superimposed. This is not observed in live cells due to their viscoelasticity which, in contrast, generate a hysteresis curve. The Hertzian model assumes that the sample is homogenous, isotropic, and has a linear elastic response. These conditions are not satisfied in living cells, nonetheless research has revealed that small indentation depths (not more than 10% cell height) coupled to a small

spherical probe radius broadly follows the Hertzian model and therefore this can be used.

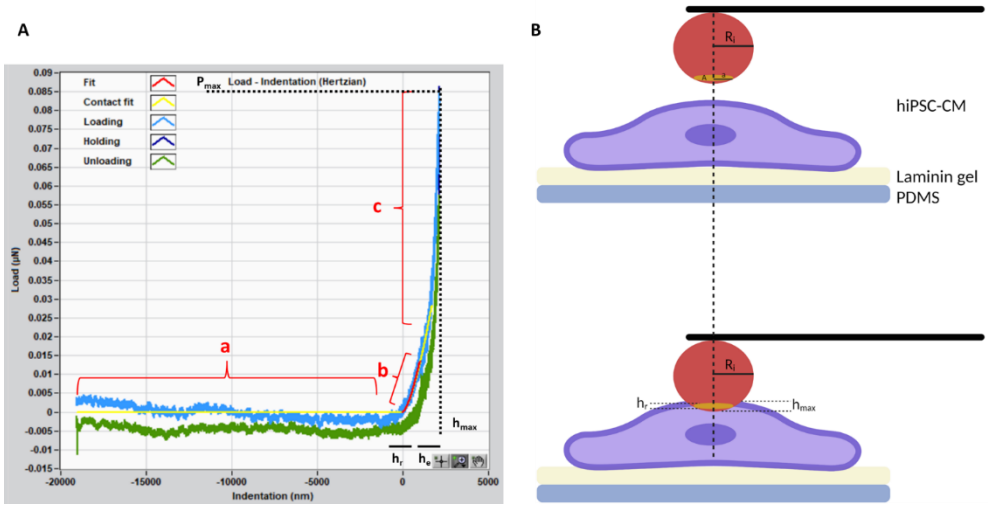

Figure 2.2: Representative example of a loading-unloading force curve acquired during nanoindentation using the Piuma Data Viewer V2.3.5. and principle of the Hertzian model A) a) *The blue line indicates the approach of the nanoindenter probe to the cell that at* ***b)*** *contacts the cell and indicates the initiation of indentation. The red line specifically measures the Young's modulus via the Hertzian model and is where the elasticity of hiPSC-CMs derives from.* ***C)*** *indicates the remainder of the indentation. The green trace indicates unloading, i.e., retraction, of the nanoindenter probe. The Piuma Data Viewer software calculates the Young's modulus from the portion of the curve as indicated by* ***b****.* ***B)*** *The Hertz model used to produce the Young's modulus. The yellow section within the probe represents the contact area (a) to the hiPSC-CM giving a contact area of radius as:* $a = \sqrt{(R_i h_{max})} h_{max}$ *is the total indentation with* h_r *being the final contact depth.* R_i *is the radius of the spherical probe.*

2.4.4 Nanoindentation of hiPSC-CMs on PDMS Substrates of Differing Elasticities

The Chiaro Piuma nanoindenter (Optics 11, Life) was mounted onto an air table at the side of the Leica DMi8 Epifluorescence Microscope (Leica Microsystems) (Figure 2.3) and secured using bolts to minimise vibrations.

The arm of the nanoindenter was positioned over either the 10x or 20x lens of the Leica DMi8 Epifluorescence and secured. Following manufacturer guidelines, the 0.49 N/m; 49 µm probe (Optics 11, Life) was selected to measure the Young's modulus of live hiPSC-CMs.

Figure 2.3: Overview of the Chiaro Piuma nanoindenter set-upA) *Set-up of the nanoindenter. (Yellow text)* ***A)*** *The nanoindenter body,* ***B)*** *The arm of the nanoindenter,* ***C)*** *Leica DMi8 Epifluorescence,* ***D)*** *closer, and alternative view showing nanoindenter arm,* ***E)*** *Probe tip. Using an inverted Leica DMi8 microscope the nanoindenter was situated to the right. The arm of the nanoindenter with the probe attached was lowered over the 10x or 20 x objective lens.* ***B)*** *Brightfield image showing the nanoindenter probe (spring constant, 0.49 N/m; radius, 49 µm) at 20x zoom highlighted by the asterisk. Scale bar= 100 µm.*

Following set-up, the Chiaro Piuma nanoindenter was calibrated using a glass bottomed petri dish using RPMI-1640 medium supplemented with T3/Dex at RT. This maintained the optical density necessary for calibrating the probe. Manufacturer's instructions recommend that calibration had a geometrical factor between 0.8 and 2.5. hiPSC-CMs on laminin coated PDMS 18 x 18 mm glass coverslips were then transferred to a plastic petri dish. RPMI-1640 medium supplemented with T3/Dex was added in addition to 20 mM HEPES (Sigma, H3375-25G) to minimise pH disruption. As hiPSC-CMs were not in a temperature-controlled environment, experiments were limited to a maximum of 1 hr at RT to mitigate any effects that may be attributable to temperature sensitivity or cell death due to this. hiPSC-CMs

were visualised using the Leica DMi8 and the nanoindenter probe was gently lowered into position approximately 100 µm above the hiPSC-CMs prior to data acquisition.

The nanoindentation was carried out with following parameters. The probe indented by a depth of 1000 nm, with a contact threshold of 0.004 and approach speed of 2000 nm/s. 1000 nm was 10% of the cell height allowing application of the Hertzian model for determination of the Young's modulus.

To elucidate the viscoelasticity further, the nanoindenter was used for dynamic mechanical analysis (DMA). For DMA, three frequencies of 1 Hz, 4 Hz, and 10 Hz were selected to stimulate the hiPSC-CMs, each for a time of 2s while indenting 1000 nm with an amplitude of 200 nm. The DMA function allowed examination of oscillatory stimulation on hiPSC-CMs.

A minimum of ten hiPSC-CMs per cell line per substrate elasticity were analysed per experiment with a minimum of three independent experiments being carried out. After nanoindentation, hiPSC-CMs were washed once using 1x PBS for 5 min and then fixed using 4% PFA in 1x PBS for 10 min at RT. Cells were then washed three times in 1x PBS for 5 min before being stored at 4^{o}C until required for immunocytochemistry.

Nanoindentation experiments examining the effect of cytoskeletal (de)stabilisers on Young's modulus of hiPSC-CMs were carried out as described but with the addition of pharmacological agents (Table 2.10). Each pair of drugs targeted either the actin cytoskeleton (cytochalasin D and jasplakinolide) or the microtubule cytoskeleton (taxol and vinblastine).

Table 2.10: Drugs used to (de)stabilise the cytoskeleton.

Drug	Concentration (µM)	Incubation time
Cytochalasin D (Tocris, 1233)	1	30 min
Jasplakinolide (Tocris, 2792)	1	45 min
Taxol (Tocris, 1097)	10	2 hr
Vinblastine (Tocris, 1256)	1	1 hr

2.4.5 Hydrodynamic application of healthy cardiac pressure onto hiPSC-CMs using a pressure chamber

To examine the effect of normal cyclic cardiac pressure, the use of a hydrostatic pressure chamber was used. In conjunction with this, different substrate elasticities were used to examine the dual effect of pressure and substrate forces on hiPSC-CMs. Experiments were carried out using the MechanoCulture TR Hydro mechanical stimulation system (CellScale Biomaterials testing) (Figure 2.4). Healthy cardiac cycling parameters were defined as 120/10 mmHg (0.015/0.0015 MPa) and the cycle is detailed in Table 2.11. These parameters (compress, hold, and recovery times) were tested for achieving reproducible and stable pressure cycling at the set conditions for long-time periods (Figure 2.5). This ensured constant levels throughout the cycle and were optimised within Dr Iskratsch's laboratory.

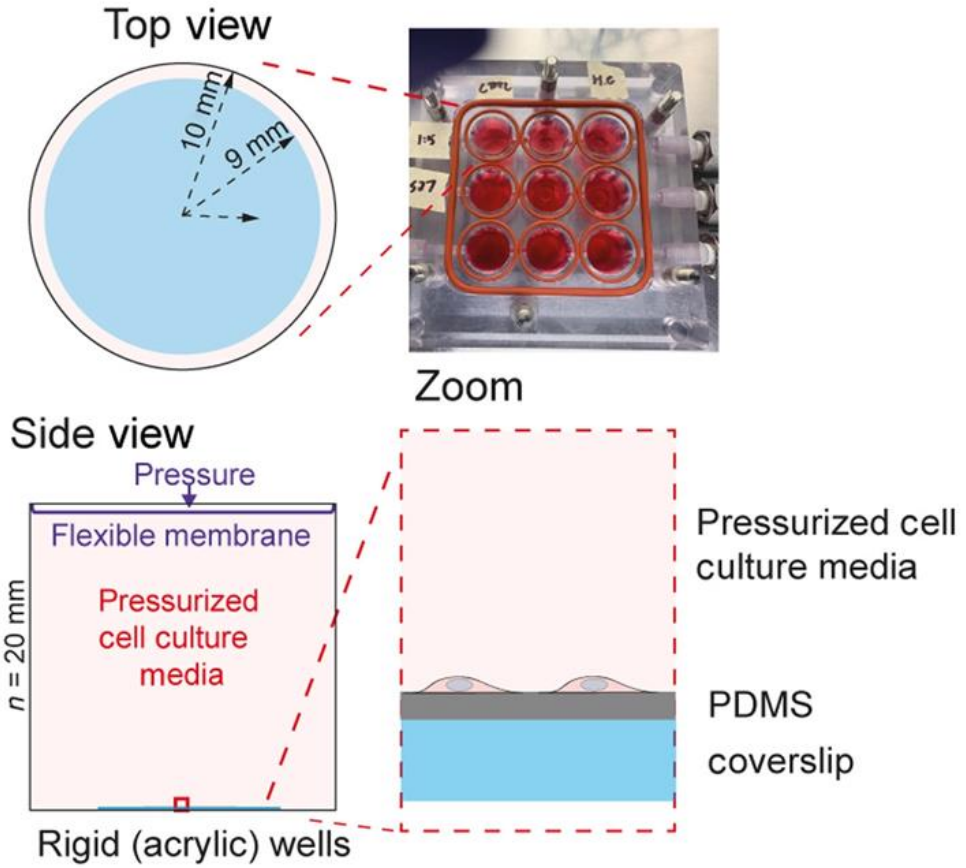

Figure 2.4: Schematic Demonstrating the MechanoCulture TR hydro Mechanical Stimulation System. *The* ***Top view*** *shows the hydrostatic chamber with a schematic of the coverslip position. This work used 18x18 mm, 10 µg mL^{-1} laminin coated PDMS coverslips with substrate elasticity of either 6 kPa or 130 kPa. The* ***side view left*** *shows how the hydrostatic pressure was applied as a downward force, via the flexible membrane, via direct contact with the culture media.* ***Side view right*** *shows a zoomed in schematic of cells on the coverslip. The hydrostatic pressure applies mechanical force to all dimensions of the cell. Image adapted from* [331]

Table 2.11: Hydrostatic chamber cycling parameters *Applied hydrostatic pressure mimicking healthy cardiac pressure (120/10 mmHg). Cycling was sinusoid and parameters were established within Dr Iskratsch's laboratory*

Parameter	Value
Pressure	120/10
Time	6hr
Frequency	1 Hz
Compress	0.2 s
Hold	0.3 s
Recovery	0.2 s
Rest	0.3 s
Repetitions	21600 (For 6 hr)

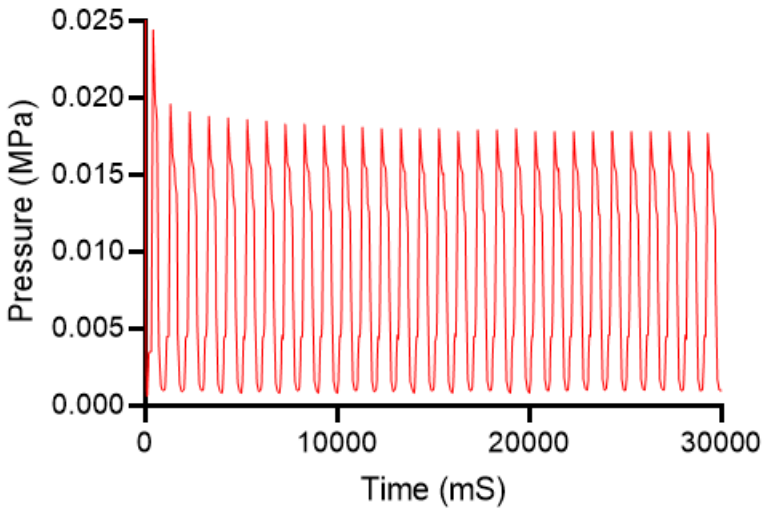

Figure 2.5: Representative Plot Displaying the Applied Pressure using the MechanoCulture TR hydro Mechanical Stimulation System. *A representative 30 s period to demonstrate the cyclic application of hydrodynamic pressure mimicking healthy cardiac pressure cycles.*

hiPSC-CMs were passaged onto 18x18 mm coverslips as described previously (§2.4.3). After 5 days, they were transferred to the hydrostatic pressure chamber- an example experimental set-up is shown in Figure 2.4. The hydrostatic chamber was sterilised using 70% isopropanol for 10 min and allowed to air dry for a following 10 min at RT in a sterile culture hood. The chamber was then washed using 1x PBS three times, each for 5 min. Afterwards, the chamber was sterilised using UV radiation for 5 min. Coverslips with hiPSC-CMs were then placed into the chamber and RPMI-1640 media was added to until each well was completely filled (total volume of media was approximately 100 mL). Then, the chamber was connected to pressurised air set to 1 bar and the experiment was carried out at 37^{o}C. In parallel to the hydrostatic chamber, coverslips with hiPSC-CMs were left in the incubator (37^{o}C, 5% CO_2) as an atmospheric pressure control. The experiment was carried out for a total of 6 hrs. Afterwards, hiPSC-CMs were fixed using 4% PFA and immunostained as described previously (§2.3).

In the case of addition of cytoskeletal drugs, these were added into the media for both the hydrostatic chamber run as well as the non-chamber. The pharmacological agents used are as described before (Table 2.10).

2.5 Cyclic 2D Equibiaxial Tension Application of hiPSC-CMs

Cyclic mechanical stretching of cells was used to mimic myocardial contraction and to assess how this may affected hiPSC-CMs. Here, the FX-5000™ tension system was used to carry out the mechanical stretching, with the cycling parameters detailed in Table 2.11. Collagen I coated 6 well bioflex® culture plates were oxygen plasma treated for 5 min and then coated with 10 µg/mL laminin for a minimum of 2 hrs at 37^{o}C. Afterwards, the culture plates were washed once with 1x PBS for 5 min.

hiPSC-CMs were then passaged (as previously described in §2.1) at a density of $5.0x10^4$ cm^{-2} and cultured overnight at 37°C and 5% CO_2. The next day, the cardiac transfer media was exchanged and hiPSC-CMs were cultured overnight, to allow recovery and spontaneous contraction to resume. Afterwards, hiPSC-CMs were transferred to the FX-5000™ tension system contained within a 37°C incubator and equibiaxial mechanical tension was applied for 6 hrs (Figure 2.6 and Table 2.12). A pre-stretching protocol was employed to help prevent detachment of hiPSC-CMs from the bioflex® membrane. Stretch application was applied at the same frequency as the pressure cycle, *i.e.* 1 Hz. This maintained consistency across experiments.

Table 2.12: Cycling Parameters for the Bioflex® Membrane Equibiaxial Tension Application. *Pre-stretch was used to prevent hiPSC-CMs from detaching before moving into the stretch cycle protocol*.

Minimum (% elongation)	**Maximum (% elongation)**	**Frequency (Hz)**	**Cycles**	**Duration (s)**	**Cycle Shape**
Pre-stretch					
0	0.5	0.5	60	120	½ SINE
0	1.5	0.5	60	120	½ SINE
0	3.0	0.5	60	120	½ SINE
0	8.0	0.5	60	120	½ SINE
Stretch					
0	10.0	1.0	21600	21600	½ SINE

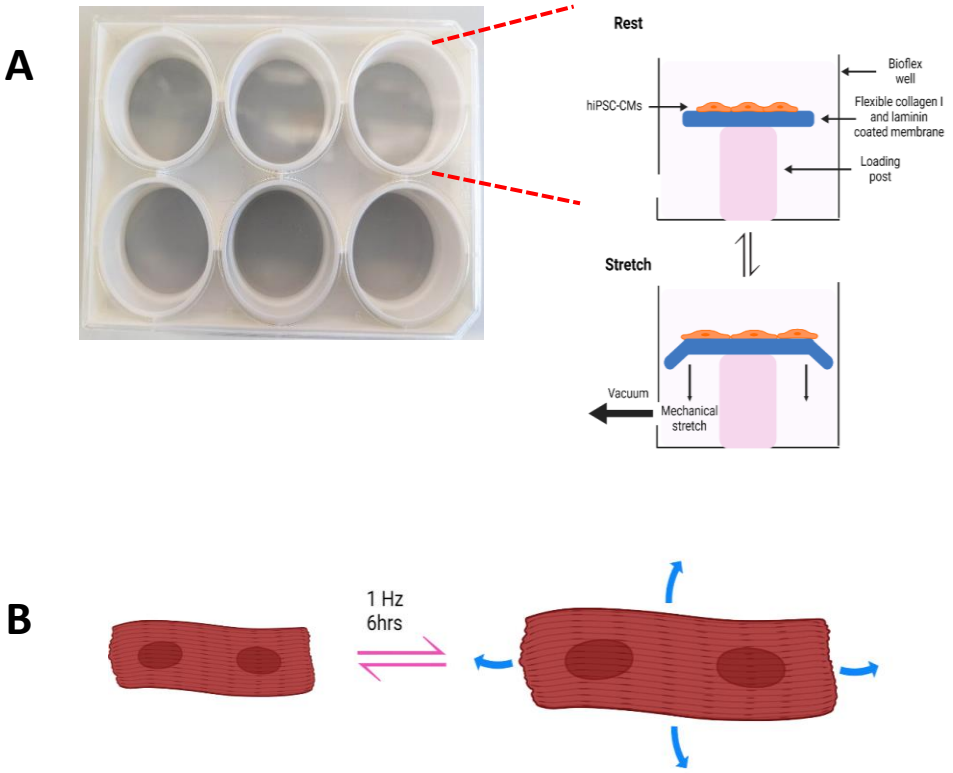

Figure 2.6: Schematic for the Bioflex® Membrane System. A) *Bioflex® 6-well plate with schematic that details function. The Bioflex plate was placed on top of the loading posts and the system was connected to a vacuum pump. At rest, the hiPSC-CMs are unstretched on the flexible membrane. During the stretch phase of the cycle, the vacuum pulls on the flexible membrane thereby generating a predefined elongation, in this case 10%. The hiPSC-CMs were subjected to this regimen in an equibiaxial manner.* ***B)*** *Schematic detailing hiPSC-CMs undergoing the rest-stretch cycle.*

2.6 Data Analysis and Statistical Analysis

All hiPSC-CM cellular and nuclear morphological parameters (area, perimeter, length, width, circularity) were determined using ImageJ Fiji. Images were loaded into ImageJ Fiji and individual hiPSC-CMs were delineated manually using polygon tool (Figure 2.7). Automation of this process was attempted using CellProfiler but the algorithm was unable to

consistently delineate cells across experiments and was therefore abandoned in favour for manual characterisation.

hiPSC-CMs were delineated, using the analyse tab, the measurements were set- *i.e.* area, shape descriptors, perimeter, and fit ellipse. The values output from this were then recorded in Excel and analysed using GraphPad Prism.

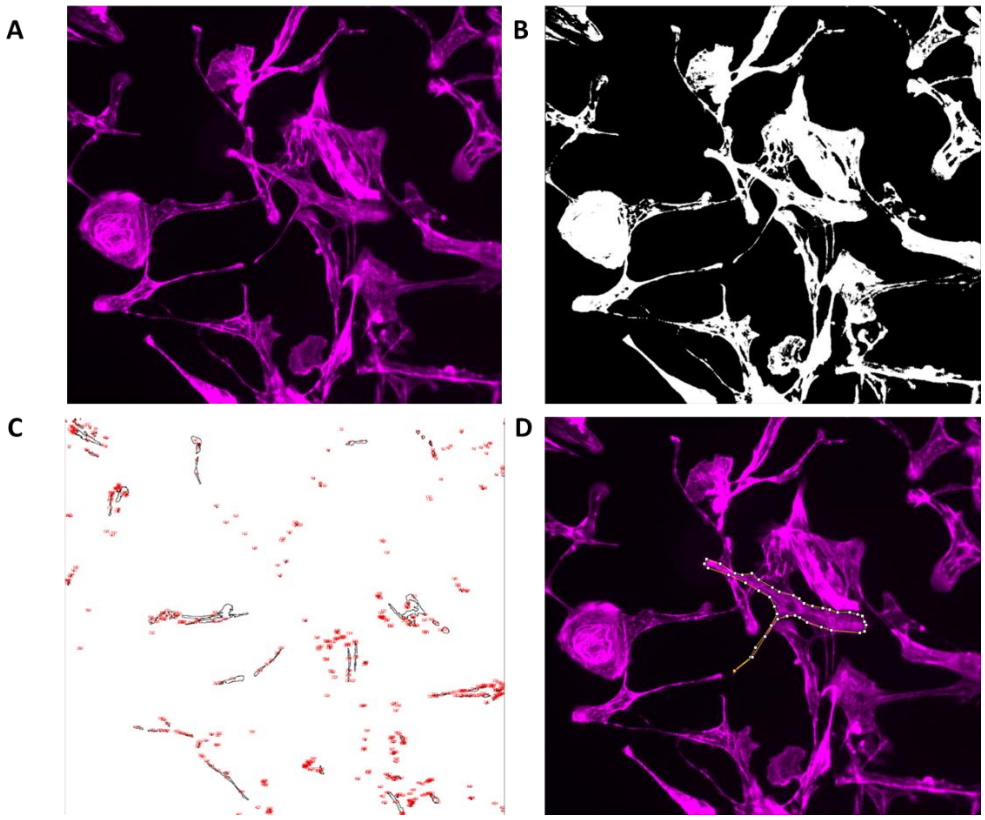

Figure 2.7: Representative Example Demonstrating the Characterisation of Cellular morphology using ImageJ Fiji: manual versus automated. A) *Original confocal image using ImageJ Fiji showing hiPSC-CMs immunostained for phalloidin.* ***B)*** *The same image from* ***A*** *thresholded. As observed, thresholding is not exact and unable to delineate individual hiPSC-CMs.* ***C)*** *Output of thresholded image from* ***B*** *for cellular morphology. Clearly the algorithm was unable to define individual hiPSC-CMs and produced highly erroneous and inconsistent results.* ***D)*** *Manually delineated hiPSC-CMs produced accurate cellular morphological characterisation.*

2.7 hiPSC-CM cell signaling and immunofluorescence data analysis

2.7.1 YAP nuclear: cytoplasmic ratio

The nuclear to cytoplasmic ratio of YAP was carried out using ImageJ Fiji. Delineation of the cell and the nucleus were performed then combined such that mean grey value intensity measured the cytoplasmic pixel intensity (Figure 2.10). Then, the nuclear mean grey value could be measured. The background fluorescence was then measured and subtracted from the cell values acquired. Using ImageJ FIJI, under 'analyse' -> 'set measurements', 'mean grey value' was selected and used to generate the cellular and nuclear YAP fluorescence intensities respectively. These values were then used to generate the nuclear to cytoplasmic YAP ratio (*Eq. 2.6)*:

$$YAP_{ratio} = \frac{YAP_{nucleus} - YAP_{background}}{YAP_{cytoplasm} - YAP_{background}} \quad (Eq.\ 2.6)$$

The laser intensity and exposure times were maintained between samples during each experiment to ensure consistency during the analysis.

2.7.2 Determining microtubule density of hiPSC-CMs

Microtubule density was determined using ImageJ FIJI and was performed according to Chen[105]. Here, hiPSC-CMs were selected and cropped (Figure 2.11). Following this, images underwent colour thresholding to delineate microtubules. From this image, a selection was made using the 'Edit' tab. The selection acted as a mask and could then be superimposed over the original cropped hiPSC-CM. The area was then measured using the 'Analyse' tab. Following this, the whole hiPSC-CM area was calculated. From this, a simple percentage was found.

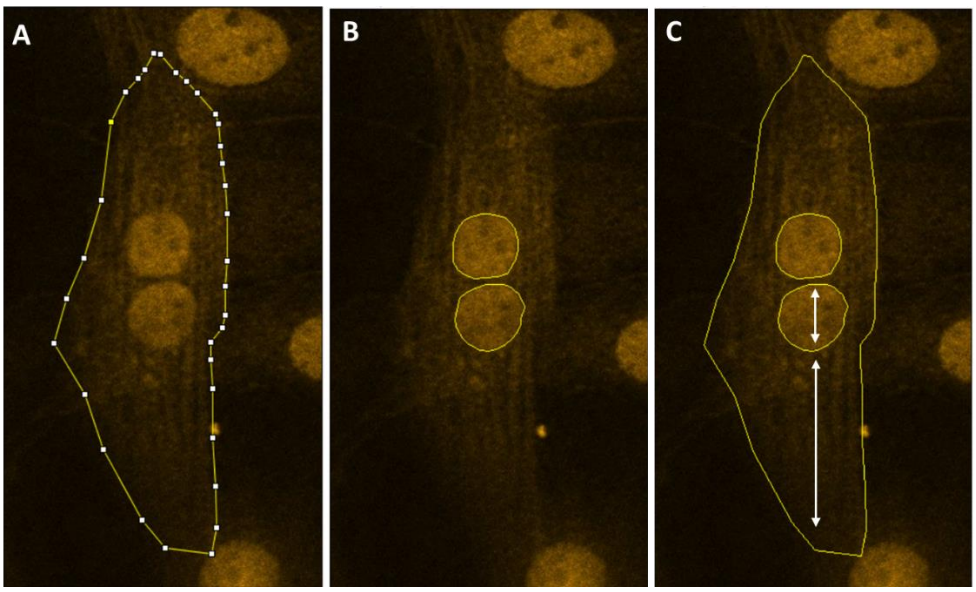

Figure 2.10: YAP Nuclear-to-Cytoplasmic Ratio. A) *Delineation of the hiPSC-CM was performed, followed by* ***B)*** *nuclei are then delineated.* ***C)*** *Regions of interest were then combined using the 'XOR' function in ImageJ FIJI. The white arrows indicate the regions that were measured to determine YAP intensity. The entire cytoplasm and each nucleus was then measured. Using the formula in Eq. 2.6, the nuclear-to-cytoplasmic ratio was determined.*

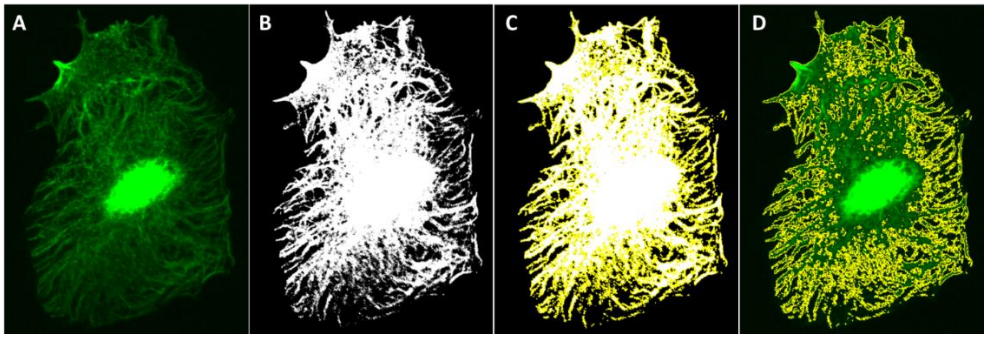

Figure 2.11: Workflow for Determining the Microtubule Density. A) *Original hiPSC-CM confocal image showing the microtubule network.* ***B)*** *Thresholding of microtubules within the image.* ***C)*** *Microtubules were then selected.* ***D****) The selection was then superimposed onto the original microtubule image and the area calculated. From this, the area percentage of microtubules can be determined.*

2.7.3 Determining Coherency of actin

Coherency is a measure of alignment of a structure and is determined using the Orientation J plugin from ImageJ FIJI. A value of 0 indicates a highly disorganised, non-aligned, isotropic structure whereas a value of 1 indicates strong alignment and organisation of a structure. To assess the alignment and organisation of the actin cytoskeleton, hiPSC-CMs were selected, and the image cropped to isolate a single hiPSC-CM. Then Orientation J plugin -> Orientation Measure was selected for the phalloidin channel. Coherency and orientation outputs were then acquired and analysed using GraphPad Prism version 9.

2.7.4 Statistical analysis

All data were plotted as Tukey boxplots and analysed using GraphPad Prism Version 9.1. Data was reported in text as mean ± standard error of the mean (S.E.M) or mean ± standard deviation (S.D.) as appropriate. Normality tests were performed to determine the normality of the data and to guide appropriate statistical analysis. For experiments comparing two samples unpaired Student's two-tailed t-test was carried out with Tukey's or Dunn's post-hoc analysis. For multiple comparisons, either a one-way or two-way analysis of variance (ANOVA) was performed with Tukey's *post hoc* test if normality was satisfied. If normality could not be assumed, data were analysed using a Kruskal-Wallis or Mann-Whitney U test. For all data, significance was indicated by stars as follows *p<0.05, **p<0.01, ***p<0.001, ****p<0.0001. Data was considered to be significant when the p value was below 0.05. Details of each test and assumptions are provided within each figure legend.

2.8 Materials

Table 2.13: List of Reagents

Reagent	Components
StemFlex medium	45 mL StemFlex + 5mL Supplement + 500 µL Pen/strep
hiPSC Freezing media	90% StemFlex media (see above) + 500 µL RevitaCell™ + 10% DMSO
RPMI 1640 +B27(-insulin)	49 mL RPMI1640 + 1 mL B27 (-insulin) + 150 µL Pen/strep
RPMI 1640 +B27 (+insulin)	49 mL RPMI1640 +1 mL B27(+insulin) + 150 µL Pen/strep
Lactate selection media	50 mL RPMI 1640 without glucose + 4 mM lactate + 500 µg/mL recombinant human albumin + 500 µg/mL L-ascorbic acid + 150 µL Pen/strep
T3/dex media	RPMI 1640 + B27(+insulin) (see above) + 0.1 µM T3 + 1 µM dexamethasone.
RNA pellet collection buffer	9 mL RLT + 1 mL β-mercaptoethanol
Matrigel	1 mL Matrigel + 9 mL DMEM/F-12 + glutamine
Laminin	10 µL laminin + 1 mL PBS
Vitronectin	10 µL vitronectin + 1 mL PBS
hiPSC-CM plating media	45 mL RPMI 1640 + B27 (+insulin) (see above) + 5 mL knockout replacement serum + 10 µL thiazovivin (2µM)

Polydimethylsiloxane (PDMS) 184	6.3mL Sylgard® 184 elastomer base PDMS + 700 µL Sylgard® 184 curing agent
PDMS 527	5 mL Sylgard® 527 part 'A' + 5 mL Sylgard® 527 part 'B'
PDMS 6 kPa	(for 10 mL) 9.5 mL 527: 0.5 mL 184
PDMS 130 kPa	(for 10 mL) 8 mL 527: 2 mL 184
Blocking buffer	(For 5 mL) 250 µL goat serum + 50 mg BSA into 4.75 mL PBS
Low Ca^{2+} Tyrode's buffe	(1 L) 140 mM NaCl + 5 mM KCl + 10 mM HEPES + 5.5 mM glucose + 2 mM $MgCl_{2.}$ + 0.9 mM Ca^{2+}. Adjust to pH 7.2.

3 Maintenance and Generation of WT and DMD hiPSC-CMs as a Disease Relevant Platform to Model DMD Associated DCM

Cell culture is a little like gardening. You sit and you look at cells, and then you see something and say, 'You know, that doesn't look right'.

Siddhartha Mukherjee

3.1 Introduction to Stem Cells

The mid-2000s witnessed the advent of human induced pluripotent stem cell (hiPSCs) technology developed, and finessed, by Yamanaka and colleagues[317]. Yamanaka and colleagues capitalised upon several decades of groundbreaking work that demonstrated somatic cell nuclear transfer was feasible. Seminal experiments demonstrated the successful transfer of a fully differentiated amphibian somatic nucleus to an enucleated oocyte, a multipotent state could be achieved. In this manner, Gurdon[332,333] showed that the cytoplasmic environment of the enucleated oocyte must contain factors mediating pluripotency.

To Identify the factors responsible for inducing pluripotency, Yamanaka et al screened 24 candidate factors, subsequently narrowing these down to four key proteins: KLF4, OCT3/4, c-MYC, and SOX2[317]. Mouse embryonic fibroblasts could be inducted into pluripotent teratoma forming cells. Afterwards, Yamanaka[318] successfully utilised this technique to induce a pluripotent state in human fibroblasts[318]. The human fibroblasts fully expressed pluripotent associated surface markers, including stage-specific embryonic antigen 4 (SSEA-4) and tumour rejection antigen 1-60 (TRA-1-60) as well as being capable of forming each of the three germ layers[318].

As the characterisation of pluripotency of the hiPSCs is used here, a brief consideration to the central transcription factors and genes involved should be given. Nanog is a homeobox domain transcription factor associated with maintaining the stemness of embryonic stem cells by blocking mesoderm formation. Its expression decreases shortly after cells undergo differentiation[334]. Expression of OCT3/4 is a critical to the maintenance of pluripotency of cells with its absence shown to be embryonically lethal and is present within the inner cell mass during development[335]. Moreover,

OCT3/4 interacts with Nanog and SOX2 to control a regulatory network maintaining pluripotency[335]. The *SRY* related gene member, SOX2, is an indispensable transcription factor working in concert with OCT3/4[336]. SOX2 and OCT3/4 are required for the progression for the formation of the epiblast during embryogenesis[337]. Similar to OCT3/4, *Sox2* null is embryonically lethal. Both stage-specific embryonic antigen 4 (SSEA-4) and tumour rejection antigen 1-60 (TRA-1-60) are glycolipid surface markers associated with pluripotency. Interestingly, SSEA-4 is not required for pluripotency and its presence decreases rapidly after differentiation[338]. As these biomarkers represent stemness, their expression was characterised.

Moreover, the iPSCs Yamanaka[318] generated showed exponential growth due to prolific telomerase activity, thereby enabling an endless supply of cells. Given this property of pluripotent stem cells, their development permits, in theory, a limitless supply of human derived cells that can subsequently undergo re-differentiation into the required cell types, underpinning their substantial value to biomedical research.

Owing to the fundamental capability of hiPSC to undergo further re-differentiation the generation of hiPSC derived cardiomyocytes (hiPSC-CMs) can be achieved pharmacologically with a degree of relative ease, primarily via modulation of the Wnt/β-catenin pathway[320].

Briefly, work by Lian[319] and Burridge[320] demonstrated that hiPSC-CMs could be manufactured pharmacologically with relative ease. Primarily, modulation of the Wnt/β-catenin pathway in a biphasic manner allows for the generation of hiPSC-CMs. The Wnt/β-catenin pathway *in vivo* acts in a biphasic manner, whereupon initial activation followed by inhibition is required to achieve full cardiogenic potential. Activation of Wnt produces ISL^+ cardioprogenitor cells and is achieved pharmacologically by inhibiting

glycogen synthase kinase 3-β (GSK-3β), the negative regulator of Wnt *in vivo*.

The initial promotion of Wnt allows it to bind in an autocrine and paracrine fashion to frizzled receptors, thereby facilitating the cytoplasmic accumulation of β-catenin. Subsequently, β-catenin translocates to the nucleus to activate Wnt sensitive genes, namely via the HMG-box transcription factors of the TCF/LEF domain family. This process is termed the canonical Wnt pathway.

Following on from this, the subsequent inhibition of Wnt is required to, in this case, interfere with the palmitoylation of Wnt. Subsequent purification using lactate and concomitant metabolic maturation allows for a well-developed and widely utilised disease relevant 2D *in vitro* platform for modelling disease.

A brief overview of the central structural and developmental and genes should be introduced. The cardiac developmental gene *insulin gene enhancer binding protein 1 (ISL-1)* is a LIM domain transcription factor instrumental in regulating downstream cardiogenic genes. Moreover, *ISL-1* seems to have a role in epigenetic regulation where it promotes cardiogenesis via an H3K27me3 alteration, leading to the upregulation of the morphogenetic genes, *MYOCD* and *MEF2C.* Expression of *ISL-1* decreases after terminal differentiation has been achieved, observed as early as E9 in murine models.

GATA4 is a zinc finger domain transcription factor that directly interacts with the homeobox domain transcription factor *NKX2.5*. Both originate from the lateral plate of the mesoderm and are biomarkers distinguishing precardiac cells. Both *GATA4* and *NKX2.5* coordinate a vast network of

transcription factors crucial to the spatiotemporal regulation of cardiogenesis.

Structural genes associated with cardiac tissues include both *TNNT2* and *ACTA2*. These are crucial, cardiac specific proteins within the cardiomyocyte cytoarchitecture. α-actinin functions as a crosslinker for actin at the Z-disc within the sarcomere[339], whilst TNNT2 is a central constituent of the troponin-tropomyosin complex localising at the sarcomere[340], making their characterisation necessary to demonstrate successful cardiac differentiation.

The limitations of hiPSC-CMs must be addressed, which include, but are not limited to, two central issues: maturation and scalability. Typically, hiPSC-CMs are described as maintaining an immature phenotype akin to foetal/embryonic stage cardiomyocytes. They lack the structural and functional maturity that is observed by adult cardiomyocytes and significant efforts are underway to minimise the gap between them (see §1.13 for details).

Another significant challenge within the cardiac stem cell field is the inter- and intra-cell line variability, including morphology, beating rate, and Ca^{2+} handling[341]. Countering the issues surrounding variation can include the use of cell lines from diverse backgrounds and the use of large-scale technical replicates. However, the scale required to mitigate the observed phenotypic variation may be difficult to implement in practice.

Throughout this work, I was primarily concerned with the role of dystrophin in cardiomyocytes and defining the underpinning pathomechanisms observed in its absence. To briefly reiterate, the absence of dystrophin is the primary cause for the catastrophic muscular dystrophy,

DMD. Given that DMD is the most prevalent muscular dystrophy, coupled to DCM as the leading cause of death in this cohort, defining the role of dystrophin in both WT and DMD cardiomyocytes is of great importance.

Moreover, establishing a patient-derived DMD relevant platform is paramount as the leading animal DMD models poorly recapitulate the cardiac phenotype observed in humans. The most common animal model is the *mdx* murine model which has proven valuable to skeletal muscle physiology in DMD but, unless carrying additional genetic knockdowns, poorly resembles the deleterious cardiac phenotype observed in humans[342]. Alternative animal models can more faithfully reproduce the cardiac phenotype observed in humans, such as the golden retriever muscular dystrophy model[311], but are difficult to acquire and maintain and are therefore uncommon. In addition to these problems, murine cardiomyocytes are physiologically distinct to that of the human with significantly higher resting heart rates (70 bpm vs 500 bpm), inversely proportional relationship between heart rate and inotropy, as well as distinct ion channel expression[343]. These factors motivate the necessity for developing platforms that are more physiologically relevant to the human.

Therefore, the primary aim for this chapter was to establish the hiPSC-CM platform that would form the basis for the subsequent work. Here, I generated hiPSC-CMs to model DMD associated DCM.

3.2 Human Induced Pluripotent Stem Cell Pluripotency and Cardiac Differentiation

3.2.1 Establishing Pluripotency and Downstream Mutational Sites

Initially, I sought to establish and maintain hiPSC colonies that could be utilised for downstream experimentation and development of the hiPSC-CM platform to model DMD-DCM (Figure 3.1). To this end, I utilised four hiPSC non-isogenic cell lines.

The hiPSCs used in this work were initially acquired via commercially available sources (see §2.8 for more detailed information). The project initially focused on two hiPSC cell lines derived from human fibroblasts, one wildtype (WT) and one DMD mutant (DMD). Firstly, the hiPSC cell line, GM25256 'CRISPRi', or WT 1 was derived from a healthy patient and the second hiPSC cell line acquired was the CENS0i002-B c.9691C>T (p. Gln3231*) 'L1060 Parental' DMD mutant, or DMD 1 (Table 3.1). Originally, the project was to leverage an isogenic control developed for the DMD 1 hiPSC cell line within the laboratory of Dr Lin. Unfortunately, the isogenic control was found to be mixed with the parental mutant line. Attempts to isolate the corrected cells was performed but were ultimately unsuccessful. Unfortunately, due to time-constraints and the impact of the COVID-19 pandemic lockdown restrictions, re-establishing an isogenic control cell line *de novo* was not possible (See §A1).

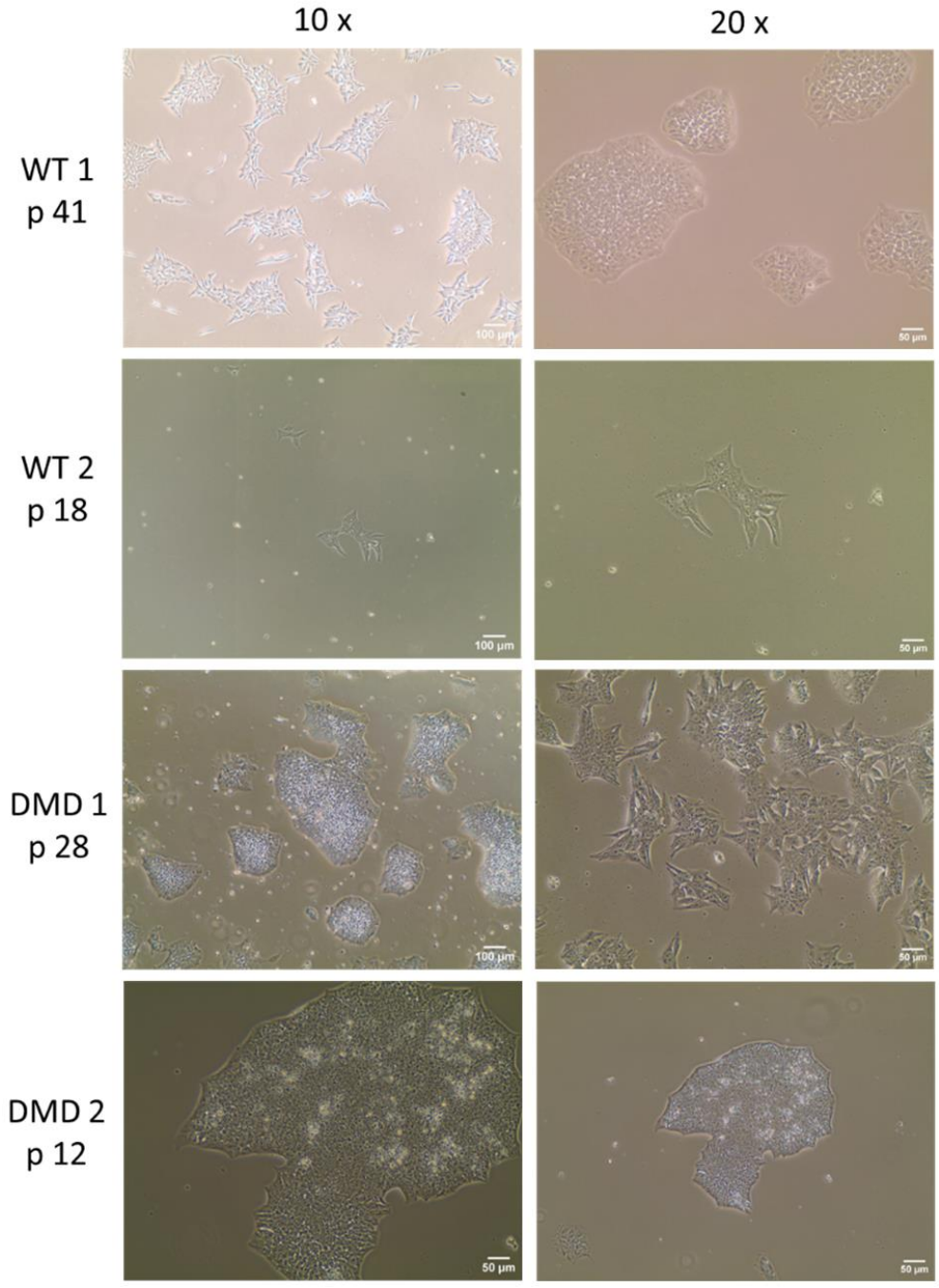

Figure 3.1: Representative Brightfield Images of hiPSC cell line Colonies. *hiPSC cell line colonies were expanded until 80% confluent then passaged for cryopreservation, expansion, or use for cardiac differentiation. Morphological characteristics were typical of hiPSCs including well defined boundaries and a classic bright white appearance under brightfield. Scale bar= 100 µm for 10 x magnification (left column); 50 µm for 20 x*

magnification (right column), N= 2 repeats for WT 2; 3 repeats for DMD 1 and DMD 2; 4 repeats for WT 1 hiPSCs.

During the latter half of the project, a second DMD mutant hiPSC cell line was acquired to support experimental findings uncovered by hiPSC cell line DMD 1. This cell line, CENS0i007-A exon 52 deletion 'L1295' DMD mutant or DMD 2, was expanded and utilised. Again, this cell line did not have an accompanying isogenic control for comparison and, due to the reasons outlined above, these were not generated for this project.

Lastly, during the final months of the project a new control cell line was acquired, the HPSI0214i-kucg_2 'KG2' or WT 2. All of the hiPSC cell lines were confirmed to be pluripotent by the companies as well as having been confirmed by several publications[344,345]. However, for the purposes of the project, pluripotency was demonstrated for WT 1, DMD 1, and DMD 2 cell lines as well as their mutational status. Due to time-constraints on the project, I was unable to carry out these verification steps for the WT 2 hiPSC cell line. hiPSC cell lines were expanded on 5 μg mL^{-1} vitronectin until approximately 80% confluent and were then split for further expansion or for use in cardiac differentiation.

Table 3.1: Overview of Patient hiPSC Cell Lines used Detailing the Mutations and Phenotype.

hiPSC Cell Line	WT 1	WT 2	DMD 1	DMD 2
Mutation	N/A	N/A	c.9691C>T (p.Gln3231*)	Exon 52 deletion
Affected Exon	N/A	N/A	67	52
Histopathology of Skeletal Muscle	N/A	N/A	Hypertrophic fibres, necrosis, and inflammatory infiltrate present.	Similar to DMD 1
Cardiac Defects	N/A	N/A	Cardiomyopathy present	Decreased fractional shortening
hiPSC Type	Conventional iPSC	Conventional iPSC	Conventional iPSC	Conventional iPSC
hiPSC Growth Media	Stemflex	Stemflex	Stemflex	Stemflex

3.2.2 Immunocytochemistry and RT-qPCR Analysis Confirmed the Pluripotent Status of WT 1, DMD 1, and DMD 2 hiPSC Cell Lines

Once hiPSC cell colonies were established and observed (Figure 3.1), immunocytochemistry (ICC) and reverse transcription quantitative polymerase chain reaction (RT-qPCR) were used to determine whether pluripotency was maintained. Pluripotency was confirmed in WT 1, DMD 1, and DMD 2 hiPSC cell lines, as determined by the expression of pluripotency biomarkers, including Nanog, Sox2, and Oct3/4. Due to the

late addition of the WT 2 hiPSC cell line, these analyses could not be carried out not performed on this cell line, however the pluripotency of this cell line was previously verified elsewhere[345].

Following the establishment of the hiPSC colonies, I next determined the pluripotent nature of the hiPSC cell lines by assessing key biomarkers. Immunocytochemistry (ICC) confirmed pluripotency in all of the hiPSC cell lines (WT 1 Figure 3.2; DMD 1 Figure 3.3; DMD 2 Figure 3.4) as determined by positive staining for Nanog, OCT 3/4, Sox 2, TRA-1-60, and SSEA-4.

Positive expression of all pluripotency biomarkers was present, providing comprehensive evidence that the cell lines were indeed pluripotent.

In addition to examining protein expression using ICC, gene expression for *NANOG* was further examined in the WT 1 and DMD 1 hiPSC cell lines at D0 and D30 of the cardiac differentiation protocol using RT-qPCR. *NANOG* expression at the start and end of the cardiac differentiation protocol demonstrated a decrease of pluripotency over time (Figure 3.5).

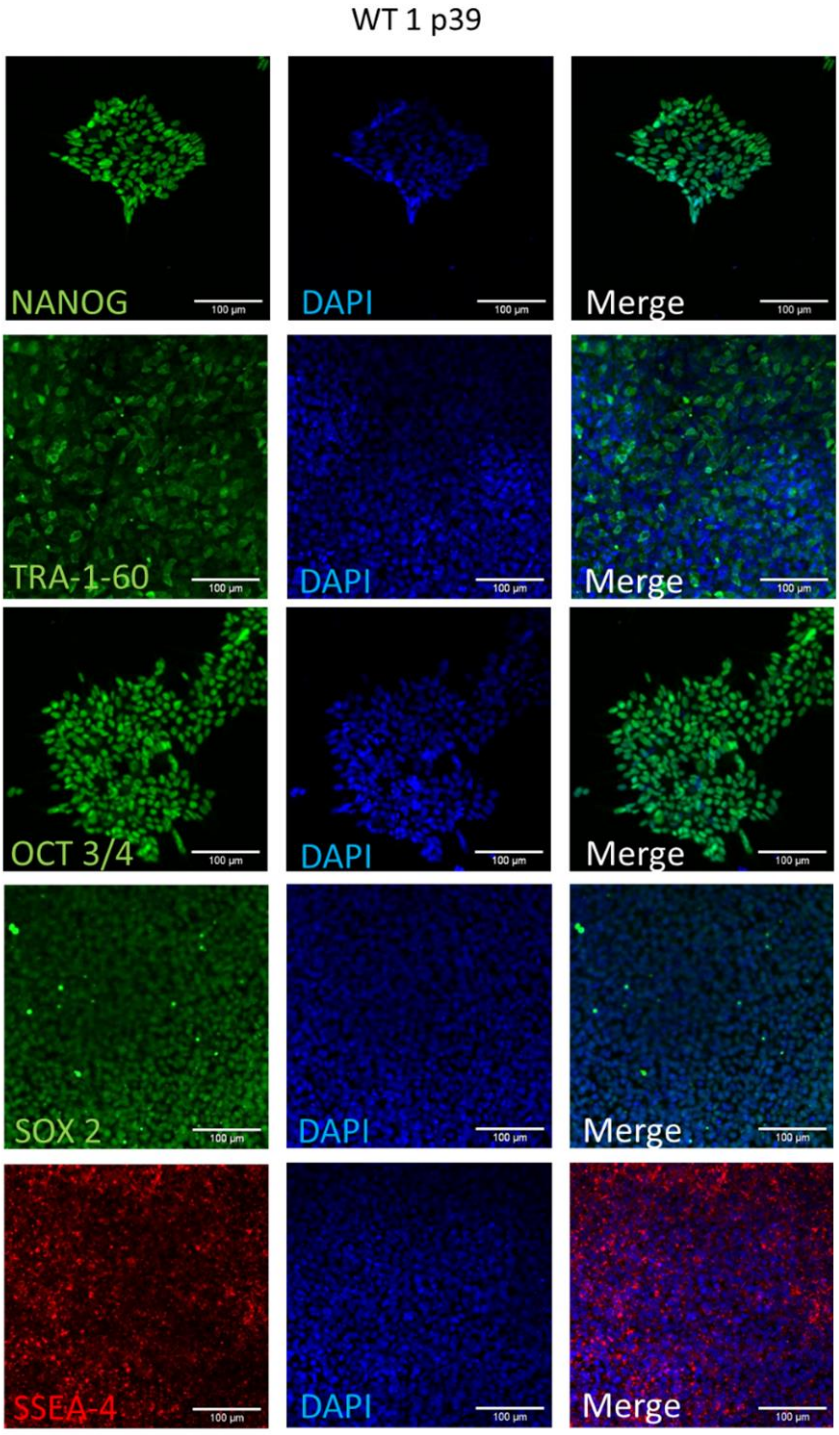

Figure 3.2: Pluripotency Expression in the WT 1 hiPSC Cell Line. *WT 1 hiPSC cell line demonstrating high expression of pluripotency biomarkers Nanog, TRA-1-60, OCT 3/4, SOX2, and SSEA-4. All cells were counterstained using DAPI. Scale bar= 100 µm, N= 3.*

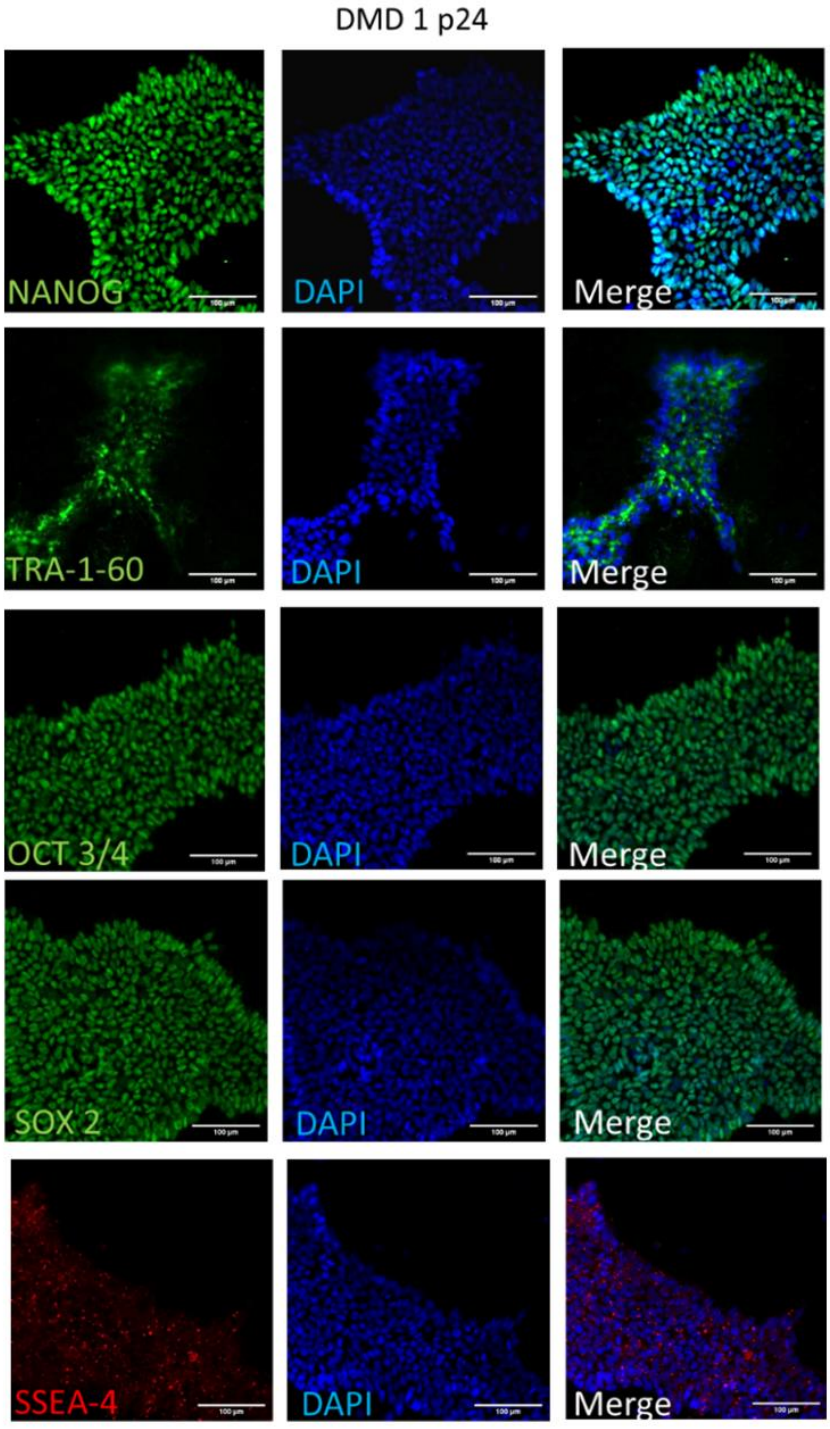

Figure 3.3: Pluripotency Expression in the DMD 1 hiPSC Cell Line. *DMD 1 hiPSC cell line harbouring the c.9691C>T (p.Gln3231*) mutation demonstrating high expression of pluripotency biomarkers Nanog, TRA-1-60, OCT ¾, SOX2, and SSEA-4. All cells were counterstained using DAPI. Scale bar= 100 µm, N= 3.*

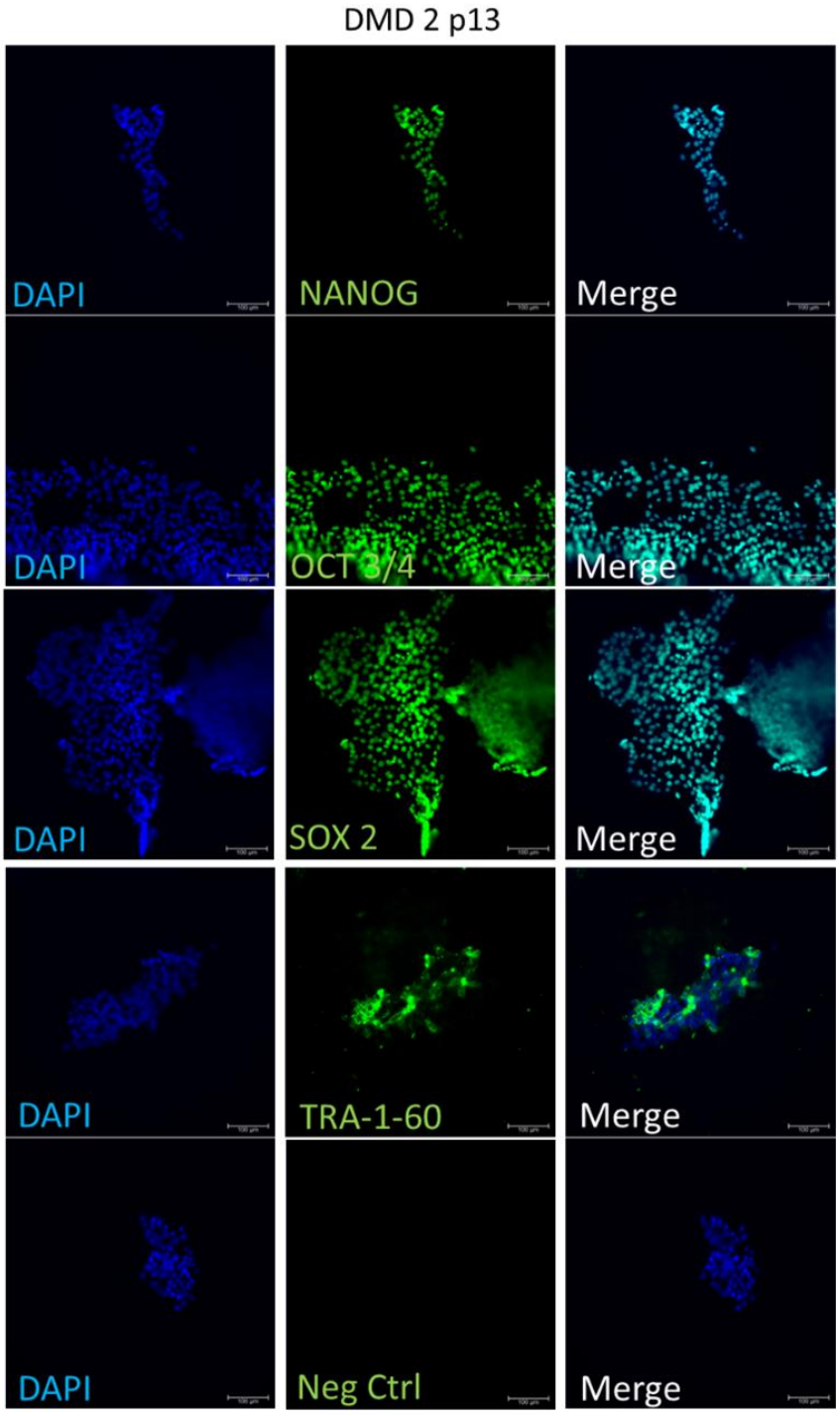

Figure 3.4: Pluripotency Expression in the DMD 2 hiPSC Cell Line. *DMD 2 hiPSC cell line harbouring the Δexon 52 mutation demonstrating high expression of pluripotency biomarkers Nanog, TRA-1-60, OCT 3/4, SOX2, and SSEA-4. All cells were counterstained using DAPI. Scale bar= 100 µm, N= 2.*

As expected, *NANOG* expression at D30 was significantly downregulated in both WT 1 and DMD 1 by 1000-fold in hiPSC-CMs indicative of an inversely proportional relationship between pluripotency and cardiogenesis. Collectively, ICC and RT-qPCR provided comprehensive evidence of pluripotency within the hiPSC cell lines, and I was satisfied that the cells generated were suitable for subsequent experimentation.

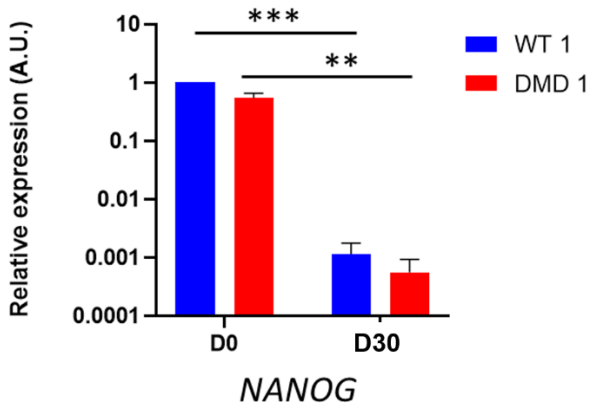

Figure 3.5: RT-qPCR Analysis of NANOG in WT 1 and DMD 1 hiPSCs at D0 and D30 of the Cardiac Differentiation Protocol *At D0, the initiation of cardiac differentiation, expression of NANOG mRNA was significantly higher compared to the end of the differentiation protocol at D30. These data confirmed an inverse relationship between cardiogenesis and pluripotency. Unpaired Student's t-test, data shown as mean ± S.E.M., p< 0.05 considered significant. N= 3 biological replicates.*

3.2.3 PCR and Gene Sequencing Confirmed the Mutational Status of DMD hiPSC Cell Lines

Having established that the hiPSC cell lines were pluripotent, the next step was to ensure that the DMD mutant cell lines harboured the expected mutations, in this case the c.9691C>T single nucleotide polymorphism (SNP) in the DMD 1 hiPSC cell line and the exon deletion, ΔExon 52, in DMD 2 hiPSC cell line. To examine DMD 1, gene sequencing was carried out over the mutational region at exon 67 (Figure 3.6) with the expected c.9691C>T

mutation present in the DMD 1, but absent in the WT 1 hiPSC cell line, confirming the presence of mutant SNP in DMD 1.

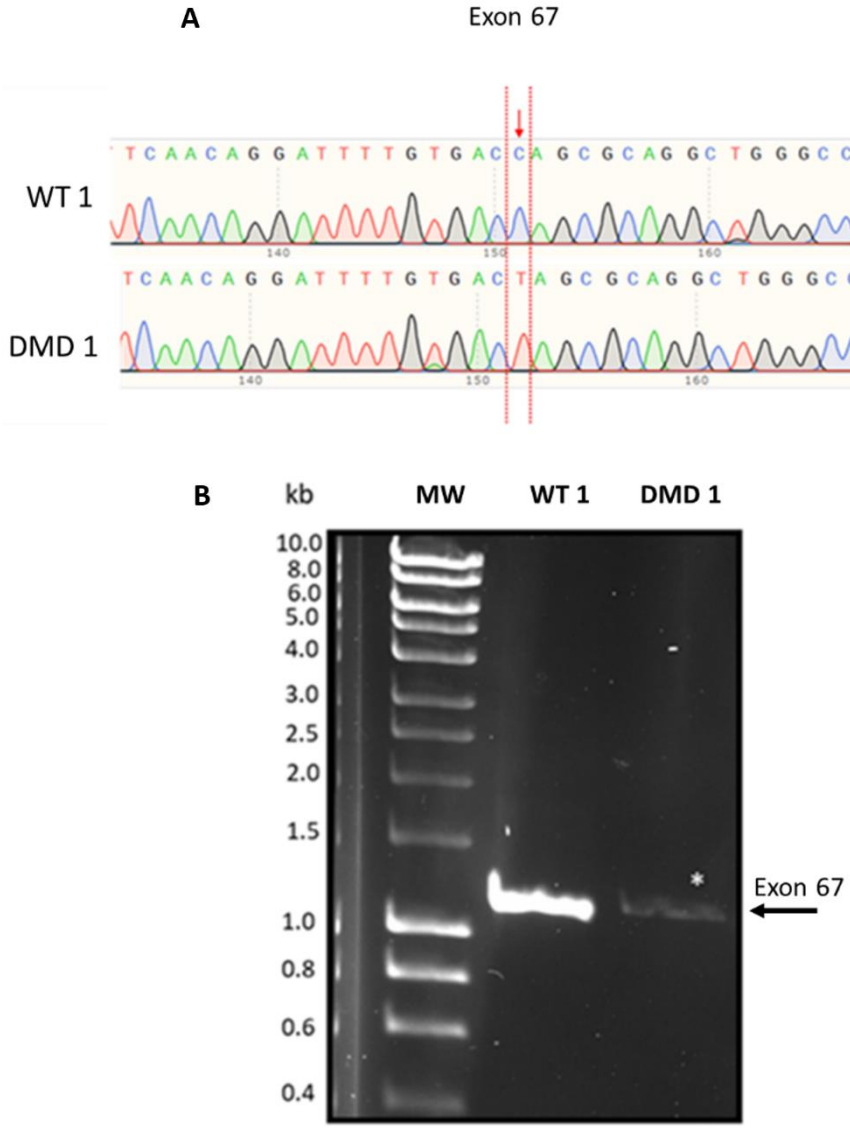

Figure 3.6: Gene Sequencing of Exon 67 Confirmed the Presence of the c.9691C>T Mutation in the DMD 1 hiPSC Cell Line. *Gene sequencing of exon 67 confirmed that DMD 1 cell line harboured the c.9691C>T SNP.* ***B)*** *Amplification of exon 67 was performed to demonstrate its presence in both WT 1 and DMD 1 cell lines and was subsequently used for gene sequencing to confirm the presence of c.9691C>T in DMD 1. N= 2 PCR of exon 67; N= 4 for gene sequencing.*

The nature of the mutation in the DMD 2 hiPSC cell line is the absence of exon 52 and, therefore, characterisation is not amenable to gene sequencing. Demonstration of the Δexon 52 mutation required the use of PCR amplification, where it was expected that exon 52 would be absent. To ensure that PCR was effective, two additional exons were amplified (exon 1 and exon 70) and performed on all of the hiPSC cell lines (except WT 2) (Figure 3.7).

The absence of exon 52 in the DMD 2 hiPSC cell line confirmed the expected mutation was present. Moreover, it demonstrated the presence of the other exons amplified, indicating that the PCR was successful, although it is important to note that exon 70 does not undergo downstream translation in the DMD 2 cell line. The DMD 2 cell line only produces a small, yet functional, isoform of dystrophin: Dp71m. This is due to the alternative internal promoters present prior to exon 52 in the *DMD* gene.

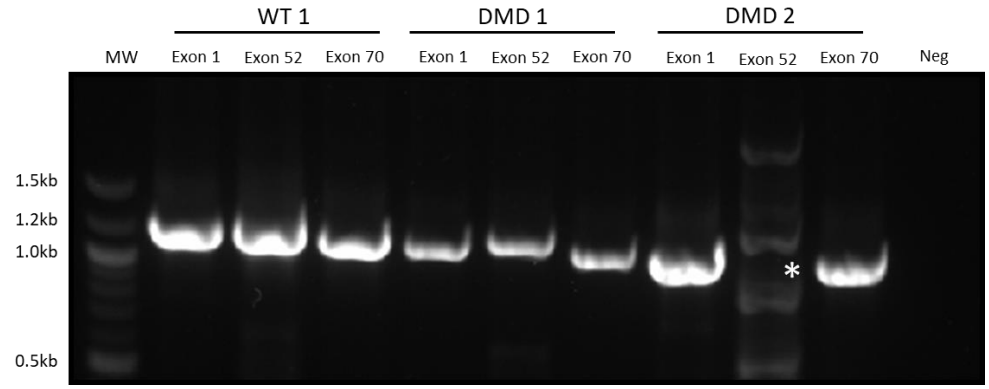

Figure 3.7: PCR Amplification of Exons 1, 52, and 70 Confirmed the Absence of Exon 52 in the DMD 2 hiPSC Cell Line. *PCR amplification of both WT 1 and DMD 1 hiPSCs revealed the presence of all exons examined (exon 1, 52, and 70). As expected, exon 52 was absent from the DMD 2 hiPSC cell line, as indicated by the white asterisk. DMD 2 amplification of exon 70 was present but does not undergo translation. N= 1.*

Lastly, the presence of all exons in the WT 1 and DMD 1 hiPSC cell lines indicated that there were no major deletions to these exons.

3.3 Manufacturing hiPSC Derived Cardiomyocytes using a Chemically Defined Protocol that Modulates the Wnt/β-Catenin Pathway

Satisfied that pluripotency and the correct mutations were confirmed, I determined that the hiPSC-CMs were suitable candidates for cardiac differentiation. Here, I aimed to generate and demonstrate successful cardiac differentiation to establish a 2D cardiac platform required for subsequent experiments throughout this work.

Here, a 2D monolayer, chemically defined cardiac differentiation protocol was used, based on modified versions of Burridge[320] and Parikh[327] protocols (Figure 3.8A). Pharmacological modulation of the Wnt pathway is sufficient to drive hiPSCs towards a cardiac lineage and is necessary for mesoderm formation (Figure 3.8B). The critical early steps of the cardiac differentiation protocol require biphasic modulation of Wnt, initially increasing β-catenin, via GSK3β inhibition using CHIR99021, and then Wnt inhibition, via the porcupine inhibitor C59, giving rise to what is termed the 'GiWi' protocol[319,320].

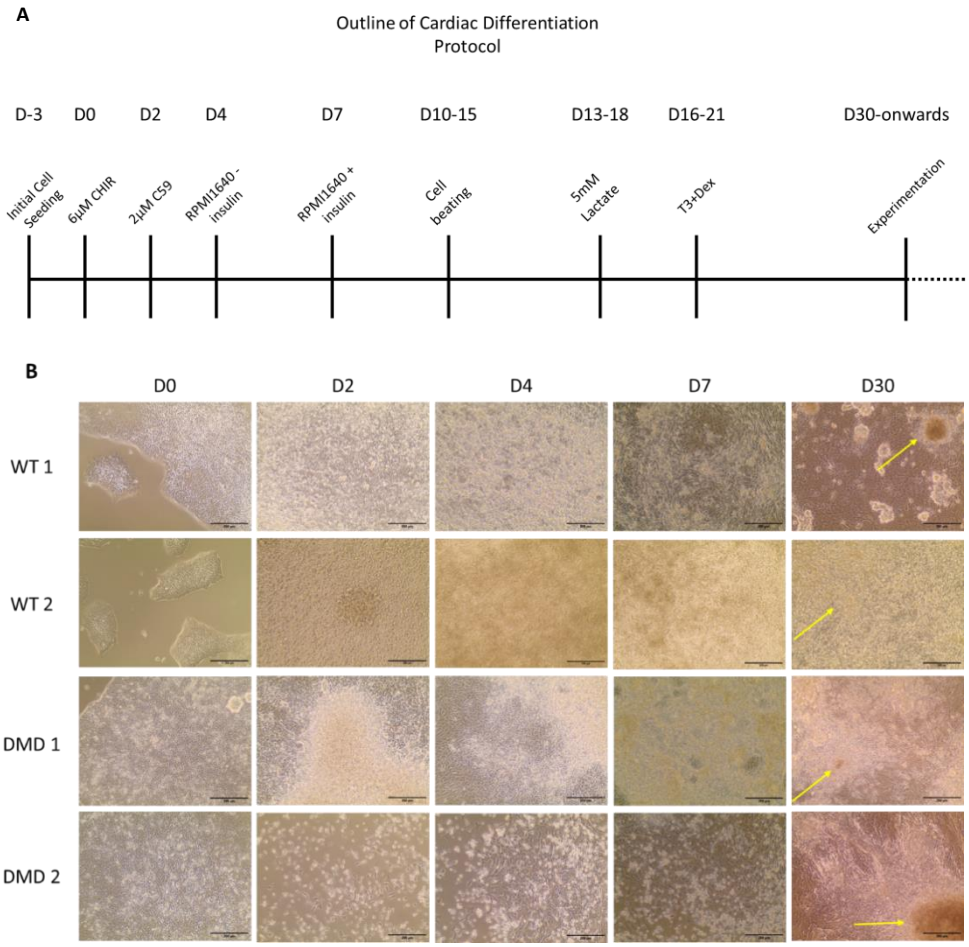

Figure 3.8: Chemically Defined Cardiac Differentiation Protocol via Modulation of the Wnt/β-catenin Pathway Utilising the 'GiWi' Method. A) *Schematic of the chemically defined protocol used, highlighting key time-points and pharmacological interventions to generate high yield hiPSC-CMs. Initial seeding density was 4.5x10^4 cm^{-2} on matrigel. At D30, hiPSC-CMs were used for various downstream experiments including nanoindentation, RT-qPCR, immunocytochemistry.* ***B)*** *Brightfield images of hiPSC-CMs at key time-points throughout the cardiac differentiation. Spontaneous beating was observed between days 7-10. Once beating initiated, hiPSC-CMs underwent metabolic selection using 4 mM lactate, starting at D10-15. Afterwards, hiPSC-CMs were treated using tri-iodothyronine (T3) and dexamethasone (Dex). T3/dex was used to further enhance maturation of the hiPSC-CMs as described by Parikh et al*[327] *and hiPSC-CMs formed large beating clusters, as shown by the yellow arrows. Scale bar= 200 µm, N= 5.*

Prior work using the WT 1 hiPSC cell line during the MRes component of my project showed that initial hiPSC seeding density has a profound influence over the cardiac differentiation efficiency, a finding reported by other groups[346]. In this work, an initial cell seeding density of $4.5x10^4$ cm^{-2} generated consistently high yield hiPSC cardiomyocytes across all hiPSC cell lines used with a mean of 89.6% across all hiPSC-CM cell lines; as determined by the cardiac specific biomarker, TNNT2. ICC positive cardiac TNNT2 cells accounted for 89.7 ± 4.0% in WT 1; 90.7 ± 4.7% in DMD 1; and 88.3 ± 2.9% in DMD 2 (Figure 3.9A and B). Due to time-constraints, I was unable to specifically quantify the percentage of TNNT2 positive hiPSC-CMs for the WT 2 cell line and relied on visual inspection of well-developed beating clusters and sarcomeric definition as determined by phalloidin ICC.

Alternate initial seeding densities were tested visually (3.5, 4.5, 5.5, and 6.5 $x10^4$ cm^{-2}) for beating aggregates and it was observed that a seeding density of $4.5x10^4$ cm^{-2} had the most consistent number of beating aggregates compared to other initial seeding densities. However, in this work the densities were not specifically analysed for cardiac TNNT2 as had been carried out during the MRes phase for the WT1 cell line. This was primarily due to time constraints, which COVID-19 pandemic restrictions factored into, and visual inspection for beating was considered appropriate. It must be noted, however, that only cells with sarcomeric patterning were utilised in subsequent data analysis.

Adult mammalian cardiomyocytes are acytokinetic but do undergo rounds of DNA synthesis with approximately 80% of murine ventricular cardiomyocytes displaying polyploidy and multinucleation[347]. This motivated me to characterise the percentage of multinucleated hiPSC-CMs here and was considered to be a feature of maturity for these cells.

Binucleation was present in WT 1, DMD 1, and DMD 2 hiPSC-CM cell lines (Figure 3.9C and D).

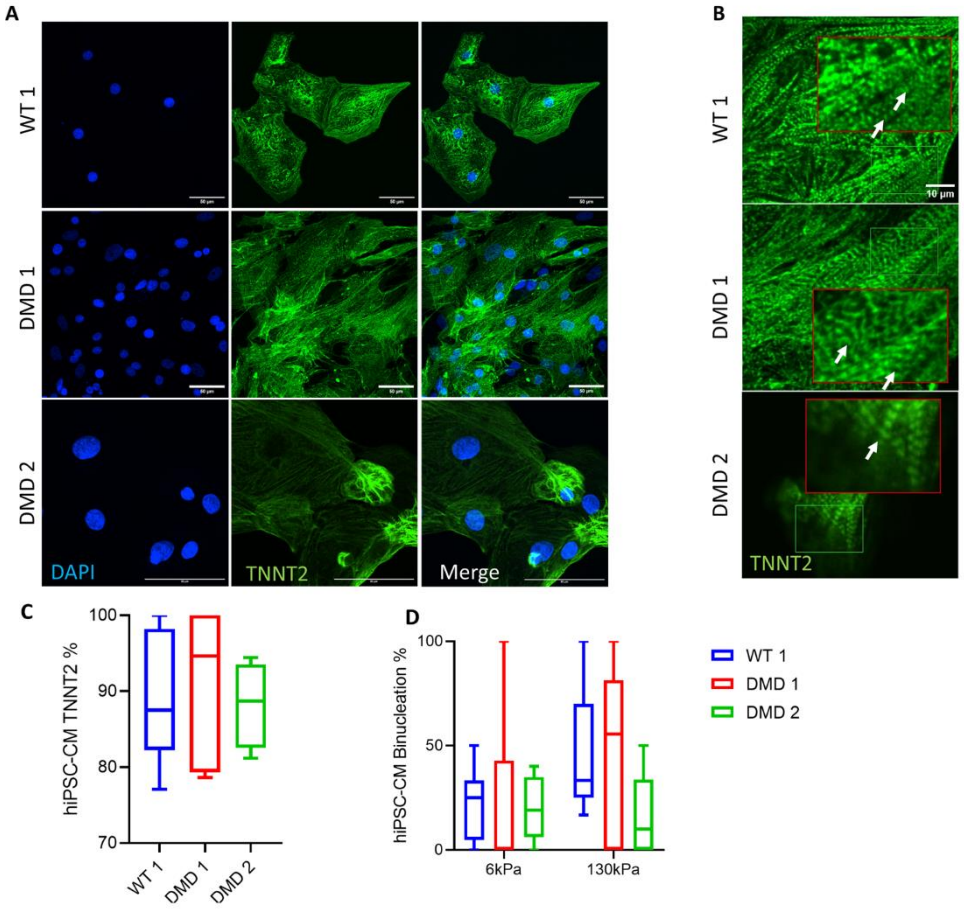

Figure 3.9: Cardiac Specific Biomarker TNNT2 Confirmed High Yield hiPSC-CMs at D30 A) *Immunofluorescence of the cardiac sarcomeric protein TNNT2 confirmed the presence of hiPSC-CMs at D30.* ***B)*** *2x zoom detailing sarcomeric localisation of TNNT2, further indicated by white arrows.* ***C)*** *Quantification of TNNT2 positive hiPSC-CMs demonstrated highly pure cardiomyocytes.* ***D)*** *Sub-populations of cardiomyocytes were binucleated, an indicator of cardiac maturation. Despite an increase in binucleation on fibrotic stiffness this was not significant and there was no difference in number of binucleated hiPSC-CMs between cell lines. One-way ANOVA, data shown as Tukey box plot, p<0.05 was significant (No significant changes). Scale bar= 50 µm, N=3.*

In this case, hiPSC-CMs were characterised whilst on laminin coated polydimethylsiloxane (PDMS) substrates of either 6 kPa or 130 kPa, representing healthy and fibrotic myocardial tissue respectively. The use of PDMS coated substrates at 6 kPa and 130 kPa forms the basis of subsequent work and is discussed in detail in §4.8.1.

The percentage of binucleated hiPSC-CMs was not different between cell lines, indicating consistency between the cell lines and differentiation protocol (WT 1; 6kPa vs 130kPa: 22.3 ± 4.6% vs 44.7 ± 14.4%; DMD 1; 6kPa vs 130kPa: 24.7 ± 14.2% vs 45.9 ± 13.3%; DMD 2; 6kPa vs 130kPa: 19.9 ± 6.1% vs 16.2 ± 6.9%).

An issue commonly encountered during chemically defined cardiac differentiation is the generation of 'off-target' cell types, namely fibroblasts. Therefore, it is necessary to subject the hiPSC-CMs to a purification stage to derive high yield cardiac populations. The purification step performed here eliminated non-cardiomyocyte populations. It is also important to state that the cardiac differentiation protocol likely produced a variety of subpopulations of cardiomyocytes (nodal, atrial, ventricular etc) as this protocol was not designed to specify subpopulation lineages. For example, the early addition of retinoic acid can promote the generation of atrial cardiomyocytes[320].

To achieve high-yield hiPSC-CM cardiac populations, the addition of lactate can be used due to cardiomyocytes' ability to derive energy from this, unlike other cell populations present. Metabolic selection here consistently yielded cardiac populations with >85% purity.

Moreover, to ensure successful cardiac differentiation, I further characterised the hiPSC-CMs via ICC and RT-qPCR for cardiac specific

developmental (*NKX2.5, ISL-1, GATA4)* and structural (*TNNT2, ACTN, MYH6/7)* genes/protein expression at the end of differentiation.

Initially, cardiac developmental gene expression was confirmed at the beginning of cardiac differentiation, indicative of cardiogenesis proceeding correctly. Based on previous reports[320,348], I characterised NKX2.5 (via both immunofluorescence and RT-qPCR), *ISL-1* and *GATA4* (via RT-qPCR) to demonstrate cardiogenesis using either D7 cardiomyocytes (in the case of *ISL-1* due to its early peak and subsequent decline of expression), and D30 cardiomyocytes (in the case of all other cardiac developmental genes/proteins as they persist into adult myocardium). ICC revealed high nuclear expression of NKX2.5 in WT 1, DMD 1, and DMD 2 hiPSC-CMs (Figure 3.10).

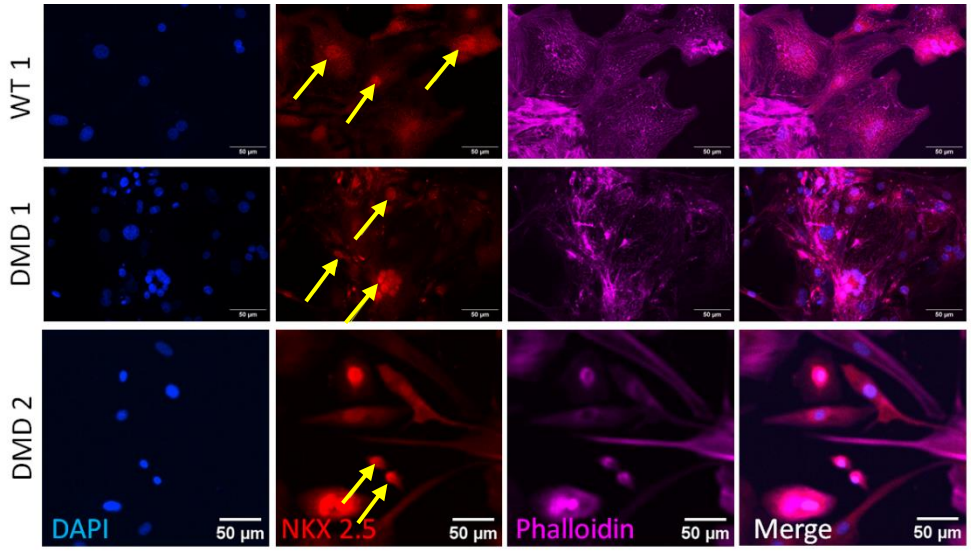

Figure 3.10: Presence of NKX2.5, a Cardiac Developmental Biomarker, Confirmed Successful Cardiac Differentiation at D30. *The presence of NKX2.5 confirmed hiPSC-CMs. NKX2.5 is a transcription factor and primarily localises to the nucleus, as indicated by the yellow arrows. Scale bar= 100 µm, N= 1 for DMD 2; N= 3 for DMD 1 and WT 1. Scale bar= 50 µm.*

Both TNNT2 (Figure 3.9) and α-actinin (Figure 3.11) were highly expressed across WT 1, DMD 1, and DMD 2 hiPSC-CMs, providing sufficient evidence that these were indeed cardiomyocytes. Moreover, ICC revealed sarcomeric localisation of TNNT2 and α-actinin, with banding patterning present, again consistent with cardiomyocyte formation. Interestingly, sarcomeric patterning was stronger in both the WT 1 and DMD 1 hiPSC-CM cell lines compared to DMD 2, where a more disorganised, foetal-like appearance was noted for α-actinin (Figure 3.11).

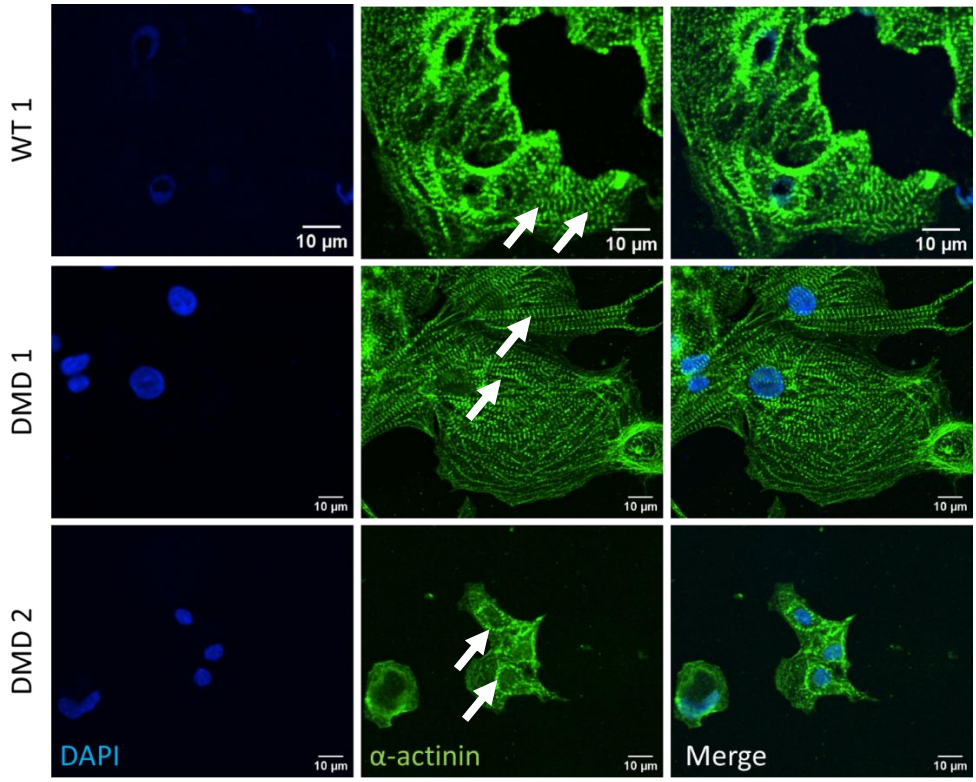

Figure 3.11: α-actinin Confirmed Successful Cardiac Differentiation. *Localisation of α-actinin at the sarcomere indicates successful cardiac differentiation (D30 hiPSC-CM). White arrows indicate sarcomeric localisation. N= 1 biological replicates for DMD 2; N= 2 for DMD 1 and WT 1. Scale bar= 10 µm.*

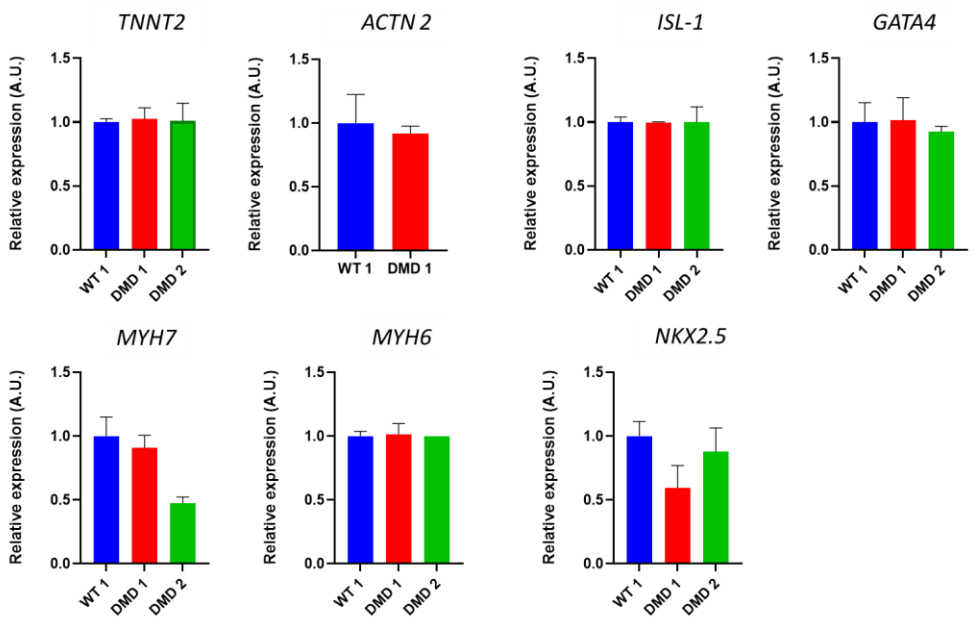

Figure 3.12: Gene Expression of Critical Structural and Developmental Cardiac Specific Biomarkers. *RT-qPCR confirmed gene expression of structural sarcomeric proteins (TNNT2, ACTN 2, MYH6, MYH7) and crucial cardiac developmental gene expression (ISL-1, GATA4, NKX2.5). RT-qPCR was performed at the end of the cardiac differentiation protocol (D30) except for ISL-1, where expression peaked at approximately D7. One-way ANOVA, data presented as mean ± S.E.M., p<0.05 considered significant (No significant changes observed), N= 3.*

Successful generation of hiPSC-CMs was further supported by RT-qPCR at the end of cardiac differentiation (Figure 3.12). Expression of crucial cardiac structural genes (*TNNT2, ACTN2, MYH6, and MYH7)* were concordant with the ICC data obtained. Moreover, cardiac developmental gene expression (*NKX2.5, ISL-1, GATA4*) was upregulated, again confirming reliable and successful differentiation for the cell lines used in this work. There was no significant difference in the expression of structural or developmental genes between hiPSC cell lines. Unfortunately, RT-qPCR for *ACTN2* was unsuccessful on DMD 2 hiPSC-CM cell line. However, given the other substantiating evidence provided, it was unlikely to be due to failed cardiogenesis.

3.4 Heart rate was significantly decreased for DMD 1 compared to other hiPSC-CM cell lines

Heart rate (HR) is a key physiological parameter and has previously been reported as being altered to some extent in patients with DMD. Moreover, it may be considered a prelude to fulminant heart failure observed in patients with DMD[349]. I therefore decided to elucidate whether there was any variation in HR between the different hiPSC-CM cell lines. HR of hiPSC-CMs at D30 at 37^{o}C was characterised by counting number of beats using brightfield microscopy over the course of 60 s, described as beats per minute (BPM), which was repeated in triplicate per experiment (Figure 3.13). All hiPSC-CM cell lines were within the expected human *in vivo* HR spectrum.

HR was found to be significantly decreased in the DMD 1 hiPSC-CM (67.6 ± 17.6 BPM) compared to WT 1 (95.3 ± 23.5 BPM) and DMD 2 (96.7 ± 37.1 BPM) by approximately 30%. Surprisingly, there was no difference in HR between DMD 1 and WT 2 (84.3 ± 24.4 BPM), despite a 20% reduction in HR observed in DMD 1 compared to WT 2. Intriguingly, DMD 2 was similar to both WT 1 and WT 2 cell lines and was increased 30% compared DMD 1 (significant). This suggests that the presence of the Dp71m isoform may be associated with regulating HR. Moreover, it supports the notion that the complete absence of dystrophin results in dysregulation of HR, as observed in DMD patients.

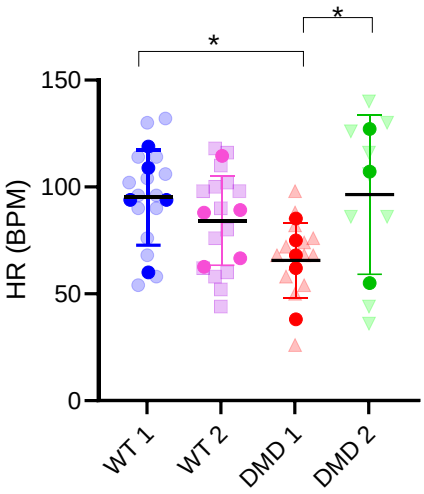

Figure 3.13: Heart Rate in DMD 1 hiPSC-CMs was Significantly Decreased at D30. *DMD 1 hiPSC-CMs had a significantly decreased HR compared to WT 1 and DMD 2 cell lines. Of note, DMD 1 was not different to WT 2, despite a 20% decrease in HR. One-way ANOVA with Tukey's post-hoc test; Data shown as mean ± S.D., p<0.05 considered significant, WT 1, WT 2, and DMD 1 hiPSC-CMs, N= 5; DMD 2 hiPSC-CMs, N= 3.*

3.5 Dystrophin is not expressed by the DMD 1 hiPSC-CM Cell Line.

Satisfied with the consistent production of pure, high yield hiPSC-CMs, as well as confirming that the hiPSCs harbour the expected *DMD* mutations, next it was important to demonstrate a lack of dystrophin by the mutant hiPSC-CMs. ICC and RT-qPCR both confirmed the absence of Dp427m in the DMD 1 hiPSC cell line (Figure 3.14). The DMD 2 hiPSC-CM cell line produces a truncated isoform of dystrophin, Dp71m and likely accounts for the low intensity immunofluorescence detected (Figure 3.14A).

RT-qPCR revealed gene expression of full length *DMD* was significantly downregulated by approximately 20 times in the DMD 1 hiPSC-CM cell line compared to WT 1, indicating reduced transcription of mRNA (Figure

3.14B). It is expected within the DMD 1 hiPSC cell line that the remaining mRNA undergoes nonsense mediated decay, although this was not examined in this work. The RT-qPCR is consistent with the immunofluorescence data whereby no translation of Dp427m is apparent.

Specifically, the N- terminus revealed significantly lower gene expression in both mutant hiPSC-CMs compared to WT 1 whereas the C-terminus was comparably expressed by DMD 2 (WT 1: 1.0 ± 0.2; DMD 2: 1.1 ± 0.4 A.U.) indicating that DMD 2 hiPSC-CM have similar expression of this region. The DMD 2 cell line is expected to produce Dp71m, which indeed retains the C-terminus site.

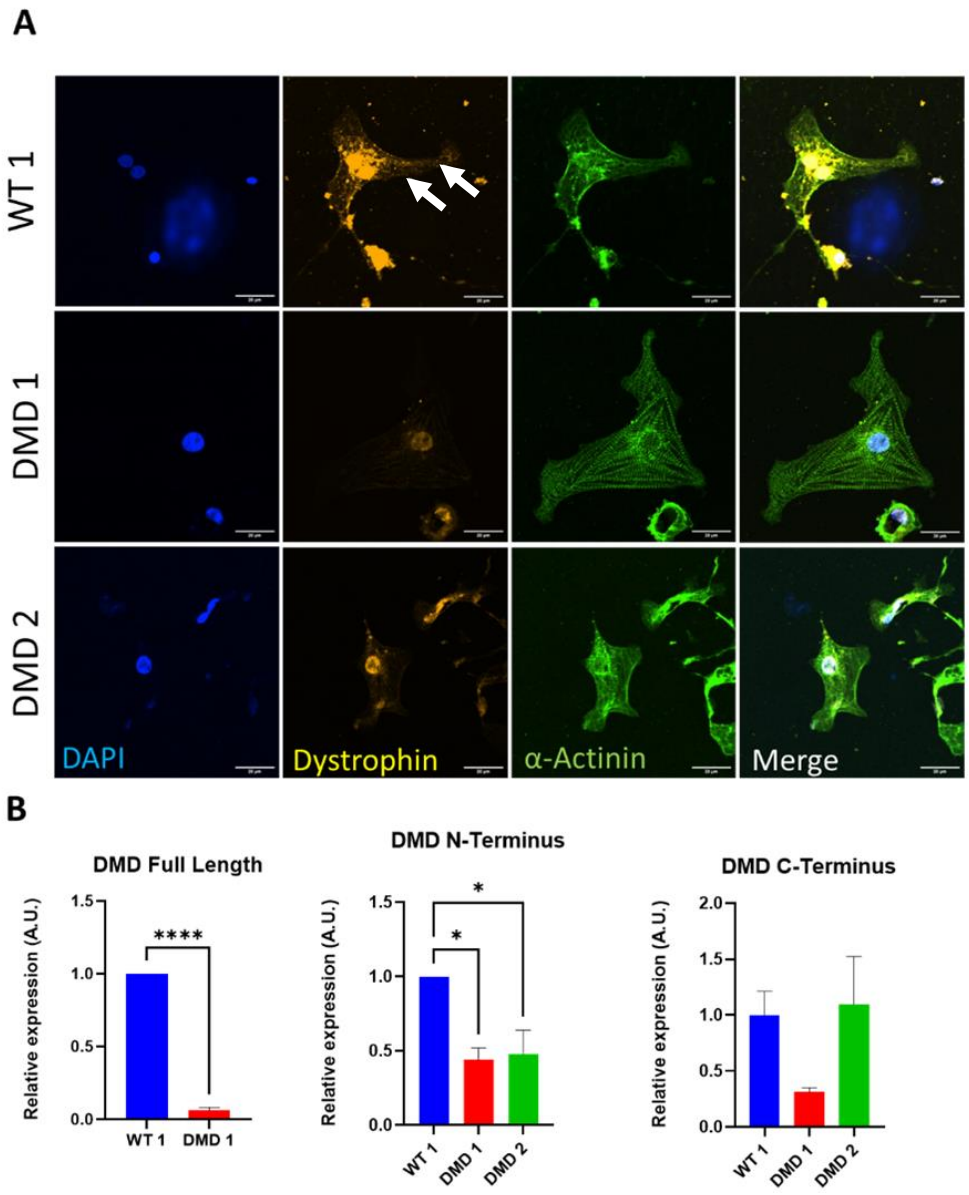

Figure 3.14: Full Length dystrophin (Dp427m) is not Expressed by the DMD 1 hiPSC Cell Line. A) *Immunocytochemistry revealed dystrophin localising at the sarcolemma in WT 1 hiPSC-CMs as indicated by the white arrow. Notably, dystrophin is absent in the DMD 1 hiPSC-CM cell line. DMD 2 shows low expression of dystrophin, likely the Dp71m isoform.* ***B)*** *RT-qPCR revealed significantly decreased gene expression of* DMD *for the DMD 1 cell line compared to WT 1. mRNA from DMD 1 undergoes nonsense mediated decay and is not translated. Primers targeting either the N- or C-termini of DMD display low expression of the N-terminus in both mutant cell lines compared to WT 1. DMD 2 produces comparable C-terminus mRNA, consistent with the retention of the CT-region required to produce the*

Dp71m dystrophin isoform. Scale bar= 20 µm, One-way ANOVA for more than two groups, unpaired student's t-test for two groups, data presented as mean ± S.E.M, p<0.05 considered significant, N= 3.

3.6 Chapter Discussion

For this chapter, I sought to establish a disease relevant platform using hiPSC-CMs to model DMD associated DCM and examine the role of dystrophin under different biomechanical contexts. I successfully maintained and differentiated hiPSCs into high-yield hiPSC-CMs, demonstrating multiple hiPSC-CM specific targets. Moreover, I confirmed the status of the mutations for the DMD 1 and DMD 2 hiPSC cell lines. Lastly, I showed that dystrophin expression was absent from the DMD 1 hiPSC-CM cell line.

3.7 Differentiation and Maturation of hiPSC-CMs

The use of hiPSC-CMs as *in vitro* models has revolutionised cardiovascular research. The advent of the small molecule modulation of the Wnt/β-catenin pathway made production of hiPSC-CMs accessible and relatively scalable for many laboratories[320,348]. Nonetheless, a significant hurdle within the hiPSC-CM field today is their foetal/embryonic like phenotype which limits their full therapeutic and research potential. hiPSC-CMs rarely have a full adult-like phenotype of primary cardiomyocytes and lack maturation. This feature has potentiated a great deal of research into furthering the maturation status of hiPSC-CMs to make them not only more physiologically relevant models but also clinically viable in regenerative medicine. That being said, hiPSC-CMs are capable of recapitulating disease phenotypes and are therefore valuable as human disease relevant models.

3.7.1 hiPSC-CM Differentiation

First, I established pluripotency using canonical biomarkers, of which Nanog, OCT3/4, and SOX2 are particularly important. Ensuring pluripotency prior to cardiac differentiation was vital in order to feel confident about subsequent experiments. The positive immunofluorescence was in concordance with the RT-qPCR data and supported my observation that the hiPSCs were pluripotent. The use of ICC and RT-qPCR to determine pluripotency is consistent with other bodies of work[319,320,350,351]. A sharp decrease in gene expression of *NANOG* as cardiac differentiation progressed was also a good indicator of functional hiPSCs, as pluripotency is inversely related to terminal differentiation[320]. Although, a limitation here would be the lack of RT-qPCR evidence of other biomarkers of pluripotency, such as OCT3/4 and SOX2, at this time-point.

Additional experiments could have further demonstrated stemness, particularly teratoma formation to characterise the three germ layers (endo-, ecto-, and meso-derm) derived from the hiPSCs. This had been carried out in the DMD 1 hiPSC cell line by a previous PhD student within Dr Lin's laboratory. Moreover, these characterisations were performed by the companies supplying the cell lines and as such I am confident in the stemness of the hiPSCs. In addition to assessing teratoma formation, analysis of the hiPSC karyotype could have been performed here. Karyotype analysis assesses chromosome level mutations, particularly effective for large deletions and insertions. This was not performed during this work and, as such, is a limitation. However, previous work within Dr Lin's laboratory did examine this aspect for the WT 1 cell line and discovered no abnormalities.

Additional consideration should be applied to the epigenome of hiPSCs[352]. Evidence suggests that the epigenetic memory of hiPSCs may predispose cells to differentiation towards their cell of origin. Recent evidence supports this notion whereby progenitor cells derived from somatic cardiac lineage demonstrated significantly upregulated cardiac specific gene expression in response to differentiation in contrast to hiPSC-CMs derived from bone marrow derived mesenchymal stem cells or human dermal fibroblasts[353]. Other work has shown that histone deacetylase activity is also an important regulator for cardiac differentiation[354]. Analysis of the epigenome was not carried out on the cell lines in this work during cardiogenesis but would make for an interesting future study.

The pharmacological modulation of Wnt, the so called 'GiWi' protocol, alongside metabolic selection produced consistently high yield hiPSC-CMs for this work with a mean ~89% TNNT2 positive across hiPSC-CM cell lines by D30. This yield is consistent with the seminal works that established the 2D monolayer and small molecule cardiac differentiation protocols. Burridge[320] had a yield of ~95% TNNT2 positive hiPSC-CMs after metabolic selection with lactate for 6 days, though the range was highly variable at 80-95%.

Moreover, Burridge[320] examined the effect of passage number on differentiation efficacy and found that there was no difference in differentiation using hiPSCs with a passage number of less than 25 versus more than 80, with other groups using up to passage 85[355]. This work did not exceed passage number 80 for cardiac differentiation and is consistent with the findings of Burridge[320] and Jelinkova[355]. Other authors did not report the passage number of cells used[356]. Laflamme[356] was able to produce a yield of 71-95% TNNT2 positive hiPSC-CMs with an average of

83%. They did not use metabolic selection for cardiomyocyte enrichment, rather they used a percoll gradient centrifugation method. Whilst the centrifugation appears to have enriched hiPSC-CMs this method may subject the cells to additional shear stress and may have a more detrimental effect compared to the metabolic enrichment alone.

As cardiogenesis proceeds it requires complex coordination between numerous transcription factors, including *NKX2.5* and *GATA4*, which are master regulators[357]. Both *NKX2.5* and *GATA4* form a transcriptional complex directing upregulation of downstream genes including *SCN5A* and *MYH6* as well as being responsible for differentiation into atrial and ventricular cardiomyocytes[357,358]. Knockout of *Nkx2.5* in murine models is embryonically lethal underscoring its importance, and SNPs in *NKX2.5* are a cause for congenital heart disease[359]. The expression of these cardiac transcription factors here, again, supports not only the success of the cardiac differentiation protocol but that the cardiac progression proceeded according to expected milestones.

In this work, I did not carry out a time-course to examine the alteration of key cardiac gene expression, thereby limiting the tracking of pluripotency/ cardiogenesis across various time-points. Nor did I examine the changes of dystrophin isoforms throughout development, which may have given additional insights between the mutants and WT. During my MRes project using the WT 1 hiPSCs, a time-series carried out over six days assessing *NKX2.5, ISL-1, TNNT2,* and *NANOG*. It revealed a trend consistent with the data presented here, whereby pluripotent gene expression decreased whilst cardiac lineage gene expression increased. However, it would be prudent to carry out such a time-series for all of the cell lines utilised and should be done in future work.

Differentiation of the hiPSC-CMs here was based on the protocol established by Burridge[320] that established the use of 6 μM CHIR99021 and 2 μM C59 as a method to modulate the Wnt/β-catenin pathway. The use of different compounds to enhance the initial phase of Wnt revealed that CHIR99021 was the most suitable in promoting high yield hiPSC-CMs (>80%) with other compounds, such as TWS119-another GSK3β inhibitor, producing very little to no TNNT2 positive hiPSC-CMs (~0%). This finding is consistent with the work here, although other compounds were not tested for efficacy in differentiation.

This work utilised a 2D monolayer 'chemically defined' protocol to produce hiPSC-CMs, a method widely used for hiPSC-CM generation[319,320,350,356]. Spontaneous beating of hiPSC-CMs was observed between D7 and D10-15 of cardiac differentiation with variability in this regard being relatively large. If hiPSC-CMs failed to beat by D15 they were discarded.

The ECM has an instrumental role in the proliferation, differentiation, and maintenance of cardiomyocytes. Consistent with Burridge[320], I used matrigel for the cardiac differentiation. Matrigel is extracted from Engelbreth-Holm-Swarm mouse sarcoma and is enriched in laminin. Laminin-521 and -511 were also both found to enhance hiPSC-CMs differentiation. After differentiation, laminin-511 was used for subsequent experiments (*i.e.* PDMS coverslips, coated with laminin-511). Interestingly, vitronectin and fibronectin were inferior to matrigel and laminin in maintaining hiPSC-CMs, in particular vitronectin[320]. hiPSC-CMs differentiated on vitronectin detached at approximately D15 which likely reflects the alteration of integrin expression throughout maturation of cardiomyocytes towards more laminin based α7β1D integrins[74,360].

Initial seeding density has an instrumental effect on the differentiation of hiPSC-CMs[361]. This work established that $4.5x10^4$ cm^{-2} consistently yielded large TNNT2 positive hiPSC-CM populations across all cell lines used. Burridge[320] examined several densities ranging from 0.6-$1.6x10^4$ cm^{-2} and revealed that TNNT2 positive populations of hiPSC-CMs were >80% across all tested densities. Laflamme[356] used $1.0x10^5$ cm^{-2} in their work, generating on average 83% TNNT2 positive hiPSC-CM populations. Hamad[361] examined a wide range of densities from $1.0x10^4$ cm^{-2} to $4x10^5$ cm^{-2} reporting no change in TNNT2 positive hiPSC-CMs produced, although there was a non-significant increase for initial seeding densities over $1.0x10^5$ cm^{-2} [361]. The variation described by these groups may be attributable to the differing (epi)genetic landscape of the cell lines used as an adjunct to cell line variability.

Given that seeding density is an important feature it should be tested and may vary between hiPSC cell lines. Prior work, during my MRes project, using the WT 1 cell line established that $4.5x10^4$ cm^{-2} was the optimal density, producing high yield TNNT2 positive hiPSC-CMs as well as beating sheets of cardiomyocytes. A small density test was carried out using the other cell line with the primary read out being spontaneous cardiomyocyte beating, as some densities were observed to not beat at all. Mainly due to time-constraints a more detailed examination was not carried out, and as such presents a central limitation to the work. A more comprehensive and evidence-based approach towards initial seeding density should be carried out.

Additionally, more techniques such as western blots and flow cytometry and more genes could have been examined to provide a more comprehensive and definitive determination of the phenotype and

maturation status of the hiPSC-CMs used. For example, gene expression and immunofluorescence for ion channels focusing on those located within the ventricles *e.g.* RYR2, SERCA2. Separation based on chamber specificity could have been achieved by analysing MLC2a and MLC2v as the latter are ventricle specific[362]. Thus, this work is limited by the likely inclusion of cardiomyocyte subpopulations. Future work may present clearer data analysis and more distinct/specific phenotypes when subpopulations are considered separately. As DMD-DCM primarily affects ventricular cardiomyocytes, examination of this particular subpopulation would be advantageous.

Determining the presence of T-tubules should also be carried out, as this is also a feature of maturation, as well as examining the action potentials of the hiPSC-CMs. However, binucleation was characterised and at least 20% of hiPSC-CMs demonstrated this feature across different the cell lines and between healthy and fibrotic Young's modulus. This feature is broadly consistent with human *in vivo* scenario whereby some 25% of cardiomyocytes are binucleated[363]. This is in contrast to murine cardiomyocytes that are approximately 90% binucleated[364]. However, the presence of binucleation is dependent upon maturity of the myocardium, which can be detected in murine models at P7[365].

In summary, the data presented here provide evidence for high yield TNNT2 positive hiPSC-CMs using a reproducible protocol. The hiPSC-CMs generated using the chemically induced protocol are consistent with previous works that established the use of 2D models. However, perhaps a fuller examination of genes at different time-points could have documented the differentiation and maturation more accurately. That being said, studies into maturation and optimisation of hiPSC-CMs can be exhaustive with no

clear end-point in sight. I determined that the work presented was sufficient evidence for showing successful hiPSC-CM production that could then be used for further experimentation.

3.7.2 Further Maturation of hiPSC-CMs

Given the general lack of maturity that hiPSC-CMs display, many groups work towards closing the phenotypic gap between embryonic/foetal hiPSC-CMs and adult cardiomyocytes. Several advanced methods are now gaining traction and are being used within labs including long-term culture[366,367], engineered heart tissue 3D culture[368], co-culture[369], substrates mimicking a native Young's modulus[83], electromechanical stimulation[368], and finally the use of more appropriate metabolites[370] (*i.e.* addition of fatty acids such as palmitic acid, oleic acid, and linoleic acid rather than the use of glucose). Together, these methods have each been shown to enhance hiPSC-CM morphology and function characteristics (T-tubule formation, action potentials, etc) but no single method has yet fully recapitulated an adult cardiomyocyte phenotype. Long-term culture has proven to be somewhat effective to advancing the maturation of hiPSC-CMs, however when compared to the *in vivo* heart, these culture times are often insignificant[366,367] (<200 days vs years of development). It is reasonable to predict that further and prolonged cell culture would promote the maturity of hiPSC-CMs, however a balance is to be struck between what is ideal and the experimental reality.

Further, it is less known how readily transferable each of these techniques are between laboratories and across cell lines. Potentially, certain cell lines are more responsive to different maturation techniques compared to others and would be an interesting series of experiments to conduct.

Here, maturation was enhanced using hiPSC-CMs that were treated using 0.1 µM T3 and 1 µM Dex for a period of 10 days before use in subsequent experiments. Both thyroid hormones and glucocorticosteroids are necessary for appropriate maturation *in vivo* with T3 being instrumental in driving key morphogenetic alterations in the cardiac environment[371], such as the phenotypic switch of titin from the compliant N2BA isoform to the stiffer N2B[372]. Moreover, T3 rises rapidly after birth and therefore I wanted to recapitulate this aspect of human physiology.

Parikh[327] observed T-tubule formation in the presence of T3/dex, a feature typically absent in hiPSC-CMs. T-tubule formation was further enhanced using a matrigel mattress, though hiPSC-CMs were less organised compared to adult cardiomyocytes. Moreover, Parikh[327] observed a significant increase in hiPSC-CM cellular morphology, particularly volume and width when T3 and Dex were used. Functionally, the addition of T3/dex led to decreased time to peak as well as increased Ca^{2+} efflux from hiPSC-CMs compared to vehicle controls. Given more time, comparison between presence/absence of T3/dex on the hiPSC-CMs used here may have given some insight into its ability for maturation and effect. Given that other groups[372–374] have reported improved cardiac phenotype when T3 or dex, are applied, I felt confident that this effect would be applicable to the cell lines used here.

In vivo, there is a phenotypic switch from MYH6 to MYH7, with MYH6 being the less mature isoform present in atria and embryonic hearts[375] whereas, MYH7 is the predominant isoform in mature left ventricles. Here, gene expression revealed the presence of both isoforms, a finding that has been reported elsewhere[320], and provides evidence that there may be some isoform switching occurring. Perhaps increased isoform switching would be

found under long-term cardiac culture or when combined with other maturation methods. As mentioned previously, examination of MLC2a and MLC2v could also have further substantiated the claim that predominantly ventricular cardiomyocytes were present. Phenotypic switching from MLC2a to MLC2v would have provided further evidence for the maturation of the hiPSC-CMs used here.

To summarise, a variety of techniques are gaining attention towards further hiPSC-CM maturation. Here, I opted for metabolic enhancement using T3 and Dex as described by Parikh[327]. Combining and optimising the methods would provide an interesting study towards further enhancing hiPSC-CMs. However, due to time-constraints this was not possible.

3.7.3 hiPSC-CMs as a Model for Duchenne Muscular Dystrophy

As mentioned previously, animal models for DMD do not fully recapitulate the phenotype, particularly that of the decompensated heart in DMD. The use of hiPSC-CMs provides a human derived platform to model DMD and can be used to generate isogenic controls, harnessing the use of CRISPR/Cas9 and AAV vectors.

Satisfied with the hiPSC-CM differentiation protocol, I re-confirmed the presence of the mutations within the DMD mutant cell lines as well as showing the absence of full-length dystrophin in the DMD 1 cell line using immunofluorescence and RT-qPCR. These methods are standard for demonstrating the absence of dystrophin and have been widely reported[313,316,350,355,376]. The addition of a western blot may have further substantiated these findings and was not performed here.

An unexplored avenue here was the characterisation of isoform switching of dystrophin as well as utrophin expression. Given that *in vivo* utrophin is

predominantly expressed in embryonic phase and is replaced by dystrophin over time, it would be interesting to examine this using the hiPSC-CMs. Moreover, some groups have reported that utrophin may compensate for dystrophin loss in DMD. Characterising utrophin expression here should be included in future work to determine the possibility of utrophin contributing to the findings reported throughout this work.

Work by Jelinkova[355] reported decreased cardiac differentiation efficiency in DMD cell lines compared to WT by characterising gene expression. The cardiac developmental gene *NKX2.5* was downregulated compared to WT, with a reduction in structural and ion channel genes *MYH6* and *RYR 2*[355]. The work presented here did not find any difference between the cardiac differentiation efficiency, as determined by TNNT2 positive hiPSC-CMs and gene expression, that was comparable across all cell lines. Jelinkova[355] also reported a decrease in spontaneous beating in their DMD cell lines, a finding inconsistent with the work here, although this was not formally characterised in this work. They also reported comparable beat rate between WT and DMD cell lines, with beat rates ranging from 50-90 BPM[355]. This contrasts with my observation that DMD hiPSC-CMs had a significantly decreased beat rate compared to WT.

3.8 Limitations and Future Work

Throughout this chapter several limitations have arisen. It should be noted that the COVID-19 pandemic presented a significant challenge to the optimisation and data acquisition throughout this work, whereby several months of time were lost. Aside from this, the most pressing limitation here is the lack of isogenic controls. The isogenic controls are the gold standard for hiPSC experimentation as it provides, in theory, the same genetic background, thus mitigating SNPs or any other unknown mutations from

confounding the data. Unfortunately, the isogenic pairs that were to be sourced from Dr Lin's laboratory were found to be irretrievably mixed and, despite several efforts by laboratory members, could not be salvaged. Examination utilising other cell lines, for example an FKRP pair, were trialled as an alternative thus widening the work to muscular dystrophies associated with the DGC as a whole. However, these cells failed to differentiate to cardiomyocytes, despite the most valiant efforts.

In attempt to counter this clear obstacle, I incorporated the use of different mutants and wild-type cell lines. However, this may have further confounded interpretation by increasing cell line heterogeneity. Nonetheless, the data collected here has been shown to be consistent with that of previously published groups. For future work, the *de novo* generation of isogenic pairs should be carried out, although this will require a substantial investment of time and characterisation to ensure success.

An additional series of experiments that may have supported the findings would be the use of siRNA to knockdown dystrophin within the WT cell lines. Utilising siRNA knockdown would provide a faster experimental platform to characterise the loss of dystrophin in the WT 1 cell line and could be implemented for a wide-range of experiments. Although, an important caveat to consider for siRNA is the incomplete knockdown efficiency thereby not faithfully recapitulating the DMD phenotype but may provide some insights to the BMD phenotype. However, this has yet to be explored and may yield some interesting findings for further experimentation.

Third, a lack of time-series and more comprehensive genetic/protein level examination. For example, carrying out time-series for certain genes across all of the cell lines, performing western blots, or analysis of wider genetic

panel may have substantiated more of the findings presented here. Nonetheless, data acquired is consistent with previous bodies of work and key genes and proteins were examined that support successful cardiac differentiation.

3.9 Chapter Summary

In summary, I successfully generated fully functional hiPSC-CMs using a chemically defined protocol modulating the Wnt/β-catenin pathway. Moreover, I re-confirmed the presence of the expected mutations for both DMD 1 and DMD 2 hiPSC cell lines, and as such, generated a human derived model for DMD. Satisfied with the consistent production of hiPSC-CMs and their mutation status, the cells could be utilised for further investigations, in particular examination into the biomechanics of dystrophin deficient hiPSC-CMs.

4 Characterising Cellular and Nuclear Biomechanics using the hiPSC-CM Model

Experience is the one thing you can't get for nothing

Oscar Wilde

4.1 Introduction to Biomechanics

Over the last two decades, an appreciation for physical forces and mechanics in the context of cells has revealed their importance towards the development, migration, regeneration, embryogenesis, repair, and pathology in cells[1]. The integration of mechanobiology with genetics and cell signalling will allow higher order understanding of cellular behaviour that may be harnessed to discover and deliver significantly improved treatment strategies and biological tools. For example, the regulation of the (epi)genome in response to different mechanical forces, experienced under differing spatiotemporal circumstances, such as embryogenesis versus mature hiPSC-CM *in situ*.

As discussed in the general introduction (§1), the central players in mechanotransduction in the context of hiPSC-CMs are the integrin adhesion complex, in particular the laminin binding integrin α7β1D, as well as the DGC. Both the integrins and DGC are conduits for bidirectional communication with the ECM, communicating biomechanical signals to, and from, the hiPSC-CMs and the nucleus, thereby regulating cellular physiology (Figure 4.1). In turn, disruption to costameric complexes is responsible for aberrant mechanotransduction and cellular behaviour, together driving the pathogenesis observed in disease states such as DMD.

A significant physiological parameter governed by physical force is cellular and nuclear morphology. FA and the DGC, in conjunction with their connection to the ECM, dictate morphology. The actin and microtubule cytoskeletons are both highly dynamic and responsive to alterations of externally applied physical forces, rearranging their structures to maintain force equilibrium as described by the tensegrity model[56]. Given the

importance that tensegrity holds for contextualising the response of cells to physical force, a fuller description is introduced here.

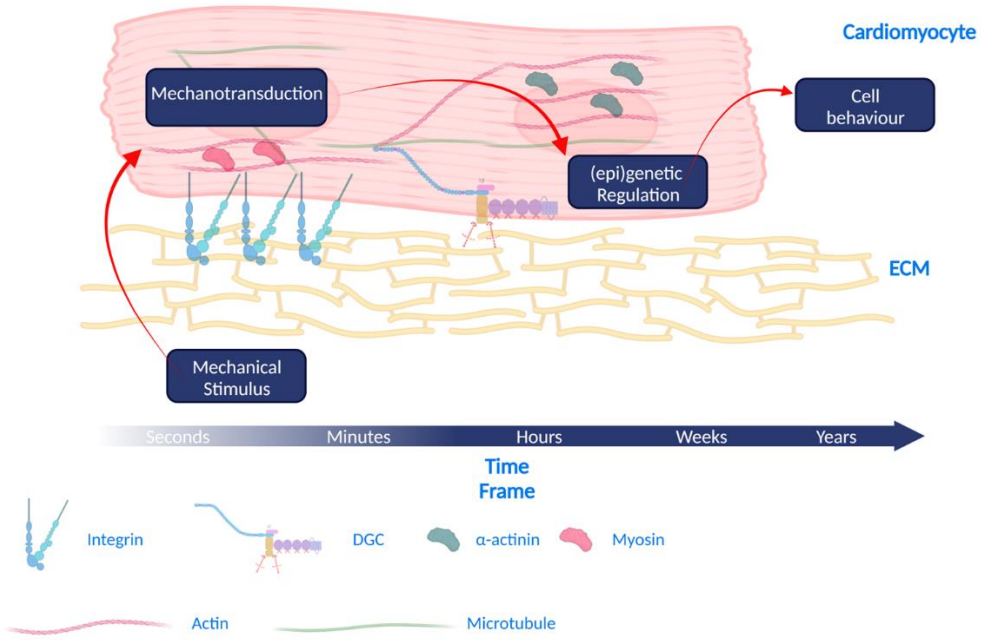

Figure 4.1: Overview of Mechanotransduction. *Mechanical stimuli, such as substrate elasticity, pressure, or stretch, are perceived by the cell via costameric regions comprising of integrins and the DGC. Substrate sensing is the result of actin and microtubule clustering thus permitting mechanosensing. Mechanosensitive proteins, such as FAK and YAP, regulate cellular processes over distinct timeframes from minutes to hours to years. Long term alterations govern cellular behaviour and adaptability, as enacted via alterations of the (epi)genome. (Epi)genetic regulation in response to mechanical signaling can effect change over a period of years. Figure created using Biorender.com*

Tensegrity architecture of cells depends upon the prestress of the cytoskeletal elements as generated by the actomyosin and microtubules (Figure 4.2). These two opposing forces balance to find a force equilibrium for the cell. The ECM adhesions, *i.e.* FAs and DGC, are poised to resist tension acting as conduits for force transmission, with some FAs acting to transmit forces inwardly while others preferentially act to transmit forces

outwardly. This allows local changes, occurring at a handful of FAs or DGC sites, leading to global changes of the cell, including detectable parameters, such as the elasticity, or Young's modulus.

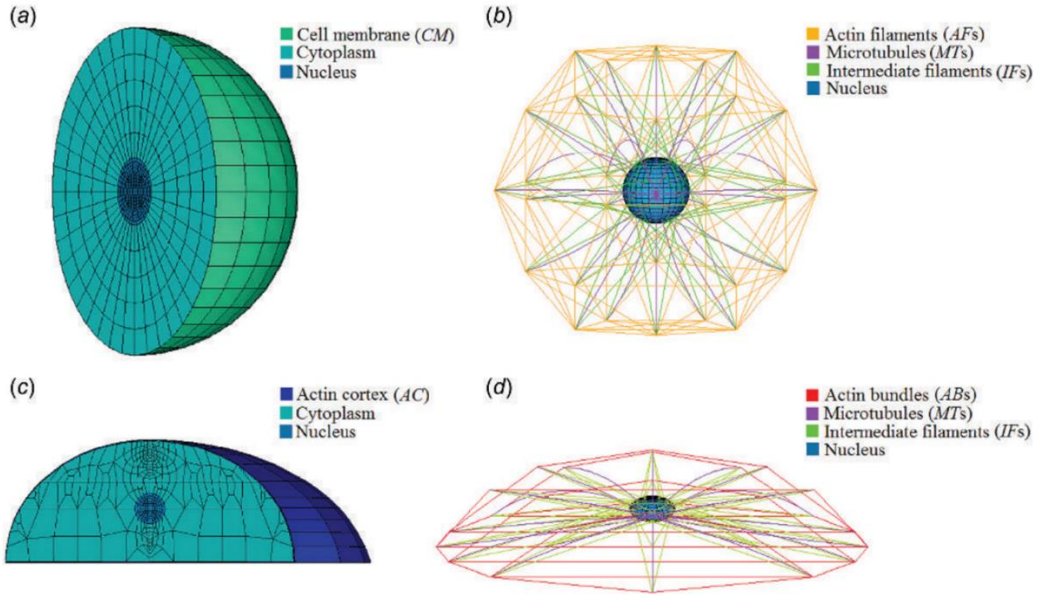

Figure 4.2: Tensegrity Model Displaying Adaptable Cytoskeletal Elements. *The tensegrity model describes how actin acts as the 'cables' that generate tension, via actomyosin contraction, against which the microtubule 'struts' resist. In turn, the microtubule cytoskeleton and ECM adhesions tend to act to 'push against' the tension generated by actin, thus acting as the compressive force. By balancing the push-pull of tension and compression forces the cytoskeleton maintains a prestressed architecture that is sensitive to, and can readjust in response to, external force application. Image adapted from* [377]

Prestress is absolutely critical to tensegrity architecture, with experimental evidence supporting this[56,378,379]. Critically, prestress is a central regulator of cellular and nuclear morphology and provides the stability for these. The Young's modulus, a measure for stiffness, and viscoelasticity can characterise the tensegrity architecture of the cell and are therefore able to provide information on the status of the underlying cytoskeleton. As tension in actomyosin increases or decreases, so does the Young's modulus.

Defining some of the mechanical parameters is required for this chapter. Cells are described as possessing both viscous and elastic properties, that is to say they are viscoelastic[380]. Elasticity defines the deformability of an object in response to an applied force, whilst viscosity refers to the resistance to flow under a given force[380,381]. Therefore, a viscoelastic object is one undergoing deformation whilst simultaneously storing and releasing mechanical energy. The ratio between the storage and dissipation of energy is given by *Tan δ*. The scaling between stress and strain gives rise to the Young's modulus[380,381] where stress (*σ)* is defined in *Eq. 4.1:*

$$\sigma = \frac{F}{A} \quad (Eq. 4.1)$$

Where, *F* is the force (in N) and *A* is area. Strain (*E*) is defined in *Eq. 4.2:*

$$E = \frac{\Delta L}{L} \ (Eq. 4.2)$$

Where *ΔL* is the change in length and *L* is the original length of the object. Together, the ratio between stress and strain gives rise to the Young's modulus, which is a measure of the stiffness of a material defined by *Eq. 4.3*:

$$YM = \frac{\sigma}{E} \quad (Eq. 4.3)$$

Where, *YM* is the Young's modulus in Pascals (Pa). Characterisation of the Young's modulus is to characterise the stiffness of the cell, which is predominantly modulated by the actin cytoskeleton[382]. Therefore, measuring the cellular Young's modulus can provide information about the underlying physiology of the cytoskeleton and overall physiology of the cell. Of course, the actin cytoskeleton is regulated by a multitude of accessory proteins, such as α-actinin and ARP2/3, which govern higher order actin formation such as the formation of actin cables that may affect the Young's

modulus[56]. Characterisation of the viscoelastic properties of cells has emerged as a biomarker for disease progression and underpins the motivation to examine this in detail throughout this chapter.

It must be noted that the mechanical behaviour of cells is inherently viscoelastic, thus an understanding of equations 4.1 - 4.3 is required for this chapter, especially the section on nanoindentation.

Therefore, viewing the mechanics of hiPSC-CMs of this chapter through the lens of tensegrity architecture, with the underlying equations in support of cellular viscoelasticity, is key to understanding and contextualising the underlying changes. In this context, I aimed to characterise the biomechanics of WT and DMD hiPSC-CMs when challenged by substrates of different Young's moduli as well as the viscoelasticity. In particular, the cellular and nuclear morphology, actin cytoskeleton and sarcomeric architecture, and viscoelastic properties of the hiPSC-CMs was examined.

4.2 Dystrophin Mechanosenses Variations in the Young's Modulus of the ECM as Determined by hiPSC-CM Cellular and Nuclear Morphology

4.2.1 hiPSC-CM Cellular Morphology

Alterations to the cardiac ECM appear as DMD progresses towards cardiac failure, including an increase in the Young's modulus from approximately 10 kPa to 130 kPa[76,83]. This change is potentiated by increased collagen type I deposition by cardiac fibroblasts and associated pro-inflammatory responses mediated by infiltrating CD40 expressing T-cells and M1/M2 macrophages[63]. Variations to the composition of the ECM are communicated through focal adhesions, including the DGC. These changes are then transduced into various physicochemical responses that are

mediated, in part, by the actin and microtubule cytoskeleton. Therefore, I postulated that the DGC, in particular dystrophin, was required to mechanosense the change between a healthy cardiac ECM Young's modulus (6 kPa) or a fibrotic Young's modulus (130 kPa).

As such, this formed the basis for my initial investigation into the effect of changing the Young's modulus on the cellular and nuclear morphology of hiPSC-CMs. Laminin coated PDMS coverslips of either 6 kPa or 130 kPa were used to examine this change. hiPSC-CMs were maintained on the coated coverslips for 5 days, to recover from passage and adjust to the new ECM. Images of hiPSC-CMs were then obtained and quantified using ImageJ to determine if any change in the morphological shape descriptors were apparent.

The cellular area for WT 1 (2788.1 ± 2552.4 μm^2 vs 4442.8 ± 3303.6 μm^2) and WT 2 (2504.9 ± 1567.4 μm^2 vs 3292.2 ± 2275.6 μm^2) significantly increased from being on a healthy cardiac Young's modulus of 6 kPa to that of the fibrotic Young's modulus of 130 kPa (Figure 4.4A). Interestingly, no change in cellular area was observed for DMD 1 (3701.2 ± 3563.8 μm^2 vs 3425.4 ± 2745.4 μm^2) and DMD 2 (2534.9 ± 2099.8 μm^2 vs 1989.6 ± 1438 μm^2). Moreover, the perimeter (Figure 4.4B) followed a similar trend as the cellular area, with an increase in WT 1 (224.7 ± 109.1 µm vs 255.6 ± 103.3 µm) but not WT 2 (234 ± 96.2 µm vs 241.9 ± 93.3 µm). Similarly, DMD 1 (284.1 ± 149.4 µm vs 251.9 ± 123.7 µm) and DMD 2 (219.3 ± 95.1 µm vs 195.3 ± 82.2 µm) were contrary to WT 1 and WT 2 and showed a decreased cell perimeter in response to the fibrotic cardiac Young's modulus.

Comparing the hiPSC-CM cell lines (Figure 4.3) revealed that DMD 1 had a significantly larger area compared to WT 1 and DMD 2 on a 6 kPa stiffness (DMD 1, 3701.2 ± 3562.8 μm^2; WT 1, 2788.1 ± 2552.4 μm^2; DMD 2, 2533.9

± 2098.8 µm^2) but was no different to WT 2 (2503.9 ± 1567.4 µm^2). Interestingly, WT 1 responded to the substrate stiffness by increasing in cell area between 6 kPa and 130 kPa (2788.1 ± 2552.4 µm^2 vs 4441.8 ± 3302.6 µm^2) which was not the case for the other cell lines. hiPSC-CM area for WT 1 was significantly increased compared to both DMD 1 and DMD 2 on 130 kPa (WT 1, 4441.8 ± 3302.6 µm^2; DMD 1, 3425.4 ± 2745.4 µm^2; DMD 2, 1988.6 ± 1437.7 µm^2). WT 2 was also significantly larger compared to DMD 1 on 130 kPa, but not to DMD 2. Of interest, DMD 1 was significantly larger compared to DMD 2 at 130 kPa (DMD 1, 3425.4 ± 2745.4 µm^2; DMD 2, 1988.6 ± 1437.7 µm^2). The perimeter followed a similar trend to the cell area.

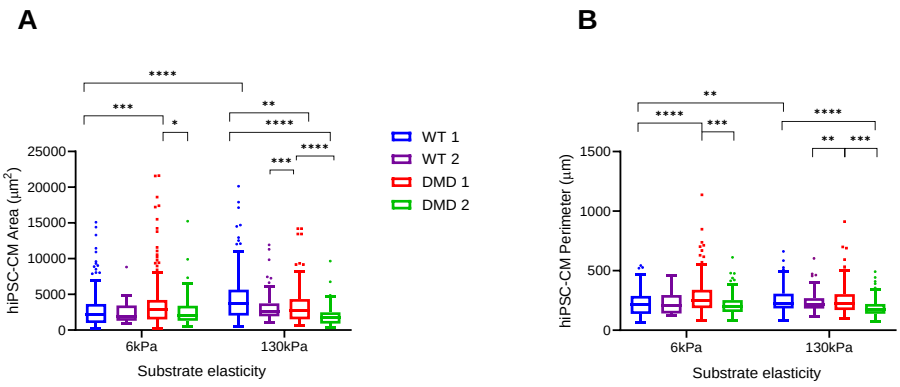

Figure 4.3: hiPSC-CM Cell Area and Perimeter between Cell Lines on Either 6 kPa or 130 kPa Substrate. *A) hiPSC-CM cell area showing that DMD 1 was significantly increased at 6 kPa compared to DMD 2 and WT 1 but not WT 2. However, at 130 kPa, DMD 1 was smaller compared to WT 1 and WT 2 but larger than DMD 2. B) Similar trend was observed as cell area. Data presented as Tukey boxplot, reported as mean ± S.D.; Mann-Whitney U test, p<0.05 considered statistically significant. N= 3 biological replicates; WT 1, 6 kPa vs 130 kPa n number of cells= 120 vs 148 hiPSC-CMs; WT 2, 6 kPa vs 130 kPa, n= 42 vs 67 hiPSC-CMs; DMD 1, 6 kPa vs 130 kPa, n= 180 vs 145 hiPSC-CMs; DMD 2, 6 kPa vs 130 kPa, n= 88 vs 83 hiPSC-CMs.*

Together, the cell area and perimeter of the hiPSC-CM cell lines here suggest a role for dystrophin in responding to alterations of the ECM, in particular the ability to mechanosense changes to the Young's modulus. Importantly, this supports the notion that DMD hiPSC-CMs are less able to adapt to the fibrotic environment, which is associated with the DMD phenotype, and may be a driver for the cardiac pathogenesis.

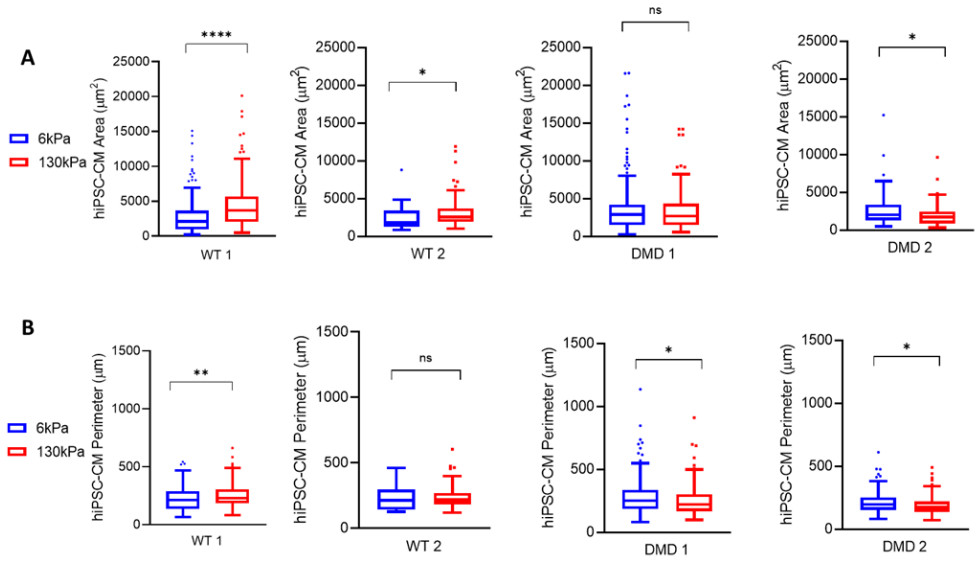

Figure 4.4: Dystrophin is a Regulator of hiPSC-CM Cell Area and Perimeter. A) *hiPSC-CM cell area and* ***B)*** *perimeter on either a 6 kPa or 130 kPa substrate. WT 1 and WT 2 hiPSC-CMs increased cell area significantly in response to increased substrate stiffness, whereas DMD 1 and DMD 2 both showed a decrease. Similar findings were observed for hiPSC-CM perimeter. Representative images are shown in Figure 4.3. Data presented as Tukey boxplot, reported as mean ± S.D.; Mann-Whitney U test, p<0.05 considered statistically significant. N= 3 biological replicates; WT 1, 6 kPa vs 130 kPa n number of cells= 120 vs 148 hiPSC-CMs; WT 2, 6 kPa vs 130 kPa, n= 42 vs 67 hiPSC-CMs; DMD 1, 6 kPa vs 130 kPa, n= 180 vs 145 hiPSC-CMs; DMD 2, 6 kPa vs 130 kPa, n= 88 vs 83 hiPSC-CMs.*

hiPSC-CMs cell morphology was further characterised using circularity and aspect ratio (defined as cell length / cell width) (Figure 4.5). Circularity significantly increased for WT 1 and DMD 1 but no change was apparent for

other cell lines. Increased circularity from 6 kPa to 130 kPa suggests that the cell becomes more rounded, with 1.0 indicating the perfect circle and 0 indicating an irregular, polygonal morphology. WT 1 showed a significant increase between 6 kPa and 130 kPa (0.62 ± 0.19 A.U. vs 0.68 ± 0.18 A.U.), whilst WT 2 hiPSC-CMs did not (0.61 ± 0.22 A.U. vs 0.70 ± 0.18 A.U.).

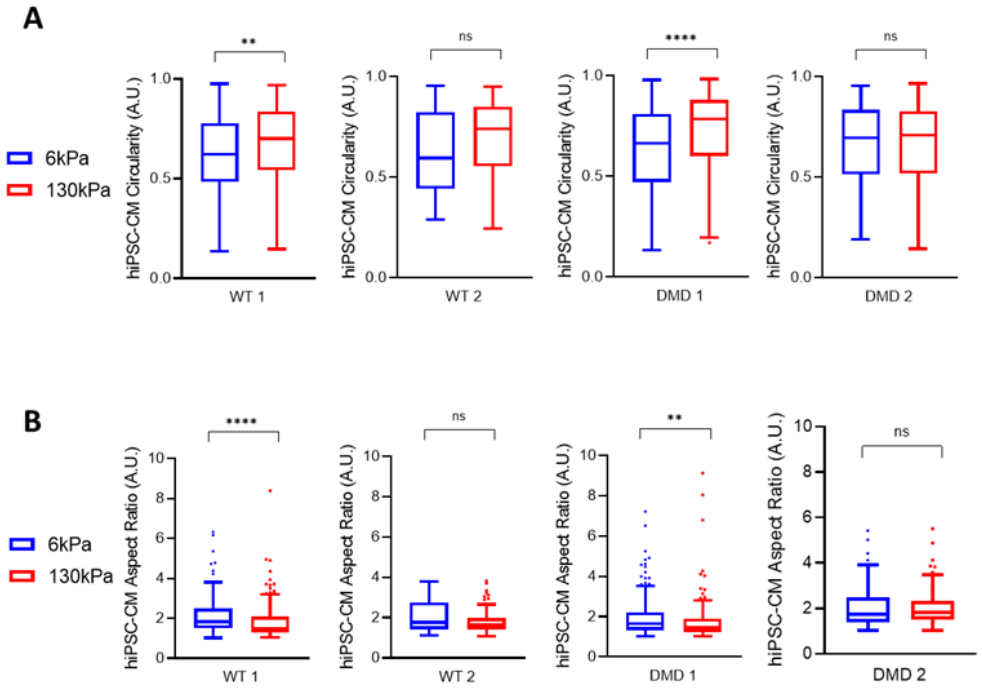

Figure 4.5: Dystrophin is not Necessary for hiPSC-CM Cell Circularity or Aspect Ratio. A) *hiPSC-CM cell circularity, where 1.0 is the perfect circle and 0 is amorphous.* ***B)*** *Aspect ratio of hiPSC-CMs. All hiPSC-CM cell lines displayed similar trends for circularity and aspect ratio (AR). WT 1 and DMD 1 had significantly increased circularity, i.e. became more rounded, on 130 kPa. Representative images are shown in Figure 4.4. Data presented as Tukey boxplot and reported as mean ± S.D.; Mann-Whitney U test, p<0.05 considered statistically significant. N= 3 biological replicates; WT 1, 6 kPa vs 130 kPa n number of cells= 120 vs 148 hiPSC-CMs; WT 2, 6 kPa vs 130 kPa, n= 42 vs 67 hiPSC-CMs; DMD 1, 6 kPa vs 130 kPa, n= 180 vs 145 hiPSC-CMs; DMD 2, 6 kPa vs 130 kPa, n= 88 vs 83 hiPSC-CMs.*

Similar to WT 1 and WT 2, DMD 1 (0.63 ± 0.21 A.U. vs 0.73 ± 0.19 A.U.) showed a significant increase in circularity when maintained on the 130 kPa

substrate. Interestingly, DMD 2 showed very little change between 6 kPa and 130 kPa (0.65 ± 0.21 vs 0.66 ± 0.20 A.U.), the reason for this was unclear. No difference in circularity was observed between the hiPSC-CM cell lines that is likely attributable to cell line variability (Figure 4.6).

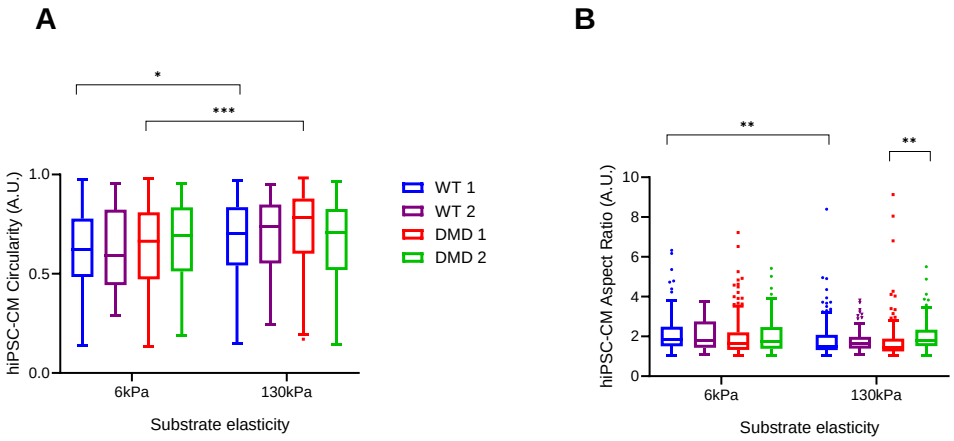

Figure 4.6: Comparison between hiPSC-CM cell lines. *Showing no difference between A) circularity or B) aspect ratio. hiPSC-CM cell circularity, where 1.0 is the perfect circle and 0 is amorphous. All hiPSC-CM cell lines displayed similar trends for circularity and aspect ratio (AR). WT 1 and DMD 1 had significantly increased circularity, i.e. became more rounded, at 130 kPa. WT 2 showed a trend towards increased circularity at 130 kPa, although this did not reach statistical significance. Representative images are shown in Figure 4.4. Data presented as Tukey boxplot and reported as mean ± S.D.; Mann-Whitney U test, p<0.05 considered statistically significant. N= 3 biological replicates; WT 1, 6 kPa vs 130 kPa n number of cells= 120 vs 148 hiPSC-CMs; WT 2, 6 kPa vs 130 kPa, n= 42 vs 67 hiPSC-CMs; DMD 1, 6 kPa vs 130 kPa, n= 180 vs 145 hiPSC-CMs; DMD 2, 6 kPa vs 130 kPa, n= 88 vs 83 hiPSC-CMs.*

The aspect ratio (AR) for all hiPSC-CM cell lines tended to decrease on the 130 kPa substrate, suggesting that hiPSC-CMs widened *i.e.,* an increase of the minor axis. This change in the AR can accord with the increased hiPSC-

CM circularity as the irregularity of the cells was more dramatic on the 130 kPa compared to the 6 kPa substrate (Figure 4.5B and Figure 4.7).

WT 1 showed a 14% significant decrease in AR (2.16 ± 1.01 A.U. vs 1.86 ± 0.96 A.U.) which was more dramatic than the 10% significant decrease observed in DMD 1 (1.98 ± 1.02 A.U. vs 1.78 ± 1.11 A.U.). There was no significant change observed for either WT 2 (13% decrease) or DMD 2 (1.5% increase) hiPSC-CMs. Given that WT 2 did not reach significance is whereas DMD 1 did suggests strong cell line variability. Nonetheless, these data here suggest that dystrophin was not required for hiPSC-CM changes in circularity or AR.

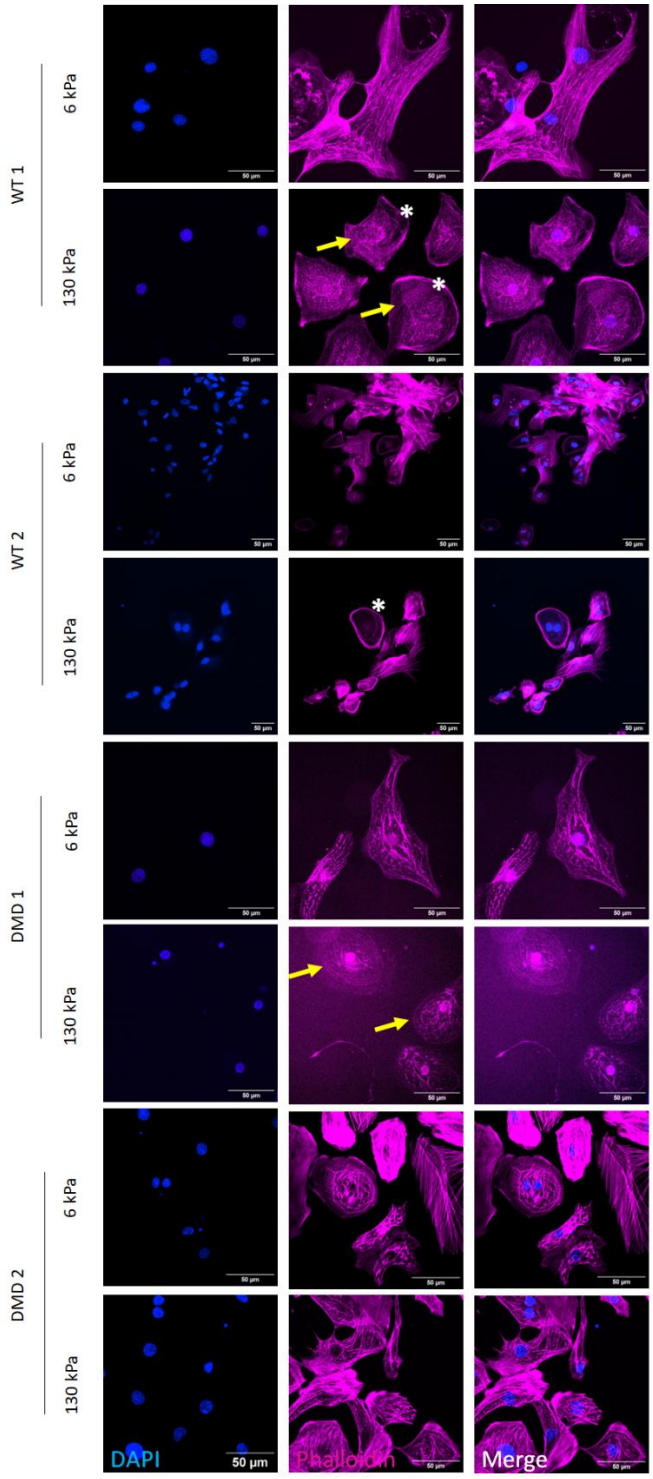

Figure 4.7: hiPSC-CMs on Either a 6 kPa or 130 kPa Laminin Coated Coverslip Mimicking Healthy or Fibrotic Cardiac ECM Respectively. *Representative immunofluorescence images of WT 1, WT 2, DMD 1, and DMD 2 hiPSC-CMs cell lines. Each cell line was plated onto*

either a 6 kPa or 130 kPa PDMS coated substrate for 5 days prior to fixation and immunofluorescence. White asterisks on WT 1 and WT 2 indicate the larger cell area observed here on 130 kPa. DMD 1 showed no significant change in cell area whilst DMD 2 showed significant decrease from 6 kPa to 130 kPa. Other morphological characteristics were altered, for example circularity was increased in both WT 1 and DMD 1 hiPSC-CMs at 130 kPa, as indicated by the yellow arrows. hiPSC-CMs were stained using DAPI and phalloidin to delineate cell and nuclear morphology. Scale bar= 50 µm. N= 3 biological replicates.

Overall, the data support a role for dystrophin in the mechanosensing of the ECM, particularly in response to changes of the Young's modulus, as demonstrated by the significant increase in morphological parameters for WT 1 and WT 2, such as cell area and circularity. DMD 1 and DMD 2 did not recapitulate the changes of cell area observed in WT 1 and, to an extent, WT 2, again, supporting the notion that dystrophin is important for mechanosensing for specifically these facets of morphology. Indeed, DMD 1 and DMD 2 appeared to show the opposite trends in terms of cell area and perimeter, but all cell lines had similarities in circularity and AR. WT 1 and DMD 1 hiPSC-CM cell lines were observed to become increasingly rounded on the 130 kPa substrate compared to 6 kPa, with a concurrent decrease in the AR- indicating a widening of the cell. These data would suggest that dystrophin influences the overall cell area and perimeter of the hiPSC-CM but is dispensable in regard to roundedness and aspect ratio.

4.2.2 hiPSC-CM Nuclear Morphology

Nuclear mechanotransduction is an important regulator governing long-term cell behaviour primarily via differential gene expression[197,198]. Mechanical signals are communicated to the nucleus via the cytoskeleton, that connects to the LINC complex downstream. In turn, the LINC complex traverses the nuclear membrane and directly interacts with chromatin, thus

regulating gene expression[383]. Because mechanical signals from the ECM are communicated across focal adhesions, I hypothesised that the absence of dystrophin in DMD mutant hiPSC-CMs result in largely unchanged nuclear morphology, contrary to my expectation for the WT hiPSC-CMs.

The nuclear area significantly increased for WT 1 (122.3 ± 62.6 μm^2 vs 136.7 ± 51.2 μm^2) and for WT 2 (147.6 ± 66.8 μm^2 vs 182.6 ± 78.3 μm^2) from a 6 kPa to a 130 kPa substrate (Figure 4.8A) whilst the nuclear perimeter for WT 1 (40.51 ± 16.4 µm vs 41.94 ± 8.1 µm) remained unchanged. However, WT 2 (45.91 ± 10.6 µm vs 50.04 ± 11.3 µm) displayed a significant increase of the nuclear perimeter (Figure 4.8A and Figure 4.8B).

In contrast, the nuclear area for the DMD mutants was observed to become significantly smaller on the fibrotic 130 kPa substrate for DMD 1 (148.8 ± 70.2 μm^2 vs 136.5 ± 67.7 μm^2). The nuclear area for DMD 2 did not decrease (114.7 ± 55.5 μm^2 vs 111.8 ± 64.7 μm^2). Interestingly, the nuclear perimeter for DMD 1 was found to be significantly decreased (43.7 ± 10.3 µm vs 41.7 ± 10.2 µm) whilst the perimeter of DMD 2 remained unchanged (38.9 ± 10.3 µm vs 38.5 ± 11.6 µm). Subsequently, I further characterised the nuclear morphology by examining the circularity (Figure 4.8C). Nuclear circularity increased in WT 1 (0.88 ± 0.13 A.U. vs 0.95 ± 0.05 A.U.) and WT 2 (0.85 ± 0.09 A.U. vs 0.89 ± 0.08 A.U.) showing that nuclei responded to the increased Young's modulus by becoming more rounded.

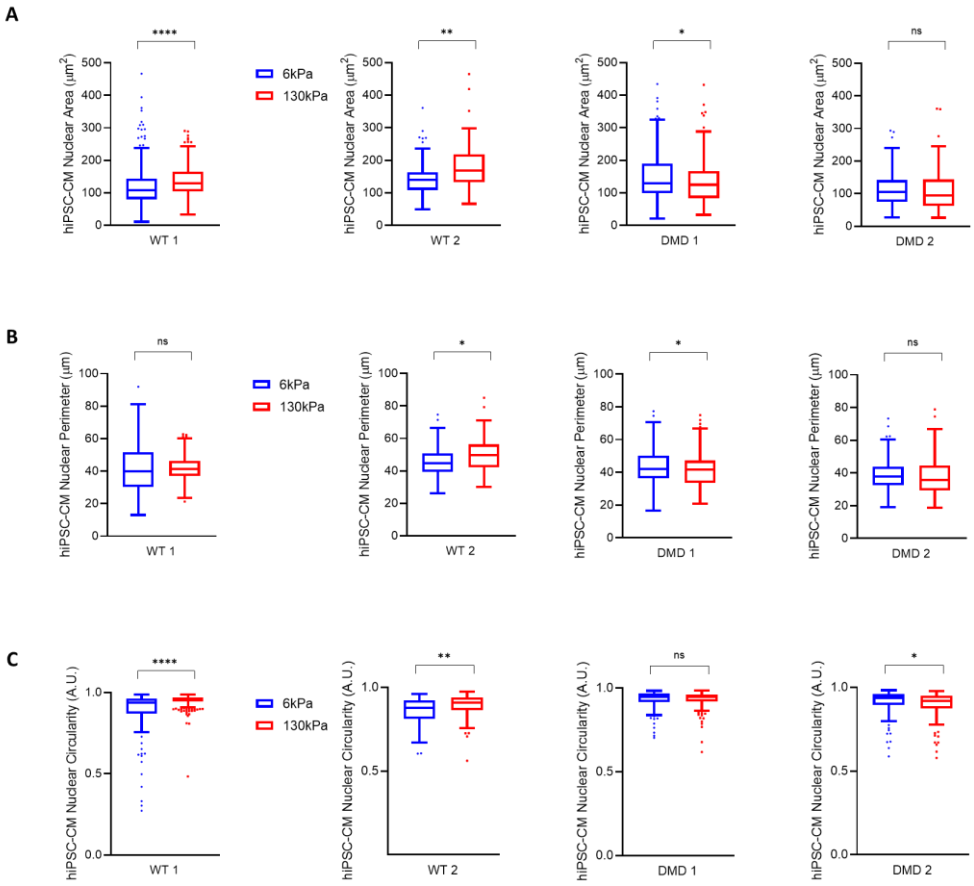

Figure 4.8: Dystrophin Plays a Role in Determining Nuclear Morphology in Response to Healthy versus Fibrotic Young's Modulus of the ECM. A) *Nuclear area,* ***B)*** *nuclear perimeter, and* ***C)*** *nuclear circularity for WT 1, WT 2, DMD 1, and DMD 2 hiPSC-CM cell lines. Representative nuclei are shown in Figure 4.4. Data presented as Tukey boxplot and reported as mean ± S.D.; Mann-Whitney U test, p<0.05 considered statistically significant. N= 3 biological replicates; WT 1, 6 kPa vs 130 kPa n number of nuclei= 138 vs 178 nuclei; WT 2, 6 kPa vs 130 kPa, n= 47 vs 62 nuclei; DMD 1, 6 kPa vs 130 kPa, n= 225 vs 187 nuclei; DMD 2, 6 kPa vs 130 kPa, n= 104 vs 105 nuclei.*

Furthermore, increased circularity suggests increased actomyosin interaction with the nucleus. Conversely, DMD 1 nuclei showed no change in nuclear circularity (0.94 ± 0.05 A.U. vs 0.93 ± 0.05 A.U.) suggesting a disconnect between the nucleus and the ECM, likely due to the lack of

dystrophin. DMD 2 showed decreased circularity (0.91 ± 0.08 A.U. vs 0.89 ± 0.08 A.U.) in response to the 130 kPa Young's modulus. This suggests that WT nuclei became increasingly rounded, whilst DMD nuclei responded differently to stiffness, by becoming elongated or not changing. Interestingly, it may suggest that expression of Dp71m may be sufficient for a degree of mechanotransduction in DMD 2 hiPSC-CMs.

Comparing the cell lines revealed significant changes to both nuclear area and perimeter (Figure 4.9). At 6 kPa, nuclei from WT 1 had a significantly decreased area compared to WT 2 and DMD 1 but were no different to DMD 2 (WT 1, 122.3 ± 62.6 μm^2; WT 2, 147.6 ± 66.8 μm^2; DMD 1, 148.8 ± 70.1 μm^2; DMD 2, 114.7 ± 55.5 μm^2). At 130 kPa, DMD 1 and DMD 2 nuclei were both significantly decreased compared to WT 2 but not WT 1 (WT 1, 136.7 ± 51.2 μm^2; WT 2, 182.6 ± 78.3 μm^2; DMD 1, 136.5 ± 67.7 μm^2; DMD 2, 111.8 ± 64.7 μm^2). Similarly, WT 1 nuclei were significantly decreased compared to WT 2.

For nuclear perimeter at 6 kPa, only DMD 2 was significantly decreased compared to both DMD 1 and WT 2, with no changes between any cell lines and WT 1 (WT 1, 40.5 ± 16.4 µm; WT 2, 45.9 ± 10.6 µm; DMD 1, 43.7 ± 10.3 µm; DMD 2, 38.9 ± 10.2 µm). At 130 kPa, WT 2 nuclei had significantly increased perimeter compared to all other cell lines with no other changes between cell lines observed (WT 1, 41.9 ± 8.0 µm; WT 2, 50.0 ± 11.3 µm; DMD 1, 41.7 ± 10.2 µm; DMD 2, 38.5 ± 11.6 µm).

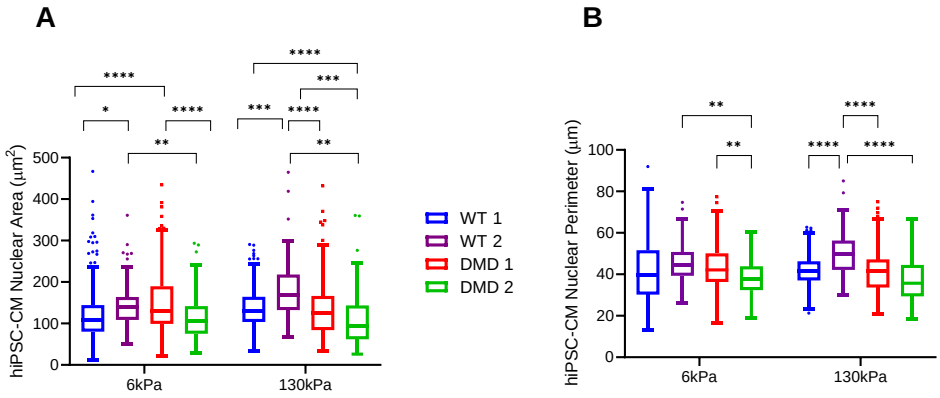

Figure 4.9: Comparison of Nuclear Morphology between hiPSC Cell Lines. *A) nuclear area was significantly altered at both 6 kPa and 130 kPa, in particular WT 2 appeared to be larger. B) Nuclear perimeter. Fewer differences were observed here, however, WT 2 was significantly increased compared to both DMD 1 and DMD 2 nuclei. Data presented as Tukey boxplot and reported as mean ± S.D.; Mann-Whitney U test, p<0.05 considered statistically significant. N= 3 biological replicates; WT 1, 6 kPa vs 130 kPa n number of nuclei= 138 vs 178 nuclei; WT 2, 6 kPa vs 130 kPa, n= 47 vs 62 nuclei; DMD 1, 6 kPa vs 130 kPa, n= 225 vs 187 nuclei; DMD 2, 6 kPa vs 130 kPa, n= 104 vs 105 nuclei.*

The nuclear shape descriptors revealed extensive changes to hiPSC-CM nuclei in response to increasing the Young's modulus of the ECM. For WT cell lines, nuclei tended to respond by increasing their area, perimeter, and circularity, thus supporting the notion that the nuclei were able to mechanosense, and respond, to their environments, and that this was likely mediated via the cytoskeleton-LINC complex interface. In contrast, DMD cell lines tended to be opposite, and showed unchanged or decreased nuclear area, perimeter, and circularity in response to 130 kPa. These data support dystrophin as a contributor towards maintaining nuclear morphology and mechanotransduction in hiPSC-CMs. An important consideration at this point is to note that nuclear volume was not

examined, which may confound interpretation of any true distinctions between the cell lines.

4.3 Nuclear Localisation of the Mechanosensitive Co-transcriptional Activator YAP Responds to Increased Substrate Stiffness in DMD 1 but not in WT 1

YAP is a well characterised mechanosensitive transcriptional co-activator[384]. Binding to TEAD within the nucleus, YAP conducts expression of genes associated with proliferation[3], embryogenesis[385], focal adhesions[386], and cytoskeletal components- including the DGC protein, *SGCD*[387].

Several groups have reported interesting changes in YAP localisation in relation to dystrophin and the DGC. Morikawa[3] showed that WT mice had decreased nuclear localisation of YAP compared to double knockout *mdx* and *Salvador* (Salvador is an upstream negative regulator of YAP). Moreover, co-immunoprecipitation assays revealed direct interaction between the PPxY domain of α-DG and YAP[3]. Moreover, it has been shown by several other groups that nuclear YAP localisation increases on stiffer substrates, thought to be mediated by more readily accessible nuclear pore complexes and the actin cytoskeleton[384]. These reports, in conjunction to my findings in the preceding section, led me to hypothesise that YAP may be differentially localised, and thus affect mechanosensitive gene regulation, in DMD 1 hiPSC-CMs (Figure 4.10).

Using fluorescence intensity, I examined the nuclear to cytoplasmic ratio for YAP on either 6 kPa or 130 kPa substrate. On 6 kPa, YAP nuclear localisation was significantly decreased in DMD 1 compared to WT 1 (6.1 ± 4.5 A.U. vs 4.4 ± 4.1 A.U.) but was not changed at 130 kPa. Interestingly, I observed no change in YAP localisation between 6 kPa and 130 kPa for either WT 1 or

DMD 1 hiPSC-CMs (WT 1 6 kPa vs 130 kPa: 6.1 ± 4.5 A.U. vs 5.1 ± 2.9 A.U.; DMD 1 6 kPa vs 130 kPa: 4.4 ± 4.1 vs 4.8 ± 3.2 A.U.).

These data indicated that YAP nuclear localisation is affected by the absence of dystrophin at 6 kPa but not at 130 kPa. This is consistent with the 6 kPa data and indicates a role of dystrophin in regulating YAP localisation. It further supports the notion that YAP localisation is mechanosensitive.

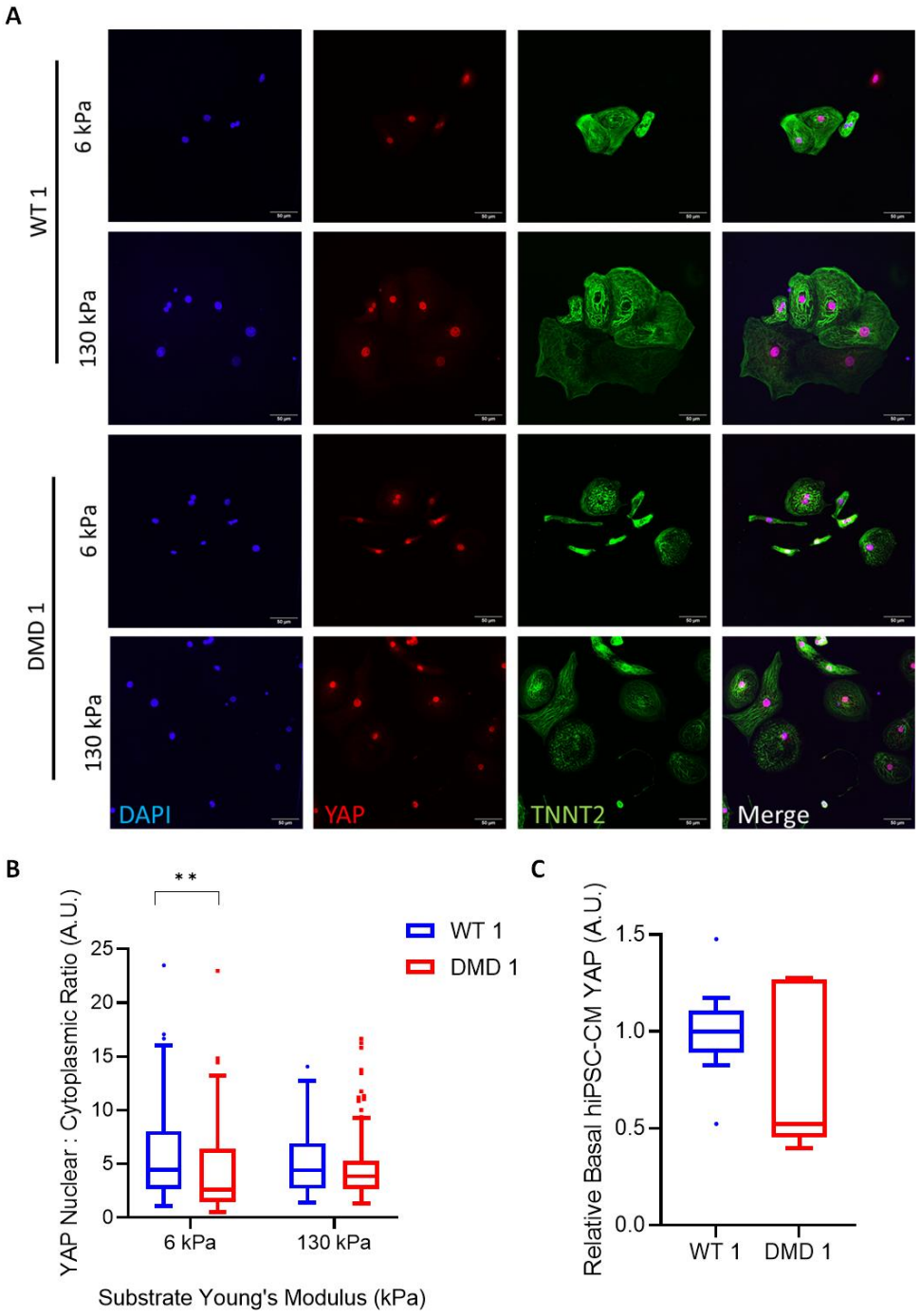

Figure 4.10: Nuclear YAP Localisation, but not Gene Expression, in DMD 1 is Decreased Compared to WT 1. A) *WT 1 and DMD 1 hiPSC-CMs were plated onto either a 6 kPa or 130 kPa laminin coated PDMS and quantified by examining the nuclear to cytoplasmic ratio.* ***B)***

quantification of the nuclear to cytoplasmic localisation of YAP in WT 1 and DMD 1. Nuclear localisation was significantly decreased in DMD 1 on a 6 kPa substrate elasticity but not 130 kPa. ***C)*** *Baseline YAP mRNA expression was determined using RT-qPCR. For* ***A*** *and* ***B*** *N= 3 biological replicates (except for WT 1 130 kPa where N= 2), WT 1, 6 kPa vs 130 kPa, n number of cells= 62 vs 44 hiPSC-CMs; DMD 1, 6 kPa vs 130 kPa, n= 76 vs 61. Scale bar= 50 µm. Data are presented as mean ± S.D; Two-way ANOVA with Bonferroni's multiple comparisons post-hoc test, p<0.05 was considered significant. For* ***C****, N=3 biological replicates; Data presented as Tukey box plot and reported as mean ± S.D.; Mann-Whitney U test, p<0.05 was considered significant.*

Leveraging RT-qPCR, I examined baseline YAP mRNA expression and observed no difference between WT 1 and DMD 1 (WT 1 vs DMD 1, 1.0 ± 0.24 A.U. vs 1.2 ± 1.7 A.U.). This suggests that gene expression of YAP is unaffected by a lack of dystrophin but, rather, its subcellular localisation is altered.

4.4 Assessment of Actin Cytoskeleton and Sarcomeres of WT 1 and DMD 1 hiPSC-CMs in Response to Differential ECM Young's Moduli

The actin cytoskeleton is integral to the overall architecture of the cell, critical for mechanotransduction, and is an instrumental constituent of the cardiac sarcomere. The sarcomere is the highly specialised contractile unit of hiPSC-CMs consisting of more than 200 known proteins and is responsible for generating both active and passive tension forces[49]. Indeed, generation of active force, via actomyosin, actuates cross-bridge cycling and is responsible for the tensile forces against which microtubules resist.

The Frank-Starling law of the heart describes the proportional relationship between sarcomere length and inotropy [49]. Here, I hypothesised that DMD

hiPSC-CMs would have altered cardiac sarcomeres as well as an altered actin cytoskeleton, that would be apparent at either 6 kPa or 130 kPa.

Comparison between WT 1 and DMD 1 sarcomere length was performed on phalloidin immunostained hiPSC-CMs with clearly delineated sarcomeric banding using Image J (Figure 4.11A and Figure 4.11B). Sarcomeres from WT 1 were significantly longer compared to DMD 1 at both 6 kPa and 130 kPa (WT 1 vs DMD 1 6 kPa, 1.94 ± 0.25 µm vs 1.69 ± 0.32 µm; 130 kPa, 1.98 ± 0.25 µm vs 1.78 ± 0.21 µm). There was no observable change between 6 kPa or 130 kPa for either WT 1 or DMD 1. These observations are indicative of defective sarcomere architecture in DMD 1 that may contribute to decreased force generation that has been previously reported for DMD[388].

In addition to sarcomere length, organisation of the actin cytoskeleton was assessed using Orientation J's coherency function (from ImageJ FIJI). Coherency bounds values between 0 and 1 where 1 indicates a highly organised, anisotropic structure, and 0 indicates a disorganised and isotropic structure. Coherency for WT 1 hiPSC-CMs was observed to be significantly increased compared to DMD 1, suggesting greater orientation and organisation in WT 1 on both a 6 kPa and 130 kPa (WT 1 vs DMD 1 6 kPa, 0.17 ± 0.15 A.U. vs 0.090 ± 0.07 A.U.; 130 kPa, 0.13 ± 0.11 A.U. vs 0.078 ± 0.068 A.U.). This data supports significant disorganisation to the actin cytoskeleton in DMD 1 hiPSC-CMs (Figure 4.11A and Figure 4.11C).

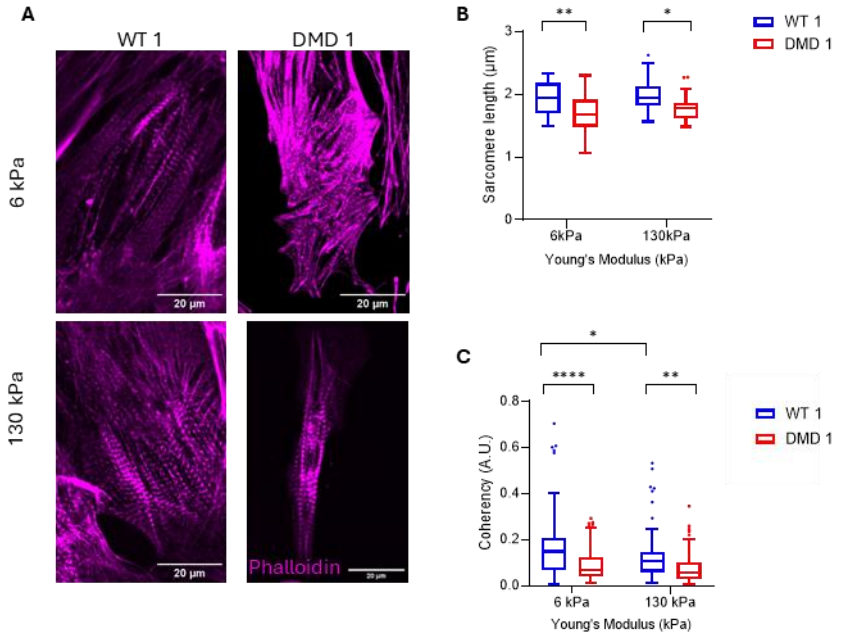

Figure 4.11: Sarcomeric and Actin Cytoskeletal Architecture were Significantly Altered in DMD 1 hiPSC-CMs Compared to WT 1. A) *Phalloidin immunofluorescence revealed altered sarcomeric and actin architecture in DMD 1, notably at 6 kPa. Note that WT 1 appears highly oriented in contrast to DMD 1 hiPSC-CMs.* ***B)*** *Quantification of sarcomere length revealed a significant decrease in DMD 1 hiPSC-CMs compared to WT 1 at both 6 kPa and 130 kPa.* ***C)*** *Coherency, a measure of orientation, where 1 represents a highly oriented and anisotropic structure and 0 represents a highly disoriented and isotropic structure, revealed the actin cytoskeleton in DMD 1 to be significantly less oriented compared to WT 1. Data are presented as Tukey boxplots but are reported as mean ± S.D. in text, analysed using Two-way ANOVA with Bonferroni's post-hoc test, $p<0.05$ was considered significant. N= 3 biological repeats; Sarcomeres analysed: WT 1 6 kPa vs 130 kPa, 409 vs 620 from 20 and 30 cells respectively; DMD 1 6 kPa vs 130 kPa, 605 vs 599 sarcomeres from 29 and 28 hiPSC-CMs respectively. WT 1 6 kPa vs 130 kPa: 77 vs 69; DMD 1 6 kPa vs 130 kPa: 87 vs 80 hiPSC-CMs.*

4.5 Examination of Pharmacologically Modifying the Cytoskeleton in Relation to Changes in the Young's Modulus of the ECM

Given that the cellular and nuclear morphology, as well as nuclear localisation of YAP were significantly altered in DMD compared to WT hiPSC-CMs, I wanted to further investigate, and to elucidate a putative mechanism, for the propagation of the mechanical force transduction in relation to dystrophin. Both the actin and microtubule cytoskeleton are integral components mediating mechanotransduction bidirectionally, to and from the ECM. As such, I used several known pharmacological agents to either stabilise or disrupt, either the actin or microtubular cytoskeleton. Based on the literature, dosages were selected and a time-series looking at the effect of the drugs was carried out and assessed using immunofluorescence and confocal microscopy in neonatal rat cardiomyocytes.

4.5.1 Destabilising the Actin Cytoskeleton: Cytochalasin D Disrupts Cellular and Nuclear Morphology in both WT 1 and DMD 1 hiPSC-CMs

Initially, I examined the actin cytoskeleton, and to do so utilised the well-known actin disruptor, cytochalasin D. Cytochalasin D inhibits actin polymerisation thus acting overall to disrupt the actin architecture. I hypothesised that cytochalasin D would disrupt the WT 1 hiPSC-CMs whilst having a minimal impact on DMD 1. Both WT 1 and DMD 1 were incubated with 1 µM cytochalasin D at 37^{o}C for 30 min prior to wash-out, fixation, and subsequent analysis.

Cytochalasin D caused a significant decrease of cell area (Figure 4.12A) and perimeter for WT 1 on the 130 kPa substrate (Area: 130 kPa no drug vs

cytochalasin D, 4441.8 ± 3302.6 μm^2 vs 2735.3 ± 1864.7 μm^2; Perimeter: 255.6 ± 103.3 µm vs 212.7 ± 62.3 µm). The effect of cytochalasin D on actin's architecture was not observed on the 6 kPa substrate.

In contrast to WT 1, cell area was not significantly changed by cytochalasin D on 6 kPa or 130 kPa in DMD 1 (Figure 4.12B) (3701.2 ± 3562.8 μm^2 vs 4338.3 ± 3427.2 μm^2 and 3425.4 ± 2745.4 μm^2 vs 2435.1 ± 2012.8 μm^2, respectively). However, a significant decrease in the cell perimeter was observed on 130 kPa in the presence of cytochalasin D (251.9 ± 123.7 µm vs 188.8 ± 72.7 µm).

These data indicated that the actin cytoskeleton was required for mechanosensing, especially on the fibrotic Young's modulus, as disruption caused significant decreases in both cell area and perimeter for WT 1. Given that the DMD 1 hiPSC-CMs did not show a change in cell area coupled to a modest decrease in perimeter suggests an already present disruption to the actin cytoskeleton, or an inability to communicate the mechanical signal within the cell.

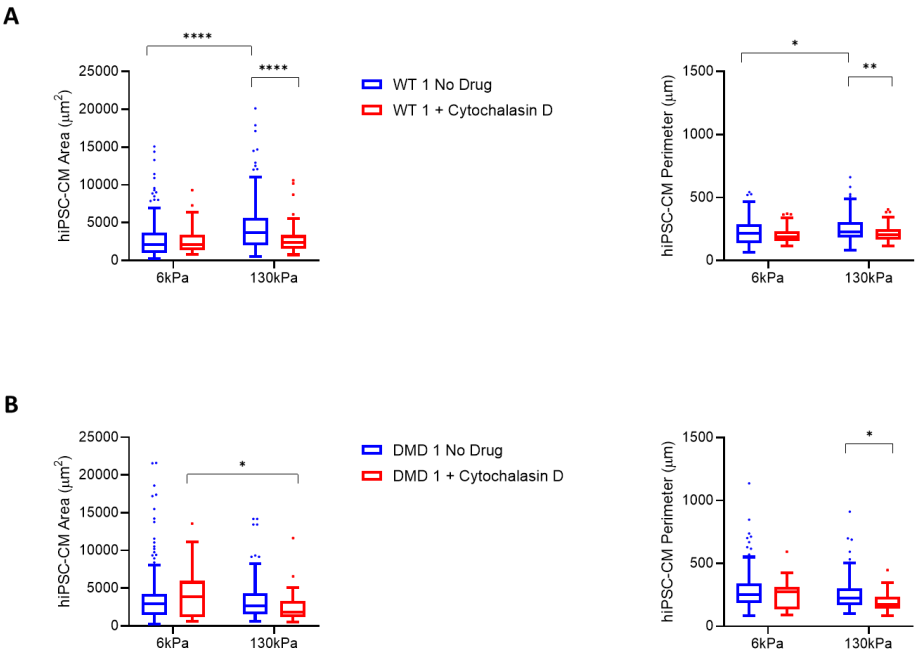

Figure 4.12: 1 µM Cytochalasin D Significantly Disrupted the Cellular Phenotype of WT 1 but not DMD 1 on 130 kPa. A) *WT 1 and* ***B)*** *DMD 1 hiPSC-CM morphological descriptors on either 6 kPa or 130 kPa PDMS substrate with 1 µM cytochalasin D for 30 min at 37°C. Representative images are shown in Figure 4.14. Data presented as Tukey boxplot and reported mean ± S.D.; Two-way ANOVA with Bonferroni's multiple comparisons post-hoc test, p<0.05 considered statistically significant. N= 2 biological replicates; WT 1 no drug 6 kPa vs 130 kPa, n number of cells= 120 vs 148 hiPSC-CMs; WT 1 + cytochalasin D 6 kPa vs 130 kPa, n= 72 vs 73 hiPSC-CMs; DMD 1 no drug 6 kPa vs 130 kPa, n= 180 vs 143 hiPSC-CMs; DMD 1 + cytochalasin D 6 kPa vs 130 kPa, n= 40 vs 40 hiPSC-CMs.*

Cytochalasin D indicated that a connection between the dystrophin and actin influences cell morphology, and given the downstream connection to the LINC complex, I wanted to examine whether this affected nuclear morphology, and to explore the potential role of dystrophin here (Figure 4.13). The addition of cytochalasin D prevented an increase in nuclear area in WT 1, which was the case for untreated samples between 6 kPa and 130 kPa (cytochalasin D nuclear area; 130.9 ± 56.0 µm^2 vs 143.7 ± 50.0 µm^2),

suggesting that actin is a key mediator in regulating nuclear area and for propagating mechanical signals within the cell.

Surprisingly, cytochalasin D caused an increase in nuclear area in DMD 1 on 6 kPa (6 kPa untreated vs treated: 148.8 ± 70.2 μm^2 vs 174.2 ± 70.3 μm^2). The underlying mechanism for this was not entirely clear but may indicate a decrease in aligned actin fibre cables, thus less nuclear constriction. Similarly, no change between 6 kPa to 130 kPa in the presence of cytochalasin D was apparent.

Additionally, the nuclear circularity for WT 1 was increased by cytochalasin D on 6 kPa by 7%, showing a more rounded nuclear phenotype. Rounding of the nucleus may indicate a lack of aligned actin stress fibres that would be consistent with the action of cytochalasin D. Interestingly, no change in circularity between 6 kPa and 130 kPa was apparent for WT 1 (0.95 ± 0.05 A.U. vs 0.95 ± 0.04 A.U.). This further supported the notion that actin is important in communicating and regulating nuclear phenotype in response to altered Young's modulus of the ECM.

Importantly, disruption to actin did not affect the circularity in DMD 1 nuclei on either stiffness, again implying that dystrophin mediates this effect via actin.

The use of cytochalasin D revealed the importance that actin plays in propagating mechanical signals from the ECM to the nucleus. Moreover, it clarified the role that dystrophin has in potentiating this, which was expected as dystrophin has several actin binding domains. Additional nuclear shape descriptors are detailed in §A2.

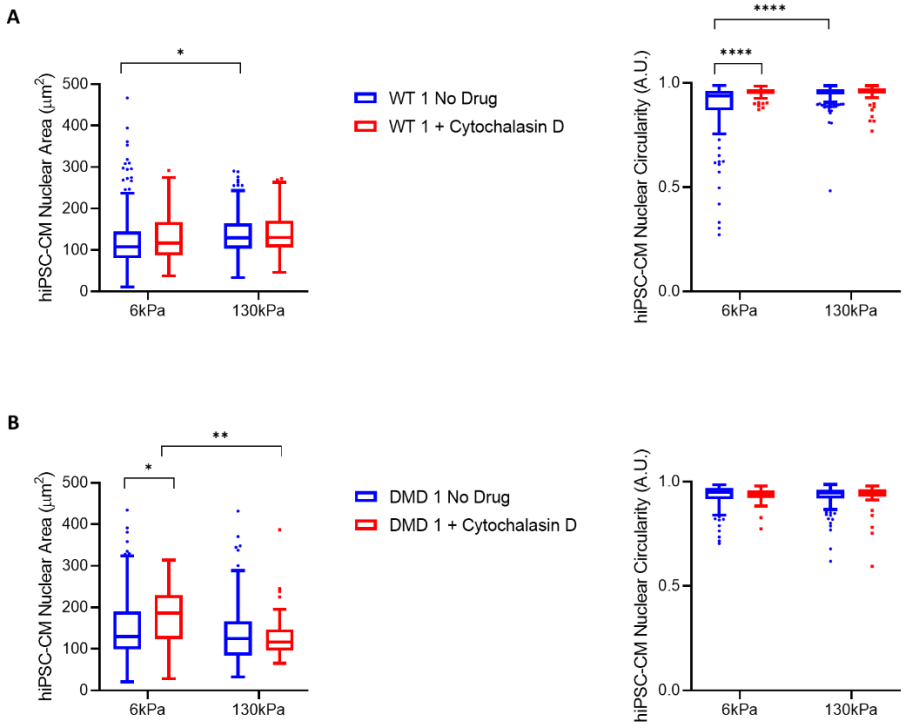

Figure 4.13: 1 µM Cytochalasin D Alters the Nuclear Phenotype in Response to Increasing Young's Modulus. *Nuclear area and nuclear circularity for* ***A)*** *WT 1 and* ***B)*** *DMD 1 hiPSC-CM cell lines in response to 1 µM cytochalasin for 30 min at 37°C. Representative nuclei are shown in Figure 4.14. Data are presented as Tukey boxplot and reported as mean ± S.D., Two-way ANOVA with Bonferroni's multiple comparison post-hoc test, $p<0.05$ was considered significant. N= 3 biological replicates (without drug); N= 2 (+ cytochalasin D); WT 1 no drug 6 kPa vs 130 kPa, n= 138 vs 178 nuclei; WT 1 + cytochalasin D 6 kPa vs 130 kPa, n= 80 vs 78; DMD 1 no drug 6 kPa vs 130 kPa, n= 226 vs 187; DMD 1 + cytochalasin D 6 kPa vs 130 kPa, n= 49 vs 50 nuclei.*

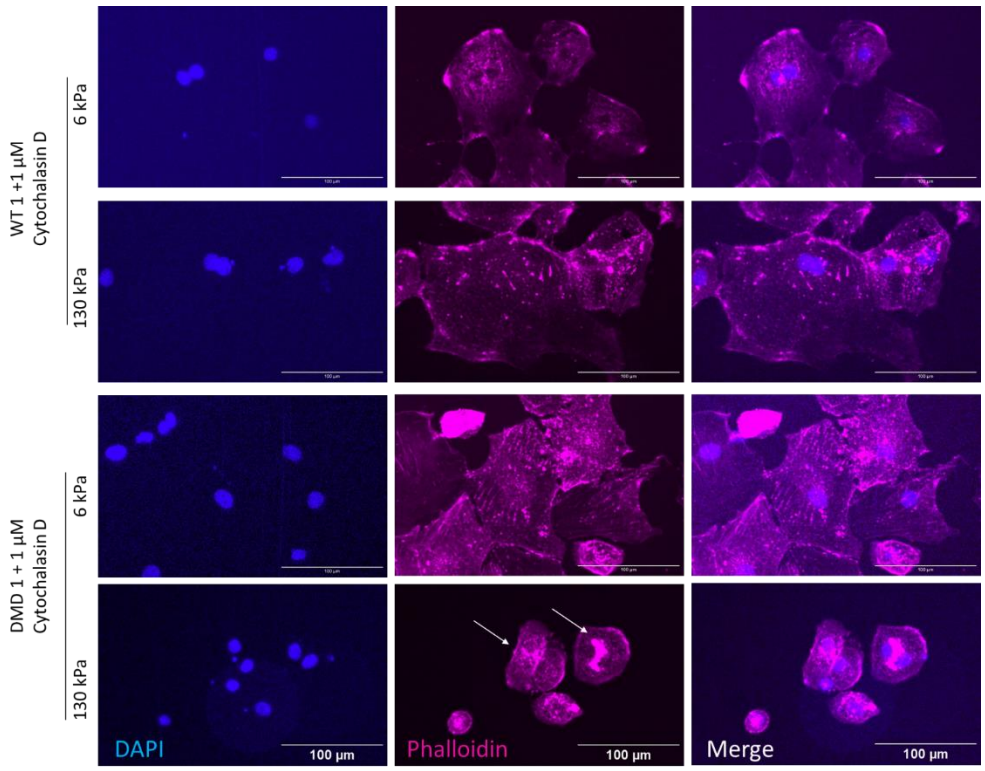

Figure 4.14: Representative Images of WT 1 and DMD 1 hiPSC-CMs Treated Using 1 µM Cytochalasin D on Either a 6 kPa or 130 kPa laminin coated PDMS Substrate. *Both WT 1 and DMD 1 hiPSC-CMs adjusted to laminin coated PDMS substrate for 5 days prior to the addition of 1 µM cytochalasin D for 30 min at 37°C. White arrows highlight the significantly smaller DMD 1 hiPSC-CMs on 130 kPa in response to the cytochalasin D treatment. Scale bar= 100 µm. N= 2 biological replicates.*

4.5.2 Stabilising the Actin Cytoskeleton: Jasplakinolide Failed to act as Expected and Appeared to Disrupt the Actin Cytoskeleton

I wanted to examine whether stabilising the actin cytoskeleton in DMD 1 would 'rescue' the phenotype, as determined by cell and nuclear morphology. To do this, I used the actin stabilising drug, jasplakinolide. However, application of 1 µM jasplakinolide for 45 min at 37 °C appeared to have the undesired effect by disrupting the actin cytoskeleton in both WT 1 and DMD 1 hiPSC-CMs (Figure 4.15).

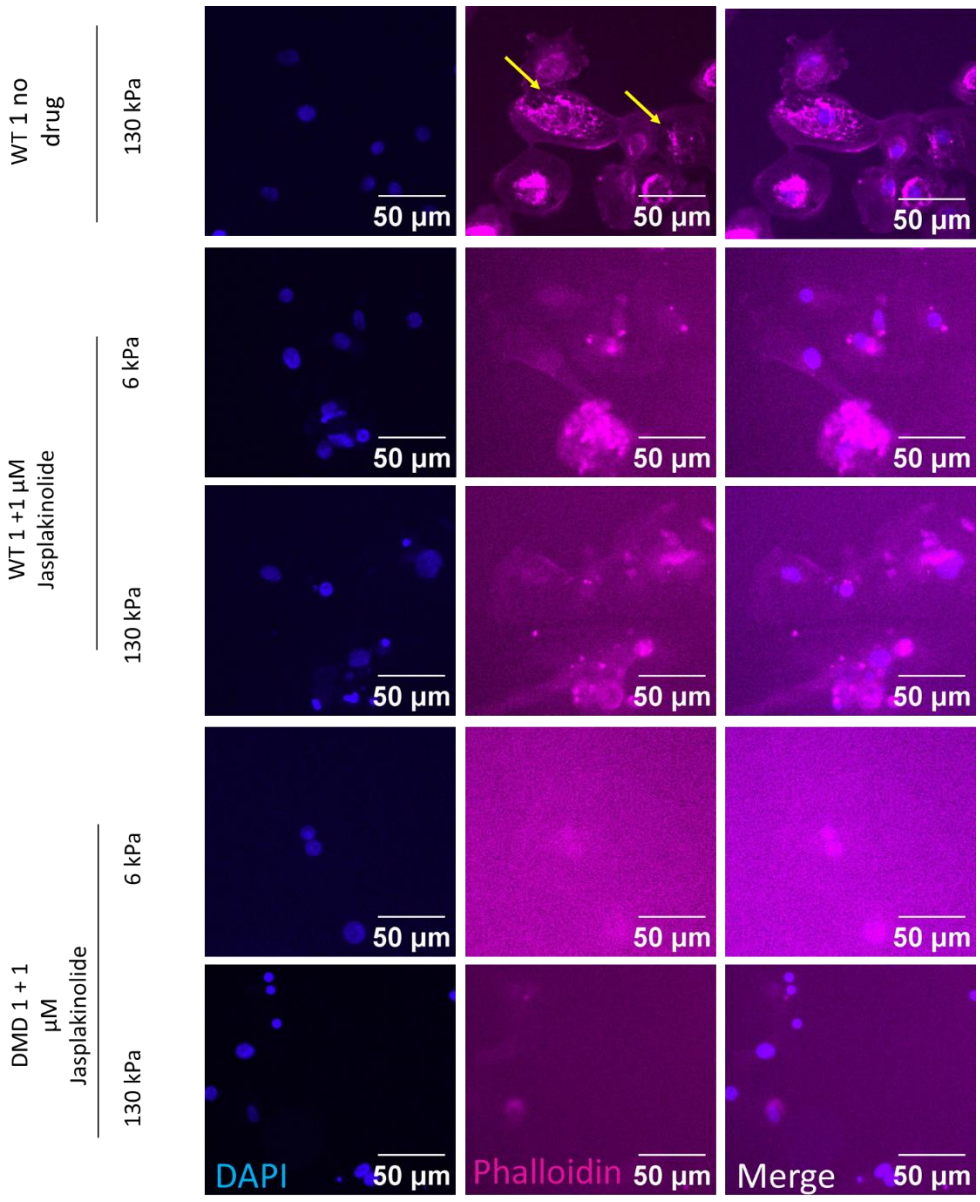

Figure 4.15: 1 µM Jasplakinolide Unexpectedly Disrupted the Actin Cytoskeleton in both WT 1 and DMD 1 hiPSC-CMs. *Representative images showing the effect of 1 µM jasplakinolide incubation for 45 min at 37°C. Jasplakinolide was originally used to examine the effect of stabilising the actin cytoskeleton, however, unexpectedly disrupted it in both WT 1 and DMD 1 hiPSC-CM cell lines. Untreated WT 1 on 130 kPa were shown to have intact sarcomeric actin. Scale bar= 50 µm, N= 2 biological replicates.*

Jasplakinolide is known to have a cytotoxic effect on hiPSC-CMs although this typically occurs at higher dosages and time-frames than that used here. Intriguingly, jasplakinolide and phalloidin compete at the same binding region on F-actin. As such, it is not possible to draw conclusions from the jasplakinolide experiments here regards actin stabilisation in DMD hiPSC-CMs.

4.5.3 Stabilising and Destabilising the Microtubule Cytoskeleton using Taxol and Vinblastine Respectively: Destabilising the Microtubule Cytoskeleton using 1 µM Vinblastine did not affect Cell Morphology but Significantly Altered Nuclear Morphology of WT 1 hiPSC-CMs

Vinblastine binds to the exterior ends of microtubules acting to depolymerise and destabilise the microtubule polymers, and thus overall microtubule framework within the cell. The rationale behind destabilising the microtubule network was to recapitulate the DMD phenotype in the WT 1 hiPSC-CMs.

The addition of vinblastine did not alter the cellular morphology of WT 1 hiPSC-CMs (Figure 4.16).

hiPSC-CM cell area for WT 1 did not significantly differ in the presence of 1 µM vinblastine on either a 6 kPa (untreated vs treated, 2788.1 ± 2552.4 μm^2 vs 2772.6 ± 1828.7 μm^2) or a 130 kPa (untreated vs treated, 4441.8 ± 3302.6 μm^2 vs 3997.6 ± 2332.4 μm^2) laminin coated PDMS substrate. A similar trend was observed for the cell perimeter in WT 1 (untreated vs treated, 6 kPa: 224.7 ± 109.1 µm vs 218.9 ± 80.1 µm; 130 kPa: 255.6 ± 103.3 µm vs 262.7 ± 74.5 µm) and these data support the notion that disruption to the microtubule cytoskeleton is less critical to regulating the

cell morphology compared to the actin cytoskeleton, as in the case of cytochalasin D described in the preceding section (§4.5).

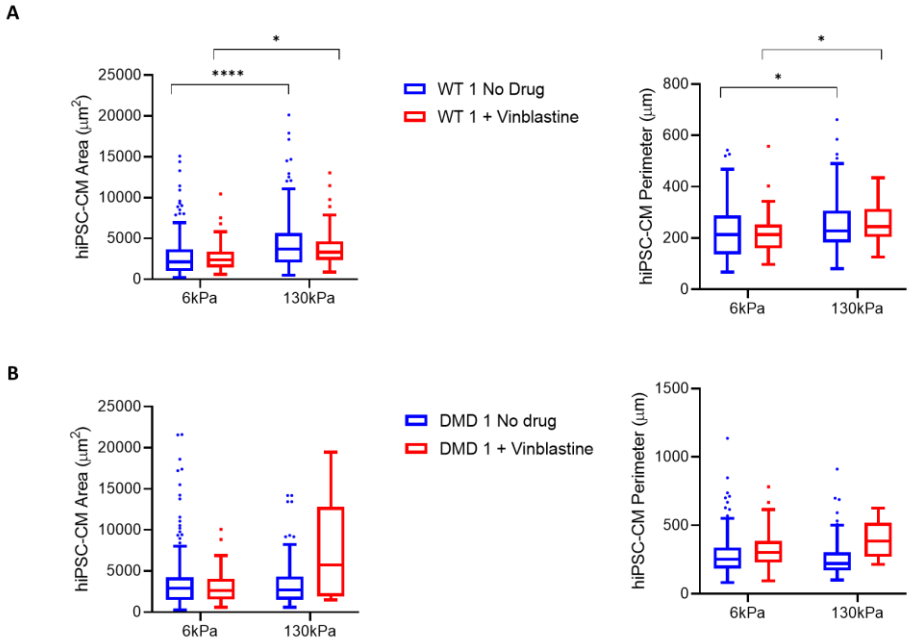

Figure 4.16: Vinblastine did not Alter the Cell Morphology of hiPSC-CMs. *WT 1* ***A****) and DMD 1* ***B****) hiPSC-CMs were incubated with 1 µM vinblastine for 1 hr at 37°C. Vinblastine did not alter the cell area or perimeter of hiPSC-CMs. Representative images are shown in Figure 4.11. Data are presented as Tukey boxplot and reported as mean ± S.D., Two-way ANOVA with Bonferroni's post-hoc test, p< 0.05 was considered significant. WT 1, N biological replicates= 2 for vinblastine; N= 3 for no drug. WT 1 no drug, 6 kPa vs 130 kPa, n number of cells= 120 vs 148 hiPSC-CMs; vinblastine, 6 kPa vs 130 kPa, n= 56 vs 73 hiPSC-CMs; DMD 1 N= 3 for no drug, 6 kPa vs 130 kPa, n= 180 vs 143; N= 2 for 6 kPa but N= 1 for 130 kPa (as such no statistics were carried out), 6 kPa vs 130 kPa, n= 31 vs 5 hiPSC-CMs.*

Due to the small *n*-number of DMD 1 hiPSC-CMs in the 130 kPa and 1 µM group, no statistics were carried out. Largely, the small *n*-number was due to insufficient DMD 1 hiPSC-CMs surviving the experiment. This was unlikely due to the vinblastine as evidenced by the survival of these cells on the 6 kPa substrate and attributable to some alternative influence. As such, no conclusions can be attributed to the disruption of the microtubule

cytoskeleton in DMD, however, there appeared to be very little difference in cell morphology on a 6 kPa substrate in the presence of vinblastine, which would be consistent with the data for the WT 1 hiPSC-CMs.

With this caveat in mind, there appeared to be no distinction in DMD 1 hiPSC-CM cell area between untreated and vinblastine at 6 kPa (3701.2 ± 3562.8 μm^2 vs 3188.7 ± 2244.8 μm^2) and the perimeter (284.1 ± 149.4 µm vs 333.0 ± 150.2 µm). It is vital to keep in mind that no statistics were carried out for DMD 1 vinblastine data, and these are merely the observations made.

On the other hand, vinblastine had a profound effect on nuclear morphology (Figure 4.17 and Figure 4.18) particularly in the WT 1 hiPSC-CMs.

All nuclear shape descriptors for WT 1 were significantly increased in the presence of vinblastine. The nuclear area significantly increased by 34% on 6 kPa (untreated vs treated 122.3 ± 62.6 μm^2 vs 164.1 ± 53.9 μm^2) and by 31% (untreated vs treated 136.7 ± 51.2 μm^2 vs 178.3 ± 78.1 μm^2) on 130 kPa. Moreover, the perimeter increased by 15% on 6 kPa (40.5 ± 16.4 µm vs 46.6 ± 8.3 µm) and 12% on 130 kPa (41.9 ± 8.1 µm vs 47.4 ± 9.4 µm) and the circularity significantly increased in the presence of vinblastine at 6 kPa (0.88 ± 0.1 A.U. vs 0.93 ± 0.05 A.U.). These data support the role that microtubules have in regulating the nuclear morphology. Previous reports have shown that microtubules counteract lamin A/C and compress the nucleus, thereby maintaining nuclear morphology[389]. Therefore, in the scenario where microtubules are destabilised, enlargement of the nucleus is expected to be observed.

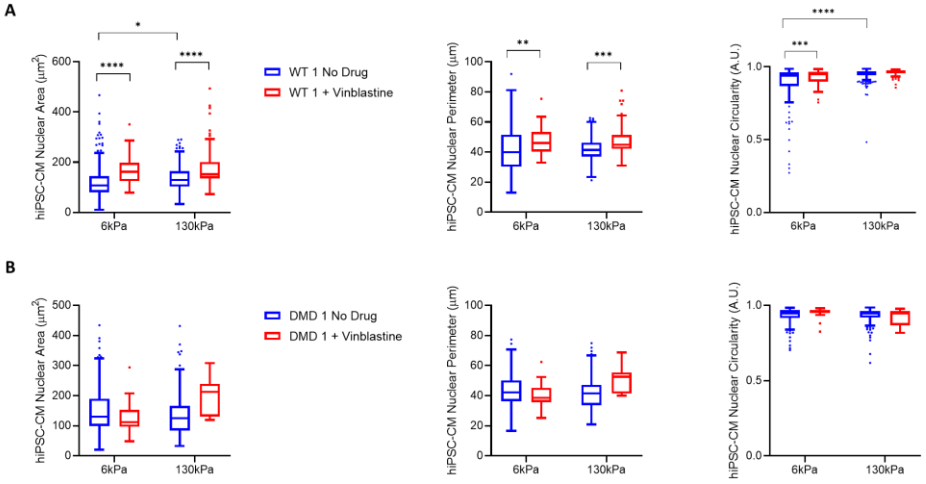

Figure 4.17: Vinblastine Significantly Alters Nuclear Morphology in WT 1 hiPSC-CMs but not DMD 1. *1 µM of vinblastine was incubated for 1 hr at 37°C for WT 1* ***A****) and DMD 1* ***B****) hiPSC-CMs. Vinblastine significantly increased all nuclear morphological descriptors in WT 1 hiPSC-CMs, supporting the notion that microtubules are important regulators of nuclear morphology. Representative images are shown in Figure 4.12. Data are presented as Tukey boxplot and reported as mean ± S.D., Two-way ANOVA with Bonferroni's post-hoc test, p< 0.05 was considered significant. WT 1, N biological replicates= 2 for vinblastine; N= 3 for no drug. WT 1 no drug, 6 kPa vs 130 kPa, n number of nuclei= 138 vs 178 hiPSC-CMs; vinblastine, 6 kPa vs 130 kPa, n= 60 vs 81 hiPSC-CMs; DMD 1 N= 3 for no drug, 6 kPa vs 130 kPa, n= 225 vs 187; N= 2 for 6 kPa but N= 1 for 130 kPa (as such no statistics were carried out), 6 kPa vs 130 kPa, n= 35 vs 7 hiPSC-CMs.*

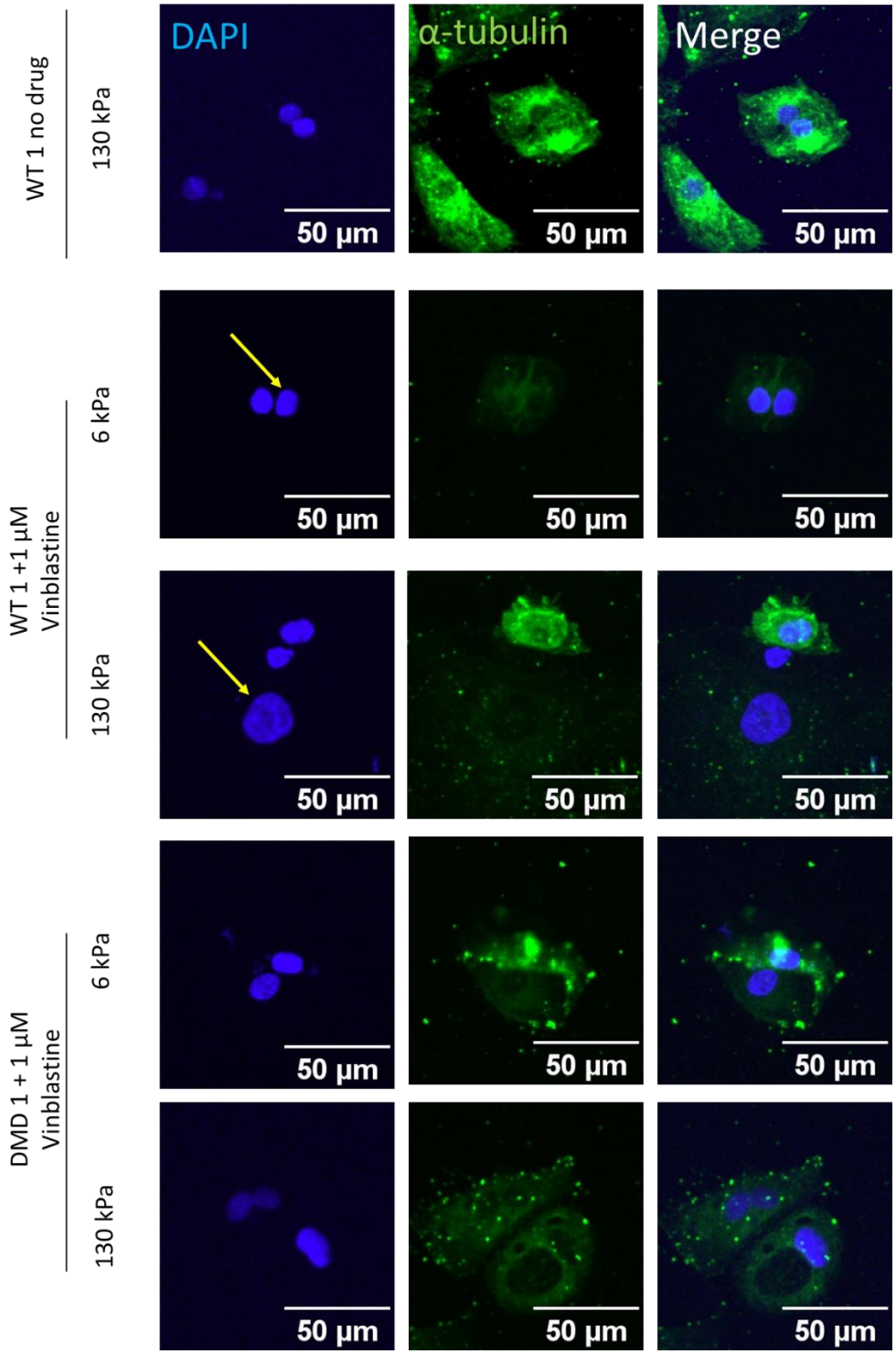

Figure 4.18: Disruption to the Microtubular Lattice Resulted in Altered Nuclear Morphology in WT 1 hiPSC-CMs using 1 µM vinblastine. *Vinblastine produced no significant changes to cell morphology of hiPSC-CMs. However, disruption to microtubules*

significantly increased the nuclear area, perimeter, and circularity of WT 1, particularly in response to 130 kPa laminin coated PDMS substrate. The yellow arrows indicate representative nuclear enlargement. Due to the small n number used for DMD 1 no definitive statements can be attributed to the impact of vinblastine here. WT 1, N= 2 for vinblastine; N= 3 for no drug. DMD 1 N= 3 for no drug; N= 1 for 130 kPa.

Due to the small *n*-number for DMD 1 on at 130 kPa treated with vinblastine, no statistics or definitive conclusions can be attributed to the effect of destabilising the microtubule lattice. However, there are two interesting comments that may be made in light of the preceding caveat: i) treatment with vinblastine on 6 kPa stiffness caused a small reduction in nuclear morphology, ii) on 130 kPa substrate, the contrary was true, and nuclear morphology increased. In any case, data relating to DMD 1 in the presence of vinblastine should be viewed as extremely preliminary.

4.5.4 Stabilising the Microtubule Cytoskeleton using 10 µM Taxol Significantly Increased Cellular and Nuclear morphology in WT 1 hiPSC-CMs

Taxol acts to stabilise microtubules by binding to β-tubulin ends. Ultimately, taxol is cytotoxic and is used clinically in the treatment against cancer, as the long-term stabilisation of the microtubule cytoskeleton disrupts its homeostatic cellular functions. As before, my rationale was to establish the effect that stabilising the microtubule cytoskeleton would have, notably on the DMD 1 hiPSC-CMs- to examine if I could make DMD 1 recapitulate the WT 1 phenotype.

Stabilisation of microtubules had three main interesting effects, i) significantly increased cell morphological parameters for WT 1 on a 6 kPa substrate. The percentage increase was 50%, 16%, and 21% between untreated and treated WT 1 for cell area (untreated vs treated: 2788.1 ±

2552.4 μm^2 vs 4190.7 ± 2296.3 μm^2), perimeter (untreated vs treated: 224.7 ± 109.1 µm vs 259.6 ± 81.7 µm), and circularity respectively (untreated vs treated: 0.62 ± 0.19 A.U. vs 0.75 ± 0.13 A.U.) ii) significantly decreased cell morphological parameters for WT 1 on a 130 kPa substrate.

The percentage decrease was 55% (4441.8 ± 3302.6 μm^2 vs 1994.8 ± 2105.9 μm^2) 32% (255.6 ± 103.3 µm vs 173.9 ± 58.3 µm), and 12% (0.68 ± 0.18 A.U. vs 0.76 ± 0.14 A.U.) at 130 kPa for cell area, perimeter, and circularity respectively; and iii) For DMD 1 hiPSC-CMs each parameter, with the exception of circularity (0.73 ± 0.19 A.U. vs 0.79 ± 0.14 A.U.), actuated a significantly decreased cell morphology and cell perimeter by 63% and 47% at 6 kPa between untreated and treated. At 130 kPa, DMD 1 hiPSC-CMs area and perimeter both decreased by 22% (Area: 3425.4 ± 2745.4 μm^2 vs 2678.2 ± 2384.3 μm^2; Perimeter: 251.9 ± 123.7 µm vs 195.6 ± 81.0 µm). The 22% decrease displayed by the perimeter was significant, whereas the decrease for cell area was not (Figure 4.19). Interestingly, microtubule bundles were more visible via immunofluorescence in WT 1 hiPSC-CMs compared to DMD 1 hiPSC-CMs, potentially indicating an inherent disruption to the microtubule cytoskeletal lattice in DMD mutant hiPSC-CMs (Figure 4.20).

Together these data indicate that stabilisation of the microtubule network leads to a differential effect that is dependent upon stiffness of the substrate for WT 1. Stabilisation of microtubules on a 6 kPa substrate led to a significant increase in cell area and perimeter, whilst on 130 kPa there was a significant decrease. The underlying mechanism for this is stiffness dependent difference is not well understood.

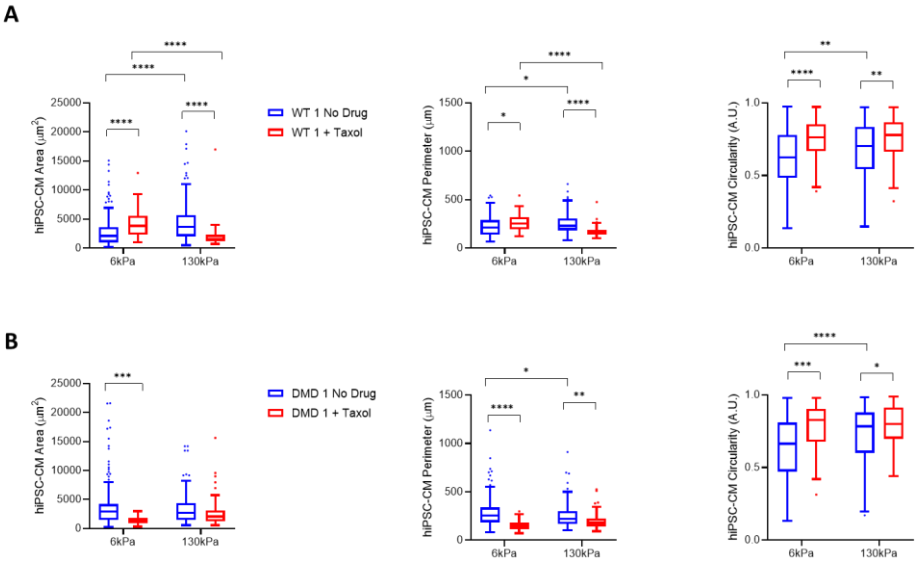

Figure 4.19: Stabilisation of Microtubules Using 10 µM Taxol Significantly Altered Cell Morphology in WT 1 and DMD 1 hiPSC-CMs. *WT 1* ***A)*** *and DMD 1* ***B)*** *hiPSC-CMs were treated using 10 µM taxol for 2 hr at 37°C to examine the effect of stabilising the microtubule cytoskeleton. All morphological descriptors were significantly altered in WT 1. In particular, microtubule stabilisation caused increased cell area, perimeter, and circularity on a 6 kPa laminin coated PDMS substrate. Other than circularity, taxol resulted in decreased cell area and perimeter at 130 kPa for WT 1. In contrast, taxol was observed to decrease cell area and perimeter for DMD 1 at 6 kPa, with only the circularity increasing in the presence of taxol. Representative images are shown in Figure 4.14. Data are presented as Tukey boxplot and reported as mean ± S.D., Two-way ANOVA with Bonferroni's post-hoc test, $p<0.05$ was considered significant. WT 1, N biological replicates= 2 for taxol; N= 3 for no drug. WT 1 no drug, 6 kPa vs 130 kPa, n number of cells= 120 vs 148 hiPSC-CMs; taxol, 6 kPa vs 130 kPa, n= 114 vs 60 hiPSC-CMs; DMD 1 N= 3 for no drug, 6 kPa vs 130 kPa, n= 180 vs 143; taxol N= 2, 6 kPa vs 130 kPa, n= 28 vs 75 hiPSC-CMs.*

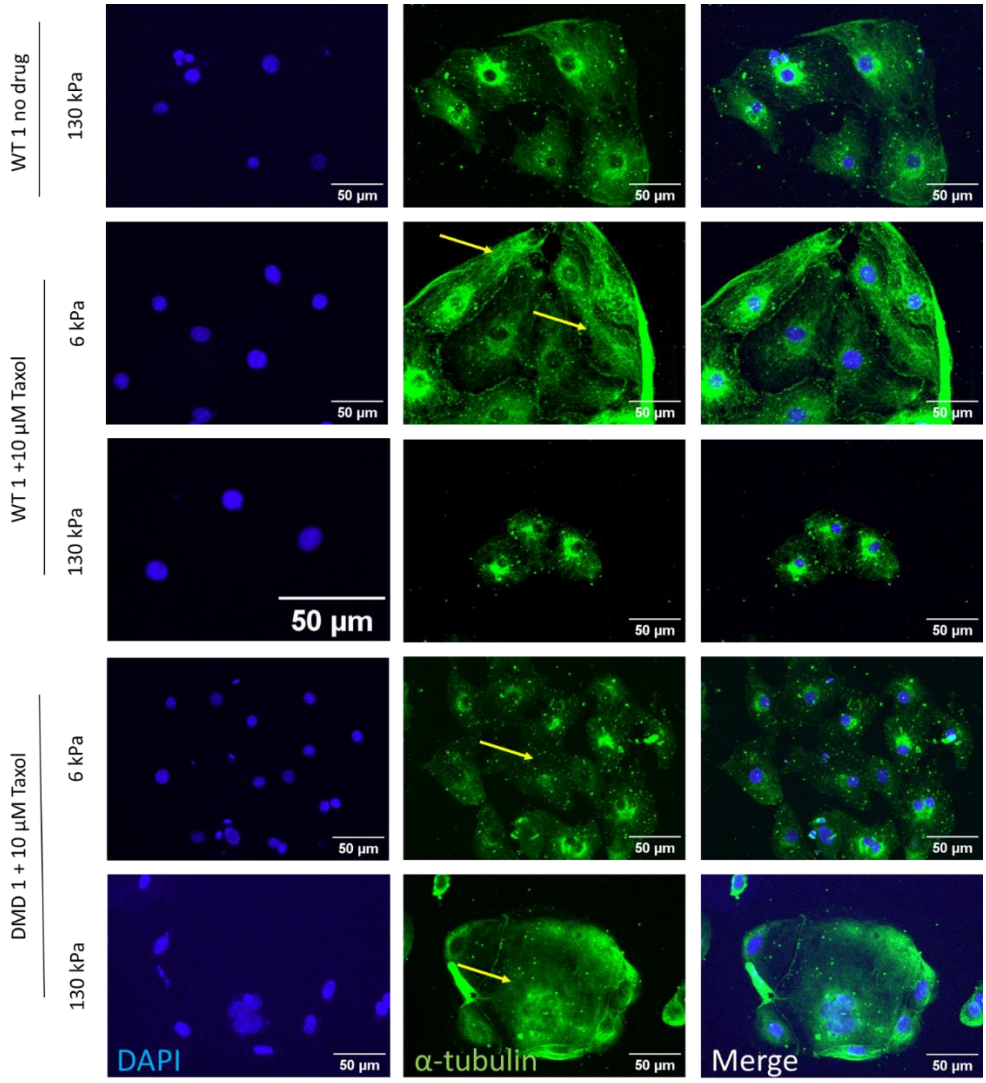

Figure 4.20: Taxol Promotes Stabilisation of Microtubules in WT 1 on a 6 kPa Substrate Resulting in Significantly Larger hiPSC-CMs. *WT 1 microtubule bundles are clearly visible (yellow arrows) whilst in DMD 1 hiPSC-CMs microtubules lack definition (yellow arrows lower panels). This suggests an inherent defect with microtubules in DMD 1. Moreover, WT 1 hiPSC-CMs were shown to enlarge in response to 10 µM taxol on a 6 kPa substrate, however this effect was contrary in DMD 1 hiPSC-CMs. On 130 kPa substrate, WT 1 hiPSC-CMs had decreased cell area and perimeter, although circularity increased. Nuclei underwent enlargement on a 6 kPa substrate for WT 1 hiPSC-CMs but this was not recapitulated in DMD 1. N= 2 biological replicates for taxol treatment; N= 3 for no treatment.*

The DMD 1 hiPSC-CMs responded similarly across stiffnesses to taxol with cell area and perimeter significantly decreasing on either a 6 kPa or 130 kPa substrate. This is consistent with previous reports showing this trend in cells[390]. This indicates that stabilisation of the microtubule cytoskeleton has role in regulating cell morphology in DMD.

The effect of microtubule stabilisation on WT 1 hiPSC-CM nuclei followed a similar trend as the cell morphology, with a significantly increased nuclear area (untreated vs treated: 122.3 ± 62.6 μm^2 vs 175.7 ± 61.8 μm^2) and perimeter (untreated vs treated: 40.5 ± 16.4 µm vs 47.8 ± 8.2 µm) on a 6 kPa substrate in response to taxol (Figure 4.21A). In contrast, on 130 kPa the nuclear area significantly decreased by 15% (136.7 ± 51.2 μm^2 vs 116.4 vs 37.6 μm^2) and by 8% in perimeter (41.9 ± 8.1 µm vs 38.7 ± 6.2 µm).

Interestingly, taxol affected DMD 1 nuclei contrariwise to WT 1 (Figure 4.21B). At 6 kPa, both the nuclear area (untreated vs treated: 148.8 ± 70.1 μm^2 vs 130.4 ± 46.1 μm^2), perimeter (43.7 ± 10.3 µm vs 41.1 ± 7.3 µm), and circularity (0.94 ± 0.05 A.U. vs 0.94 ± 0.04 A.U.) were unaffected by taxol. Intriguingly, whilst cultured on 130 kPa, there were significant increases observed for nuclear area (untreated vs treated 136.5 ± 67.7 μm^2 vs 173.7 ± 60.0 μm^2), perimeter (untreated vs treated 41.7 ± 10.2 µm vs 47.4 ± 7.9 µm), and circularity (0.93 ± 0.05 A.U. vs 0.95 ± 0.03 A.U.).

In sum, both the actin and microtubule cytoskeleton are central to governing cellular and nuclear morphology. Cytochalasin D strongly implicated the actin cytoskeleton and dystrophin as being required for regulating cell and nuclear morphology. Taxol further supported this notion. Sadly, the immunofluorescence for jasplakinolide failed and the *n* number for vinblastine were too small to draw inferences from these.

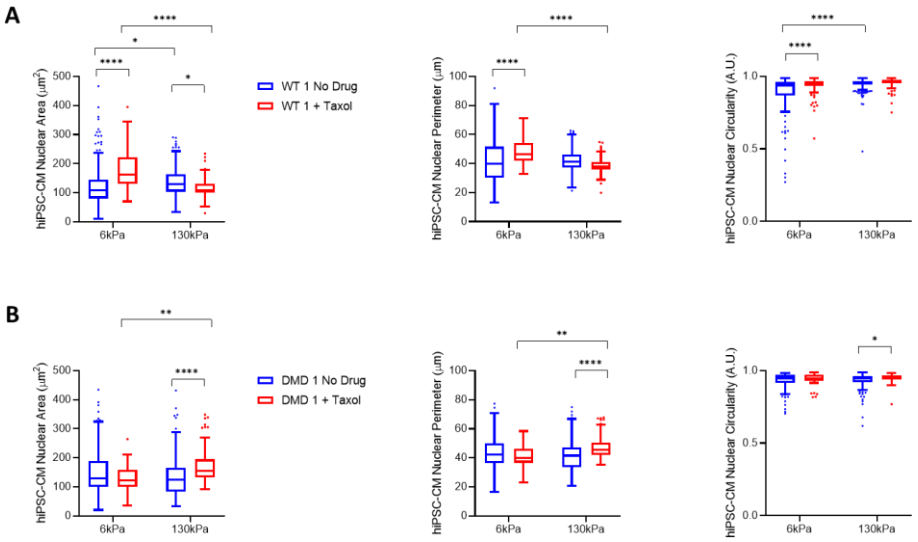

Figure 4.21: Nuclear Morphology was Altered in Response to 10 µM taxol on either a 6 kPa or 130 kPa laminin Substrate for both WT 1 and DMD 1 hiPSC-CMs. *hiPSC-CM nuclei from WT 1* ***A)*** *or DMD 1* ***B)*** *were characterised in response to 10 µM taxol for 2 hr at 37°C. On 6 kPa, WT 1 nuclei had a significantly increased nuclear area, perimeter, and circularity, whilst the opposite was found on 130 kPa. DMD 1 nuclei were not found to be different in response to taxol on 6 kPa but were significantly increased on the 130 kPa substrate. Representative images are shown in Figure 4.14. Data are presented as Tukey boxplot and reported as mean ± S.D., Two-way ANOVA with Bonferroni's post-hoc test, $p<0.05$ was considered significant. WT 1, N= 2 biological replicates for taxol; N= 3 for no drug. WT 1 no drug, 6 kPa vs 130 kPa, n number of nuclei= 138 vs 178 nuclei; taxol, 6 kPa vs 130 kPa, n= 134 vs 70 nuclei; DMD 1 N= 3 for no drug, 6 kPa vs 130 kPa, n= 225 vs 187; taxol N= 2, 6 kPa vs 130 kPa, n= 35 vs 79 nuclei.*

4.6 Nanoindentation as a Means for Determining the Young's Modulus of hiPSC-CMs

4.6.1 Determination of the Young's Modulus in hiPSC-CMs to Examine Cytoskeletal Function as well as Interrogating their Viscoelastic Properties via Dynamic Mechanical Analysis

Within cardiomyocytes, titin is the major contributor to the overall passive stiffness and prestress, with contributions provided by the actomyosin and microtubule networks. The cytoskeleton responds to alterations of the ECM that are transduced via FAs. I wanted to assess the impact on the Young's modulus of hiPSC-CMs in the absence of dystrophin, as is the case for DMD, as well as examine whether the Young's modulus was dependent on ECM substrate stiffness.

As before, hiPSC-CMs were plated onto laminin coated PDMS coverslips with a Young's modulus of either 6 kPa or 130 kPa stiffness and allowed to recover for 5 days prior to experimentation. At 6 kPa, the Young's modulus of WT 1 was significantly larger compared to DMD 1 (3.2 ± 2.7 kPa vs 1.9 ± 1.8 kPa) but was comparable to DMD 2 (3.2 ± 2.7 kPa vs 2.9 ± 2.91 kPa) (Figure 4.22).

Similarly, at 130 kPa the Young's modulus of WT 1 was significant larger compared to both DMD 1 (4.0 ± 3.1 kPa vs 1.5 ± 1.3 kPa) and DMD 2 (4.0 ± 3.1 kPa vs 2.4 ± 2.0 kPa). This suggests that the WT 1 hiPSC-CMs are rigidity sensing and adapting to the ECM, whereas the DMD mutants were unable to do so. No cell line displayed a significant increase in Young's modulus between 6 kPa and 130 kPa.These data support WT 1 mechanosensing the ECM and could adapt which was in contrast to DMD mutants. These data support the requirement of dystrophin for this phenomenon.

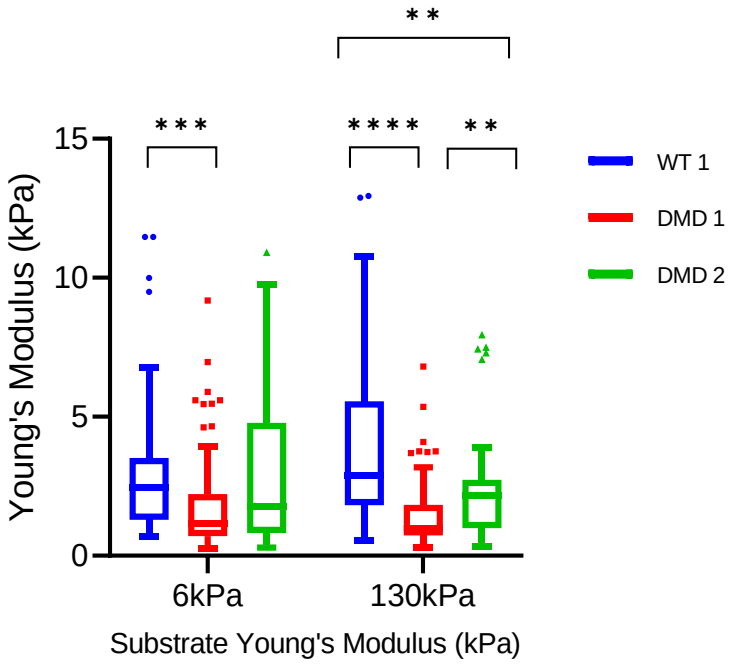

Figure 4.22: Nanoindentation Revealed an Important Role for Dystrophin in Adapting to ECM Stiffness. *hiPSC-CMs were plated onto a laminin coated PDMS substrate of either 6 kPa, or 130 kPa and allowed to recover for 5 days prior to experimentation. WT 1 hiPSC-CMs had a significantly larger Young's modulus compared to DMD 1 at 6 kPa and both DMD 1 and DMD 2 at 130 kPa. No significant differences were observed between 6 kPa and 130 kPa. Data are presented as Tukey boxplot and reported as mean ± S.D., N= 5 biological replicates for both WT 1 and DMD 1; N= 3 for DMD 2. WT 1, 6 kPa vs 130 kPa, n number of cells= 46 vs 59 hiPSC-CMs; DMD 1, 6 kPa vs 130 kPa, n= 77 vs 64 hiPSC-CMs; DMD 2, 6 kPa vs 130 kPa, n= 35 vs 45 hiPSC-CMs.*

To characterise the viscoelastic properties of the hiPSC-CMs more fully, I used dynamic mechanical analysis (DMA), which uses oscillatory indentations at different frequencies to measure the elastic, or storage modulus, *E'*, and the viscous, or loss modulus, *E''*. Together, the ratio between *E"* and *E'*, *Tan δ* that provides insight into the dissipation of energy of the material, in this case, elastic energy stored by hiPSC-CMs. I analysed

the hiPSC-CMs in response to three frequencies, 1 Hz, 4 Hz, and 10 Hz (Figure 4.23).

The elastic modulus *E'* for WT 1 showed a frequency dependent alteration with increases from 1 Hz to 10 Hz observed for both 6 kPa and 130 kPa. However, there was no significant difference of *E'* between 6 kPa and 130 kPa (Figure 4.23A). *E'* tended to increase in frequency dependent manner. In contrast, the loss modulus *E"* was significantly increased in WT 1 hiPSC-CMs between 6 kPa and 130 kPa at all frequencies (Figure 4.17B), indicating a change in cytoskeletal arrangements, such as cross-linking of α-actinin[391,392]. Interestingly, the loss modulus was significantly increased at all frequencies on a 6 kPa substrate. In contrast, a significant increase at 130 kPa was observed between 1 Hz and 10 Hz. The *Tan δ* for WT 1 (Figure 4.23C) was significantly increased between 6 kPa and 130 kPa at 4 Hz by 30%. Moreover, there was a significant increase between 4 Hz and 10 Hz on 6 kPa substrate (6 kPa vs 130 kPa, 0.30 ± 0.24 A.U. vs 0.40 ± 0.21 A.U.) as well as between 4 Hz and 10 Hz on a 130 kPa substrate (6 kPa vs 130 kPa, 0.39 ± 0.12 A.U. vs 0.45 ± 0.17 A.U.).

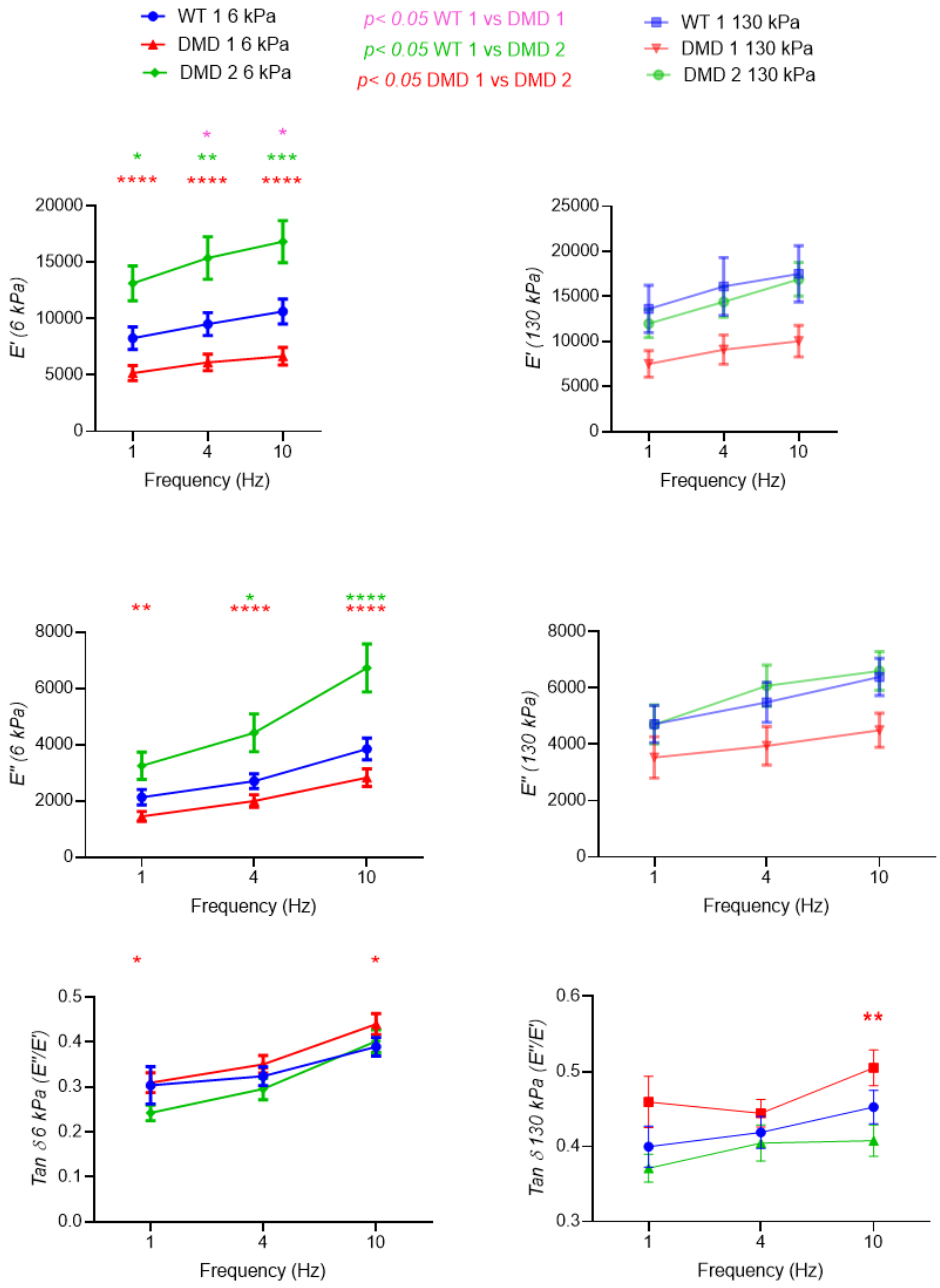

Figure 4.23: Dynamic Mechanical Analysis Reveals Alterations in the Elastic, E', (Storage), Viscous, E", (Loss) Moduli, and Tan δ in hiPSC-CMs on either a 6 kPa or 130 kPa PDMS substrate. A) *The E' (elastic storage) component did not significantly increase between 6*

kPa and 130 kPa for hiPSC-CM cell lines. Nevertheless, there was a frequency dependent increase in E'. ***B)*** *The E" (viscous loss) modulus was significantly increased in WT 1 between 6 kPa and 130 kPa at all frequencies indicating greater dissipation of mechanical energy in response to increased substrate stiffness. Similarly, DMD 1 showed increased loss modulus at 1 Hz and 4 Hz, although was not significantly changed at 10 Hz. DMD 2 showed no significant change.* ***C)*** *The Tan δ (ratio between viscous and elastic moduli, E"/E') revealed significant increases between 6 kPa and 130 kPa as well as within each of these groups for WT 1, DMD 1, and DMD 2 hiPSC-CMs. Data are presented as mean ± S.D., Two-way ANOVA with Tukey's post-hoc test applied, p<0.05 was considered significant. N biological replicates= 5 for both WT 1 and DMD 1; N= 3 for DMD 2. WT 1, 6 kPa vs 130 kPa, n number of cells= 41 vs 60 hiPSC-CMs; DMD 1, 6 kPa vs 130 kPa, n= 59 vs 59 hiPSC-CMs; DMD 2, 6 kPa vs 130 kPa, n= 30 vs 43 hiPSC-CMs.*

Similar to WT 1, the DMD 1 hiPSC-CMs displayed a frequency dependent increase to the *E'* on both the 6 kPa and 130 kPa substrates. There was no significant difference in *E'* between 6 kPa and 130 kPa, again consistent with the WT 1 data (Figure 4.17A). Interestingly, *E'* was significantly larger in WT 1 compared to DMD 1 on 130 kPa (WT 1 vs DMD 1, 10 Hz: 17510.0 ± 24289.8 A.U. vs 10022.0 ± 12308.9 A.U.) indicating greater elasticity of WT 1 hiPSC-CMs. The viscous component of DMD 1 also displayed frequency dependent increases, similar to *E'*. Moreover, viscosity altered in response to substrate, with significant differences between 6 kPa and 130 kPa at 1 Hz and 4 Hz (DMD 1, 6 kPa vs 130 kPa, 1 Hz: 1450.6 ± 1327.8 A.U. vs 3536.4 ± 5116.0 A.U.; 4 Hz: 1995.9 ± 1685.2 A.U. vs 3949.9 ± 4771.5 A.U.). No change was observed between WT 1 and DMD 1 regarding *E"*. The *Tan δ* was significantly larger between 6 kPa and 130 kPa at 1 Hz and 4 Hz for DMD 1 (6 kPa vs 130 kPa, 1 Hz: 0.31 ± 0.15 A.U. vs 0.46 ± 0.23 A.U.; 10 Hz: 0.44 ± 0.12 A.U. vs 0.51 ± 0.16 A.U.) indicating that either elasticity decreased, or viscosity increased. No change of *Tan δ* was found between WT 1 and DMD 1.

Similar to both WT 1 and DMD 1, There was a frequency dependent increase to the *E'* in DMD 2, although this was not significant between substrates. Nor were any changes to *E'* found between WT 1 and DMD 2. Contrariwise to WT 1 and DMD 1, there was no significant change to *E"* between 6 kPa and 130 kPa. However, there was a significant increase in *E"* in DMD 2 compared to WT 1 on the 6 kPa substrate at 10 Hz (WT 1 vs DMD 2: 3849.4 ± 2491.6 vs 6726.9 ± 4675.5 A.U.), suggesting that DMD 2 had a larger viscosity compared to WT 1. Similar to DMD 1, there was a significant increase of *Tan δ* between 6 kPa and 130 kPa at 1 Hz (0.25 ± 0.09 A.U. vs 0.37 ± 0.12 A.U.) indicating either decreased elasticity, or increased viscosity, whilst on 130 kPa. No significant differences of *Tan δ* were observed between WT 1 and DMD 2 for any given substrate stiffness or oscillation.

In sum, these data suggest differences in viscoelastic properties in response to increased Young's modulus of the substrate. Moreover, all cell lines displayed frequency dependent increases in elasticity, viscosity, and *Tan δ.* Interestingly, the *Tan δ* supports the notion that the viscous component was the dominant effect in the hiPSC-CMs in response to stimulation.

4.7 Further Interrogation Into the Role of the Cytoskeleton in Regulating the Young's Modulus of hiPSC-CMs in Response to Pharmacological Manipulation of the Cytoskeleton

As defined by the tensegrity model, the cytoskeleton particularly influences the stiffness, or Young's modulus, of the cell. To further examine the role of the cytoskeleton, I used stabilising or destabilising drugs, as before in the substrate stiffness section (§4.5), to examine the Young's modulus.

Depolymerising the actin cytoskeleton had a profound impact towards the Young's modulus of the WT 1 hiPSC-CMs (Figure 4.24A) at both 6 kPa (3.2 ± 2.7 kPa vs 1.3 ± 0.5 kPa) and 130 kPa (4.0 ± 3.1 kPa vs 1.2 ± 0.7 kPa). Here, disrupting the cytoskeleton led to significant decreases in hiPSC-CM stiffness, supporting the role of actin in determining stiffness of the cell. Moreover, preventing microtubule polymerisation (Figure 4.24B) also led to a significant reduction in the Young's modulus of WT 1 hiPSC-CMs at both 6 kPa (3.2 ± 2.7 kPa vs 1.3 ± 0.6 kPa) and 130 kPa (4.0 ± 3.1 vs 1.5 ± 0.9 kPa). Again, this supports a role for the microtubule cytoskeleton as a contributor towards the cellular Young's modulus.

Stabilisation of the actin cytoskeleton could not be performed due to the uncertainty surrounding the use of jasplakinolide, as described earlier (§4.5). The addition of the microtubule stabilising drug, taxol, caused no change in Young's modulus at 6 kPa (3.2 ± 2.7 kPa vs 2.8 ± 2.9 kPa) whilst surprisingly, caused a significant decrease at 130 kPa (4.0 ± 3.1 kPa vs 2.3 ± 1.4 kPa).

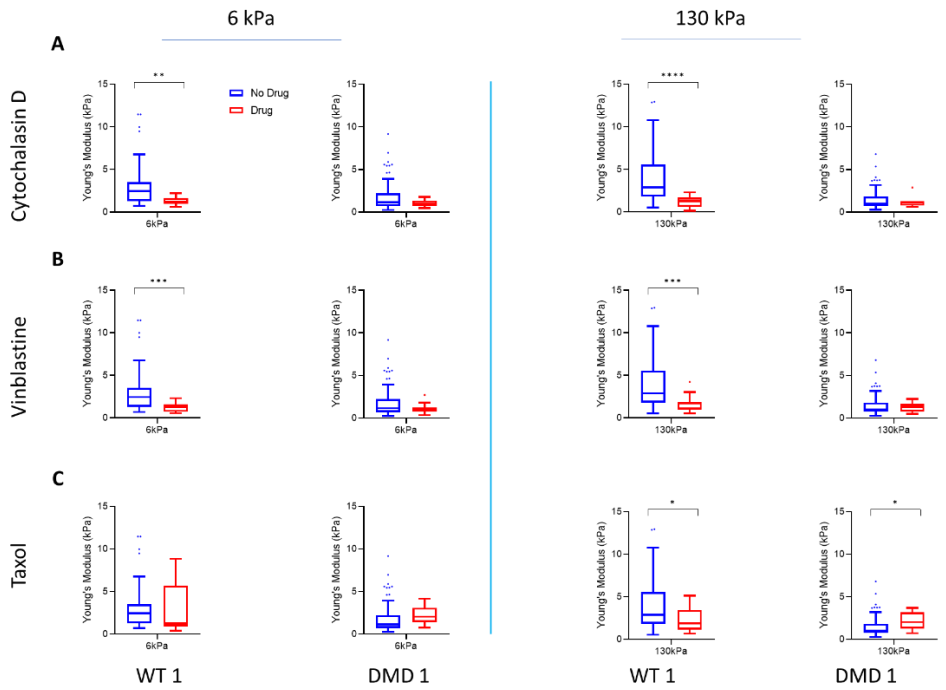

Figure 4.24: Young's Modulus of WT 1 or DMD 1 hiPSC-CMs on either a 6 kPa or 130 kPa Laminin Substrate in Response to Cytoskeletal Modulators. A) *hiPSC-CMs were treated using 1 µM cytochalasin D for 30 min at 37°C prior to PBS washout and nanoindentation. Disruption to the actin cytoskeleton resulted in a significant decrease in Young's modulus for WT 1 but no change in DMD 1 hiPSC-CMs.* ***B)*** *hiPSC-CMs were treated using 1 µM vinblastine for 1 hr at 37°C displaying a similar pattern to cytochalasin D, whereby WT 1 had a significantly decrease Young's modulus whilst DMD 1 was unaffected.* ***C)*** *In this case, hiPSC-CM microtubules were stabilised using 10 µM taxol for 2 hr at 37°C. At 6 kPa there was no significant increase in Young's modulus for either WT 1 or DMD 1. There was a significant increase in Young's modulus for DMD 1 on 130 kPa suggesting that stabilisation of microtubules could mitigate some of the cytoskeletal disruption observed in DMD hiPSC-CMs. Data are presented as Tukey boxplot and reported as mean ± S.D., Two-tailed Mann-Whitney U test where P<0.05 was considered significant. N= 3 biological replicates for untreated hiPSC-CMs; N= 1 for treated hiPSC-CMs. WT 1, cytochalasin D, 6 kPa untreated vs treated, n number of cells= 46 vs 11; 130 kPa untreated vs treated, n= 59 vs 15; WT 1 vinblastine, 6 kPa untreated vs treated, n= 46 vs 12; 130 kPa untreated vs treated, n= 59 vs 15; WT 1, taxol, 6 kPa untreated vs treated, n= 46 vs 19; 130 kPa untreated vs treated, n= 59 vs 16; DMD 1 cytochalasin D, 6 kPa untreated vs treated, n= 77 vs 10; 130 kPa untreated vs treated, n= 64 vs 7; DMD 1 vinblastine, 6 kPa untreated vs treated, n= 77 vs*

13; 130 kPa untreated vs treated, n= 64 vs 13; DMD 1, taxol, 6 kPa untreated vs treated, n= 77 vs 11; 130 kPa untreated vs treated, n= 64 vs 13

Interestingly, destabilising the actin cytoskeleton in DMD 1 did not have any effect at either 6 kPa (1.8 ± 1.8 kPa vs 1.0 ± 0.4 kPa) or 130 kPa (1.5 ± 1.3 kPa vs 1.3 ± 0.8 kPa). These data suggest that the actin cytoskeleton is already disrupted and the addition of the depolymerising cytochalasin D has no further affect in DMD. A similar observation was made when vinblastine was added. These data also suggest an already inherent disruption to the underlying microtubule network.

Strikingly, the addition of taxol to the DMD 1 hiPSC-CMs led to a significant increase of Young's modulus at 130 kPa (1.5 ± 1.3 kPa vs 2.1 ± 1.0 kPa); and had no effect at 6 kPa (1.8 ± 1.8 kPa vs 2.2 ± 1.0 kPa). This was in opposition to the observations made in WT 1 hiPSC-CMs and may suggest an unknown mechanism of microtubule regulation in DMD. These data suggest that stabilising the cytoskeleton can elevate the Young's modulus in DMD 1, although this does not achieve compatibility to the WT 1 without taxol (4.0 ± 3.1 kPa vs 2.1 ± 1.0 kPa; significant).

Together, these data support the role of the actin and microtubule cytoskeleton in regulating the Young's modulus of the cell. Moreover, they revealed an already dysfunctional cytoskeleton in the DMD hiPSC-CMs. This indicated that dystrophin is required for mechanosensing, and for cell adaptability to, changes in substrate elasticity.

4.8 Chapter Discussion

Here, I explored how alterations in the cardiomyocyte microenvironment, *i.e.* ECM, regulate and influence, underlying cardiomyocyte behaviour. I observed marked distinctions in cardiomyocyte behaviour on healthy 6 kPa compared to fibrotic 130 kPa substrate elasticities. Moreover, the absence of dystrophin potentiated these differences. Subsequently, I focused on the contribution of the cytoskeleton in governing cell and nuclear morphology, and the interaction between cytoskeleton and dystrophin. Moreover, I showed that dystrophin is required for regulating the Young's modulus of cardiomyocytes and that interaction between dystrophin and the cytoskeleton is vital to this.

4.8.1 Altering substrate elasticity has a profound impact on cellular and nuclear morphology

The cardiac ECM is responsible for transmitting contractile forces as well as other mechanical signals[63]. Matrix rigidity governs cellular behaviour and cardiomyocytes can adapt to these changes of microenvironmental niche[86]. Marked alterations to the microenvironment encourage pathological phenotypes observed in disease states, such as DCM.

To model hiPSC-CM responses to elasticity representing a healthy or fibrotic myocardium, and the role of dystrophin in this context, I leveraged the use of the synthetic polymer, polydimethylsiloxane (PDMS). PDMS is commonly utilised to form a hydrogel for cells for a multitude of reasons, but importantly here, for the ease by which its elasticity can be tuned. It is within this context that I explored the role that dystrophin may have towards mechanosensing alterations to the elasticity of the environment.

hiPSC-CMs harbouring mutations in *DMD* displayed an inability to adapt to shifts of substrate elasticity, which was in stark contrast to both of the WT hiPSC-CMs cell lines used. The morphological metrics examined here revealed significant adjustments in both WT cell lines, notably the increase in cell and nuclear area and perimeter in response to differing substrate elasticity. The phenotype displayed by the WT hiPSC-CMs is consistent with many other bodies of work that have also demonstrated an increase in cell area, and other morphological metrics, in response to increased substrate elasticity[393–396]. Reports by Chang[103] provided evidence consistent with the findings here whereby several DMD hiPSC cell lines had significantly decreased cell areas in contrast to WT hiPSC-CMs at both a healthy and fibrotic stiffness (they used 10 kPa and 35 kPa PDMS respectively). Moreover, the substrate stiffness had functional consequences for DMD hiPSC-CMs in the work by Chang[103] where they reported disrupted Ca^{2+} handling mechanics, including rapid time-to-peak and delayed decay tau.

At 6 kPa, DMD 1 hiPSC-CMs had a significantly larger cell and nuclear area, perimeter, and circularity compared to WT 1 hiPSC-CMs. Increased cell morphology of DMD hiPSC-CMs has been reported by other groups[316,397–399]. Intriguingly, increased cell area is a feature uncovered by murine models of DMD, thereby validating my *in vitro* hiPSC-CM model for examining the cardiac phenotype of DMD. At 130 kPa, WT 1 hiPSC-CMs were significantly larger compared to other cell lines, including WT 2, and this may indicate an increased sensitivity of this cell line to mechanical stimuli, which may have overridden the DMD hiPSC-CMs inherent larger size observed at 6 kPa. Alternatively, it may represent the intrinsic variability between hiPSC cell lines that is well acknowledged within the field.

The connectivity between the ECM-cytoskeleton extends to the nucleus via the LINC complex, allowing for nuclear mechanotransduction[194]. Here, I provided evidence suggesting that nuclear mechanics are altered in DMD mutant hiPSC-CMs compared to WT. Nuclear morphology underwent different changes, for example decreasing in area and perimeter in response to increasing substrate elasticity. Altered nuclear morphology coupled to differential cytoskeletal dynamics have been shown to alter gene expression by altering localisation of heterochromatin and histone proteins[400].

Nuclei of anisotropically aligned cells became, perhaps unsurprisingly, increasingly elliptical *i.e.* flattened, in shape, that may be due to increased actin cytoskeletal dynamics, such as stiff cable formation. Previous work has shown nuclei to be sensitive to alterations in substrate elasticity, where softer substrates tended to promote a more rounded phenotype[401]. Interestingly, DMD 1 nuclei were significantly larger compared to other cell lines, as determined by area and perimeter. Moreover, DMD 1 nuclei were substantially more rounded compared to WT hiPSC-CM counterparts. This peculiarity is a feature observed in certain disruptions of the LINC complex whereby nuclei tend to be larger and is thought to be mediated by the uncoupling between the nucleus and cytoskeleton or due to mislocalised proteins, such as lamin A/C such as the recent work by Wallace[402], uncovered defective nuclear mechanics in mutant *LMNA* hiPSC-CMs.

Whilst full-length dystrophin does not itself localise to the nucleus, the nucleo-cytoskeletal connection to the ECM is adversely affected. This acts to negatively impact cytoskeletal prestress and perception of mechanical force by the nucleus. It was shown that nuclear mechanotransduction is dependent upon actomyosin tension- a feature that was shown to be

significantly disrupted in DMD 1 hiPSC-CMS in this work and is discussed more below[400]. This is consistent with previous reports where uncoupling the LINC complex abolished nuclear mechanosensing[401]. Unlike Wallace[402], I did not extensively characterise nuclear fragility or specifically aim to assess nuclear elasticity, and this is an avenue for further future exploration.

Another potential explanation accounting for observations in nuclear morphology is the expression, and nuclear localisation, of small isoforms of dystrophin, such as Dp71[403]. The nuclear localisation of Dp71 is dependent on a functional microtubule network, a feature lacking in DMD cardiomyocytes[299,403]. Examination of specific isoforms and their cellular *locale* was not considered in this work, however, provides an exciting avenue for further work. Detailing the role of specific isoforms and their potential contributions towards mechanotransduction in DMD could be critical, especially in light of the micro- and mini-dystrophin therapeutic strategies being developed[404].

4.8.2 YAP localisation was altered in DMD

I next examined the effect that a lack of dystrophin would have on the nuclear localisation of the mechanosensitive transcriptional co-activator, YAP. YAP has garnered significant attention particularly in the regenerative field for its potential in promoting cardiomyocyte proliferation, with YAP being central to kickstarting the growth cycle. Previous work showed that YAP localised to, and is sequestered by, the DGC and thus, the DGC is at the forefront in regulating the cardiac cell cycle[3]. On stiff substrates (>10 kPa), YAP was shown to promote gene expression for cardiac cell anchorage including multiple integrins and laminin subunits[405]. When YAP was

silenced via knockdown, the anchorage capacity of cardiomyocytes was decreased[405].

Here, I reported that the nuclear localisation of YAP was significantly decreased in DMD 1 hiPSC-CMs compared to WT 1 whilst on 6 kPa elasticity. This data agrees with previous reports showing decreased and defective YAP nuclear localisation in DMD cardiomyocytes[3,387]. It is interesting that I did not observe this difference between the cell lines at the fibrotic 130 kPa elasticity. This was an unexpected observation, notably for the WT 1 cell line, as it has previously been shown that YAP localisation increases in response to stiffer substrates[384]. Moreover, there was no significant increase within the WT 1 cell line between 6 kPa and 130 kPa. It may be that the responses observed here were due to culture time. Elosegui-Artola[384] performed experiments and analysis within 4-8 hr after seeding of cells and may have noted an acute effect of YAP localisation. Here, my cells were seeded and allowed to recover for 5 days and may reflect a more chronic response to YAP nuclear localisation. Moreover, both Morikawa[3] and Elosegui-Artola[384] utilised murine fibroblast cells whereas I used a hiPSC-CM model that may further confound these interpretations.

However, recent work by Yasutake[376] utilised DMD hiPSC-CMs and examined nuclear localisation of YAP. They reported significantly decreased nuclear localisation of YAP in DMD hiPSC-CMs compared to a non-isogenic WT as well as an isogenic corrected DMD cell line. These data are consistent with my findings, although, Yasutake[376] did not examine the effect that substrate stiffness had on YAP localisation. Other reports[406] have shown that nuclear localisation of YAP is mechanoresponsive to stiffness in hiPSCs. Hsiao[406] described increased nuclear YAP localisation in response to elevated cell density, that can modulate mechanical force perceived by

individual cells. Moreover, Pagliari[407] reported that substrate Young's moduli in excess of 20 kPa promoted nuclear localisation of YAP. My data is consistent with these reports, in that nuclear YAP was observed in hiPSC-CMs at both 6 kPa and 130 kPa. Why this did not achieve significance between the substrate stiffnesses for WT 1 remains unknown and is inconsistent with many of the reports discussed here. Increasing the *n* number of cells examining this effect would be of significant interest here to further tease apart the role of YAP in the WT and DMD cardiomyocytes.

Further, I reported no significant difference in gene expression of *YAP* using RT-qPCR. This suggests that it is not strictly gene expression affected in DMD but, rather, the localisation of the protein. In turn, mislocalised YAP has a profound impact on downstream transcriptional targets and cellular mechanotransduction, that may contribute to the DMD pathology.

Importantly, the RT-qPCR data here was not derived from hiPSC-CMs cultured on different substrate elasticities, but from cells maintained within 24 well plates, and therefore are considered to be baseline. Further work should be guided towards the acquisition of mRNA from hiPSC-CMs cultured on different substrate elasticities to support the preceding localisation findings. Moreover, co-immunoprecipitations and western blots could further determine whether YAP is mislocalised, and to what extent, within my hiPSC-CM model. However, recently I harvested WT 1 and DMD 1 hiPSC-CMs subjected to different substrate elasticities for analysis leveraging the assay for transposase-accessible chromatin with sequencing (ATAC-Seq); a powerful method for examining gene expression. It is expected that I will be extensively analysing this data-set as part of future work to better determine what changes are apparent between the hiPSC-

CMs in response to differing elasticity. It will be interesting to determine if YAP accessibility is differential between conditions and genotypes.

4.8.3 Sarcomere length and the actin architecture were significantly disorganised in DMD hiPSC-CMs

Substrate stiffness is a determinant for the maintenance of myofibril and sarcomere architecture, that in turn dictates cardiomyocyte mechanics. Here, I employed the use of coherency to determine actin organisation. Values close to 1 indicate highly organised and anisotropic structures, whilst values close to 0 indicate highly disorganised and isotropic structures. Higher coherency, *i.e.,* higher orientation and organisation, is required for homeostatic cardiac physiology. This is apparent when hiPSC-CMs have been cultured onto functionalised nanopatterns that not only promote alignment[395,408] but increase Ca^{2+} handling and force generation[409].

Consistent with work by Atmanli[397] I showed that DMD 1 hiPSC-CMs had a shorter sarcomere length compared to WT 1. Moreover, significant reductions in sarcomere density were reported by Eguchi[410] that may be applicable to this work (although sarcomere density was not specifically analysed here). However, the report by Eguchi[410] does support the notion that sarcomeres are disrupted in DMD and that this is the cause for the density decrease observed. In contrast, Pioner[316] reported no difference in sarcomere length between DMD and WT hiPSC-CMs. This may be attributable to hiPSC-CMs maturity as Pioner[316] examined sarcomere length at D20. In contrast, I employed the use of T3 and dexamethasone to further advance maturation of my model, with T3 specifically enhancing sarcomere maturity[327]. Moreover, my hiPSC-CMs were not used experimentally until D30.

Moreover, the work presented here is consistent with the majority of work examining sarcomere length in DMD and with murine models demonstrating significant reduction in sarcomere length[411]. Not only does this validate the hiPSC-CM model utilised here, but also supports the findings consistent with the DMD phenotype more generally.

WT 1 hiPSC-CM sarcomeric architecture displayed regularity and the healthy length of approximately 2 µm[412]. Sarcomeric length is an important consideration as extensive deviations from the 2 µm length cause highly inefficient cardiac dynamics. This is especially the case when sarcomere length falls to < 1.8 µm showing diminished maximal velocity[413], that may account for the decreased force generation in DMD cardiomyocytes.

I showed that WT hiPSC-CMs on both 6 kPa and 130 kPa had a more anisotropic and organised actin cytoskeleton in contrast to DMD 1. This was demonstrated by using the coherency output from OrientationJ. This finding is particularly important considering the significant decrease in Young's modulus observed (Chapter 4; 4.6). Given that the actin cytoskeleton is a vital determinant for cell stiffness, providing evidence supporting its disorganisation, therefore, agrees with the significantly decreased Young's modulus displayed and may be a significant factor contributing towards the underlying viscoelasticity of the hiPSC-CMs.

Although not directly assessed here in this body of work, I would hypothesise that force generation would be decreased in DMD hiPSC-CMs, especially in view of the disorganised sarcomeric and actin cytoskeletal architecture. This could be examined as part of future work utilising nanopillar arrays. Moreover, disruptions to the actomyosin network may compromise rigidity sensing in DMD hiPSC-CMs heightening their inability

to adjust morphologically to alterations of their environment, consistent with the cell morphology data presented here.

4.8.4 Nanoindentation revealed the Young's modulus to be significantly decreased in DMD hiPSC-CMs

The elastic modulus of WT 1 hiPSC-CMs was significantly larger compared to both DMD 1 and DMD 2, and this was apparent at both 6 kPa and 130 kPa (although WT 1 vs DMD 2 at 6 kPa was not significant).

Furthermore, the significantly decreased elasticity in DMD 1 is consistent with the disrupted actin cytoskeleton and altered cellular morphology I discussed earlier. This is consistent with work by Pasternak, Wong, and Elson[125] where they described a significant decrease in elasticity of dystrophic myotubes compared to healthy murine myotubes. Additionally, Liu[414] showed hiPSC-CMs derived from patients with DCM had significantly decreased elasticity when compared to healthy samples, again a finding that I report here in this work. Moreover, the values reported by Liu[414] of up to 5 kPa in healthy hiPSC-CMs are consistent with the values reported here.

The elasticity of native human cardiac tissue is reported at approximately 10 kPa, which exceeds the values presented in this work[83]. However, this likely reflects the difference in maturity between the models. A report by Liu[414] reported hiPSC-CM Young's modulus values on the magnitude of 5 kPa, not inconsistent with the work here. It would be interesting to utilise 3D constructs with co-culture to examine whether there is a compensation in tissue elasticity for DMD.

4.8.5 DMA analysis reveals alterations to the viscoelastic nature of DMD hiPSC-CMs

Using dynamic mechanical analysis (DMA), I revealed significant alterations to the *E'*, *E",* and *Tan δ* in DMD 1 and DMD 2 compared to WT 1 and to one another at both 6 kPa and 130 kPa substrate elasticities. Firstly, I found that all hiPSC-CMs displayed a frequency dependent linear increase in *E', E",* and *Tan δ*. Furthermore, at 6 kPa, I reported that WT 1 had a significantly larger *E'* compared to DMD 1, indicative of WT 1 capacity for elastic storage, implicating dystrophin in this capacity. Unexpectedly, DMD 2 was significantly more elastic compared to WT 1. There was no significant difference in viscosity between WT 1 and DMD 1, although DMD 2 appeared to be more viscous than either. Interestingly, the *Tan δ* remained unchanged between the cell lines. However, *Tan δ* DMD 1 was non-significantly larger than WT 1 suggesting that it is less elastic. Moreover, similar findings were observed at 130 kPa. These data support the notion that dystrophin is a strong contributor towards viscoelasticity of cells. This is supported by the work of Le[8], who showed the SR domain of dystrophin to function as a molecular spring. This spring-like action by dystrophin naturally lends itself to the storage-dissipation cycles, that is to say elastic and viscous components.

4.8.6 Does tensegrity account for the observations made?

Tensegrity is a theoretical framework to conceptualise how mechanical force influences the overall cellular viscoelasticity and mechanical behaviour of cells[208]. Under tensegrity, the central determinants are the actin and microtubule cytoskeleton, that acts as 'cables' and 'struts' respectively, whereby prestress is generated by actomyosin contraction[415]. This differs from alternative models that view cellular structure as a continuum. Tensegrity has shown itself capable of accurately predicting cell behaviour under certain assumptions, such as microtubules bearing compressive force similarly to struts in theoretical tensegrity models[391,392].

For example, the tensegrity model's second assumption is that both *E'* and *E''* will linearly increase, at a given frequency, in accordance with a weak power law[391,392]. This is supported by experimental evidence[416], and is consistent with the data acquired here whereby *E', E''*, and *Tan δ* demonstrated frequency dependent increases. Interestingly, the data here also supports a role for dystrophin in mediating this.

However, the tensegrity model is limited by its assumption of static elastic behaviour of cells[392]. In reality, cell behaviour typically follows a viscoelastic rheological profile. Attempts to compensate for this include the viewing of the cell into divisible compartments, such as investigating the contribution of cortical versus deep cytoskeleton towards cell mechanics. Moreover, tensegrity models often fail to include critical aspects of the cytoskeleton such as the intermediate filaments[392].

Other reports have suggested that the underlying model describing stress-dependent stiffness and relating this to the weak power law of rheology is

poorly defined. Moreover, tensegrity is not capable of predicting power-law rheology[392].

Another aspect worth consideration is the inherent nature of the cytoskeleton itself. Prestressed cytoskeletal filaments develop and modulate mechanical stress by changing their spacing, orientation, and lengthening[416]. For example, F-actin undergoes extensive cross-links, especially in cardiomyocytes. Important cross-linkers include α-actinin, and this modulates the stiffness of the F-actin network, such that it elevates stiffness[417]. Considering that DMD cardiomyocytes appeared to have disrupted actin and microtubule architectures, it may be that actually cross-linking bears more importance in governing stiffness here.

On balance, the tensegrity model is a useful lens for viewing cellular dynamics and to account for aspects of the viscoelastic nature of cells. However, it must be utilised under the knowledge and assumption of the aforementioned caveats that may affect the interpretation of the data. Here, the data are broadly consistent with what tensegrity has to offer. That is to say, the expected alteration to the actin and microtubule cytoskeleton resulted in altered mechanics, such that, the Young's modulus of the cardiomyocytes decreased.

4.8.7 Pharmacological modulation of the cytoskeleton revealed DMD was already impaired

Modulating the stability of the cytoskeleton was conducted to more fully examine the role that it, and dystrophin, had in determining mechanosensing and viscoelasticity. Using cytochalasin D, I observed negative regulation of actin in hiPSC-CMs at both 6 kPa and 130 kPa, regarding cell morphology. This was perhaps not entirely surprising as actin

is a key moderator of cell morphology and spreading. I then hypothesised that cytochalasin D would decrease the Young's modulus in WT 1 and DMD 1 hiPSC-CMs. As expected, Young's modulus significantly decreased in WT 1 hiPSC-CMs in response to cytochalasin D at both 6 kPa and 130 kPa, a feature consistent with other groups[418,419]. Surprisingly, cytochalasin D had no significant effect on DMD 1 hiPSC-CMs, suggesting that the underlying actin cytoskeleton was already dysregulated. Why cytochalasin D did not further decrease the Young's modulus in DMD 1 hiPSC-CMs here is not known. Moreover, I found a similar trend in the presence of the microtubule destabilisation agent, vinblastine, that is again consistent with the work by others[420].

Lastly, I hypothesised that stabilising the cytoskeletal network had potential to 'rescue' the Young's modulus of DMD 1 to that of untreated WT 1 hiPSC-CMs. In other words, stabilisation could potentially increase the Young's modulus to that of healthy phenotype. Indeed, as expected stabilisation of the microtubule network significantly increased Young's modulus in DMD 1, particularly at 130 kPa. However, the Young's modulus was still significantly lower compared to WT 1. Nevertheless, this notion is consistent with other work[420] and is an exciting avenue for further exploration. It may well be, given that some of these pharmaceuticals are used therapeutically, a viable adjunct to DMD therapy. However, careful dosage with extensive monitoring would be required as these drugs are typically utilised against cancer.

4.8.8 Accounting for the unexpected finding of jasplakinolide

Informed by the cell and nuclear morphological assays, jasplakinolide was not carried forward for examination by nanoindentation. But what are the explanations underlying jasplakinolide's apparent adverse effect? It has

been reported (and this was noted at the end of my time within the laboratory) that jasplakinolide and phalloidin compete for the same binding site along F-actin filaments. Therefore, the use of phalloidin to visualise the effect of jasplakinolide on the cytoskeleton may have failed as a direct result of this[421]. Therefore, jasplakinolide may actually have functioned as intended despite the data presented here indicating the contrary. However, this is a speculative argument at present and would require confirmation.

A second explanation may be the cytotoxic nature of jasplakinolide that has been documented in cardiomyocytes[422]. Schweikart[422] reported substantial cell death in cardiomyocytes in concentrations of jasplakinolide of ≥10 µM up to 30 µM. Schweikart[422] reported above 80% cardiomyocyte viability in the presence of 1 µM jasplakinolide for a period of up to 10 hrs. Moreover, Wang[423] also used and visualised sarcomeric actin banding in the presence of 1 µM jasplakinolide. It is therefore unlikely, but not strictly impossible, that the hiPSC-CMs utilised here displayed an increased sensitivity to jasplakinolide resulting in apoptosis. Although, I hypothesise that using an alternative F-actin marker would remedy the discrepancy observed here. Thus, future work should be directed towards establishing the effect of jasplakinolide, particularly given the importance of the actin cytoskeleton towards the Young's modulus and viscoelastic properties of cells.

4.9 Limitations Within the Chapter

Heterogeneity between cell lines is a widely acknowledged phenomenon within the stem cell field, and therefore, isogenic controls would have been preferred here (See §3 and §A1 for further detail). As a result of time-constraints I was unable to generate, validate, maintain, and differentiate *de novo* isogenic cell lines. Nevertheless, future work should use, where

possible, isogenic pairs or murine models to clarify and substantiate the findings reported by this work.

Cardiac differentiation also carries significant variation, in other words 'batch-to-batch' variation, despite adherence, as far as possible, to safeguarding the reproducibility of the protocol. That being said, it is not uncommon or unknown for studies to employ the use of non-isogenic controls in contrast to their mutant models. Data reported here under this caveat should not be disregarded as a result of this.

Further analysis into downstream targets of YAP should also have been carried out. Indeed, RT-qPCR for *CTGF* and *ANKRD* were attempted but failed. Additional techniques to perturb YAP could also have been leveraged, including looking at YAP in response to cytoskeletal drugs used here. Future work should aim to complete these avenues to further tease apart the role that dystrophin may have over YAP localisation.

The addition of DMSO only controls whilst examining the effect of cytoskeletal drugs may have provided more information to the exact contribution the drug of interest was generating in contrast to the drug of interest with DMSO. In the future, should these experiments be repeated, this step should be performed alongside.

4.10 Future Work

This chapter has provided an extensive number of avenues for further work regarding the dissection of cardiomyocyte biomechanics and the contribution of dystrophin in this capacity. A particularly interesting avenue would be to improve the cardiac model to better recapitulate the physiological scenario. For example, employing the use of 3D co-cultures or organ-on-a-chip models would provide excellent platforms for examining

tissue level mechanics, such as elasticity, where cell-cell interactions may be explored, including connexin 43 and tissue level electrophysiology. The use of 3D engineered heart tissues would allow for more full and in-depth tissue level determination of viscoelasticity. Moreover, introducing specific subpopulations of cardiomyocytes here could provide interesting information as to whether differential myocardial layers contribute differently to tissue viscoelasticity. 3D models mimicking healthy and fibrotic environments could also be developed to further explore the impact of this on cell behaviour and tissue-level dynamics.

Another aspect ripe for examination would be the use of different ECM constituents, such as fibronectin, agrin, collagens, matrigel, or combinations of these to better mimic the true cardiac ECM. Here, I utilised only laminin as the matrix component for experiments, as this is the major binding partner for α-DG as well as the major cardiac integrin, α7β1D. It has been shown in previous works, using neonatal rat cardiomyocytes, that different ECM constituents differentially regulate cardiac morphology as well as traction forces[424]. Therefore, exploration of this would provide a more comprehensive examination as to *how* the underlying ECM constituents modulate cardiomyocyte behaviour. Again, modulating the composition of the ECM could reveal underlying pathomechanisms that contribute towards DCM.

Further, directly examining the role that dystrophin has in governing cytoskeletal and nuclear dynamics could be carried out using magnetic tweezers or magnetic twisting cytometry. In these experiments, the stimulation on α-DG could provide key insights towards how the DGC alters the cytoskeleton, YAP localisation, as well as potentially assess cross-talk to integrin complexes. These experiments could then be performed using

DMD hiPSC-CMs, where it would be expected that these features would be absent.

Recently, I received the ATAC-seq data set examining WT 1 and DMD 1 hiPSC-CMs that were cultured on either 6 kPa or 130 kPa for 5 days. Full analysis of this data-set has yet to occur but is a high priority item. The ATAC-seq data may reveal differential gene expression between genotypes and/or substrate elasticities. It will be exciting to visualise and ascertain what distinctions are present and whether these can be related to the data presented throughout this chapter. I would expect to observe some form of differential expression, notably within cytoskeletal elements and mechanosensitive proteins based on the work here.

Lastly, scaling up these preliminary findings to *in vivo* models could provide an excellent opportunity to validate the model and results found here. Whilst much of the work is consistent with previous findings, confirmation here would be preferable and could be determined using *in vivo* models. Moreover, application of the techniques utilised here could further our understanding in pathophysiology of DMD, importantly examining tissue level elasticity and assessing the efficacy, or lack thereof, of using a cytoskeletal stabilising agent as a potential therapeutic strategy.

4.11 Chapter Summary

Herein, I demonstrated the important contribution towards cell and nuclear morphology, mechanosensitive protein localisation, and Young's modulus and cellular viscoelasticity imparted by dystrophin. Moreover, dystrophin appears to be required for appropriate organisation of the actin cytoskeleton and sarcomere formation. In sum, I provide evidence

supporting dystrophin as a critical modulator of mechanotransduction within cardiomyocytes.

5 Examining the Response of hiPSC-CMs under Cyclic Cardiac Pressure and Equibiaxial Stresses

The world is full of magical things patiently waiting for
our wits to grow sharper

Bertrand Russell

5.1 Chapter Introduction

Following on from the preceding chapter, I wanted to further investigate the response of WT and DMD hiPSC-CMs to mechanical load, namely healthy cardiac pressure of 120/10 mmHg and myocardial contractile stretch. The cardiac cycle is comprised of several distinct stages and is characterised by adjustments in both pressure-volume and contractility as blood tracts through the various chambers and is broadly defined by states of diastole and systole and is described well by pressure-volume loops (Figure 5.1). Diastole defines the relaxation and filling of cardiac chambers with blood and is the phase whereby cardiomyocytes are stretched *i.e.,* is the preload. In contrast, the systolic phase describes the contraction and ejection of blood. The aortic pressure and wall stress defines the afterload against which blood is ejected.

An intimate relationship between volume of blood and pressure, termed preload, has a significant impact on cardiomyocyte contractility, as defined by the Frank-Starling law of contraction. The relationship between pressure-volume and inotropy are proportional, therefore, changes within the preload have a profound impact on cardiac output, stroke volume, and ejection fraction. Importantly, preload increases the sensitivity of thin filaments to Ca^{2+}, and thereby increasing the preload allows more Ca^{2+} to bind, and the larger the force produced by the sarcomeres in the healthy myocardium.

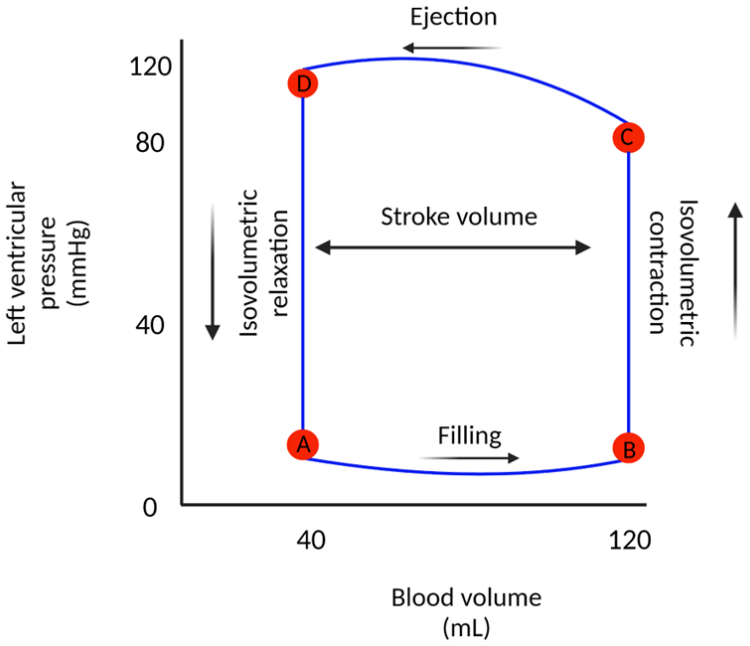

Figure 5.1: Left Ventricular Pressure-Volume Loop. *Pressure volume loop detailing diastole and systole. At 10 mmHg the mitral valve opens* ***(A)*** *allowing blood to fill to 120 mL, until the mitral valve closes* ***(B)****- this is the end diastolic volume. Isovolumetric contraction then occurs, and the pressure increases from 10 mmHg to 120 mmHg until the aortic valve opens* ***(C).*** *Ejection occurs at this point with peak systolic pressure reaching 120 mmHg and the aortic valve closing at* ***(D)****- this is the end systolic volume. The end diastolic volume minus the end systolic volume is equal to the stroke volume (~70 mL). Isovolumetric relaxation occurs pressure decreases to approximately 10 mmHg. Image created using Biorender.*

The contractile apparatus of the cardiomyocyte is chiefly composed by actomyosin crossbridge cycling within the sarcomeres with the sum of all actively engaged sarcomeres generating force production[49]. According to the Frank-Starling law, the force generated is dependent on sarcomere length and is maximal at native sarcomere length. More recent work suggested this to be related to mechanical stress-sensing and signalling from thick filaments leading to the Ca^{2+} activation of the thin filaments[425]. As such volume and/or pressure overload are significant contributors to

myocardial remodelling. In DCM, as occurs in DMD, eccentric remodelling is commonly observed, defined by decreased wall thickness and increased chamber radius[426]. Overall, this functions to decrease systolic output as described by the Law of Laplace[427] (*Eq. 5.1)*.

The Law of Laplace relates pressure (P) and tension (T) to wall stress (S) and wall thickness (W) to the radius of the chamber (r):

$$P = \frac{2T}{r} = \frac{2SW}{r} \quad (Eq. 5.1)$$

Broadly, as the radius increases in DCM, the curvature decreases resulting in decreased tension, and thus the ejection fraction subsequently falls. In contrast to healthy myocardium where the Frank-Starling law accounts for the dominant effect, in the DCM myocardium, the Law of Laplace describes the dominant effect.

Additionally, the sarcolemma within DMD hearts suffer from structural instability resulting in microtears over time[289]. Cumulatively, microtears damage the cardiomyocyte by permitting pathological Ca^{2+} entry. Excess intracellular Ca^{2+} further compounds the underlying structural dysfunction observed via several distinct mechanisms, such as promoting necroptosis via elevated ROS production[289].

Furthermore, consideration of the cardiac ECM in DMD should be provided. The relationship between the cardiac ECM and cardiomyocytes across the costameric region is considered to be bidirectional and the cardiac ECM has a critical role in dissipation of lateral force transmission generated by cardiomyocyte contraction. Moreover, the ECM framework provides stability towards the passive mechanical state of the myocardium and can become severely disorganised in DMD[428,429]. Elevated TGF-β secretion is

one such example and is a promoter of collagen fibrillogenesis that, in conjunction with the extensive fibrofatty and inflammatory *milieu*, is a cause for grave pathological alterations of the ECM within DMD associated DCM[92]. This disruption of the myocardium further confounds the contractile ability by decreasing passive elasticity of cardiomyocytes, thereby directly impacting overall functionality of the myocardium.

Therefore, leading on from the work shown in the preceding chapter, I wanted to delve further into the response of hiPSC-CMs under these physiological cardiac stressors, namely, cardiac pressure to mimic left ventricular blood pressure and equibiaxial stretch to mimic the *in vivo* cardiac contraction cycle.

5.2 Stretching WT 1 hiPSC-CMs Induces Cellular and Nuclear Morphological Alterations not Recapitulated in DMD 1 hiPSC-CMs

The cardiac environment is mechanically active undergoing contraction-relaxation cycles throughout the duration of life. Mechanical stretch of the environment will be subject to myocardial elasticity, that is in turn, contingent upon the composition of the ECM. Cardiomyocytes housed within the myocardium will experience not only individually generated contractions but also the overall contraction due to the syncytial network. This coupled to the notion that DMD cardiomyocytes are structurally less stable, motivated me to examine how they cope under physiological myocardial stretch.

Using the Flexcell® system, hiPSC-CMS were subjected to a 6-hr sine-wave cyclic stretch of 1 Hz at 10 % elongation, thus mimicking healthy myocardial contraction. Initially, I characterised whether the cellular and nuclear

morphology altered in response to stretch (Figure 5.2). Strikingly, the cell area, perimeter, and circularity were significantly increased in WT hiPSC-CMs when subjected to stretch, whereas in opposition, the DMD hiPSC-CMs showed no change (Figure 5.3). Stetch induced a 44% increase in cell area for WT 1, and for WT 2 hiPSC-CMs. In contrast, DMD 1 and DMD 2 cell areas did not increase in response to stretch. The cell perimeter and circularity followed a similar trend, with only the WT hiPSC-CMs significantly responding to cyclic stretch.

Given that mechanotransduction extends to the nucleus and is a known regulator of nuclear morphology, I subsequently characterised whether the cyclic stretch regimen here induced any nuclear alterations. Similar to the observations made in the cellular morphology, the nuclear morphology was significantly altered in response to stretch for the WT hiPSC-CMs (Figure 5.4). WT 1 nuclei demonstrated a significant increase in area of 17% in response to stretch, as well as 9% increase in perimeter. The circularity in WT 1 nuclei did not alter significantly (unstretched vs stretch: 0.92 ± 0.07 A.U. vs 0.91 ± 0.06 A.U.). Nuclei in the WT 2 cell line demonstrated a similar response to stretch to WT 1, with nuclear area increasing by 32%, cell perimeter by 17%, and again, no alteration to the nuclear circularity (unstretched vs stretch: 0.91 ± 0.05 A.U. vs 0.89 ± 0.06 A.U.).

In stark opposition to the WT hiPSC-CM nuclei, DMD 1 nuclei demonstrated no significant response to stretch for any of the morphological parameters.

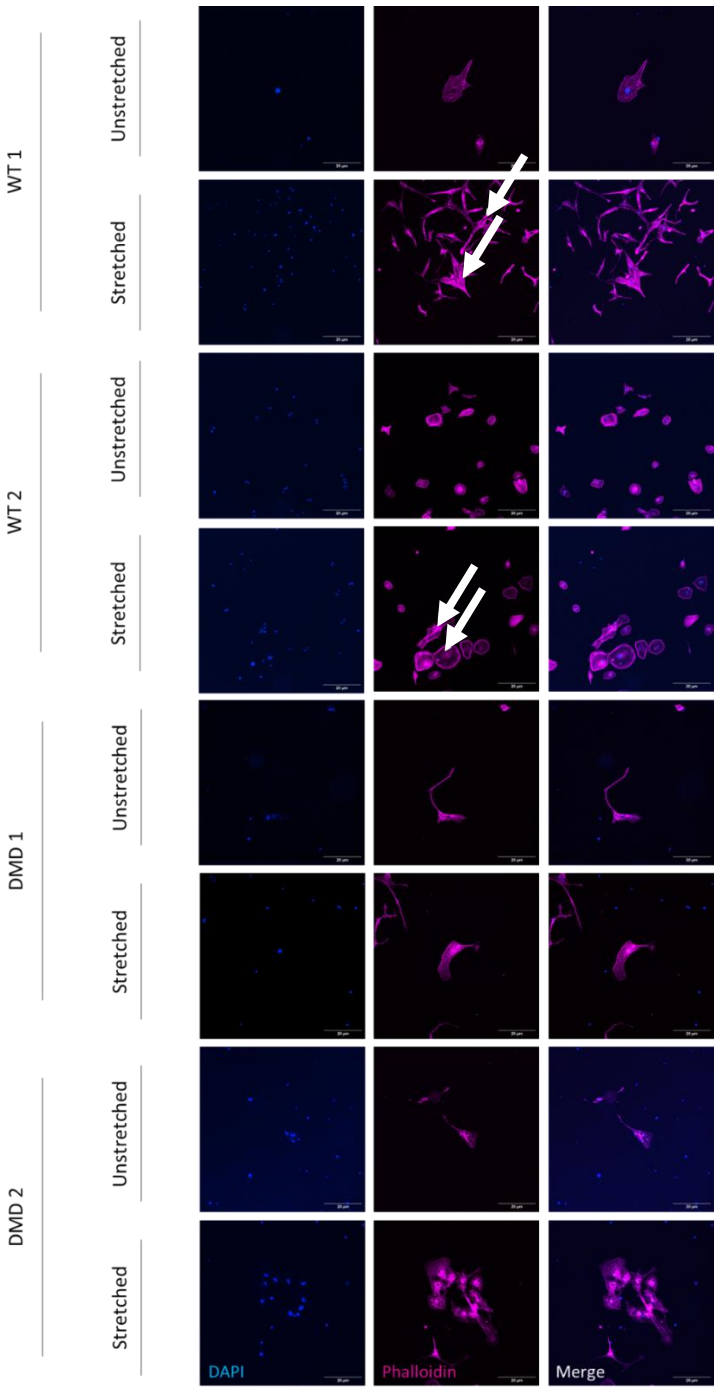

Figure 5.2: WT and DMD hiPSC-CMs on Collagen and Laminin Coated Flexcell Membrane Subjected to Either Cyclic Stretch or No Stretch. *hiPSC-CMs plated onto the flexcell membrane and allowed to recover for 48 hrs prior to experimentation. Representative*

figures showing that equibiaxial stretch caused a significant increase in WT hiPSC-CMs whilst DMD 1 hiPSC-CMs were unaffected. N= 3 biological replicates

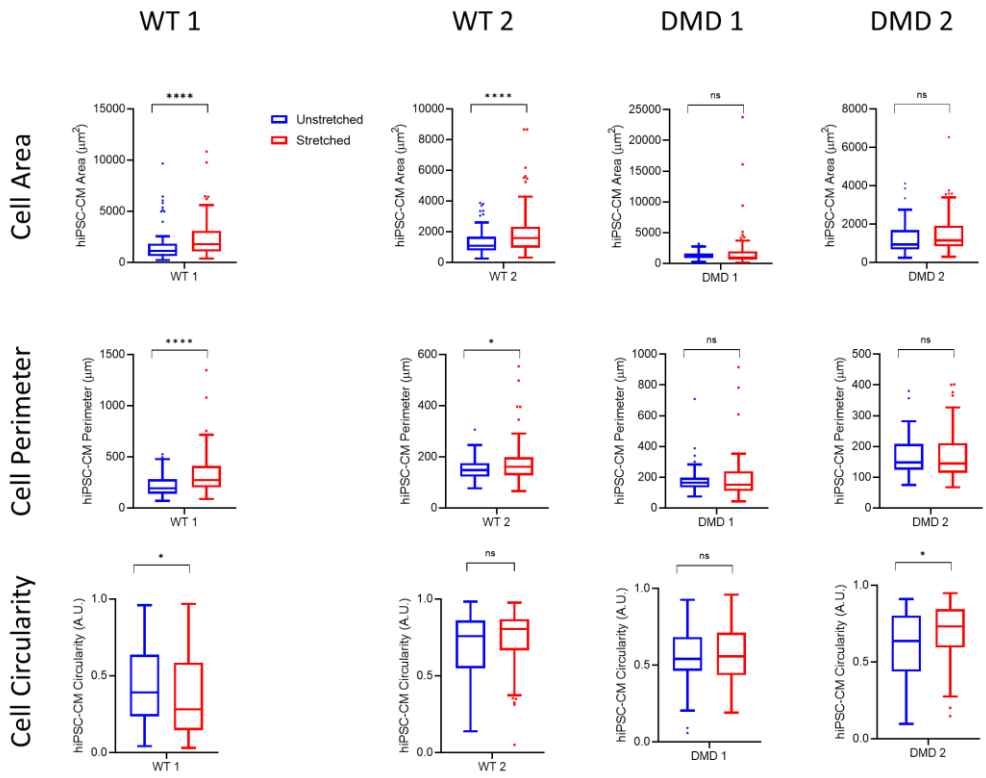

Figure 5.3: Quantification of Cell Morphology Descriptors in Response to Equibiaxial Cyclic Stretch. *WT and DMD hiPSC-CMs were subjected to either no stretch or a 6 hr cyclic stretch (10% elongation) at a frequency of 1 Hz. Both WT hiPSC-CMs responded to stretch by significantly increasing cell area, perimeter, and circularity (WT 1 only here). In contrast, DMD hiPSC-CMs showed no change in response to stretch. N= 3 biological replicates. Data analysed by a two-tailed Mann-Whiteny U test where p<0.05 was considered significant. Data are presented as Tukey boxplot and reported in text as mean ± S.D. Number of cells analysed per condition: WT 1, unstretched vs stretched: 86 vs 114 hiPSC-CMs; WT 2, unstretched vs stretched: 98 vs 157; DMD 1 unstretched vs stretched: 102 vs 164; DMD 2 unstretched vs stretched: 59 vs 76.*

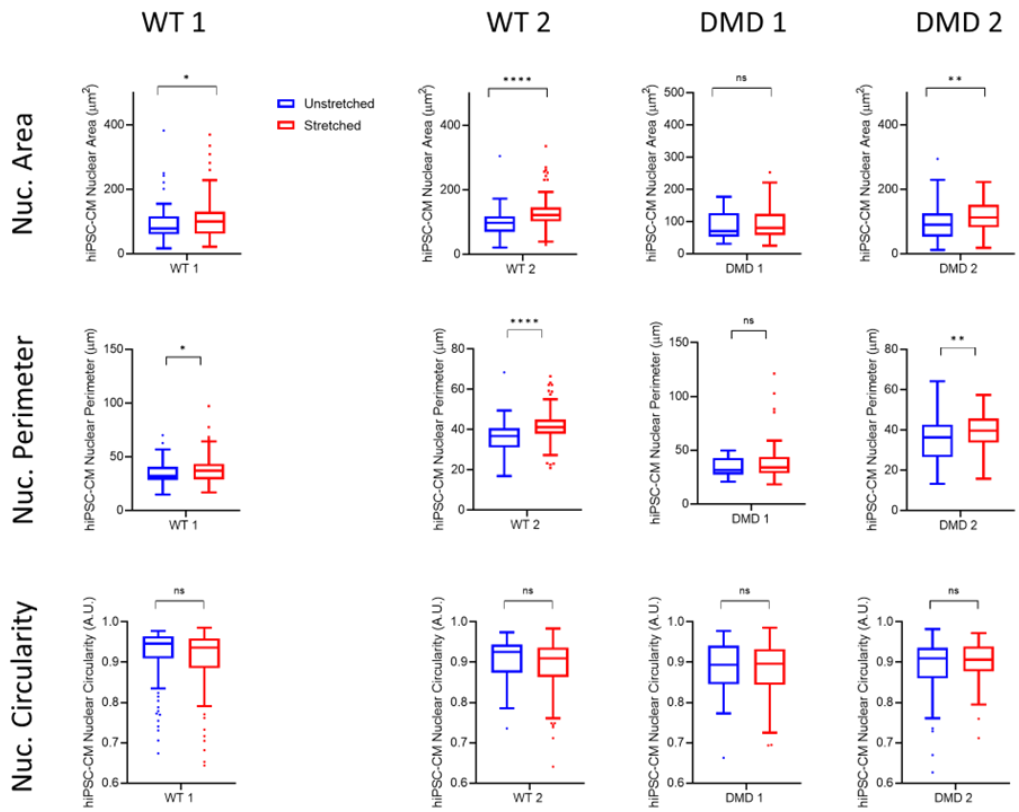

Figure 5.4: Quantification of hiPSC-CM Nuclei in Response to Either Equibiaxial Cyclic Stretch or no Stretch. *Morphological characteristics of hiPSC-CM nuclei were characterised after cells were subjected to either no stretch or 6 hr cyclic stretch (10 % elongation; 1 Hz). WT nuclei significantly altered their morphology in response to equibiaxial stretch, whereas DMD nuclei did not. This supports a role for dystrophin in mechanotransducing stretch stimuli. N= 3 biological replicates. Data analysed by a two-tailed Mann-Whiteny U test where p<0.05 was considered significant. Data are presented as Tukey boxplot and reported in text as mean ± S.D. Number of nuclei analysed per condition: WT 1, unstretched vs stretched: 89 vs 134; WT 2, unstretched vs stretched: 105 vs 174; DMD 1, unstretched vs stretched: 30 vs 89; DMD 2 unstretched vs stretched: 76 vs 94.*

The nuclear area for DMD 1 increased by 11% and showed a change in perimeter of 5%, both non-significant. Circularity of DMD 1 nuclei did not alter in response to stretch (unstretched vs stretch 0.89 ± 0.07 A.U. vs 0.88 ± 0.07 A.U.)

Intriguingly, DMD 2 nuclei behaved more consistently with the WT nuclei than DMD 1 nuclei, showing a significant increase in nuclear area of 26% and a significantly increased nuclear perimeter of 13% in response to stretch. Similar to DMD 1, there was no alteration in nuclear circularity (unstretched vs stretch: 0.89 ± 0.07 A.U. vs 0.90 ± 0.05 A.U.).

Comparison between cell lines revealed a significant increase in cell area between WT 1 and DMD 1 and DMD 2. The WT 2 cell line showed a significant increase in cell area between DMD 1 but not DMD 2. There was no difference between WT 1 and WT 2 or between DMD 1 and DMD 2. Interestingly, only WT 1 showed a significantly increased perimeter compared to the other cell lines in response to stretch (Figure 5.5A).

In contrast, WT 1 nuclei were not significantly different compared to DMD 1 nuclei in response to stretch, but their individual behaviour was- *i.e.,* WT 1 nuclei demonstrated a significant increase in nuclear area whilst DMD 1 nuclei did not, and this still supports a role for dystrophin in communicating mechanical signals to the nucleus. Interestingly, WT 2 nuclear area was significantly increased compared to both DMD 1 and DMD 2 nuclei. Lastly, DMD 2 nuclear area was significantly different compared to DMD 1 (Figure 5.5B).

In sum, these data support a role for dystrophin being necessary to respond to a stretch stimulus, due to the fact that in DMD hiPSC-CMs there are no significant changes to cellular and nuclear morphology. In contrast, WT hiPSC-CMs, that do produce and localise dystrophin, respond to stretch.

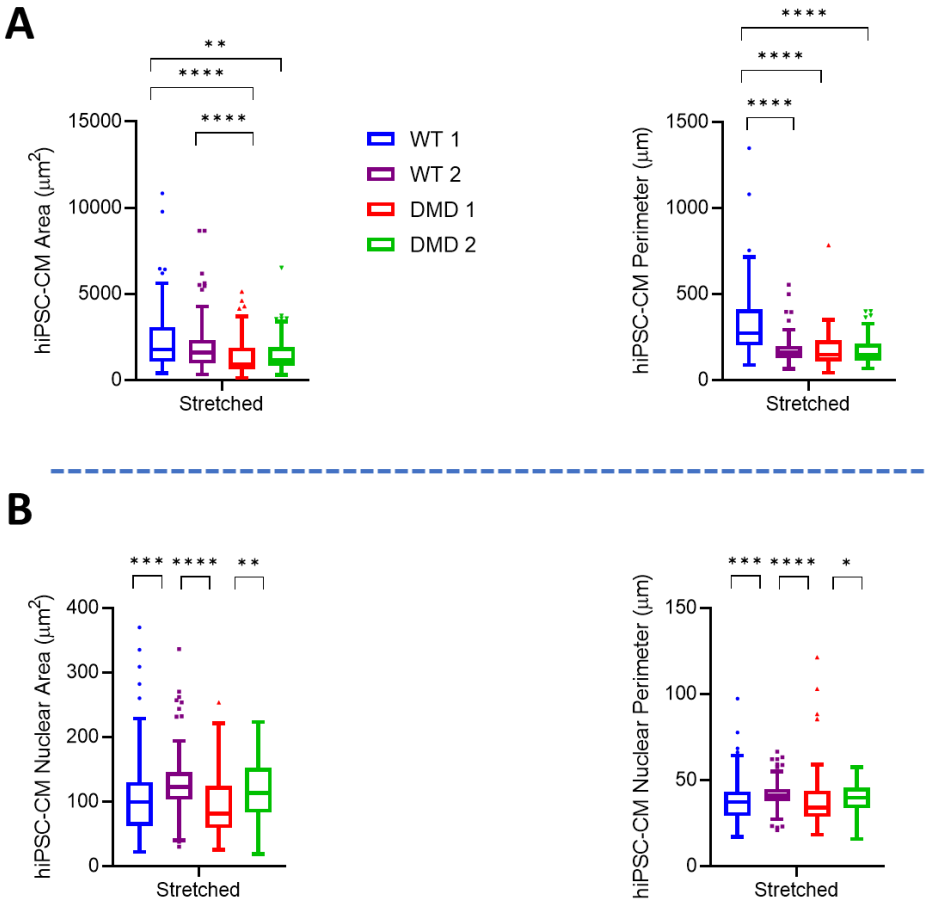

Figure 5.5: Comparison Between hiPSC-CM Cell Lines in Response to Cyclic Stretch. A) *hiPSC-CM cell area and perimeter,* ***B)*** *nuclear area and perimeter. N= 3 biological replicates. Data are presented as a Tukey boxplot and reported in text as mean ± S.D. Data analysed using Kruskal-Wallis test with Dunn's post-hoc test applied; p<0.05 was considered significant.*

5.3 Preliminary Data Showing That Nuclear Localisation of YAP is Not Altered in Response to Cyclic Stretch

Next, I wanted to characterise the response of YAP to cyclic stretch to observe whether it underwent mechanotransduction in response to mechanical cyclic stretch. Intriguingly, YAP did not change nuclear localisation in response to cyclic stretch (Figure 5.6), suggesting that the

effect of stretch on cell area is independent of YAP. Due to the lack of response the experiment was repeated only once.

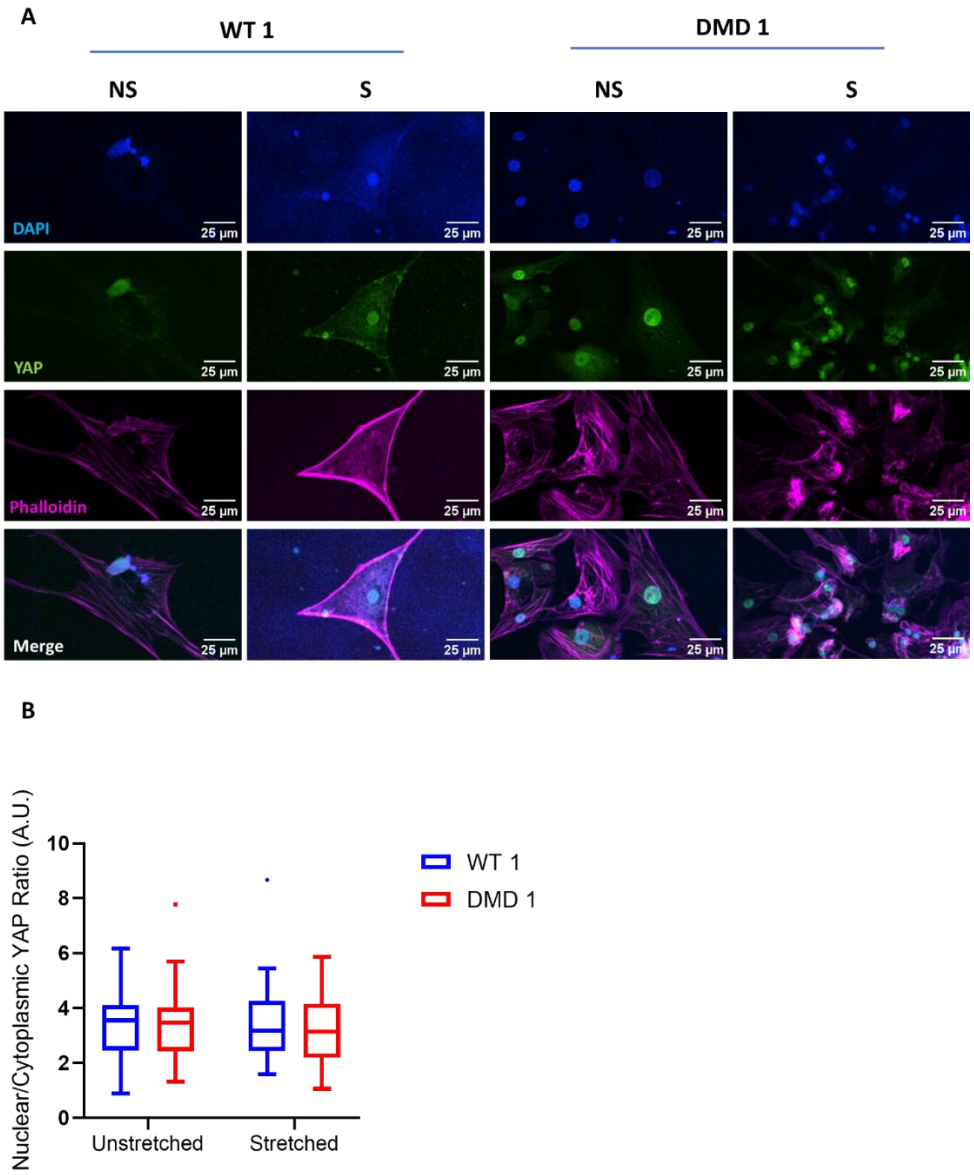

Figure 5.6: Preliminary Data of Nuclear to Cytoplasmic Ratio of YAP in Response to Cyclic Stretch. A) *Immunofluorescence showing YAP localisation in both WT 1 and DMD 1 hiPSC-CMs subjected to either no stretch or equibiaxial stretch,* ***B)*** *quantification of the immunofluorescence intensity. N= 1. Data are presented as a Tukey boxplot and are reported in the text as mean ± S.D. Statistics were not performed due to the N number.*

5.4 Healthy Cardiac Pressure leads to Alterations in Cellular and Nuclear Morphology in both WT and DMD hiPSC-CMs

5.4.1 hiPSC-CM Cellular Alterations in Response to Systolic Healthy Cardiac Pressure

Filling and ejection of blood results in cyclic pressure changes within the heart and the cyclic cardiac pressure generated impacts cardiomyocyte differentiation, homeostasis, and physiology. I wanted to examine the effect of healthy cardiac pressure (herein referred to as cardiac pressure) on WT and DMD hiPSC-CMs and employed the use of a cyclic cardiac pressure chamber to mimic cardiac pressure cycle (120/10 mmHg) over a 6-hr period whilst being maintained at 37^{o}C. hiPSC-CM cellular and nuclear morphology was then characterised to discern any patterns of similarity, or dissimilarity, between the cell lines in response to 120/10 mmHg. The selection of 6 hr as our time-point was based on previous work conducted within Dr Iskratsch's laboratory that found this to not negatively impact the cellular response, which was a critical consideration provided that the pressure chamber is sealed, thus preventing gas exchange. Later work within Dr Iskratsch's laboratory uncovered safe oxygen working levels beyond 12h[420]. The response to cyclic cardiac stress of all four hiPSC-CM cell lines was examined on both the 6 kPa and 130 kPa laminin coated PDMS substrate.

Characterisation of hiPSC-CM cellular morphology (Figure 5.7) revealed a significant decrease in cell area at 6 kPa in response to cardiac pressure for all cell lines, except for WT 2, which demonstrated no change of cell area in response to cardiac pressure.

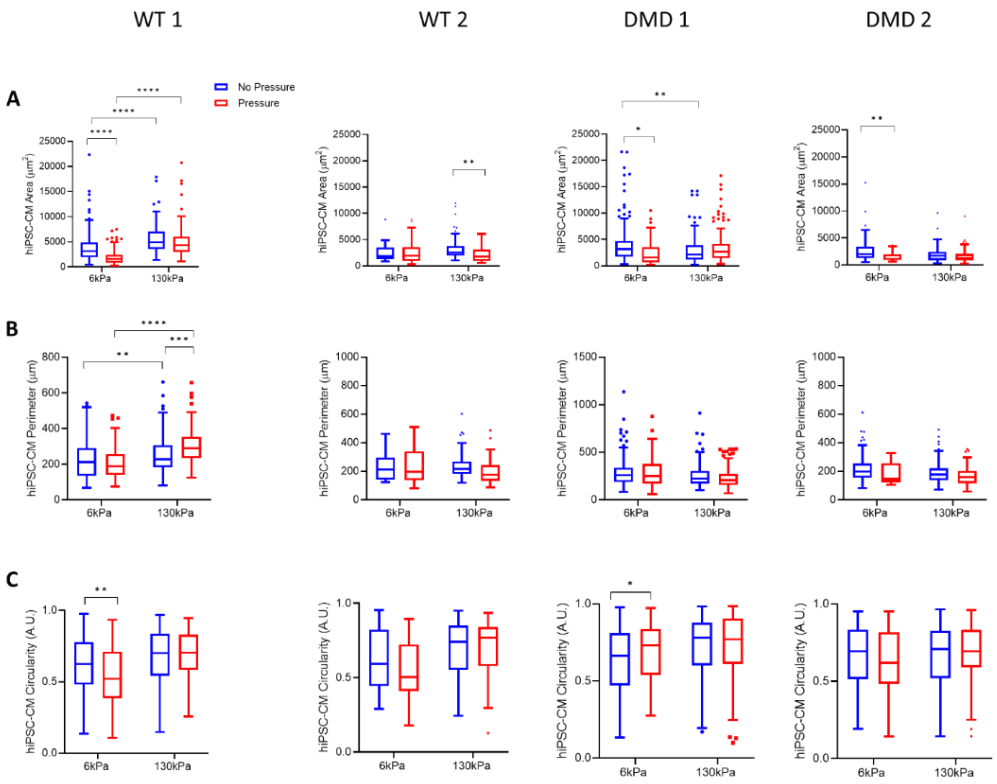

Figure 5.7: Cellular Morphology of hiPSC-CMs on Either a 6 kPa or 130 kPa laminin Substrate in Response to Cardiac Pressure of 120/10 mmHg. *Cell area was significantly decreased in all cell lines at 6 kPa except for WT 2. Interestingly, WT 2 was the only cell line observed to decrease cell area on the 130 kPa in response to systolic LVP.* ***B)*** *Cell perimeter did not change in response to systolic LVP, except for WT 1 at 130 kPa,* ***C)*** *Circularity only changed for WT 1 at 6 kPa. In contrast, DMD 1 became more circular at 6 kPa. hiPSC-CMs on 130 kPa did not change circularity in response to LVP. N = 3 biological replicates for all cell lines. Data presented as Tukey box plot and reported in text as mean ± S.D. Data analysed using 2-way ANOVA with Bonferroni's post-hoc test applied. P<0.05 was considered significant. Number of cells (n): WT 1, no pressure 6 kPa: 115; pressure: 136; WT 1, no pressure 130 kPa: 148; pressure: 98; WT 2, no pressure 6 kPa: 42; pressure: 40; WT 2, no pressure 130 kPa: 67; pressure: 39; DMD 1, no pressure 6 kPa: 182; pressure: 100; DMD 1, 130 kPa no pressure: 143; pressure: 139; DMD 2, no pressure 6 kPa: 81; pressure: 31; DMD 2, no pressure 130 kPa: 83; pressure: 83.*

All data are 6 kPa no pressure vs pressure: WT 1: 3950.8 ± 3215.4 µm^2 vs 1951.6 ± 1461.5 µm^2; WT 2: 2503.9 ± 1567.4 µm^2 vs 2661.8 ± 2305.5 µm^2;

DMD 1: 4005.0 ± 3639.9 μm^2 vs 2543.2 ± 2523.5 μm^2; DMD 2: 2387.9 ± 1388.7 μm^2 vs 1535.2 ± 847.0 μm^2. Representative images shown Figure 5.8-Figure 5.11.

Interestingly, the hiPSC-CM cell perimeter at 6 kPa did not significantly change in response to cardiac pressure for any of the cell lines, although, the perimeter for WT 1 increased whilst on the 130 kPa (255.6 ± 103.3 µm vs 308.5 ± 112.9 µm) in response to cardiac pressure. No change in perimeter was observed for other cell lines under any of the other pressure or substrate elasticity conditions. Circularity at 6 kPa was significantly decreased for WT 1 (0.62 ± 0.19 A.U. vs 0.54 ± 0.21 A.U.) but not for WT 2. However, DMD 1 showed an increase in circularity and no change in DMD 2 hiPSC-CMs. This indicated that the morphology of the hiPSC-CMs became less rounded, *i.e.,* more polygonal, with the exception of DMD 1 which became more rounded, in response to cardiac pressure.

When hiPSC-CMs were challenged using both the 130 kPa fibrotic substrate and cardiac pressure, the cell area was unaltered for hiPSC-CM cell lines- the exception being WT 2 (3292.2 ± 2274.6 μm^2 vs 2108.7 ± 1323.4 μm^2). Cardiac pressure did not affect cell perimeter on 130 kPa for all cell lines, with the exception of WT 1 which significantly increased its cell perimeter by 21%. Lastly, and unexpectedly, the circularity did not change in response to cardiac pressure at 130 kPa for any of the hiPSC-CM cell lines, indicating no change to the overall roundedness of the cells.

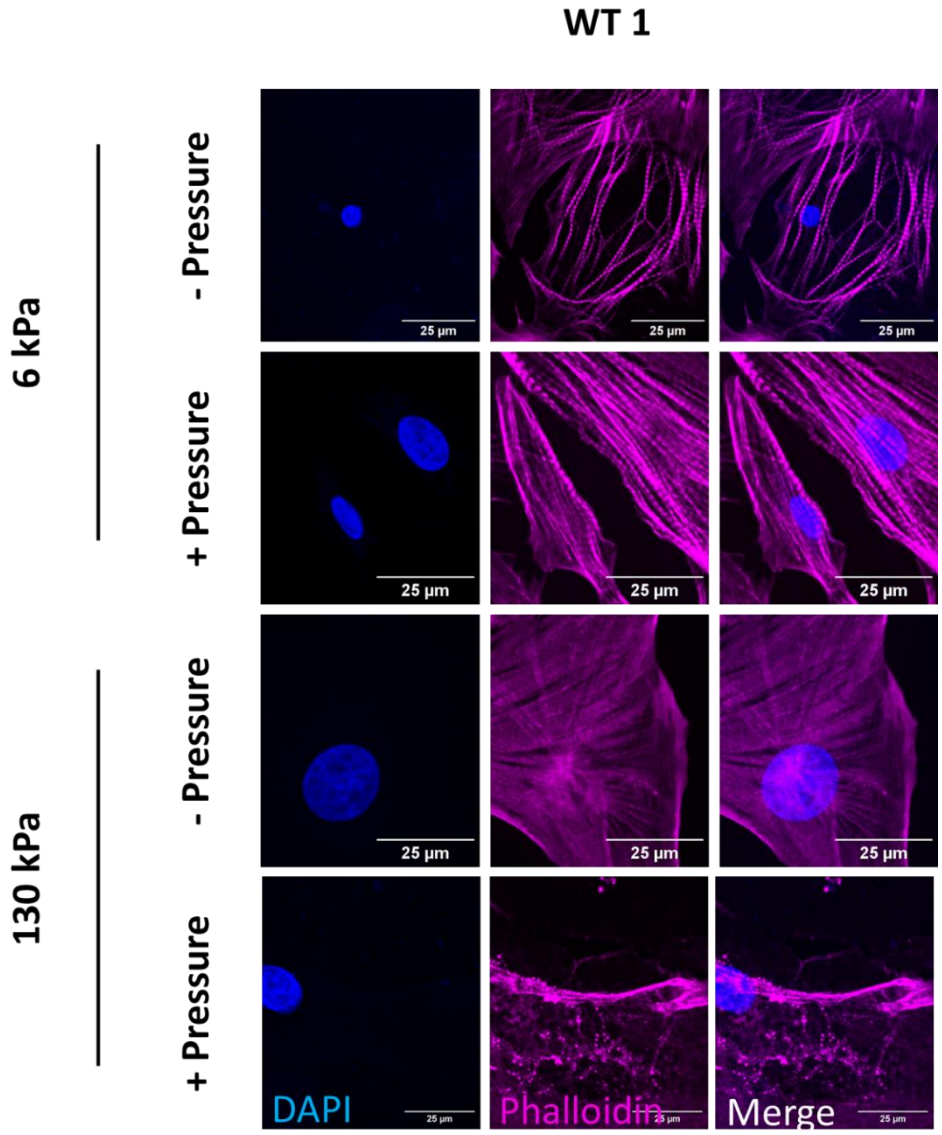

Figure 5.8: WT 1 hiPSC-CMs on Either 6 kPa or 130 kPa Laminin Substrate in Response to 6 hr; 120/10 mmHg Cardiac Pressure. *Immunofluorescence demonstrating the effect of cyclic cardiac pressure on WT 1 hiPSC-CMs. Quantification shown in Figure 5.7 and Figure 5.12. Scale bar = 25 µm*

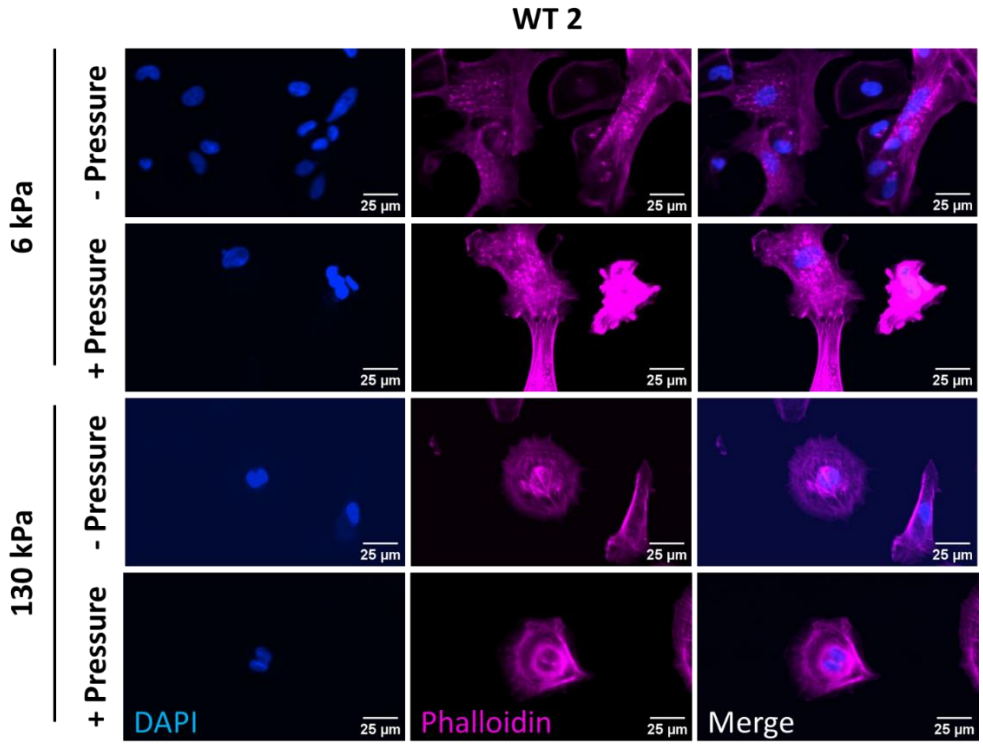

Figure 5.9: WT 2 hiPSC-CMs on Either 6 kPa or 130 kPa Laminin Coated Substrate in Response to 6 hr; 120/10 mmHg Cardiac Pressure. *Immunofluorescence demonstrates the effect of cyclic cardiac pressure on WT 2 hiPSC-CMs. Quantification shown in Figure 5.7 and Figure 5.12. Scale bar = 25 µm*

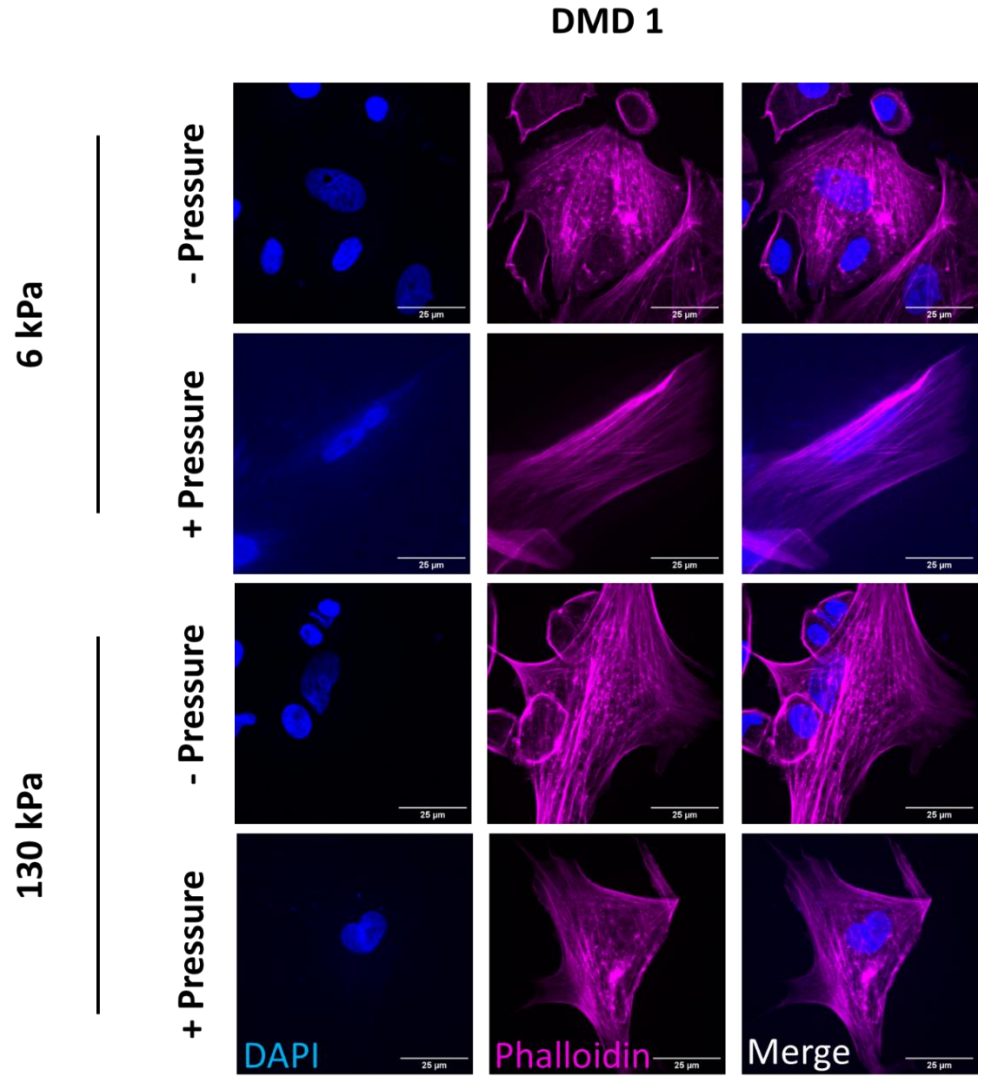

Figure 5.10: DMD 1 hiPSC-CMs on Either 6 kPa or 130 kPa Laminin Coated Substrate in Response to 6 hr; 120/10 mmHg Cardiac Pressure. *Immunofluorescence demonstrates the effect of cyclic cardiac pressure on DMD 1 hiPSC-CMs. Quantification shown in Figure 5.7 and Figure 5.12. Scale bar = 25 µm*

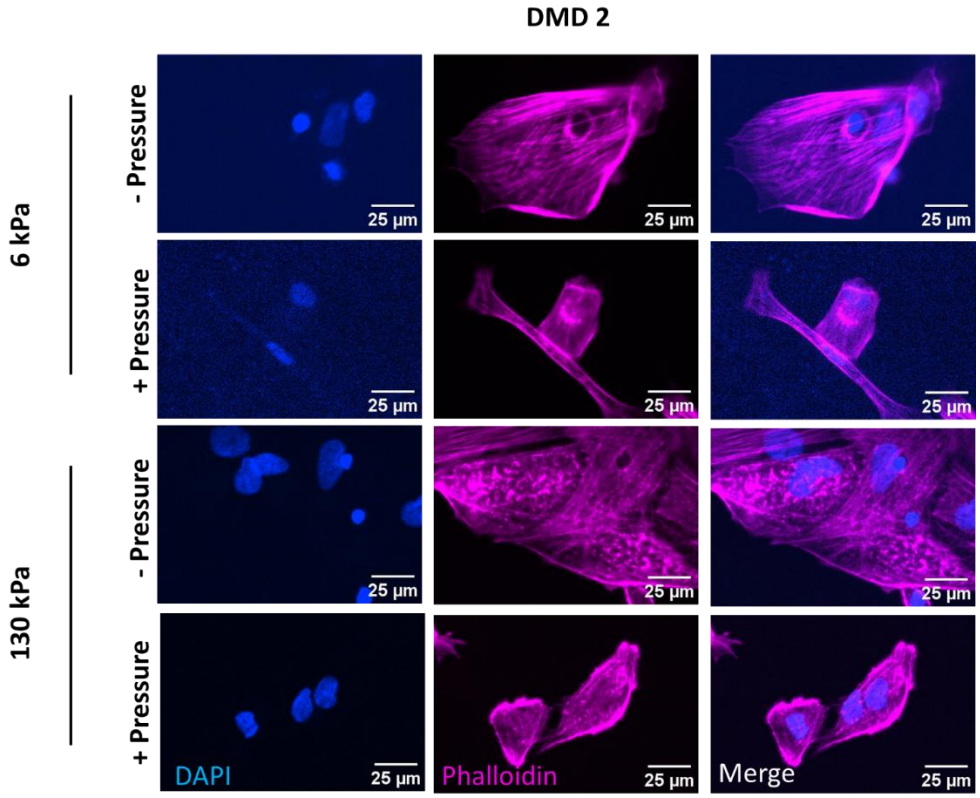

Figure 5.11: DMD 2 hiPSC-CMs on Either 6 kPa or 130 kPa Laminin Coated Substrate in Response to 6 hr; 120/10 mmHg Cardiac Pressure. *Immunofluorescence demonstrates the effect of cyclic cardiac pressure on DMD 2 hiPSC-CMs. Quantification shown in Figure 5.7 and Figure 5.12. Scale bar = 25 µm*

Together these data indicate that hiPSC-CMs do respond to the compressive force generated by cyclic cardiac pressure in that generally they become smaller, notably at 6 kPa. This is to be expected as the pressure produced within the chamber acting to compress the cells from all directions. Generally, the cell lines follow similar trends to one another *e.g.,* mostly decrease cell area and perimeter and this would suggest that dystrophin is not strictly required for hiPSC-CMs response to cardiac pressure. At 130 kPa, there was no change in area for WT 1 and a significant decrease for WT 2. Interestingly, DMD 1 and DMD 2 do not display a further

decrease in cell area potentially owing to an inability to withstand the fibrotic substrate elasticity.

5.4.2 hiPSC-CM Nuclear Alterations in Response to Systolic Healthy Cardiac Pressure

Next, I sought to characterise whether cardiac pressure had any effect upon the nuclei of the hiPSC-CMs, to reveal whether the pressure was being transduced inwardly via the LINC complex, according to the tensegrity model. I hypothesised here that the shape descriptors would decrease in response to cardiac pressure as pressure would be transmitted along the actin and microtubule cytoskeleton, thereby acting to compress the nucleus. Further, I hypothesised that the absence of dystrophin would mitigate this effect and the nuclei of DMD hiPSC-CMs would remain, largely, unaffected by the cyclic cardiac pressure.

Nuclear area was significantly increased (Figure 5.12A) in response to cyclic cardiac pressure on 6 kPa for WT 1 (119.8 ± 55.2 μm^2 vs 136.8 ± 68.2 μm^2) which contrasted with all other cell lines that showed no change. Similarly, nuclear perimeter (Figure 5.12B) was significantly increased in WT 1 hiPSC-CM nuclei (40.5 ± 16.4 µm vs 46.9 ± 11.4 µm) whereas WT 2 and DMD 1 demonstrated no change in perimeter. In contrast, DMD 2 nuclei were observed to significantly decrease in response to cyclic cardiac pressure on 6 kPa (38.9 ± 10.2 µm vs 34.1 ± 9.8 µm). Interestingly, circularity (Figure 5.12C) appeared to significantly decrease for both WT 1 and DMD 1 cell lines (WT 1: 0.88 ± 0.13 A.U. vs 0.75 ± 0.16; DMD 1: 0.94 ± 0.05 A.U. vs 0.88 ± 0.08 A.U.), but no change was observed for either WT 2 or DMD 2 cell lines.

Nuclear area at 130 kPa was observed to significantly increase for WT 1 and DMD 1 (WT 1: 136.7 ± 51.2 μm^2 vs 180.2 ± 68.8 μm^2; DMD 1: 134.9 ± 64.3 μm^2 vs 170.8 ± 70.4 μm^2) whilst DMD 2 and WT 2 revealed no change in response to cyclic cardiac pressure. Nuclear perimeter followed a similar trend as nuclear area on 130 kPa, with WT 1 and DMD 1 showing significant increases (WT 1: 41.9 ± 8.1 µm vs 53.6 ± 14.3 µm; DMD 1: 41.7 ± 10.2 µm vs 53.6 ± 23.7 µm). In contrast, DMD 2 and WT 2 displayed no change to nuclear perimeter. Lastly, in all cases, nuclear circularity was unchanged except for WT 1 which was significantly decreased (0.95 ± 0.05 A.U. vs 0.86 ± 0.09 A.U.) in response to cyclic cardiac pressure, indicating a polygonal morphology.

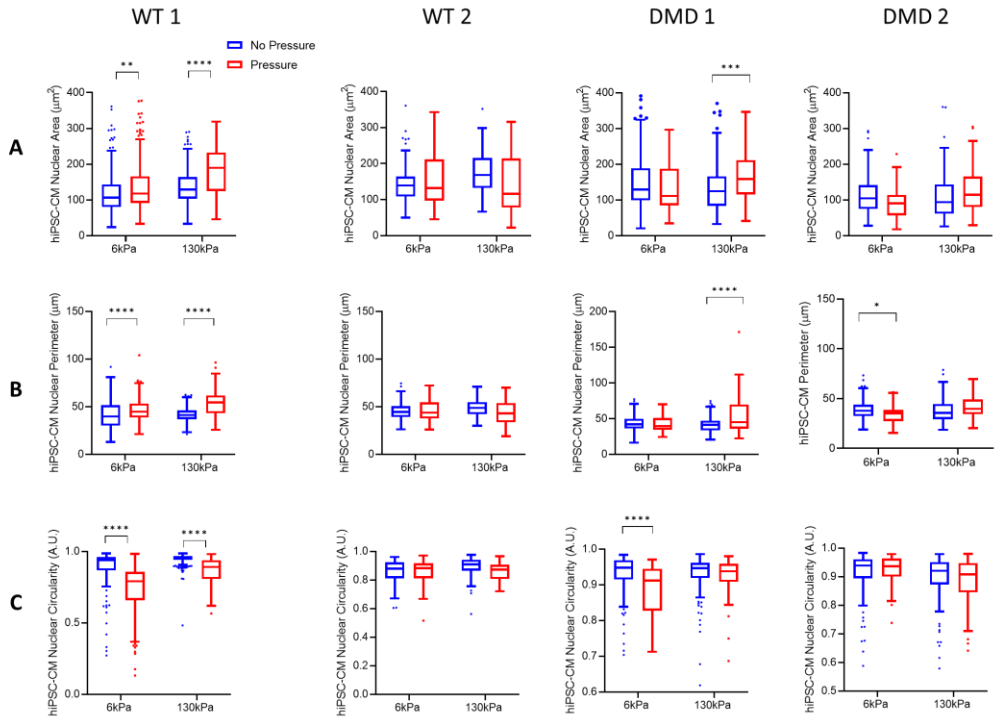

Figure 5.12: hiPSC-CM Nuclei Respond to Cardiac Pressure of 120/10 mmHg. A) *Nuclear area significantly increased at 6 kPa and 130 kPa for WT 1 and at 130 kPa for DMD 1 in response to cardiac pressure.* ***B)*** *Nuclear perimeter followed a similar trend as nuclear area,* ***C)*** *nuclear circularity generally decreased for all cell lines, with this being significant*

for WT 1 and DMD 1. N = 3 biological replicates for all cell lines. Data presented as Tukey box plot and reported in text as mean ± S.D. Data analysed using 2-way ANOVA with Bonferroni's post-hoc test applied. P<0.05 was considered significant. Number of nuclei (n): WT 1, no pressure 6 kPa: 138 ; pressure: 246; WT 1, no pressure 130 kPa: 178; pressure: 127; WT 2, no pressure 6 kPa: 47; pressure: 43; WT 2, no pressure 130 kPa: 60; pressure: 23; DMD 1, no pressure 6 kPa: 225; pressure: 45; DMD 1, 130 kPa no pressure: 187; pressure: 105; DMD 2, no pressure 6 kPa: 104; pressure: 37; DMD 2, no pressure 130 kPa: 105; pressure: 144.

Comparing the hiPSC-CMs, the cell area displayed no change at 6 kPa, however the perimeter of WT 2 was significantly increased compared to DMD 1 (WT 2, 234.3 ± 96.2 µm; DMD 1, 173.7 ± 80.6 µm, Figure 5.13). However, at 130 kPa, the cell area of WT 1 was significantly larger compared to all other cell lines (WT 1, 5096.3 ± 3262.4 μm^2; WT 2, 2108.7 ± 1323.5 μm^2; DMD 1, 3453.5 ± 3043.6 μm^2; DMD 2, 1677.1 ± 1235.7 μm^2). Similar observations were made for the hiPSC-CM perimeter. Consistent with cell area at 130 kPa, the perimeter of WT 1 was significantly larger compared to all of the other cell lines (WT 1, 308.1 ± 112.9 µm; WT 2, 198.2 ± 89.9 µm; DMD 1, 230.1 ± 106.9 µm; DMD 2, 167.6 ± 62.5 µm). However, given the inconsistency between WT 1 and WT 2, it is difficult to make clear assertions to the role of dystrophin under cyclic pressure, but the data do suggest a potential role of dystrophin in regulating cellular morphology.

My initial hypothesis expected to observe a decrease in nuclear area and perimeter but an increase in circularity for WT hiPSC-CMs, indicating mechanotransduction of the inward compressive force. I expected that this effect would be negligible for DMD hiPSC-CM nuclei, as the connection between the cytoskeleton and dystrophin is disrupted. However,

surprisingly, I often observed the opposite effect- increased nuclear area, perimeter, and decreased circularity, in response to cyclic cardiac pressure. Finally, qualitatively, the actin cytoskeleton in DMD hiPSC-CMs appeared to less well organised compared to WT hiPSC-CM cell lines, consistent with the results from the preceding chapter.

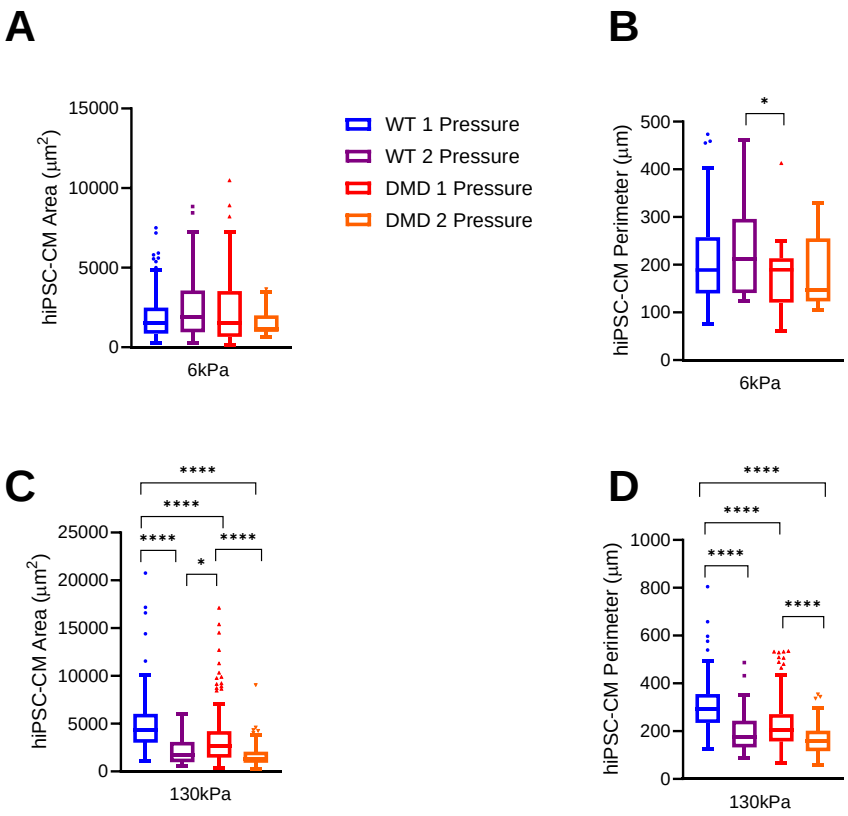

Figure 5.13: Comparison between hiPSC-CMs subjected to cardiac cycling pressure. A*) No change in cell area when subjected to pressure,* ***B****) The perimeter of WT 2 was significantly larger compared to DMD 1 but no other changes were observed.* ***C****) WT 1 was significantly larger compared to all other hiPSC-CMs in response to pressure. Interestingly, WT 2 was smaller compared to DMD 1, which in turn was larger than DMD 2.* ***D****) The perimeter of WT 1 was larger than all other cell lines. DMD 1 also displayed a significantly larger perimeter compared to DMD 2. Data presented as Tukey box plot and reported in text as mean ± S.D.*

Data analysed using 2-way ANOVA with Bonferroni's post-hoc test applied. P<0.05 was considered significant. N= 3.

Collectively, these data indicate that hiPSC-CMs used in this project were sensitive to left ventricular cyclic cardiac pressure, as demonstrated by the changes in cell morphology described. However, due to the variability between cell lines, the interaction between the presence/absence of dystrophin and pressure has been difficult to distil. Moreover, here I only tested physiological pressures, but effects might have been detectable or more pronounced under pressure overload conditions.

5.5 Microtubule Density is Increased in Dystrophic hiPSC-CMs and Unaffected by the Addition of Cardiac Cyclic Pressure

Extensive evidence implicates the microtubule cytoskeleton in a variety of failing heart models, including dilated cardiomyopathy and in DMD[59]. In particular, research shows elevated proliferation of the microtubule network, *i.e.* increased density, speculated to act as an adaptive compensatory response to increased mechanical stresses. However, over time, and in addition to posttranslational modifications, most notably detyrosination[60], this hyper dense microtubule network becomes deleterious to the functional ability of the cardiomyocyte, including healthy localisation of connexin 43 at intercalated discs[62].

In this vein, I wanted to examine whether the microtubule network was altered in my hiPSC-CM model in response to i) absence of dystrophin, ii) changes in substrate stiffness, and iii) in response to cardiac pressure. Here, I characterised the microtubule density as a function of overall cell area to examine whether the microtubule network was altered (Figure 5.14A). First, the microtubule network in DMD hiPSC-CMs was significantly larger

compared to WT. Here, DMD 1 hiPSC-CMs displayed a significantly hyperdense microtubule network in contrast to WT 1 at 6 kPa (DMD vs WT, 29% increase). Further, when challenged on a fibrotic elasticity, microtubule density in DMD 1 displayed an 8% increase compared to WT 1 (non-significant; Figure 5.14B). These data indicate that the absence of dystrophin does indeed impact the microtubular architecture.

Secondly, the microtubule density was shown to be sensitive to substrate elasticity. WT 1 hiPSC-CMs demonstrated a significant increase between 6 kPa and 130 kPa, where microtubule density increased by 20% in response to the altered elasticity. Interestingly, DMD 1 hiPSC-CMs did not recapitulate this phenotype and there was no difference of the microtubular network density between 6 kPa and 130 kPa with a <1% decrease change observed. This suggests that dystrophin is required for mechanosensing alterations in substrate elasticity and is responsible for communicating this mechano-information to the microtubules. Whereas the absence of dystrophin seemingly interferes with mechanotransduction. Strikingly, it also indicates that DMD 1 hiPSC-CMs already display a quite dense microtubule network, a finding consistent with previous reports.

Finally, I sought to examine if the microtubule network responded to application of cardiac pressure. It was intriguing to find that microtubule density appeared not to be sensitive to the application of pressure as demonstrated by apparent lack of change in both WT 1 and DMD 1 hiPSC-CMs.

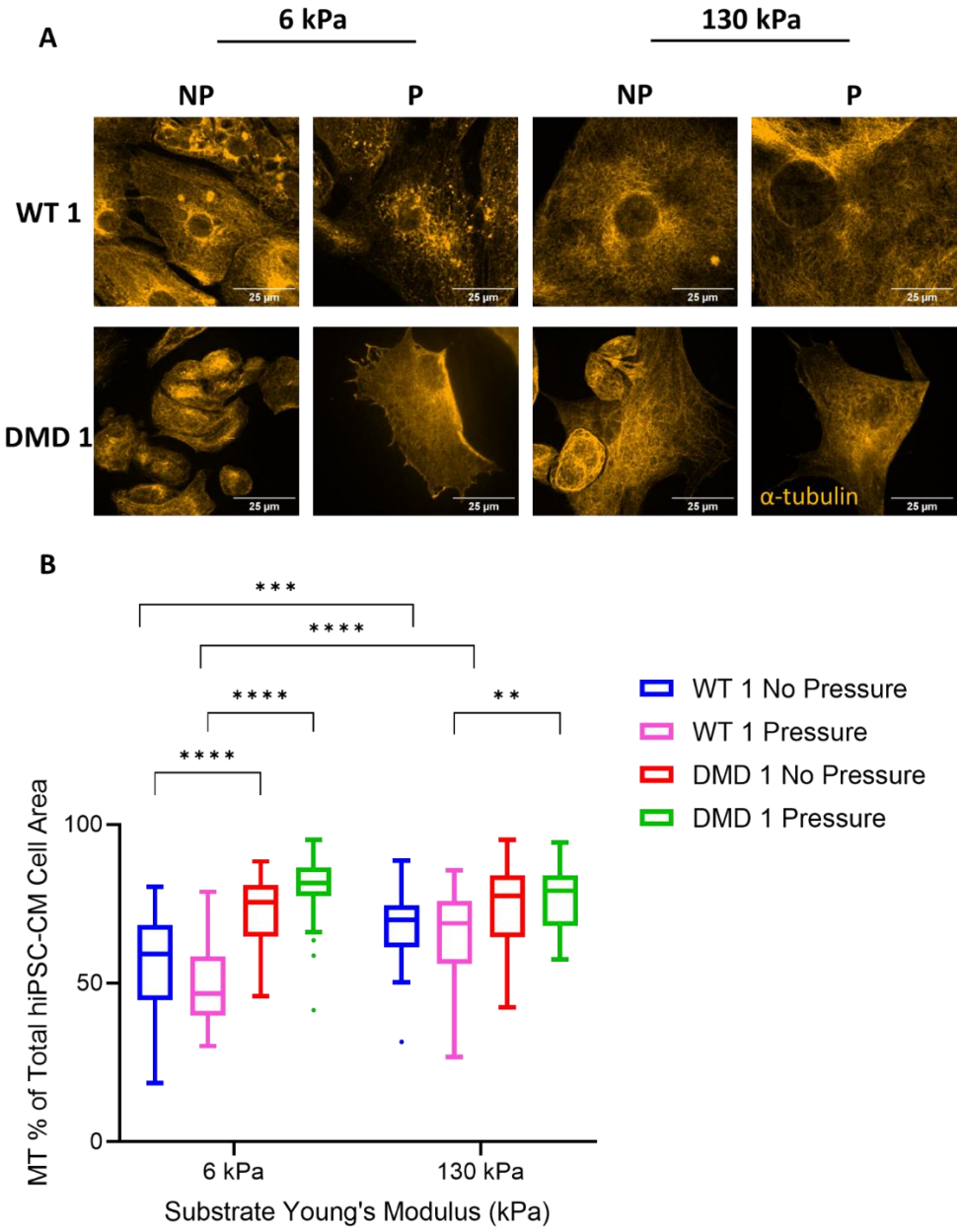

Figure 5.14: Microtubule Density is Mechanosensitive to Substrate Elasticity but not Cyclic Cardiac Pressure. A*) Immunofluorescence of α-tubulin for WT 1 and DMD 1 hiPSC-CMs on either a 6 kPa or 130 kPa laminin coated PDMS substrate in response to either atmospheric pressure (NP) or cyclic cardiac pressure of 120/10 mmHg (P),* ***B****) Quantification of microtubule density. Data are reported as Tukey box plot and reported in text as mean ± S.D. Data analysed using 2-way ANOVA with Bonferroni's post-hoc test. P<0.05 was*

considered significant. Biological replicate N= 3; hiPSC-CM cell number, n: WT 1, 6 kPa no pressure: 43; WT 1, 6 kPa pressure: 39; WT 1, 130 kPa no pressure: 32; WT 1, 130 kPa pressure: 32; DMD 1, 6 kPa no pressure: 36; DMD 1, 6 kPa pressure: 25; DMD 1, 130 kPa no pressure: 40; DMD 1, 130 kPa pressure: 36.

5.6 The Mechanosensitive Co-Transcriptional Activator, YAP, is Mislocalised in Dystrophic hiPSC-CMs Which is Not Further Exacerbated by Pressure

Previous groups[3,233] have shown the mechanosensitive co-transcriptional activator, YAP to be dysregulated in DMD, primarily in terms of nuclear to cytoplasmic ratio localisation. As a result of YAP's dysregulated localisation, the primary consequence is its loss of function. In particular, its involvement in cell proliferation, cell cycle regulation, and importantly, mislocalisation was shown to promote cardiomyocyte necrosis. Moreover, other studies have shown YAP nuclear localisation to increase as substrate elasticity increases, mainly via the increased opening of nuclear pore complexes[384]. Lastly, relatively recent work demonstrated that YAP was required for survival in mice subjected to a transaortic constriction model for pressure overload[430]. Therefore, based on the results from Chapter 4 where YAP was decreased at 6 kPa for DMD 1 hiPSC-CMs, in conjunction with previous groups work, I wanted to assess the impact on YAP localisation in DMD 1 hiPSC-CMs in response to cardiac pressure.

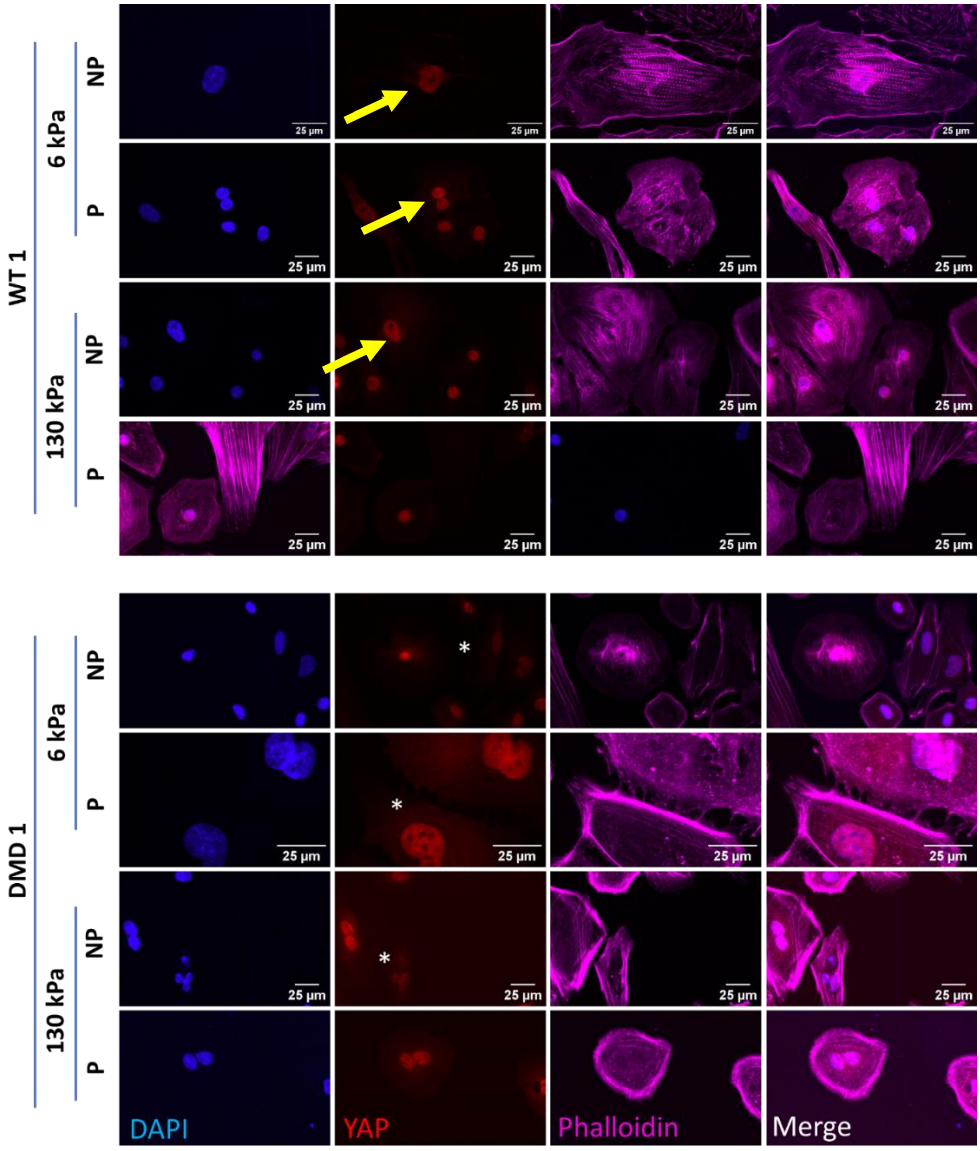

Figure 5.15: Nuclear YAP Localisation in Response to both Substrate Elasticity and Cyclic Cardiac Pressure. *hiPSC-CMs were plated on either a 6 kPa or 130 kPa laminin coated PDMS substrate and subjected to either atmospheric pressure (NP) or cyclic cardiac pressure (P) of 120/10 mmHg for 6 hr. The yellow arrows indicate increased nuclear YAP localisation in WT 1 hiPSC-CMs whilst the white asterisks indicate elevated cytoplasmic YAP in DMD 1 hiPSC-CMs. Quantification of the nuclear: cytoplasmic ratio is in Fig. 5.10. N= 2 biological replicates.*

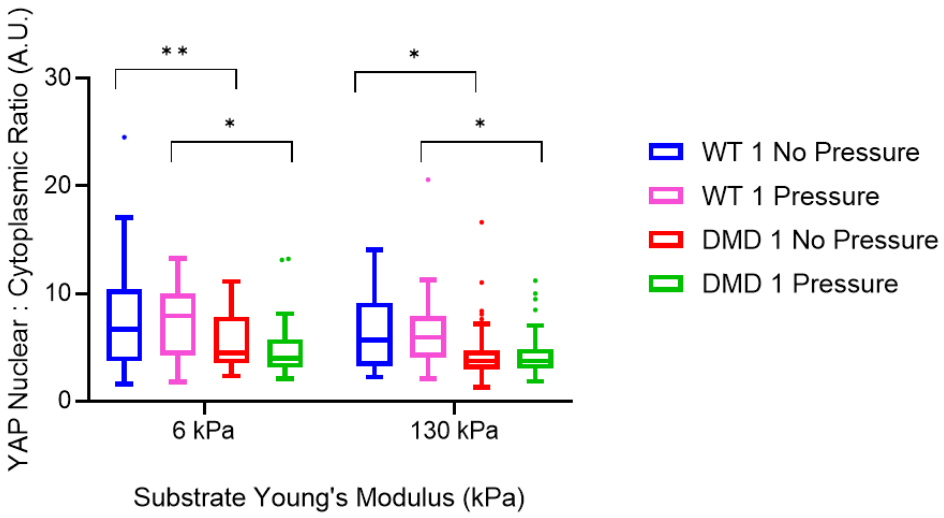

Figure 5.16: Quantification of the Nuclear to Cytoplasmic YAP Ratio for WT 1 and DMD 1 hiPSC-CMs in Response to both Substrate Elasticity and Cyclic Cardiac Pressure. *Quantification of hiPSC-CMs subjected to either atmospheric pressure (no pressure) or to cyclic cardiac pressure (pressure) of 120/10 mmHg for 6 hr. Representative images are shown in Fig. 5.9. N= 2 biological replicates, data analysed using 2-way ANOVA with Bonferroni's post hoc test and presented as Tukey's boxplot. Data are reported in text as mean ± S.D., $p<0.05$ was considered significant. Number of hiPSC-CMs per condition: WT 1, 6 kPa, no pressure= 46; with pressure= 25; WT 1, 130 kPa, no pressure= 25; with pressure= 49; DMD 1, 6 kPa, no pressure= 31; with pressure= 24; DMD 1, 130 kPa, no pressure= 66; with pressure= 60.*

YAP localisation in DMD 1 hiPSC-CMs showed a differential response dependent upon substrate elasticity. At both 6 kPa and 130 kPa, YAP nuclear localisation was significantly decreased compared to WT 1 hiPSC-CMs (WT 1 vs DMD 1, 6 kPa, pressure: 7.5 ± 3.1 A.U. vs 5.0 ± 2.9 A.U.; At 130 kPa: 6.2 ± 3.1 A.U. vs 4.1 ± 1.9 A.U.). This supports the notion that dystrophin plays a role in YAP localisation (Figure 5.15 and Figure 5.16).

Consistent with the finding in §4, nuclear localisation of YAP was observed to significantly decrease, even in the absence of the additional pressure stimulus (See previous chapter for more details). These data show that

whilst dystrophin plays a role in mechanosensing substrate elasticity, the mechanosensing of pressure is not mediated by dystrophin.

5.7 Discussion

In this chapter, I wanted to assess the impact of physiological mechanical stressors using the hiPSC-CM models developed to interrogate how dystrophin may be involved in the mechanoresponse to stretch and pressure. I split these two stimuli into separate experiments to isolate the effect from one another. Although, in the case of cyclic cardiac stress, this was coupled to different substrate elasticities.

In particular, I hypothesised that dystrophin is important as a mechanosensor, mediating force transmission in response to cyclic stretch and cyclic cardiac pressure, and that its absence would abrogate these observations. Indeed, I found that DMD hiPSC-CMs did show altered response compared to WT to these stimuli, revealing a role for dystrophin in mechanotransduction. Moreover, the data also validates the use of the hiPSC-CM model here for such experiments.

5.7.1 DMD hiPSC-CMs Demonstrate Increased Sensitivity to Cyclic Cardiac Stress

Firstly, I wanted to characterise the hiPSC-CMs in response to cyclic cardiac force that mimicked a healthy left ventricular pressure cycle of 120/10 mmHg to assess the effect on hiPSC-CMs and the role, if any, that dystrophin may have in mechanotransduction. In conjunction with cyclic cardiac pressure, different substrate elasticities were used to mimic healthy (6 kPa) and fibrotic (130 kPa) myocardial stiffnesses, with the aim of examining the dual effect of these mechanical cues, that would be present, in the DMD myocardium upon the hiPSC-CMs.

The application of pressure in this context is not solely from above the cell, but rather equal pressure from all angles. It was therefore expected that cell and nuclear morphology would decrease in response to the compressive force generated by the cyclic cardiac pressure which was what was observed for DMD hiPSC-CMs whilst on the 130 kPa substrate. In general, hiPSC-CMs behaved as expected under the compressive cyclic cardiac force, decreasing their overall area and perimeter. Unexpectedly, in some cases the opposite was observed, for example WT 1 cell perimeter at 130 kPa (Fig.5.2B), which may be attributable to the cyclic application of the cardiac pressure or underlying cellular response acting to reinforce the cytoskeleton, *i.e.* readjustment in accordance with tensegrity. That is to say, perhaps the nature of the cyclic application of force here rather than continual force can account for the findings. Alternatively, perinuclear actin caps may have promoted elongation and flattening of the cell and nucleus. Khatau[431] demonstrated this effect on nuclei in response to forces, although analysis of the volume and/or height of hiPSC-CMs and nuclei would be required. Unfortunately, the volume of nuclei was not examined and is the fault of the author. However, other reports examining nuclear morphology have prioritised cell area, perimeter, and circularity. Nonetheless, future work examining nuclear volume will be of upmost importance to further decipher the exact nature of any changes.

It is important to note here that, due to the manual method of delineating cell and nuclear boundaries, it is possible that in some cases human error may have generated erroneous results. To counter this, in future, increasing the data set as well as automating data analysis would better improve the overall interpretation and clarify the role for dystrophin here.

Previous groups have reported that the application of exogenous pressure caused cells to become smaller and more rounded[432–434]. Consistent with these groups, WT 1 and DMD 1 hiPSC-CMs did decrease in area and perimeter however, unexpectedly, did not become more rounded as described by circularity. Surprisingly, these changes were not observed for WT 2 or DMD 2 hiPSC-CMs. Here, I expected that all cells would become more circular in response to pressure. As has been described by previous groups, the absence of dystrophin mechanically weakens cardiomyocytes, rendering them susceptible to mechanical injury. It was therefore expected that DMD hiPSC-CMs would experience cyclic cardiac force more intensely compared to WT cell lines. Interestingly, this was not the case at 6 kPa but WT 1 was significantly larger compared to all other cell lines at 130 kPa. This may suggest either the heterogeneity between cell lines and/or a role of dystrophin in regulating, or protecting, against cardiac cyclic stress. Based on the data here, it is not possible to distinguish between these possibilities and further work is required to clarify.

In only a singular case did the circularity meet my initial expectations - DMD hiPSC-CMs on the 6 kPa substrate coupled to cyclic cardiac pressure. Intriguingly, the other cell lines failed to trend towards roundedness, with either no apparent change or, in the remarkable case of WT 1 on 6 kPa, becoming significantly less rounded; although, *in vivo* cardiomyocytes are not rounded in response to cardiac pressure and this finding may reflect that, to a small degree. Therefore, it is possible that the observations made here are expected and consistent with that found *in vivo* and the hypothesis requires revision.

Bourns et al.[434] observed that BSC-1 epithelial cells subjected to very large pressures of 430 atm (equivalent to 326800 mmHg) resulted in

heterogeneous cellular morphology, with large proportions of cells retracting and becoming rounded, whilst others had many spindle-like appendages and were less rounded. Of particular interest was their finding that epithelial cells fixed under pressure retained more of a rounded phenotype compared to those where pressure was released and cells were allowed to recover, even for as little as 5 min, prior to fixation. BSC-1 epithelial cells were observed to be polygonal and, above pressures of 290 atm, comprised of multiple surface microvilli as revealed by electron microscopy. This report may account for the polygonal finding in some of the cell lines reported in this thesis and opens up an avenue for further experimentation regarding the pressure experiments and fixation methods.

Furthermore, a study by Yamaguchi[435] examined the effect of high-pressure applied to isolated left ventricular murine cardiomyocytes and reported altered cell morphology. Specifically, they found that the width, or minor axis, of cardiomyocytes increased as a function of increasing pressure (0.1 MPa-20 MPa), giving a lower aspect ratio. This finding is inconsistent with the data here, where I reported either no change in aspect ratio, *i.e.* cells proportionately alter width and length, or increased aspect ratio, indicative of either lengthening of the cardiomyocytes or decreased width, for WT 1. However, Yamaguchi[435] utilised significantly larger hydrodynamic forces than I did; used murine cardiomyocytes and not iPSCs; and applied pressure for a shorter duration than I did here. Together, the different methods may account for conflicting observations. Interestingly, Yamaguchi [435] did report a decrease in sarcomere length in response to hydrodynamic pressure, which is an aspect not characterised here primarily due to a lack of time; although this would be an excellent follow up experiment.

Interestingly, on a healthy myocardial elasticity, there were no significant differences in cell area in response to cyclic cardiac stress between cell lines, indicating that perhaps it is the dual effect of pressure and fibrosis that causes significant alterations in cell morphology in DMD; with the structurally weaker DMD cardiomyocytes being less able to adapt to both mechanical stresses. In further support of this notion, cell perimeter of DMD hiPSC-CMs was not significantly different between cell lines on a 6 kPa substrate but was so on the fibrotic 130 kPa substrate. Although, an important caveat here is the assumption that the sarcolemma of the DMD hiPSC-CMs was structurally fragile which was not specifically tested during this thesis.

Why some of the hiPSC-CM cell lines reacted to cyclic cardiac pressure in this manner whilst others became more rounded is difficult to account for and may simply be a product of cell line variation. Alternatively, it may be that dystrophin counteracts the cyclic cardiac pressure preventing the cell from rounding, a finding consistent with the data here. This would be appropriate as to dystrophin's role as a mechanoprotector as well as being vital to the structural integrity of the sarcolemma.

I subsequently went onto to characterise nuclear morphology of hiPSC-CMs under cyclic cardiac pressure. Primarily, this was to examine whether compressive force was transduced inwardly. Cells perceive external forces at focal adhesions, of which the DGC is a component, and force is transmitted along actin stress fibres to the LINC complex[400,436,437]. Here, mechanical force can regulate a multitude of biological phenomenon including nuclear morphology[438], gene expression[197,198], and epigenetics[383,439]. Previous work has demonstrated the requirement for nesprin-1 (an outer nuclear membrane LINC complex protein connecting to

F-actin) as being essential for nuclear force perception. Indeed, disruption to the LINC complex uncouples nuclear mechanotransduction and is responsible for multiple disease states, including DCM[440] I therefore reasoned that uncoupling actin and microtubules, but from the sarcolemmal aspect, due to lack of dystrophin, should produce a similar effect on DMD nuclei. So, I hypothesised that nuclei would be less receptive to externally applied forces in DMD compared to WT, *i.e.* display no change to their nuclear morphology.

Here, the data stratifies into one of two distinct areas. Either the nuclei compressed under hydrodynamic pressure, or they did not and, surprisingly, their morphological parameters increased. Previous groups have shown, using a variety of methods to deliver external pressure to cells, that nuclei tend to compress under force, consistent with my hypothesis.

WT 1 and DMD 1 nuclei responded by increasing nuclear area and perimeter, with a concomitant decrease in circularity. These findings were contrary to the original hypothesis and were unexpected. However, the report by Khatau[431] is consistent with this data here. To confirm these data, Z-stack slices should be obtained and analysis of the nuclear height, volume, and average area performed, which as mentioned previously was not performed. Moreover, this underpins the necessity for isogenic pairs whereby relative effects can then be considered. Indeed, due to the large cell to cell variability increasing the overall *n* number here should help to clarify underlying effects that may be attributable to dystrophin.

Overall, hiPSC-CMs did appear to respond to the cyclic cardiac force imposed upon them and, in general, responded in a manner consistent with previous groups. DMD 1 and DMD 2 displayed significantly decreased

cell area and perimeter compared to WT 1 in response to cyclic pressure on a 130 kPa substrate. This indicates that there may be a role for dystrophin here and that DMD hiPSC-CMs did experience pressure more prominently compared to WT. However, confounding this interpretation, WT 2 was either no different or, was itself, smaller compared to DMD 1. The relevance of cellular morphology in response to mechanical cues is the influence over cardiomyocyte function, for example, sarcomeric architecture vital to cardiac contractiliy[441].

I have identified some key problems for the pressure data that are likely due to data acquisition and methods rather than describing novel biological phenomenon. In regard to the specific role of dystrophin, it has been difficult to distil out due to some of the issues discussed. Therefore, the role of dystrophin in regulating cellular and nuclear morphology under cyclic cardiac pressure remains unanswered fully and ambiguous, warranting further experimentation to confirm what role, if any, it plays.

5.7.2 The Microtubule Network is Dysregulated in DMD hiPSC-CMs that is Unaffected by Cardiac Pressure

Previous reports indicated that the microtubule network is severely dysregulated in both failing hearts and DMD[59,105,299], and responsible for Ca^{2+} dysregulation, X-ROS generation, and decreased diastolic elasticity. Therefore, I set out to ascertain whether microtubules were affected in my hiPSC-CM model and how they may respond to the dual effect of substrate elasticity and cyclic cardiac pressure. Here, I used microtubule density as a percentage of total cell area to determine changes to in microtubule density, as was utilised by Chen[105].

Interestingly, substrate stiffness, but not cyclic cardiac pressure, had an effect on microtubule density here. DMD hiPSC-CMs demonstrated significantly elevated microtubular density at 6 kPa compared to WT. Although, Although, no change was not observed at 130 kPa.

Excitingly, the microtubule density significantly increased between 6 kPa and 130 kPa for WT hiPSC-CMs, indicative of mechanosensation as described by tensegrity. This phenomenon is consistent with previous reports that found ECM stiffness to regulate microtubule polarity and density[442]. Moreover, this was absent in the DMD hiPSC-CMs that failed to demonstrate this effect. Dystrophin directly interacts with microtubules via its SR24 WW domain[199] and may communicate mechanical signals throughout the microtubule lattice. These data here support this conclusion and, in the absence of dystrophin the microtubule network is unable to adapt to the elasticity of the stiff substrate.

The addition of cyclic cardiac pressure to substrate elasticity did not affect either WT or DMD hiPSC-CMs. There was no significant difference between WT no pressure or WT pressure at either 6 kPa or 130 kPa (same for DMD), indicating that hiPSC-CMs used here were more sensitive to substrate elasticity than to pressure.

Bourns[434] reported little change in microtubule density in response to pressures up to 290 atm. At 320 atm, they reported an extreme depolymerisation in microtubules in response to pressure that they reasoned was due to interference in tubulin binding kinetics. This agrees with the data here showing that pressure does not affect the microtubule cytoskeleton. Although, interestingly, Bourns'[434] utilised pressure far exceeding those used here and observed *in vivo,* suggesting microtubules are less responsive to this particular mechanical stimulus. Moreover, other

reports have shown that microtubules appear to be particularly robust against high pressures, with one study reporting no microtubule disassembly even when subjected to 9 MPa[443]. Similar to the work here, these experiments were performed *in vitro* and not *in vivo* where it has been reported that microtubule depolymerisation more readily occurs. This is thought to be due to the overall disruption of cellular mechanics in response to pressure.

Considering previous reports have shown dysregulation of microtubules in DMD, this makes them an attractive therapeutic target. Dysregulated microtubules promote diastolic dysfunction due to elevation in passive viscoelasticity, *i.e.* decreased elasticity, rendering the overall cardiomyocyte stiffer. Moreover, posttranslational modifications have been implicated in microtubule dysfunction such as, de-tyrosination[60,420]. Additionally, microtubules have been implicated in transitioning between adaptive and maladaptive hypertrophy with a denser microtubule cytoskeleton being positively correlated with heart failure[444,445], consistent with the phenotype described in DMD patients. Moreover, it is consistent with the data presented here, thus validating my model for examining DMD.

Treatment of cardiomyocytes using colchicine or nocodazole to depolymerise the microtubule network were found to ameliorate the disease cardiac phenotype. These aspects were not explored during this work, primarily due to time. However, following up on the effect of the microtubule cytoskeleton in DMD, and the interplay between dystrophin and microtubules generally, would be a fascinating to follow-up and supplement the data presented here.

5.7.3 Nuclear Localisation of YAP is Not Sensitive to Cardiac Pressure Between WT and DMD hiPSC-CMs

I next sought to establish if the mechanosensitive transcriptional co-activator YAP was responsive to cyclic cardiac force. Here I expected that mechanical stimulation from pressure would increase the nuclear localisation of YAP. Given previous reports showing decreased and dysregulated YAP in DMD[3,376], I expected a lower nuclear to cytoplasmic ratio in the DMD cell line.

Consistent with the data presented in the preceding chapter, examination of the nuclear to cytoplasmic YAP ratio revealed a substantial decrease in DMD on both a 6 kPa and 130 kPa substrate compared to WT. Indeed, there was no change in nuclear YAP localisation in WT hiPSC-CMs subjected to pressure, but further work is required to discern any difference.

Nuclear localisation of YAP has previously been shown as sensitive to cyclic pressure *in vitro*[446,447] and pressure overload *in vivo*[430,448]. In particular, Park[447] demonstrated that cyclic pressure dephosphorylated serine residue 127, a key phosphorylation site on YAP that, when phosphorylated by LATS1, prevents its nuclear localisation. Moreover, they demonstrated that YAP nuclear localisation was contingent upon both actin and microtubule networks. Moreover, it hints at some of the mechanisms underpinning YAP localisation, for example the dephosphorylation of Ser127.

The data here contrasts with previous findings that YAP localisation is mechanosensitive to cyclic pressure. Secondly, in conjunction with the previous findings, the work here showed altered actin and microtubule networks in DMD hiPSC-CMs and may hint at the mechanism at play here, although this will require further validation.

Therefore, the hiPSC-CM model developed here may be utilised to develop therapeutic targets aimed at promoting YAP nuclear localisation, a feature significantly dysregulated in DMD.

5.7.4 Cyclic Stretching Induces Cellular and Nuclear Morphological Alterations in WT Cell Lines Demonstrating that Dystrophin is to Mediate this Response

Finally, I endeavoured to examine whether dystrophin was required for mounting cellular and nuclear morphological alterations to cyclic stretch. Cyclic stretch was selected as mechanical stimulus to mimic the contractile myocardial *milieu*. Other groups have utilised stretch to examine cardiac maturation[449], to mimic cardiac hypertrophy[450], and for YAP localisation[451].

The protocol utilised was derived from combining methods from two previous groups[452,453]. Previous reports suggested that hiPSC-CMs subjected to 10% elongation at 1 Hz were liable to detach[454] and Kreutzer[453,454] developed a pre-stretch ramp cycle (detailed in the methods section) that allowed hiPSC-CMs to adapt to the cyclic strain applied. In combination with this, the remainder of the cycling parameters (detailed in methods) were obtained from Quinlan[452].

Originally, I hypothesised that cyclic stretch would increase cellular and nuclear size (*i.e.* area, perimeter) in WT and that the DMD hiPSC-CMs would be largely unaffected, again due to the uncoupling of the ECM to the cytoskeleton.

In agreement with my hypothesis, I observed that cyclic stetch induced significant increases in cell and nuclear area and perimeter in WT cell lines, which were strikingly absent from DMD cell lines. Consistent with this data was the decreased circularity observed in WT hiPSC-CMs, indicating a move

from a circular morphology towards a polygonal one. Previous work has demonstrated that cyclic stretch induced stress-strain on the cytoskeleton is communicated to the nucleus[446]. Driscoll[446] reported an increase in nuclear area and height that was dependent upon an intact actin cytoskeleton. They observed that when depolymerisation of actin using cytochalasin D led to abrogation of the nuclear alterations observed[446].

Their data supports the findings presented here, where nuclei in WT hiPSC-CMs positively responded to cyclic stretch, whereas DMD 1 did not. As mentioned previously, alterations to the cellular and nuclear morphology are important determinants for cardiomyocyte function[441]. Therefore, the inability of DMD hiPSC-CMs to mount morphological alterations in line with WT cells, implies underlying cellular dysfunction. However, in this chapter no overt functional assays of DMD to confirm this notion were performed.

This data supports that requirement for dystrophin in mediating this observation and is likely due to its direct interaction to the actin and microtubule cytoskeleton frameworks, especially with actin which is a known regulator of cell morphology.

Furthermore, the nuclear morphology of DMD 2 hiPSC-CMs responded similarly to both WT cell lines, whilst the DMD 1 cell line did not. This is particularly striking as the DMD 2 cell line produces the truncated, but functional, Dp71m isoform of dystrophin. In opposition to this, DMD 1 has a complete absence of dystrophin. This data suggests that, despite no apparent cellular level changes observed in DMD 2, Dp71m may be a viable mechanotransducer communicating mechanical signals to the nucleus. Previous groups have reported nuclear localisation of Dp71 using C2C12 cell line although did not offer any functional rationale for its presence other than to speculate that it may regulate transcription factors[455].

Perhaps more compellingly, further work using distinct Dp71 isoforms (Dp71f) were shown to be associated with the actin cytoskeleton in platelets and were a vital component in platelet cytoskeletal rearrangement during aggregation[456]. Lastly, it has also been reported that Dp71 associated with focal adhesion complexes, in particular the β-integrin subunit, talin, vinculin, and α-actinin in neuronal PC12 cells[227]. Together, the data provided by these groups suggests that Dp71 may indeed be mediating some of the compressive force perceived by the DMD 2 hiPSC-CM cell line and was able to be an effective mechanotransducer. Unfortunately, this aspect was not further explored during this work but would make for an exciting future project.

Lastly, similar to the cyclic cardiac pressure assays, I wanted to examine whether YAP localisation was mechanosensitive to cyclic stretch. Multiple groups have demonstrated that cyclic stretch facilitates increased nuclear YAP localisation[384,457], that may be dependent upon intact actin cytoskeleton, nesprin-1, and may be regulated by elevated c-Jun N-terminal (JNK) kinase[457]. Here, I observed no apparent change in YAP nuclear localisation in response to the cyclic stretch regimen between WT and DMD cell lines. However, this experiment is limited by the small *N* number.

5.7.5 Limitations, Future Work, and Chapter Conclusions

The work presented in this chapter is not without limitation. Isogenic pairs mitigate the genetic differences apparent between cell lines, allowing examination of the mutation in question.

To compensate for this, future work could utilise the WT 1 and WT 2 hiPSC cell lines in conjunction with siRNA against dystrophin. Indeed, I aimed to carry out this experiment, however the siRNA arrived after my time in the

laboratory concluded. However, the use of siRNA could clarify the above experiments, in particular the cellular and nuclear morphology in response to cyclic cardiac pressure. Moreover, characterisation of cellular and nuclear morphology could be improved by the addition of Z-stacks to determine volume and an average cell/nuclear area that may prevent erroneous interpretations. Unfortunately, these were not ascertained during the project. Nonetheless, the nuclear parameters presented here are consistent with many other groups, which we extensively characterised. However, future work should characterise nuclear volume[241,458,459].

The microtubule experiments were limited by assessment of total α-tubulin alone and within a singular Z-plane. Better characterisation would be achieved by performing Z-stacks to assess different aspects of the microtubule lattice, for example the surface cortical layer versus the internal layer. Further, whilst the microtubule density was significantly increased, confidence in the data could be improved by the addition of western blotting. Finally, it would be interesting to examine the impact of (de)polymerisation drugs to further tease apart the role of the microtubules under different mechanical stresses.

The characterisation of nuclear YAP localisation was performed using a singular method based on the immunofluorescence intensity, and as such, are limited. Further experimentation supplementing these data could include RT-qPCR and western blots to determine if the protein expression was altered. Assessment of phosphorylated YAP, and the ratio to YAP, could also be conducted to determine the response of YAP more fully to pressure. For cyclic stretch, these experiments should also be performed in addition to bolstering the *N* number, which in this case was only 1. Examination of

downstream genes of YAP, such as *CTGF* and *ANKRD1*, could also be carried out to determine its activity.

To characterise the mechanism of YAP more fully, rather than simply demonstrating its localisation, more comprehensive experiments could be carried out including the effect of the cytoskeleton on YAP localisation. For example, treatment using cytochalasin D or nocodazole to disrupt actin or microtubule respectively could elucidate the interaction between these components. Moreover, this could clarify the role of dystrophin in these contexts. More sophisticated experimental setups such as optogenetics could also further clarify how pressure or cyclic stretch affect YAP. However, these were not performed here primarily due to time-constraints.

The response of hiPSC-CMs to stretch was limited by assessing this in isolation, which was in contrast to the majority of the complementary mechanical experiments carried out throughout this work. It would have been of particular interest to examine the dual effect of substrate stiffness and cyclic stretch to better mimic the fibrotic cardiac environment. Some groups have reportedly developed a method for utilising PDMS in conjunction with the Flexcell® device for this purpose. This would be an exciting avenue to explore. Furthermore, similar to the pressure chamber, the pressure experiments were limited by a lack of a more comprehensive characterisation mechanosensitive genes and proteins. Given the nature of the mechanical stimuli, the interaction between WT and DMD could reveal interesting aspects of focal adhesion proteins including FAK, pSRC, and integrin activation, potentially revealing cross-talk between dystrophin and integrin focal adhesion complexes.

Lastly, it would be interesting to examine longer term effects of cyclic stretch and cyclic cardiac pressure upon the hiPSC-CMs. The current

modality of pressure application in our laboratory limits extended use (>18-24 hr) due to it being unable to facilitate gas exchange. However, the Flexcell® system could allow for longer term assays to be performed. Carrying out various time-series to assess the effect of pressure or stretch may reveal, as yet undiscovered, nuances that complement the current data.

In conclusion, this chapter sets out a role of dystrophin in mechanotransduction particularly in response to cyclic stretch but that it is dispensable for pressure sensing. The data revealed that DMD hiPSC-CMs were less capable of adapting to the mechanical stimuli compared to WT. Moreover, localisation of the transcriptional co-activator YAP was not shown to be significantly downregulated in DMD compared to WT in response to pressure nor cyclic stretch. These data support dystrophin as being instrumental in the perception of physiologically relevant mechanical stimuli, such as stretch, but is not required for pressure sensing. Moreover, they enhance our understanding of how hiPSC-CMs afflicted by DMD respond to such stimuli. The data here offers a hint at therapeutic targets, for example YAP.

6 General Discussion

I can't understand why people are frightened of new ideas. I'm frightened of old ones.

John Cage

One of the mot cowardly things ordinary people do is to shut their eyes to facts.

C.S. Lewis

6.1 General Discussion

Evidence has revealed dystrophin as a critical mechanoprotector of the sarcolemma in striated muscle tissue, actuated via its spring-like action[8], that is inherent to the extensibility afforded by the SR domains. Additionally, dystrophin localises and stabilises the protein constituents of the DGC[135], forming a macromolecular complex. Mechanosensitive accessory proteins localise here, thereby effecting the DGC as a signalling nexus. The *locale* of dystrophin at the costameric[460] region of cardiomyocytes, perfectly positions dystrophin for its performance in this capacity, where it dissipates laterally transmitted mechanical forces[460]. Moreover, dystrophin forms interactions to the actin[461] and microtubule[199] cytoskeleton, connecting the cardiomyocyte to the ECM.

Mutations within the *DMD* gene are the cause for the severe, monogenic, X-linked disease Duchenne muscular dystrophy (DMD), which is characterised by the absence of dystrophin[462]. Critically, DCM has been revealed as the primary cause of death in the DMD population, with the majority of patients succumbing to end-stage heart failure by their third decade[325]. Therapeutic strategies are currently palliative with no effective cures available. Therefore, the elucidation of the underpinning molecular mechanisms that drive the DMD associated DCM is vital.

The work presented here aimed to better characterise and define the role of dystrophin regards mechanotransduction. A summary of key findings between cell lines, relative to WT 1, are presented in Table 6.1.

Table 6.1: Comparison of hiPSC cell lines from key experiments. *All measurements presented are relative to WT1*

			WT2	DMD1	DMD2
Substrate Stiffness	6 kPa	Cell Area	-	↑	-
		Cell Perimeter	-	↑	-
		Nuclear Area	↑	↑	-
		Nuclear Perimeter	-	-	-
	130 kPa	Cell Area	-	↓	↓
		Cell Perimeter	-	-	↓
		Nuclear Area	↑	-	↓
		Nuclear Perimeter	↑	-	-
Cardiac Pressure (120/10 mmHg)	6 kPa	Cell Area	-	-	-
		Cell Perimeter	-	-	-
		Nuclear Area	↑	↑	-
		Nuclear Perimeter	-	-	-
	130 kPa	Cell Area	↓	↓	↓
		Cell Perimeter	↓	↓	↓
		Nuclear Area	↑	-	↓
		Nuclear Perimeter	↑	-	-
Cyclic Stretch	Stretched	Cell Area	-	↓	↓
		Cell Perimeter	↓	↓	↓
		Nuclear Area	↑	-	-
		Nuclear Perimeter	↑	-	-
Young's Modulus	6 kPa		N/A	↓	-
	130 kPa		N/A	↓	↓
Sarcomere Length	6 kPa		N/A	↓	N/A
	130 kPa		N/A	↓	N/A
YAP (nuclear to cytoplasmic ratio)	6 kPa		N/A	↓	N/A
	130 kPa		N/A	-	N/A
Heart Rate	bpm		-	↓	-

6.2 Chapter 3: Development of hiPSC-CMs

In Chapter 3, I sought to develop and characterise the hiPSC and hiPSC-CM cell lines that would be used throughout the PhD project. This aspect was fundamentally critical to the overall project. First, I ensured that the hiPSC cell lines were pluripotent via immunocytochemistry (ICC) and RT-qPCR characterisation, consistent with reports from other groups[319,320,327,463]. Specifically, examination of critical pluripotency biomarkers (NANOG, SOX2, OCT3/4, SSEA-4, TRA-1-60) was sufficient to determine pluripotency. Teratoma formation assays to assess pluripotency were not performed in this work as this had been carried out previously within Dr Lin's laboratory. Further, a karyotype assay could have been conducted to demonstrate whether the hiPSCs had acquired any chromosomal mutations, specifically insertions-deletions. Again, this had previously been conducted within Dr Lin's laboratory with no such mutations reported. However, karyotyping was not routinely performed, which is a key critique. Assessing the karyotype of hiPSCs should be routinely carried out to ensure the quality of the hiPSCs is being maintained.

Nevertheless, sufficiently satisfied with the pluripotency and growth of the hiPSCs, I next sought to ensure that the correct mutations were present. To assess mutations within the hiPSCs, I leveraged PCR and genome sequencing to show the Δexon 52 deletion and the c.9691C>T (p.Gln3231*) respectively. For the DMD hiPSC cell lines utilised, the mutations were correct.

An unfortunate aspect of this project was the lack of isogenic controls. Isogenic controls mitigate inherent cell line variability by maintaining the same genetic background to the mutant cell line, except without the mutation. It had been expected from Dr Lin's laboratory to acquire such

hiPSCs but, due to contamination events and mixed populations, these cells were unavailable. Therefore, in addition to statistically comparing cell lines directly, here I compared trends from within individual cell lines to one another. For example, WT 1 responded to cyclic stretch whereas DMD 1 did not. Due to time-constraints, I was unable to *de novo* generate isogenic cell lines for the project and isolation from mixed populations failed.

Secondly, I successfully generated hiPSC-CMs for the four cell lines utilised throughout this project. The protocol was primarily based on work by Burridge[320], with the addition of triiodothyronine and dexamethasone as described by Parikh[327]. hiPSC-CMs displayed positive expression of key structural and cardiogenic proteins, including TNNT2, α-actinin, NKX2.5, and ISL-1, as determined by RT-qPCR and ICC[326,397]. Moreover, I demonstrated that DMD hiPSC-CMs lacked dystrophin expression compared to WT. Future work could explore the impact of dystrophin on the maturation of hiPSC-CMs as well as how this may be modulated by the addition of drugs such as Triiodothyronine and dexamethasone.

Furthermore, DMD 1 hiPSC-CM displayed a significantly decreased heart rate compared to WT 1 and DMD 2 hiPSC-CMs, a finding consistent with the observed DMD cardiac pathology[104]. Interestingly, this may be attributable to the fact that DMD 2 expresses the small Dp71 dystrophin isoform known to localise at T-tubules within cardiomyocytes. Plausibly, Dp71 may play a role in maintaining excitation-contraction coupling that the DMD 1 cell line cannot due to the total absence of all dystrophin isoforms. Further work directed at dissecting apart the distinct roles between dystrophin isoforms will be an exciting future project, and this can also be couple with the preceding point examining the effects of dystrophin on maturation of cardiomyocytes.

Despite the success of the cardiac differentiation protocol there were several limitations to the work. The future inclusion of isogenic pairs will further clarify the role of dystrophin in the function of cardiomyocytes. Further characterisation of hiPSCs and hiPSC-CMs could have been performed, such as teratoma formation assays to more fully demonstrate pluripotency, and karyotyping to exclude unexpected chromosomal abnormalities. However, these had been previously carried out within Dr Lin's laboratory as well as by the companies the cell lines were acquired from. In conjunction with the data that I acquired, I felt sufficiently confident about the status of the hiPSC cell lines. Furthermore, the successful differentiation of the hiPSC cell lines towards a cardiac lineage strongly supports this conclusion.

With regards to hiPSC-CMs, these could also have undergone a more thorough characterisation process than presented. For example, additional genes may have been characterised, such as *MEF2C, MESP1,* or *GJA1*[320]; ion channel expression could have been determined, such as MLC2V and MLC2A[464]; and western blots could have been performed to quantify the protein levels of cardiac specific proteins. That being said, the characterisation here is consistent with that of many groups[320,327,348,355,463,465]. Whilst there is potential for more extensive characterisation, I felt sufficiently confident that the hiPSC-CMs generated were functionally adequate. hiPSC-CMs spontaneously contracted and displayed positive expression of cardiac genes and proteins via ICC and RT-qPCR. The detail provided by groups such as Burridge[320] and Lian[319] is likely due to their initial development and improvement of cardiac protocols, whereby exhaustive characterisation is required.

Despite significant efforts to advance maturation, hiPSC-CMs are limited by their foetal-/embryonic-like maturity[343]. The development of 3D engineered heart tissues (EHTs) has advanced not only the maturity of hiPSC-CMs but also improved the platform to better reproduce the physiological *in vivo* scenario[388,466,467]. 3D EHTs can be developed as small array platforms requiring as few as 16,000 hiPSC-CMs to function[466]. Co-culturing hiPSC-CMs with endothelial cells and fibroblasts further enhances 3D EHTs whilst improving their similarity to *in vivo* myocardial tissue. This appears to be a direction that the cardiomyocyte field is increasingly embracing, and the work here would benefit immensely from the use of 3D EHTs. Not only can single-cell hiPSC-CMs be isolated from the 3D EHT for analysis, but it also offers the potential to explore tissue level dynamics. The ability to analyse the mechanical and functional distinctions in DMD would be significantly advantageous to our understanding of the DMD cardiac pathology.

In sum, I successfully generated WT and DMD hiPSC-CMs from functional and maintainable hiPSCs that displayed biomarkers consistent with cardiac differentiation and were considered to be suitable for further experiments.

6.3 Chapter 4: Biomechanics of hiPSC-CMs

For Chapter 4 I sought to elucidate the mechanics of hiPSC-CMs on either a healthy or fibrotic substrate elasticity. Moreover, I wanted to assess how dystrophin may have potentiated any detectable effect. In general, the hiPSC-CMs were capable of mechanosensing and responding to alterations of their environment, as determined by altered cell and nuclear morphology.

Substrate stiffness is a well characterised regulator of cardiomyocyte function[83,468,469]. Here, WT 1 and WT 2 hiPSC-CMs increased cell area in response to increased substrate stiffness. This was absent in DMD 1 hiPSC-CMs. Moreover, the perimeter was shown to increase in WT 1 hiPSC-CMs as well as the circularity. DMD 1 displayed alterations to these morphological metrics too. Previous reports have shown increased cell area in response to increased Young's modulus[83,86,470–472], with the requirement for an intact cytoskeletal network throughout the entire cellular network. It is interesting that the cell area did not increase in DMD 1 hiPSC-CMs here and suggests the requirement of dystrophin to mediate this response.

Moreover, substrate elasticity governs the architecture and dynamics of the cytoskeleton[396]. Previous groups demonstrated the importance of native cardiac elasticity for optimal beat rate, force production, cytoskeletal architecture, and sarcomeric[472]. Alterations of the Young's modulus in the substrate can result in these features becoming increasingly disrupted. For example, sarcomeric banding of F-actin and α-actinin[470] was lost in cardiomyocytes cultured on large Young's moduli (> 50 kPa). The work here agrees with these studies, particularly with regard to the coherency of actin, as supported by the WT 1 data. Fundamentally, these studies reported that ECM dynamics may be viewed as an extension of cell behaviour, and thus, if the ECM-cell interface is disrupted, the cardiomyocyte is incapable of governing this. DMD 1 hiPSC-CMs displayed a significant reduction in coherency of the actin cytoskeleton consistent with an isotropic and disorganised structure that may be a significant contributor to DMD's inability to adapt to fibrotic-like stiffness. Moreover, sarcomere length was significantly decreased in DMD 1 compared to WT 1 hiPSC-CM, again suggesting cytoskeletal disorganisation and dysregulation,

and is supported by other groups' findings[316,388,472]. Additionally, decreased sarcomere length may lead to decreased force production as reported by others, although force production was not directly analysed within this PhD.

The localisation of the mechanosensitive transcriptional co-activator, YAP was also significantly decreased in DMD 1 hiPSC-CMs compared to WT whilst on a healthy substrate stiffness. This supports the notion that DMD 1 hiPSC-CMs are less able to mechanosense microenvironmental signals to enact genetic alterations. However, at 130 kPa there was no significant change between WT 1 and DMD 1 hiPSC-CMs. This was likely due to the *n* number sample size and further work is required here to clarify this result, especially as this is inconsistent with other groups showing elevated nuclear YAP localisation as force increases[384,473]. A reduction in the number of actin fibres may account for this phenomenon in DMD 1 hiPSC-CMs whereby less force is applied to the nuclear pore complexes, though this fails to account for the observation in WT 1.

Next, I sought to determine the Young's modulus of the hiPSC-CMs and how this may be affected by altered substrate elasticity using nanoindentation. WT 1 hiPSC-CMs were significantly stiffer compared to both DMD 1 and DMD 2 hiPSC-CMs. This suggests an underlying disruption to the actin cytoskeleton, a key determinant of cellular viscoelasticity in this case[271,415]. The decreased Young's modulus of DMD hiPSC-CMs is consistent with the decreased coherency of actin I described earlier. Moreover, it implicates dystrophin as a critical regulator of cardiomyocyte stiffness. It is unlikely that the decreased stiffness is due to dystrophin alone *per se*, but more likely attributable to the ECM-cell interface mediated by dystrophin's connection to the underlying cytoskeleton. In this manner, dystrophin

permits mechanotransduction and allows the cytoskeleton to respond to environmental changes[132,461]. Dystrophin appears to have a role towards rigidity sensing and modulation of the actin cytoskeleton accordingly to maintain force equilibrium, as described by tensegrity[189].

In addition to this, the viscoelasticity was significantly different between the cell lines as revealed by dynamic mechanical analysis. Consistent with previous groups[391] there was a frequency dependent increase in *E', E",* and *Tan δ.* At 6 kPa WT 1 was shown to be significantly more elastic compared to DMD 1, which is consistent with the role of dystrophin acting as a molecular spring.

In sum, these data indicate that DMD hiPSC-CMs are less able to mechanosense and adapt to changes within their microenvironment. This is extremely important in the context of the extensive ECM changes observed *in vivo*[104]. DMD associated DCM is typified by extensive fibrosis and fibrofatty infiltration, altering the myocardial landscape. Alone, the fibrosis observed is a cause of architectural disruption to the sarcomeres and cytoskeleton, that seems to be exacerbated in DMD hiPSC-CMs[210,472]. The inability to perceive the environment, via dystrophin, leads to altered long-term responses, such as those governed by YAP nuclear localisation[3]. The altered viscoelastic properties also support a disruption of cytoskeletal dynamics as well as its architecture. Overall, the data supports a role of dystrophin towards mechanotransduction and regulating the cytoskeleton of cardiomyocytes.

6.4 Chapter 5: hiPSC-CM response to cyclic stretch and healthy cyclic cardiac pressure

Finally, I wanted to examine the response of hiPSC-CMs to physiologically relevant mechanical stimuli. To address this, I examined healthy cyclic cardiac pressure and cyclic equibiaxial stretch, mimicking haemodynamic pressure and myocardial stretch respectively. Application of healthy cyclic cardiac pressure revealed significant alterations to cell and nuclear morphological metrics in both the WT and DMD hiPSC-CMs. As expected, the majority of cell lines displayed a decrease in cell area in response to pressure application but, interestingly, only on a 6 kPa substrate. Strikingly, there was no change in cell perimeter in response to pressure[433–435], except for the unexpected observation of a significantly increased perimeter of WT 1 in response to pressure on a 130 kPa substrate. It may be that the WT 1 response to substrate elasticity was dominant compared to the response to pressure application. Lastly, WT 1 displayed decreased circularity at 6 kPa, whilst DMD 1 showed the opposite and increased, and no other changes of circularity were observed.

At 6 kPa, cell morphology was not different between the hiPSC-CM cell lines except that WT 2 had a significantly larger perimeter compared to DMD 1. On 130 kPa, the cell area of WT 1 was significantly larger compared to all other cell lines, whilst WT 2 was significantly decreased compared to DMD 1. This perhaps suggests that dystrophin is not required for pressure sensing and rather suggests heterogeneity that was inherent between the cell lines.

Initially, I hypothesised that WT nuclei would be smaller and rounder in the presence of pressure given that force is transduced along prestressed actin cables. I expected either no change, or the opposite, in DMD nuclei because of the uncoupling between ECM and cardiomyocyte. Intriguingly, the WT 1 nuclear area and perimeter increased in response to pressure

application at both 6 kPa and 130 kPa. In addition to this, DMD 1 nuclei behaved similarly at 130 kPa. These changes, whilst contrary to my initial hypothesis, may be supported by the transmission of force along actin cables causing a flattening of the nucleus and therefore increased area and perimeter. Indeed, this has been reported by Khatau[431], where they demonstrated that perinuclear actin caps effectively flatten the nucleus. Confirmation of this would require examination of nuclear volume and/or height to assess this. Interestingly, the DMD hiPSC-CMs may only be able to mount nuclear area change to large forces, and may explain why it is only apparent whilst on the 130 kPa elasticity.

It is interesting that pressure resulted in a less dramatic alteration to cardiomyocyte phenotype compared to stretch, hinting at a potential differential in mechanical perception by the cell. Further work here should perhaps look to pressure-overload to examine the role of dystrophin. By increasing the physiological challenge, the phenotype(s) that precipitate may be more exaggerated, permitting a better interpretation of how dystrophin functions here.

Interestingly, the microtubule network was significantly dysregulated in DMD 1 hiPSC-CMs. Previous work has revealed elevated microtubule density and altered posttranslational modifications of microtubules in DCM, consistent with the findings here[59,105]. The application of pressure did not further alter the hyperdense microtubule network in DMD 1 hiPSC-CMs. WT 1 hiPSC-CMs did not develop hyperdense microtubules under pressure to that comparable of the DMD mutant. This suggests that microtubules are less sensitive to pressure as a mechanical stimulus. Further work here may further tease apart the mechanisms and the potential connection between mechanical force and microtubule formation. Hyperdense

microtubule networks have been correlated with decreased contractility and are a driver of heart failure[299,474]. Particularly, detyrosination seems to be associated with poor cardiac function and subsequent poor prognosis in patients. One report showed that elevated microtubule density was responsible for increasing the viscoelasticity of failing cardiomyocytes[59]. It is unclear whether this may be a contributing factor in the work presented here, as the report did not separate the storage and loss moduli components. Future work could examine whether any posttranslational modifications are present within the DMD hiPSC-CM microtubules and to what extent this may impact the functionality of the cardiomyocytes.

Mimicking myocardial contractility using Flexcell® revealed significant increases in WT cell and nuclear area that were absent in DMD 1 and DMD 2 hiPSC-CMs. This strongly supports the necessity of dystrophin for mechanotransduction and for regulating the cytoskeleton. Intriguingly, this suggests that, unlike beat rate where Dp71 may maintain excitation-contraction coupling, here it was insufficient to mediate stretch. This finding hints at the possibility that larger dystrophin isoforms are required to mediate the stretch mechanical stimuli.

Stretching confirmed that the ECM-cell connection via dystrophin is a critical regulator of nuclear morphology, as the absence of dystrophin completely abrogated this effect. Surprisingly, the nuclear localisation of YAP was apparently unaffected by stretch, however this data is very preliminary and requires further *n* number sampling. I hypothesise that given the strong response of the WT 1 hiPSC-CMs to stretch, increasing the *n* number will reveal some differences in YAP expression compared to DMD hiPSC-CMs.

In sum, Chapter 5 reaffirmed that the hiPSC-CM model utilised throughout this work was suitable for physiological modelling. In addition to this, it seems that mechanical stretching had a more profound effect on the phenotype of cardiomyocytes compared to cyclic pressure. Nevertheless, alterations to cell and nuclear morphology broadly followed expected trends here. The nuclear localisation of YAP was significantly decreased in DMD hiPSC-CMs, revealing a mechanism that may drive the DMD associated DCM phenotype *in vivo*.

6.5 Limitations and Future Work

As discussed, isogenic pairs are excellent controls as they mitigate the background genetic differences observed between cell lines. Therefore, future work should aim to overcome this limitation via one of several distinct strategies. Firstly, *de novo* generation of isogenic pairs may be performed. However, this can be a difficult and time-consuming task that may detract from the main objective of examining the effect of dystrophin upon biomechanics. Nevertheless, they are an important component of this objective and should be considered as a valuable investment of time. Secondly, the use of the CRISPRi to knockdown the *DMD* gene or, indeed, any gene associated with the DGC has significant potential. However, there are also concerns over the efficacy of the process and tolerance to the doxycycline that can interfere with its knockdown capacity. Unfortunately, CRISPRi was unfortunately unable to be used (see Appendix 1) during this project. However, this is something that further work should give serious consideration to. Extensive characterisation will be required to demonstrate the efficacy of the guide RNA vector and absence of 'off-target' mutations or knockdowns but, similar to the development of isogenic pairs, may well be a worthy investment of time. Lastly, the use of siRNA within the WT 1 and WT 2 hiPSC-CM cell lines can allow for intra cell line comparison of dystrophin knockdown. The siRNA arrived after my time in the laboratory had expired, however it is available for future work to be undertaken. This would give a quicker indication as to the effect of dystrophin knockdown compared to development of either isogenic controls or CRISPRi knockdown and may yield some interesting avenues to pursue by confirming or eliminating certain conclusions.

Other future work could be directed towards a more extensive characterisation of gene and protein expression. For example, in Chapter 3 a more exhaustive panel of genes and proteins demonstrating both pluripotency and cardiogenesis could have been performed. It would be interesting to carry out time-series and initial seeding density tests here to examine the spatiotemporal effects on cardiogenesis, with particular attention to expression of utrophin and dystrophin isoforms. It would be interesting to note whether dystrophin undergoes significant isoform switching in cardiomyocytes and if this is affected by mutations within the gene, especially whether utrophin compensates for loss of dystrophin in the DMD cell lines. Moreover, it would be exciting to explore the impact that different dystrophin isoforms have on development as well as critical physiological parameters, such as excitation contraction coupling. Here, further work could have explored this by further probing between DMD 1 and DMD 2 hiPSC cell lines and this is an aspect that should be looked at in the future.

Furthermore, development of 3D EHTs to better mimic the *in vivo* cardiac environment would greatly strengthen the work and allow tissue level dynamics to be considered and how the absence of dystrophin translates to tissue level pathologies.

For Chapter 4 and 5, sampling of hiPSC-CMs in response to changes in substrate stiffness, pressure, or stretch as a means for quantifying gene/protein expression levels, such as YAP. However, as mentioned beforehand, I have recently acquired access to ATAC-seq data for WT 1 and DMD 1 hiPSC-CMs that were on laminin coated PDMS substrates of either 6 kPa or 130 kPa. It is expected that this data should be of significant interest and may reveal some interesting differential gene expression, acting as a

remedy to the lack of gene expression data in response to substrate elasticity.

Further examination into the focal adhesion and potential crosstalk with integrins should be of particular interest. Originally, the project planned to leverage DNA origami technology to examine focal adhesions, and this is an aspect of the project that may be performed in future. DNA origami has the potential to examine in detail focal adhesion composition in response to specific ligand signalling.

Alternative experiments that may be performed could include functional assays such as the inclusion of nanopillar arrays to determine whether force generation is decreased in the absence of dystrophin. Calcium handling experiments and patch clamping of mechanosensitive ion channels may reveal the role of dystrophin here too.

A wealth of future work may be carried out on the basis of the data provided here. The platform developed is ripe for many avenues of exploration including gene expression in response to mechanical stimulation, focal adhesion formation and potential for integrin crosstalk, functional assays to further determine the contribution of dystrophin to cardiomyocyte mechanics (such as nanopillar arrays), development of assays to examine the role of dystrophin in cytoskeletal dynamics directly (such as magnetic bead and optical tweezers), and the development of improved cardiac differentiation platforms to better mimic *in vivo* (such as 3D EHTs with co-culture of endothelial cells and fibroblasts). This may incorporate improved differentiation media better aligned to *in vivo* such as free fatty acids as well as electromechanical pacing.

6.6 Summary

In conclusion, I successfully generated and implemented a physiologically relevant hiPSC-CM platform for modelling DMD associated DCM. I was able to demonstrate significant alterations to the cellular and nuclear morphology, alongside disruption of cytoskeletal architecture, and sarcomere length. DMD hiPSC-CMs displayed decreased nuclear YAP localisation in response to mechanical stimulation, such as healthy cyclic cardiac pressure, as well as an inability to mechanosense and respond to cyclic stretch. Together, these data support my original hypothesis that dystrophin is required for mechanosensing, mechanotransduction, and mounting a response in cardiomyocytes to mechanical stimulation. My data supports the conclusion that, in the absence of dystrophin as is the case for DMD, mechanotransduction in cardiomyocytes is severely diminished and is a likely contributor to the overall disease phenotype observed. The data here may provide some insight that may be harnessed in the future towards the development of novel therapeutic strategies.

A1 “Down the rabbit hole…”: hiPSC, hiPSC-CMs, and Vector Assembly

Absence of evidence is not evidence of absence

Carl Sagan

A1.1 DMD 1 hiPSCs Clones Displayed a Mixed Population

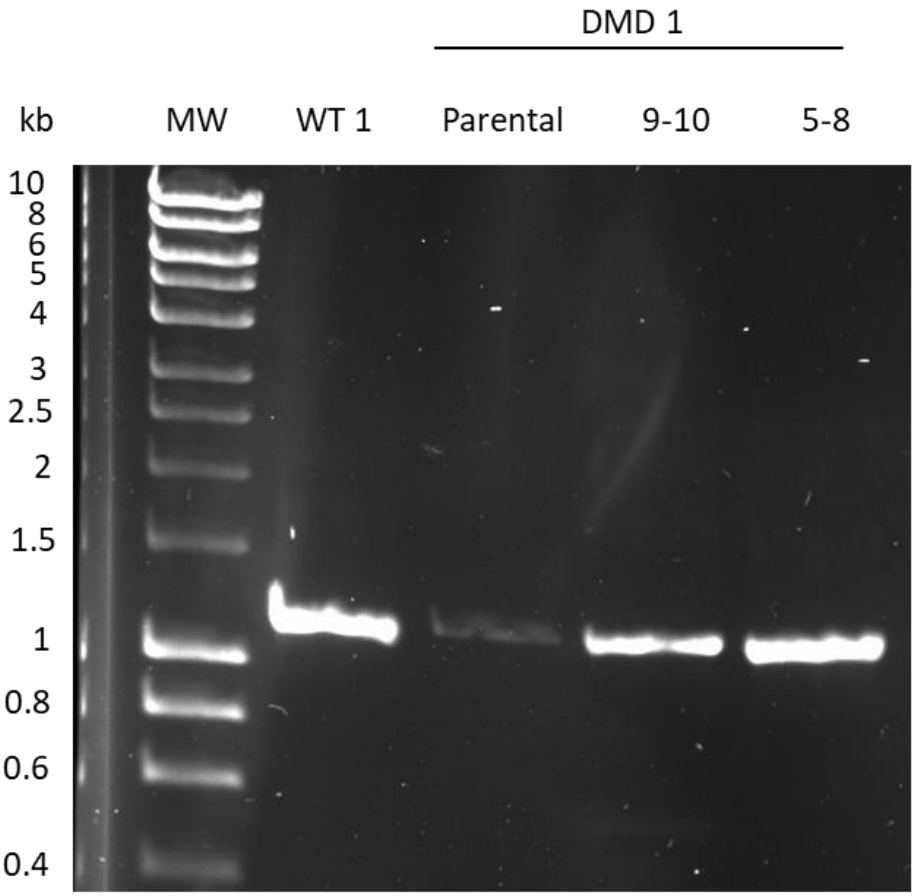

Figure A1.1: PCR amplification of exon 67. *WT 1 and DMD 1 mutant with supposedly CRISPR corrected isogenic clones, 9-10 and 5-8. PCR amplification of exon 67 containing the c.9691C>T (p.Gln3231*) mutation. N= 3*

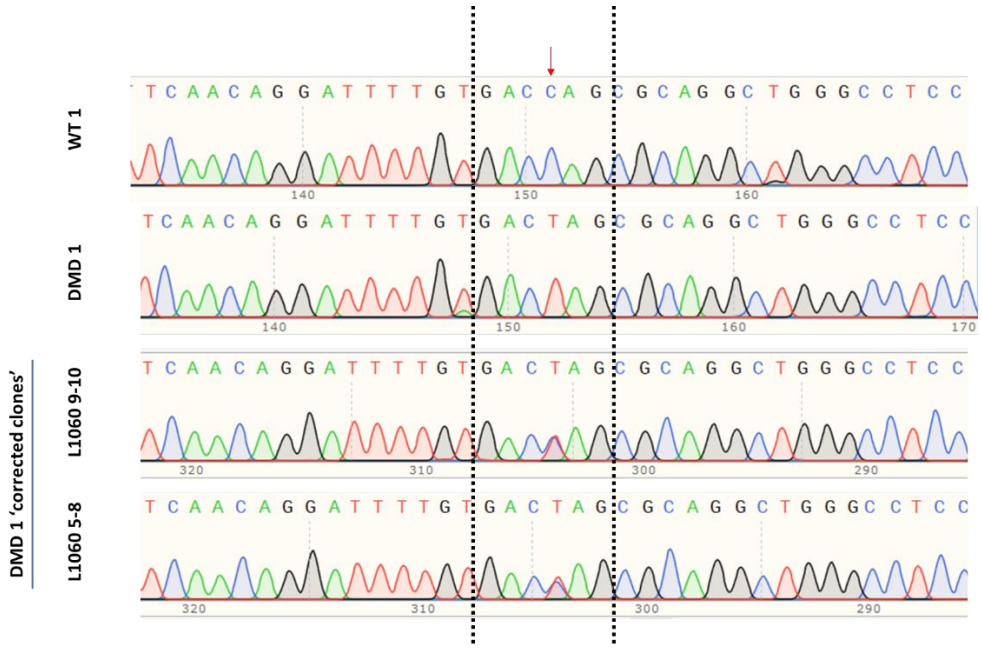

Figure A1.2: DMD 1 CRISPR corrected clones were a mixed population (forward primers shown here). *Gene sequencing revealed that both WT 1 and DMD 1 parent mutant had expected gene sequence. DMD 1 'corrected clones' were mixed populations and could not be used. Unmixing was attempted by several members within Dr Lin's laboratory, but these attempts failed. N= 3*

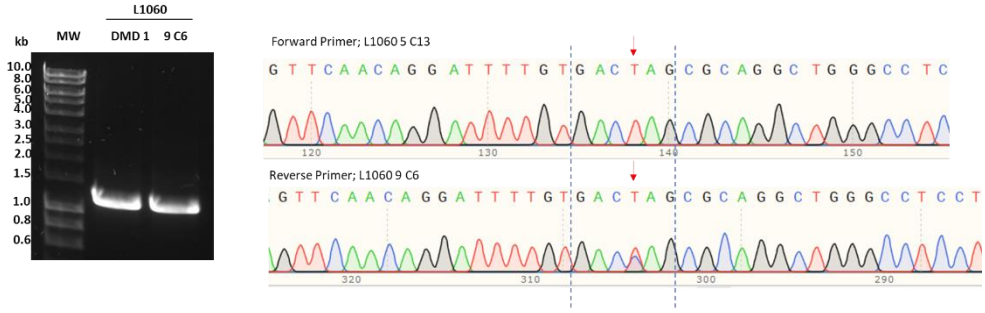

Figure A1.3: PCR amplification and gene sequencing revealed 'corrected clone' L1060 9 C6 was also mixed population. N= 4

A1.2 FKRP hiPSCs Clones Were Isogenic but Failed to Differentiate

Subsequently, I then attempted to use another isogenic cell line whereby the parent contained a mutation within the *FKRP* gene (c.1364C>A). This mutation affects the glycosylation of the α-DG via the FKRP protein and therefore disrupts the ECM-cell interface. The idea behind this was to widen the characterisation to muscular dystrophies in general.

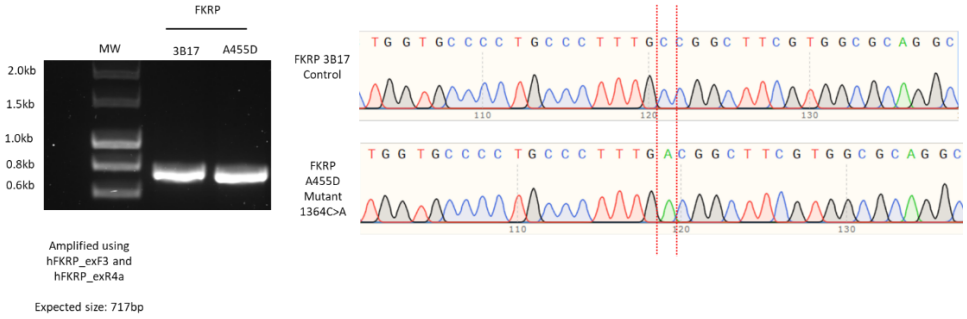

Figure A1.4: PCR amplification and gene sequencing revealed the expected mutation in FKRP mutant and successful CRISPR correction in FKRP 3B17 control. N= 2

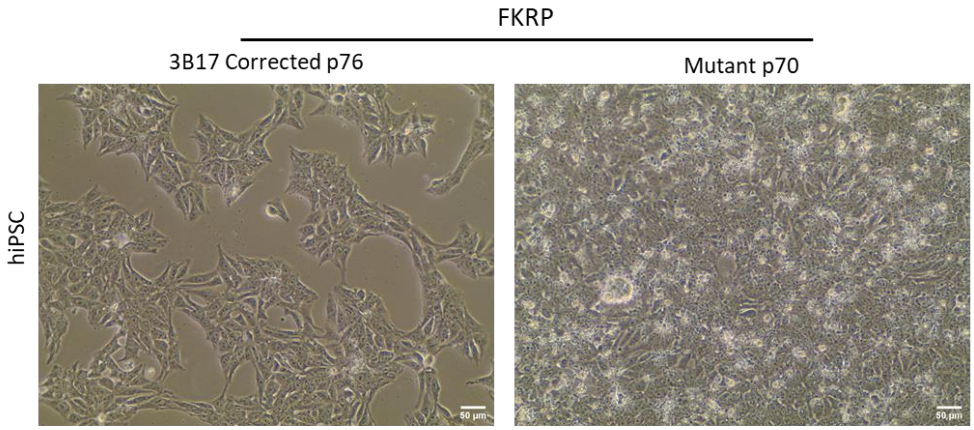

Figure A1.5: Brightfield images of FKRP CRISPR corrected and FKRP mutant hiPSCs. *N= 3, scale bar= 50 µm.*

The FKRP mutant had successfully been CRISPR corrected generating *bona fide* isogenic pair. Unfortunately, the FKRP hiPSCs failed to respond to the cardiac differentiation protocol with significant quantities of cell death. Despite altering cell density and/or CHIR concentration, FKRP hiPSCs continually failed to respond to cardiac differentiation.

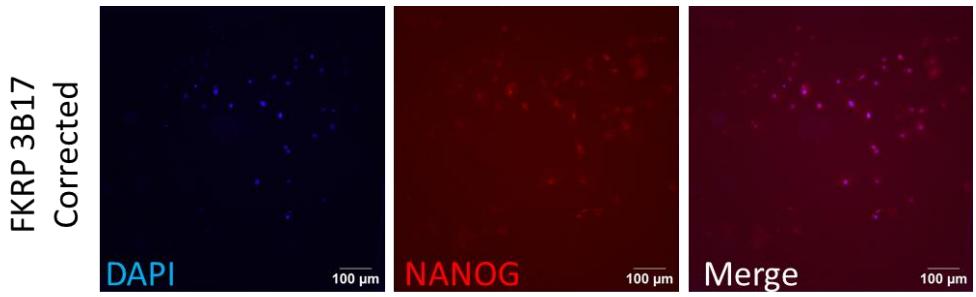

Figure A1.6: FKRP 3B17 CRISPR corrected hiPSCs were positive for NANOG. *NANOG immunofluorescence confirmed FKRP corrected hiPSCs were pluripotent. This assay was not carried out on the FKRP mutant hiPSC line. N= 1.*

In sum, a considerable period of time was devoted to the expansion, maintenance, and confirmation of various hiPSC cell lines. Unfortunately, the isogenic pairs were either mixed population that could not be rescued or would not differentiate to cardiomyocytes- indeed FKRP hiPSCs died after treatment with CHIR.

A1.3 Vector Assembly for use in CRISPRi

The WT 1 CRISPRi hiPSC cell line contains a doxycycline sensitive inducible deactivated Cas9 and KRAB domain repression domain CRISPR element[326]. In the absence of doxycycline, this element is not expressed, and the cell line is phenotypically WT. In the presence of doxycycline and a guide RNA (gRNA), target genes can be repressed, and in theory is a highly tuneable and powerful platform. The CRISPRi cell line has been validated by Mandegar[326].

Here, I aimed to develop and produce a modifiable vector that would allow the insertion of any developed gRNA, that could then be used to transfect CRISPRi hiPSCs and hiPSC-CMs. Unfortunately, development of the vector presented some significant challenges, some of which I solved. Others, I was unable to remedy in the time available and this aspect of the project was abandoned. Later, it was agreed to try use siRNA on the CRISPRi cell line as this was a better-established technique, but there was a significant delay in the acquisition of the siRNA, and their arrival was some time after my departure from the laboratory.

A1.4 Vector Design

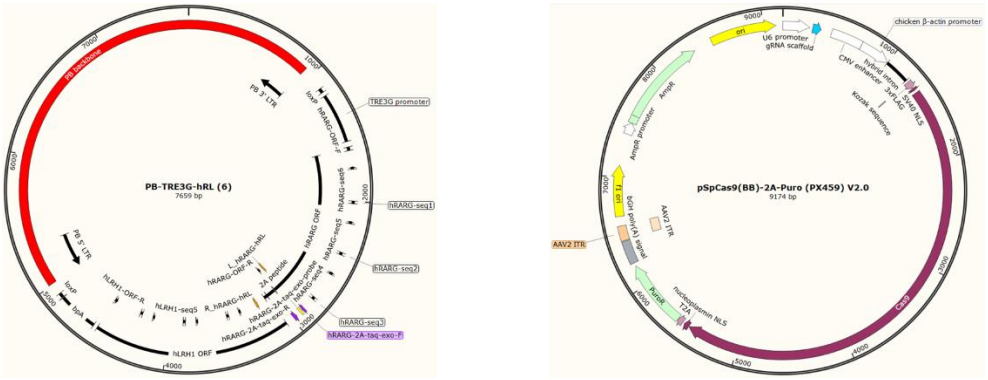

Figure A1.7: Initial vectors for developing novel CRISPRi vector. *On the left (**PB Vector)**, a vector already present within Dr Lin's laboratory that could be used for the piggybac transposon. On the right (**PX459)**, vector was bought containing a U6 promoter and gRNA insertion site and puromycin selection cassette.*

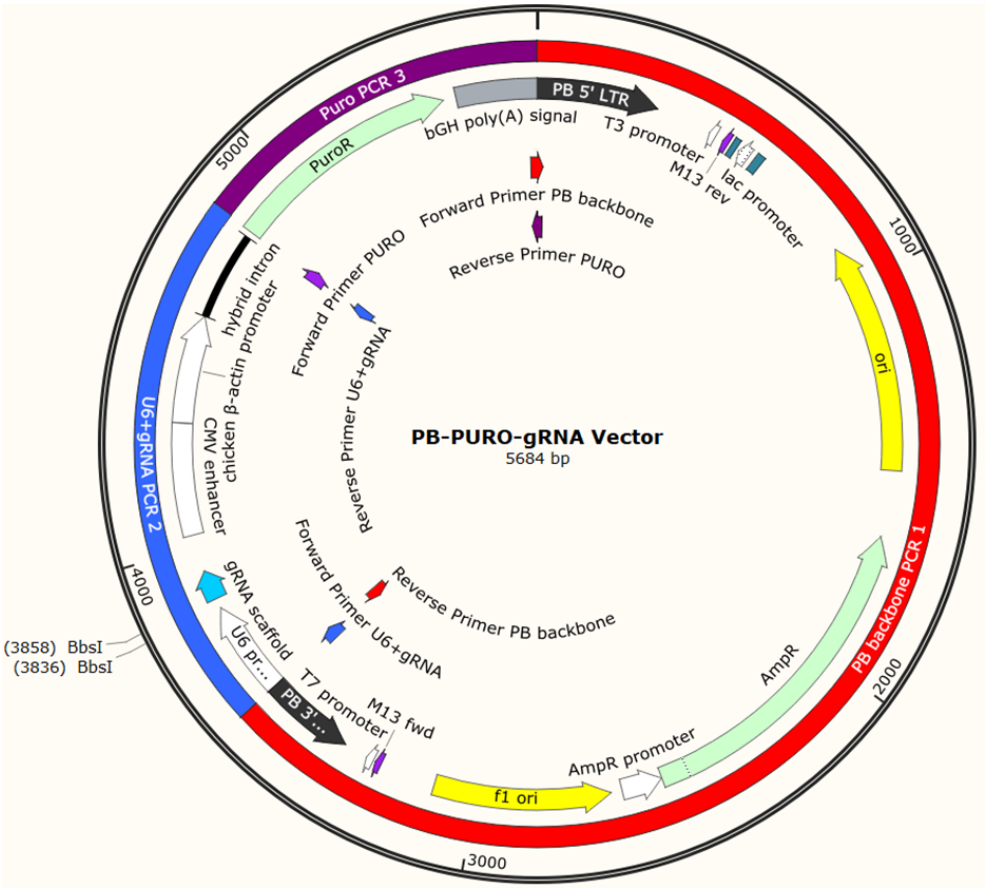

Figure A1.8: Novel vector design for use in CRISPRi hiPSCs. *Using vector fragments from Figure A1.7, amplification of the U6+gRNA, Piggybac, and Puro regions could be carried out. These could then be assembled for amplification in E.coli. This could then be purified, stored, and transfected to the CRISPRi cell line. In theory, this vector would allow the insertion of any gRNA into the U6+gRNA (Blue) into this vector via the BbsI site.*

Table A1.1: Vector fragments and associated primers used for amplification. *Primers from Integrated DNA Technologies, UK*

Vector Fragment	**Primer Sequence**	**Fragment size (bp)**
U6 + gRNA	F 5’ TTCTTCTATAAAGTAACAAAGAGGGCCTATTTCCCATGAT 3’ R 5’ TTGGACCGGTGCCACCATGGTGACCGAGTACAAGCCCAC G 3’	1252 bp
Piggybac backbone	F 5’ AATAGCAGGCATGCTGGGGAGATATCTATAACAAGAAA AT 3’ R 5’ TTCTTCTATAAAGTAACAAAGAGGGCCTATTTCCCATGAT 3’	3591 bp
Puromycin	F 5’ TTGGACCGGTGCCACCATGGTGACCGAGTACAAGCCCAC G 3’ R 5’ AATAGCAGGCATGCTGGGGAGATATCTATAACAAGAAA AT 3’	840 bp

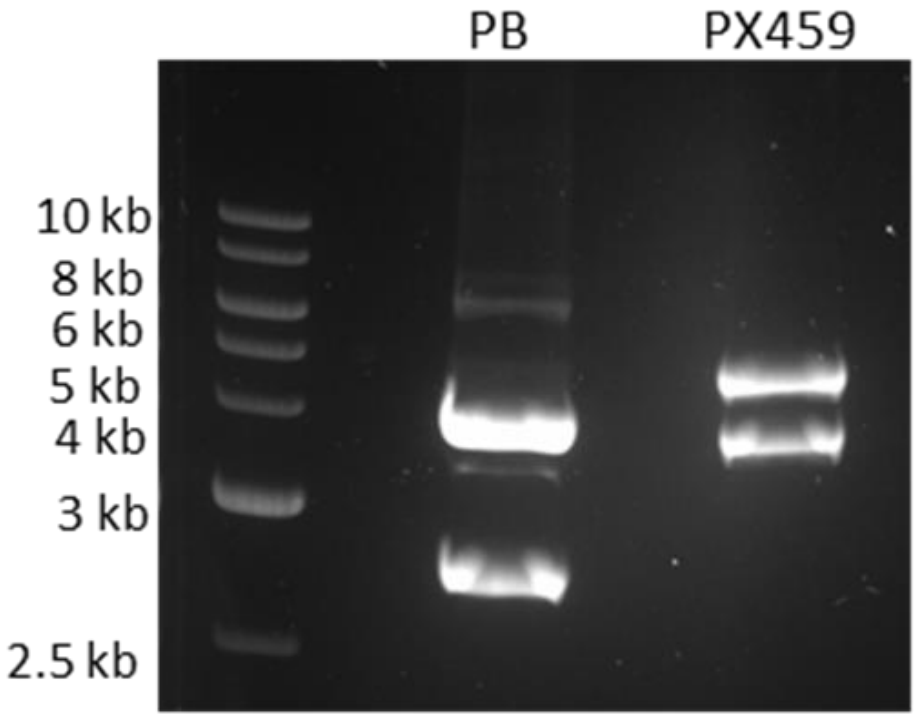

Figure A1.9: PCR amplification and restriction digest of PB and PX459 vectors. *BSAI and ECONI were used for restriction digest. This confirmed that both PB and PX459 could be used to amplify the fragments required for developing the novel CRISPRi vector. 1% agarose gel electrophoresis. N= 2.*

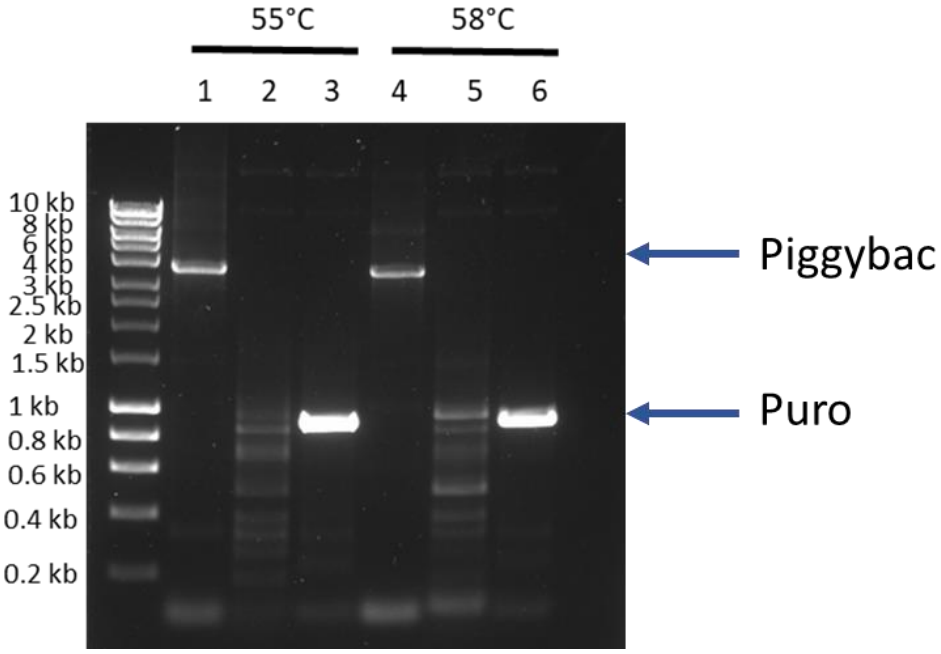

Figure A1.10: Amplification of Piggybac and Puro fragments was success at annealing temperatures of 55^{o}C and 58^{o}C. U6+gRNA failed. *To optimise the PCR amplification of the vector fragments, two annealing temperatures were used. Both Piggybac and Puro were amplified successfully and at the expected band sizes. The U6+gRNA fragment failed to amplify. 1% agarose gel electrophoresis. N= 2*

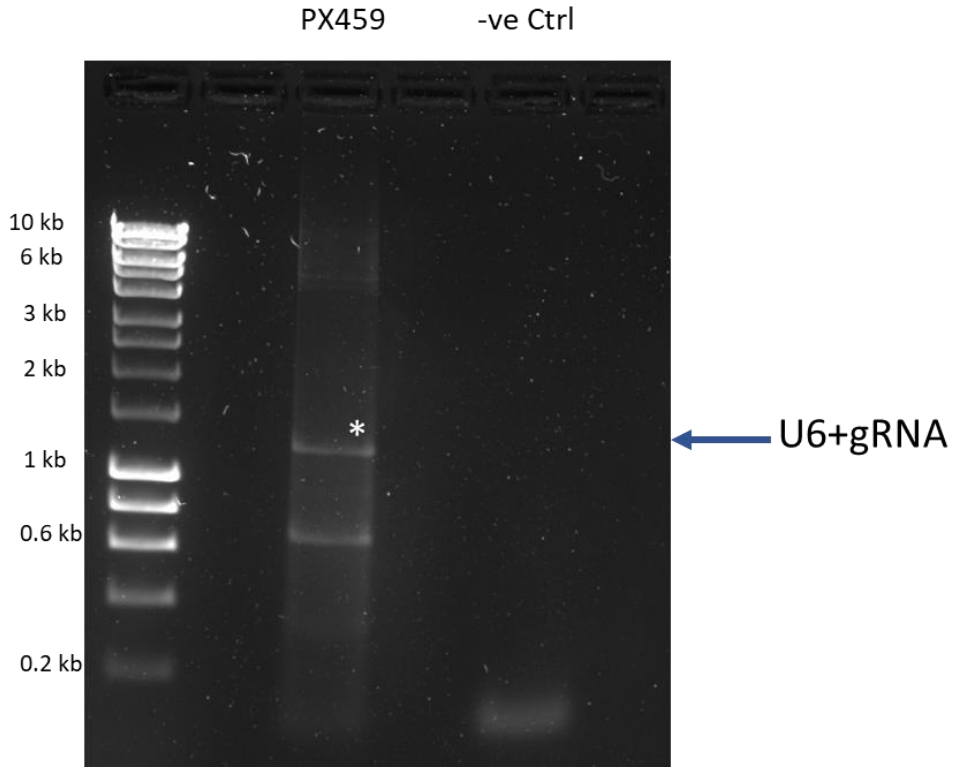

Figure A1.11: Amplification of U6+gRNA. *To facilitate the amplification of the U6+gRNA region (which has a large G-C ratio), the addition of 5% DMSO was added to the reaction. This appeared to facilitate the reaction at the expected band size of ~1200 bp. An off-target product at ~ 600 bp appears to have amplified. 1% agarose gel electrophoresis. N= 2*

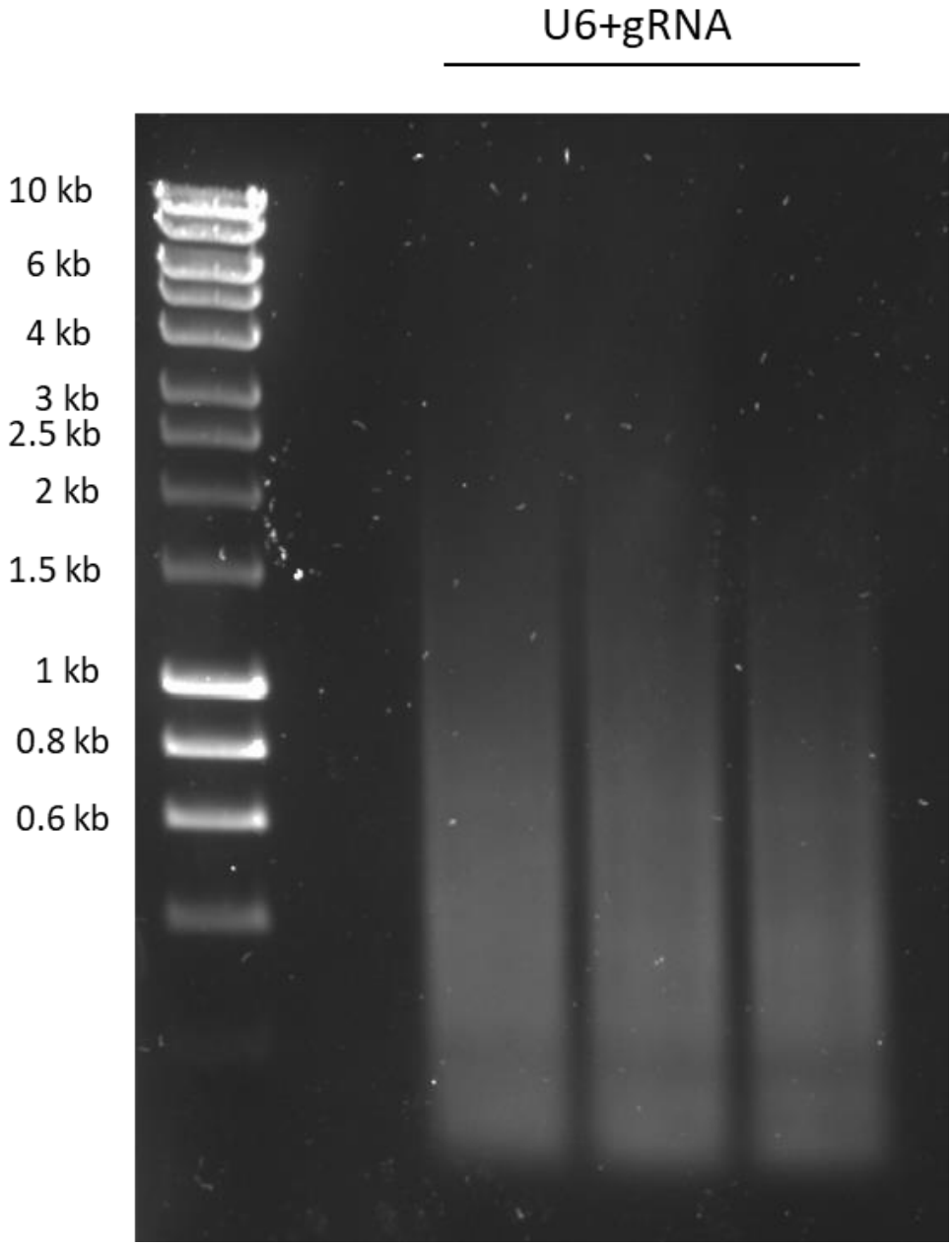

Figure A1.12: Purification of U6+gRNA fragment from Figure A1.11 and re-amplification.

Attempts to isolate and re-amplify the U6+gRNA product from the 1% agarose gel failed.

N= 2

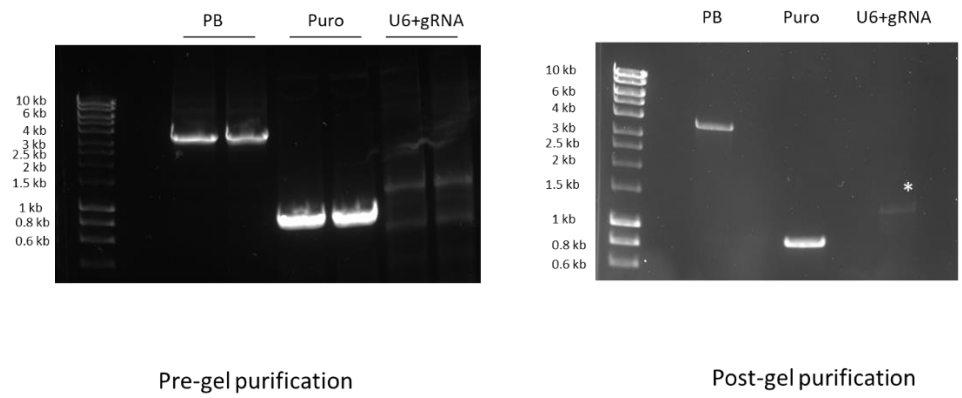

Figure A1.13: Purification and re-amplification of vector fragments. *On the left were non-purified vector fragments. Each was cut from the 1% agarose gel (According to kit instructions) and the DNA from these fragments was then re-run. The aim was to amplify the specific PCR fragments. This was largely successful for both the Piggybac (PB) and puromyocin (Puro) fragments. The U6+gRNA fragment demonstrated very little amplification as indicated by the white asterisk. N= 3*

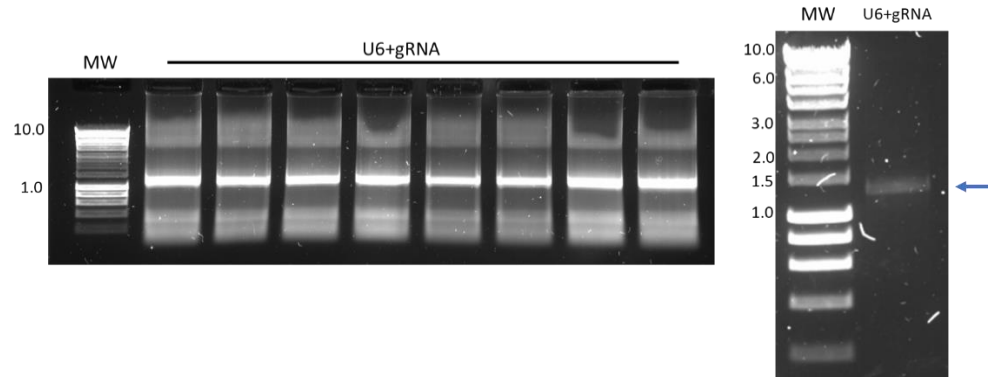

Figure A1.14: Further attempts to amplify U6+gRNA. *Amplification and purification of the U6+gRNA fragment was particularly troublesome. After successfully solving the initial amplification reaction with optimised ramp-up and DMSO addition, the next stage was to purify the fragment and re-amplify this, as had been done with the Piggybac and Puro fragments. It can be seen on the* ***right*** *that when all of the U6+gRNA fragments were cut from the gel and pooled together and re-amplified, the yield was surprisingly low (blue arrow). However, the band was present without the off-targets that were visible on the left-hand side. N= 1*

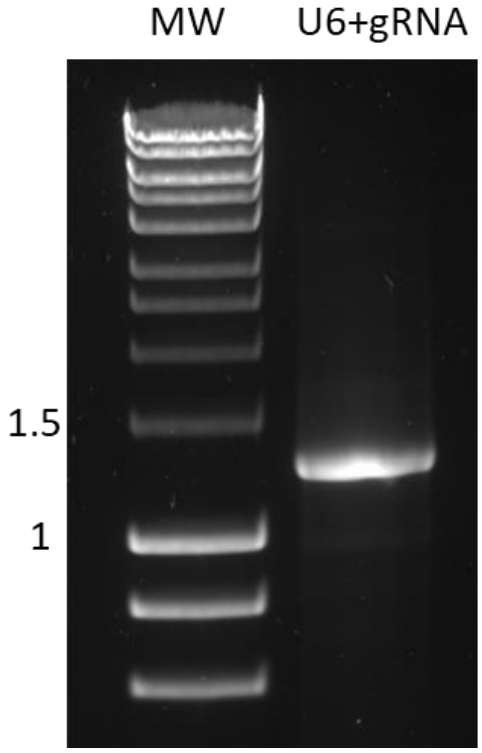

Figure A1.15: Successful purification and amplification of the U6+gRNA fragment. *After several attempts, eventually purification and re-amplification of the U6+gRNA fragment was successful. N= 1*

Having successfully optimised the conditions required for the amplification of the vector fragments followed by purification and subsequent re-amplification, I could then look to assemble the vector.

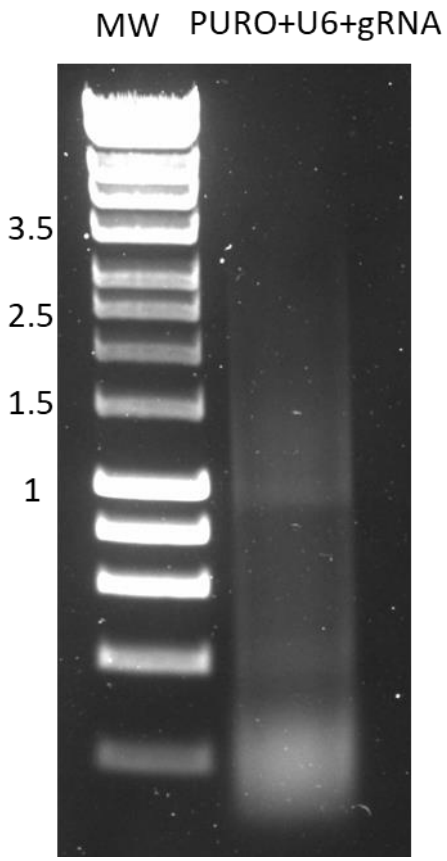

Figure A1.16: Failed PCR of vector fragments. *The initial attempt to assemble the vector via PCR amplification failed.*

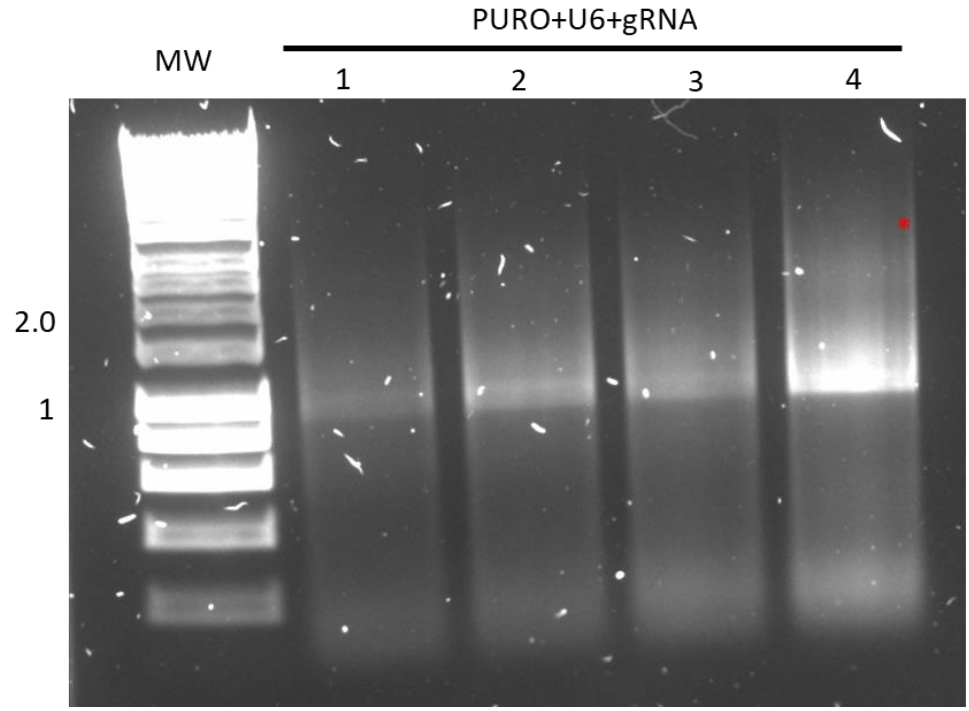

Figure A1.17: Optimisation of PCR amplification of vector fragments. *Here, I looked at different annealing temperatures and DMSO concentrations.* ***1)*** *5% DMSO; 55°C;* ***2)*** *2.5% DMSO; 55°C;* ***3)*** *5% DMSO 58°C;* ***4)*** *2.5% DMSO 58°C. The reactions failed as the expected band was approximately 5.6 kb.*

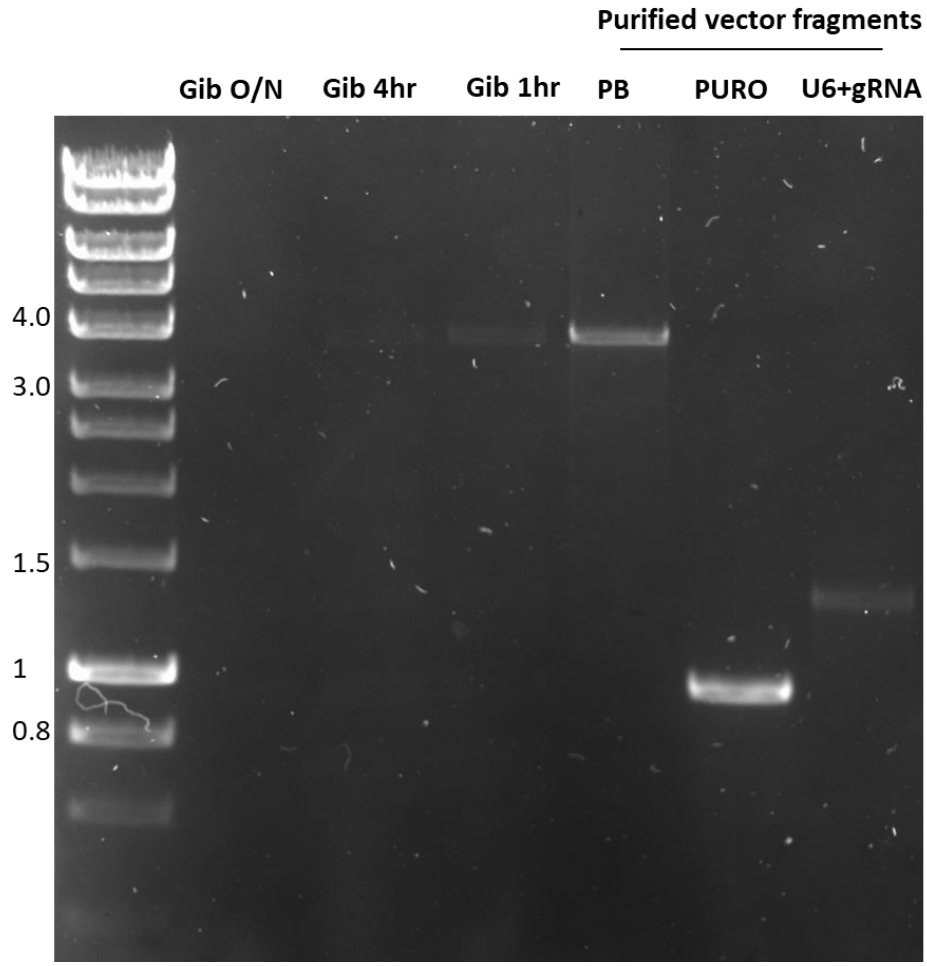

Figure A1.18: Gibson assembly as a means to assemble the vector. *Given the failure of using PCR to join the fragments together Dr Lin suggested the use of Gibson assembly. Here, Gibson assembly at different time-points was carried out. Gib O/N= overnight. The products, alongside original PCR products for comparison, were gel electrophoresed at 100 mV for 30 min. 1% agarose gel. All attempts to assemble the vector here failed. N= 2.*

Subsequently, I thought to focus on the ligation between the Puromycin and Piggybac region and then to use classic restriction enzymes to insert the U6+gRNA fragment and thus completing assembly of the vector. Unfortunately, by this time it was decided that time was running out and that experiments should re-focus on the biomechanics of the hiPSC-CMs. This was especially true given that each of these sets of experiments had to

be conducted at different centres across London. Therefore, vector assembly was abandoned. Unfortunately, outsourcing vector assembly to an external company was not explored. Therefore, the use of the vector to knockdown DGC proteins was, in essence, halted.

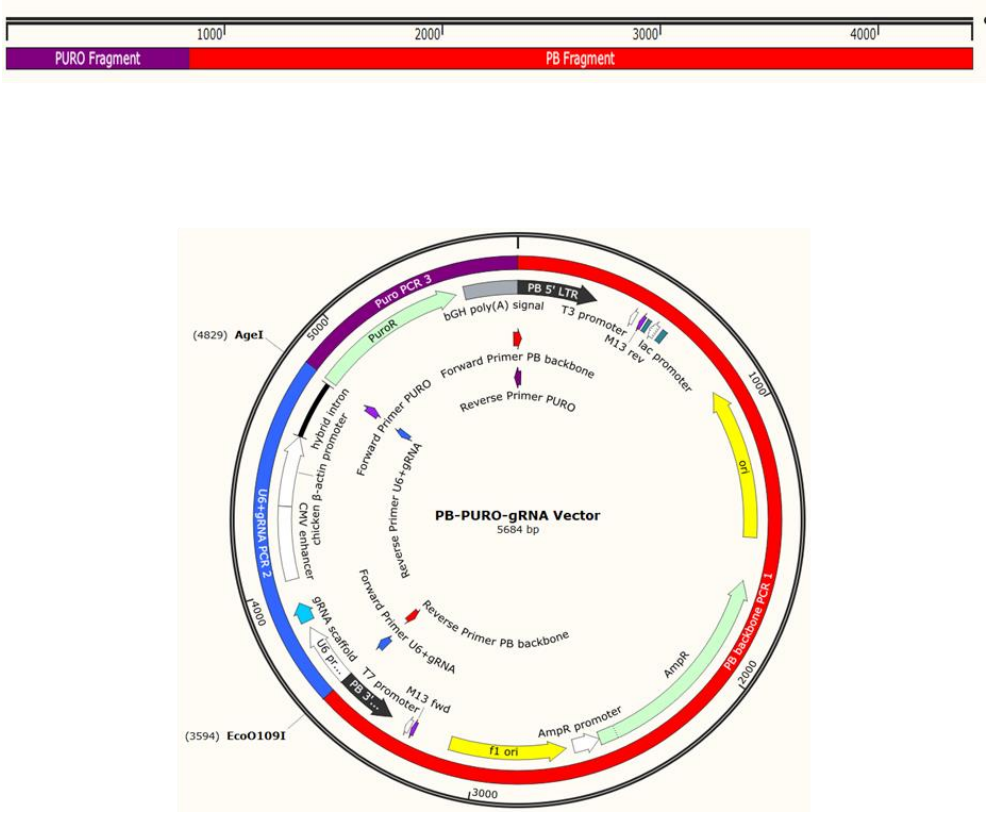

Figure A1.19: Two-step assembly proposition. TOP: *Initial reaction would focus on ligating Puromycin and Piggybac fragments. These fragments displayed the least resistance to amplification, purification, re-amplification.* ***BOTTOM****: If reaction shown at the top was successful, the use of restriction enzymes AgeI and Eco0 1091 could be used to insert the U6+gRNA fragment. However, it was agreed due to lack of time to re-focus experimental efforts.*

A2 Supplementary Figures Comparing hiPSC-CM Cell Lines

A2.1 Comparison between hiPSC-CM Cell Morphology on Different Substrate Elasticities

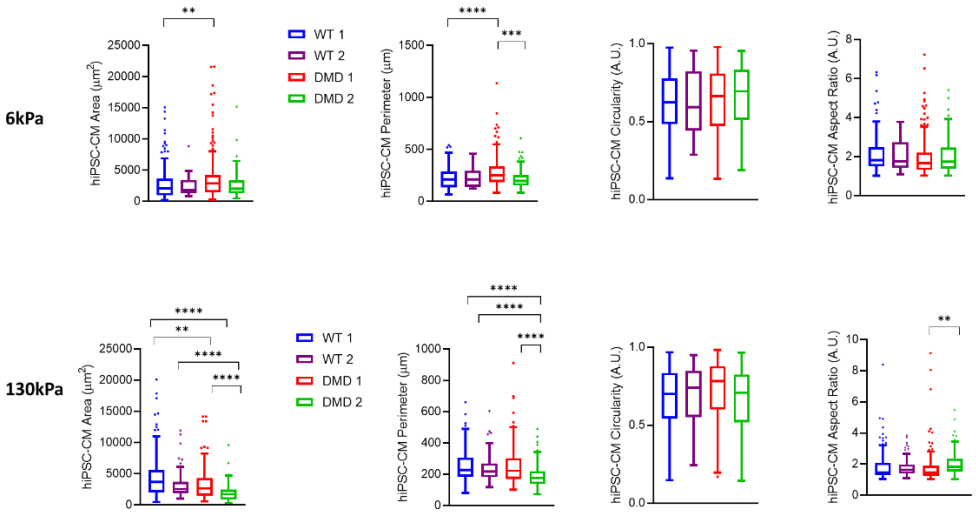

Figure A2.1: Cell morphology comparison between hiPSC-CM cell lines on either a 6 kPa or 130 kPa substrate. *Data analysed via two-way ANOVA with Tukey's post hoc test applied, p<0.05 was significant. N= 3 biological replicates.*

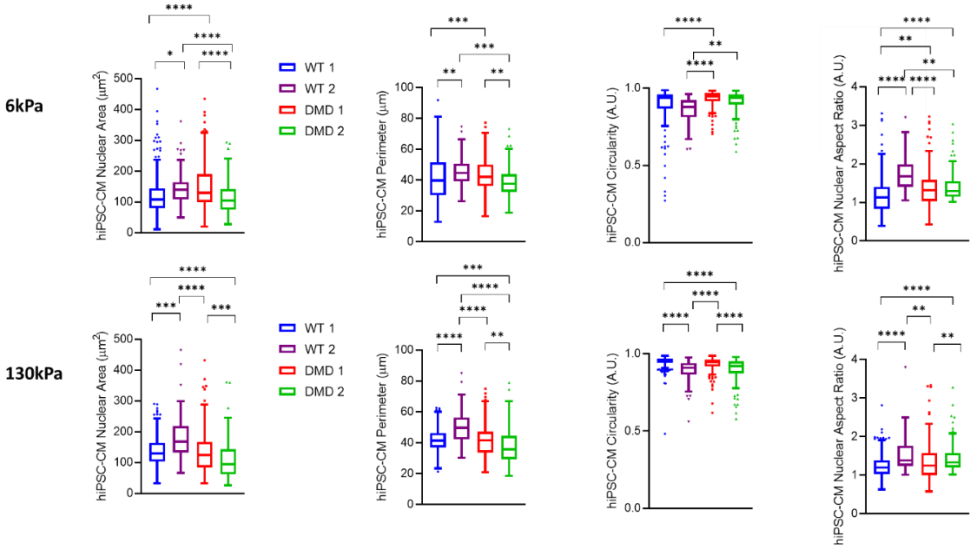

Figure A2.2: Nuclear morphology comparison between hiPSC-CM cell lines on either a 6 kPa or 130 kPa substrate. *Data analysed via two-way ANOVA with Tukey's post hoc test applied, p<0.05 was significant. N= 3 biological replicates.*

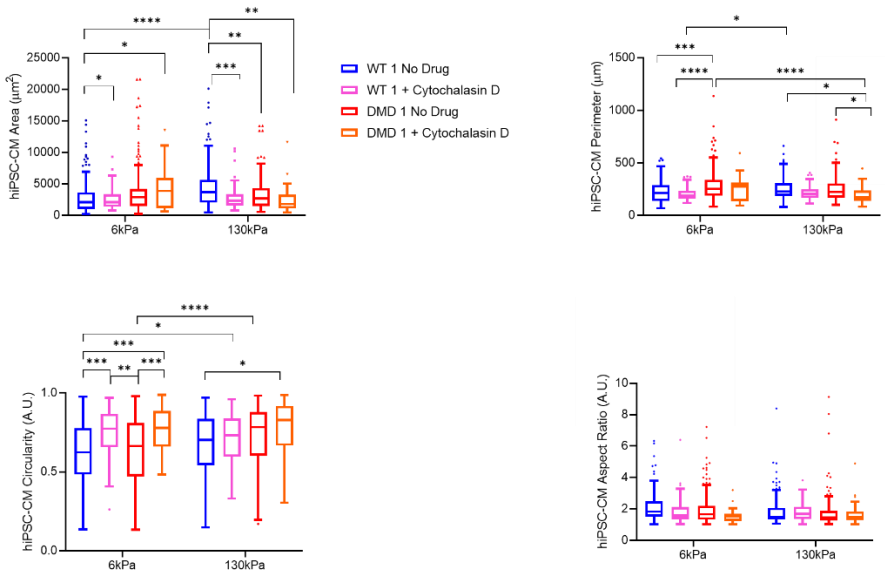

Figure A2.3: Cell morphology with 1 µM cytochalasin D comparison between hiPSC-CM cell lines on either a 6 kPa or 130 kPa substrate. *Data analysed via two-way ANOVA with Tukey's post hoc test applied, p<0.05 was significant. N= 3 biological replicates.*

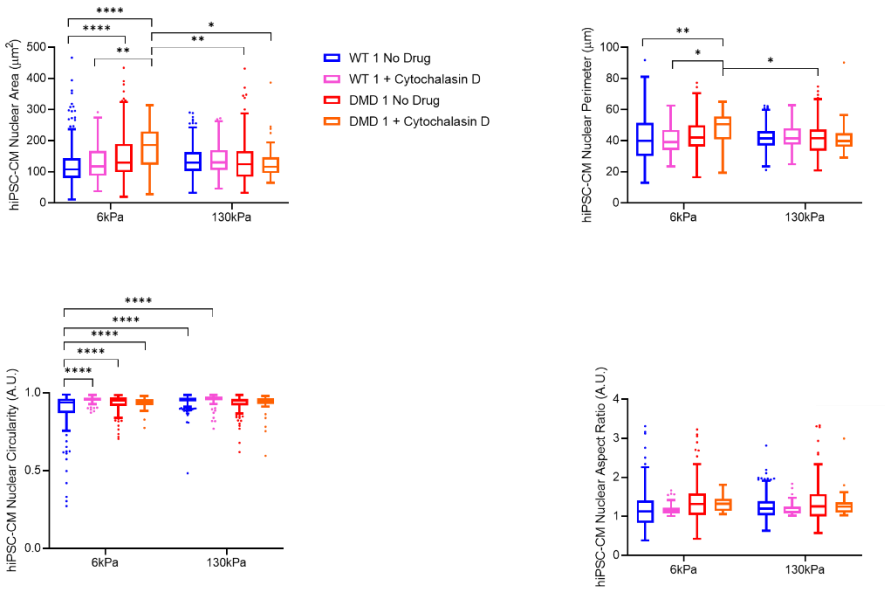

Figure A2.4: Nuclear morphology with 1 µM cytochalasin D comparison between hiPSC-CM cell lines on either a 6 kPa or 130 kPa substrate. *Data analysed via two-way ANOVA with Tukey's post hoc test applied, p<0.05 was significant. N= 3 biological replicates.*

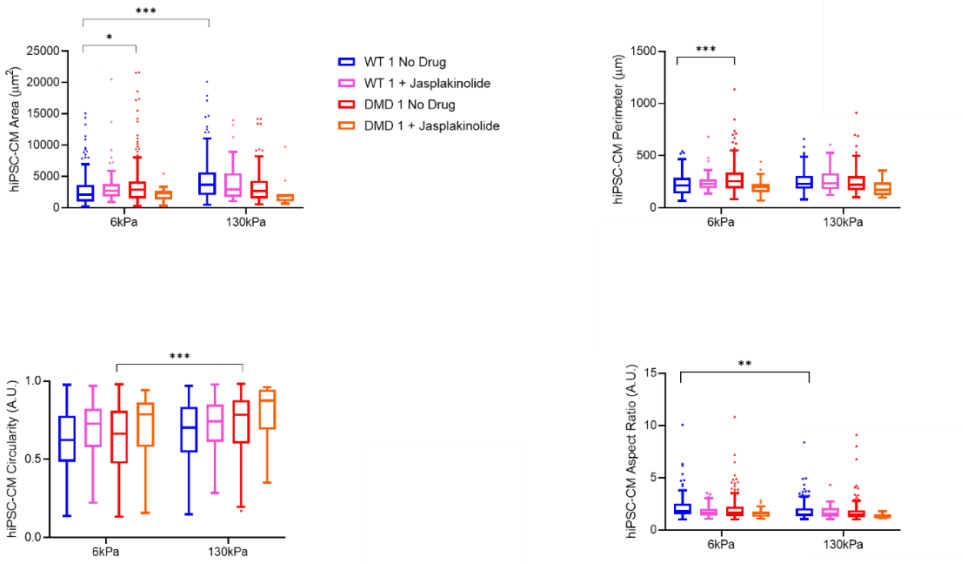

Figure A2.5: Cellular morphology with 1 µM jasplakinolide comparison between hiPSC-CM cell lines on either a 6 kPa or 130 kPa substrate. *Data analysed via two-way ANOVA with Tukey's post hoc test applied, $p<0.05$ was significant. N= 3 biological replicates.*

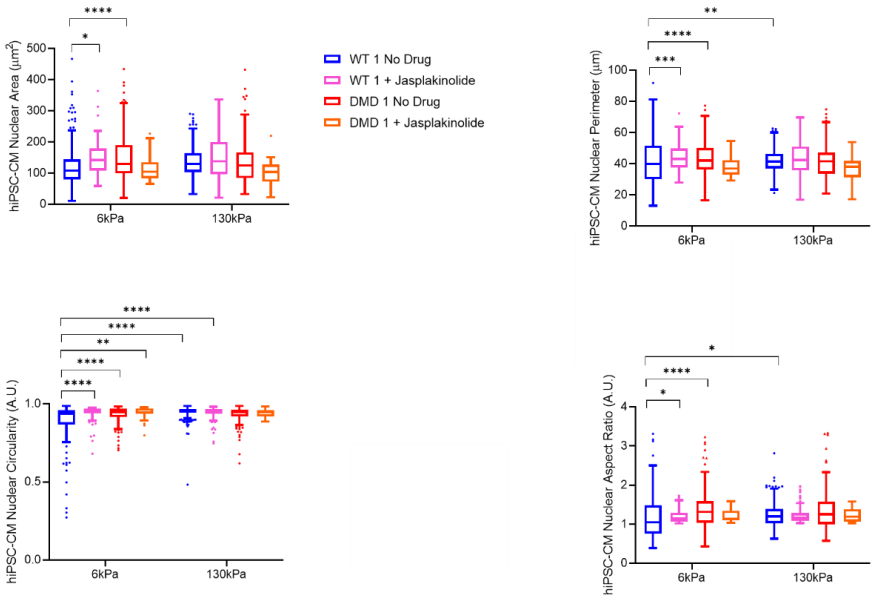

Figure A2.6: Nuclear morphology with 1 µM jasplakinolide comparison between hiPSC-CM cell lines on either a 6 kPa or 130 kPa substrate. *Data analysed via two-way ANOVA with Tukey's post hoc test applied, p<0.05 was significant. N= 3 biological replicates.*

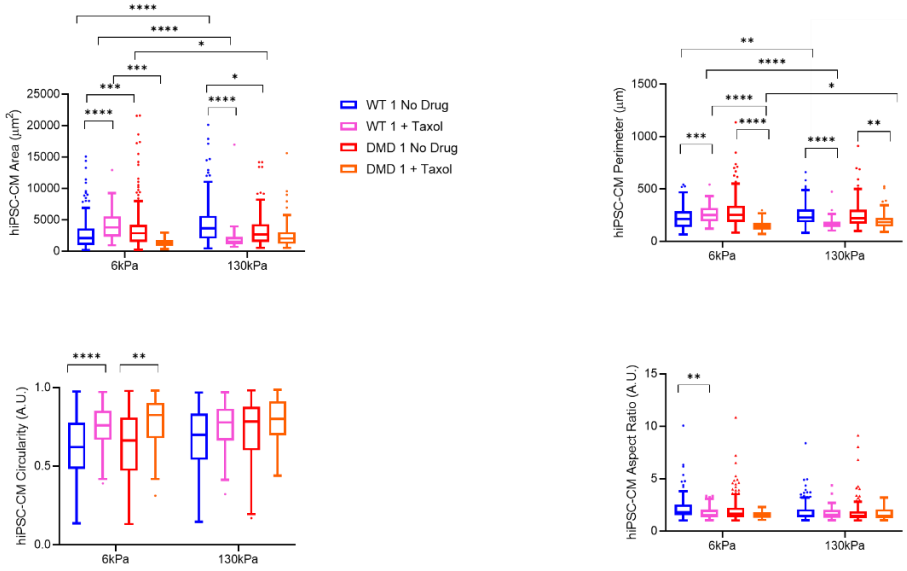

Figure A2.7Figure A2.5: Cellular morphology with 10 µM taxol comparison between hiPSC-CM cell lines on either a 6 kPa or 130 kPa substrate. *Data analysed via two-way ANOVA with Tukey's post hoc test applied, p<0.05 was significant. N= 3 biological replicates.*

Figure A2.8: Nuclear morphology with 10 µM taxol comparison between hiPSC-CM cell lines on either a 6 kPa or 130 kPa substrate. *Data analysed via two-way ANOVA with Tukey's post hoc test applied, p<0.05 was significant. N= 2 biological replicates.*

Figure A2.9: Young's modulus comparison between hiPSC-CM cell lines on either a 6 kPa or 130 kPa substrate in response to cytochalasin D. *Data analysed via two-way ANOVA with Tukey's post hoc test applied, p<0.05 was significant. N= 1 for treated vs N=3 for untreated biological replicates.*

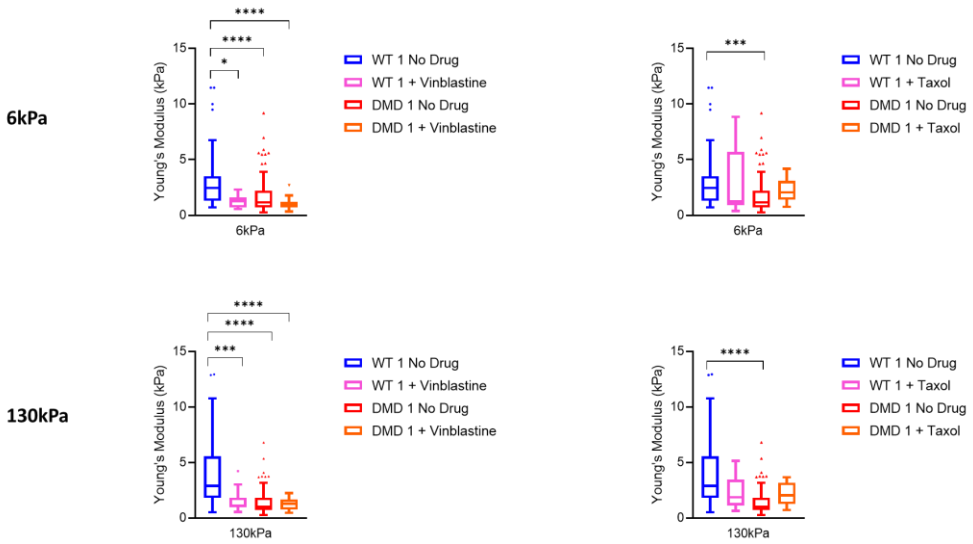

Figure A2.10: Young's modulus comparison between hiPSC-CM cell lines on either a 6 kPa or 130 kPa substrate in response to vinblastine or taxol. *Data analysed via two-way ANOVA with Tukey's post hoc test applied, p<0.05 was significant. N= 1 for treated vs N=3 for untreated biological replicates.*

A3 Comparison between Cell Line Experimental Averages

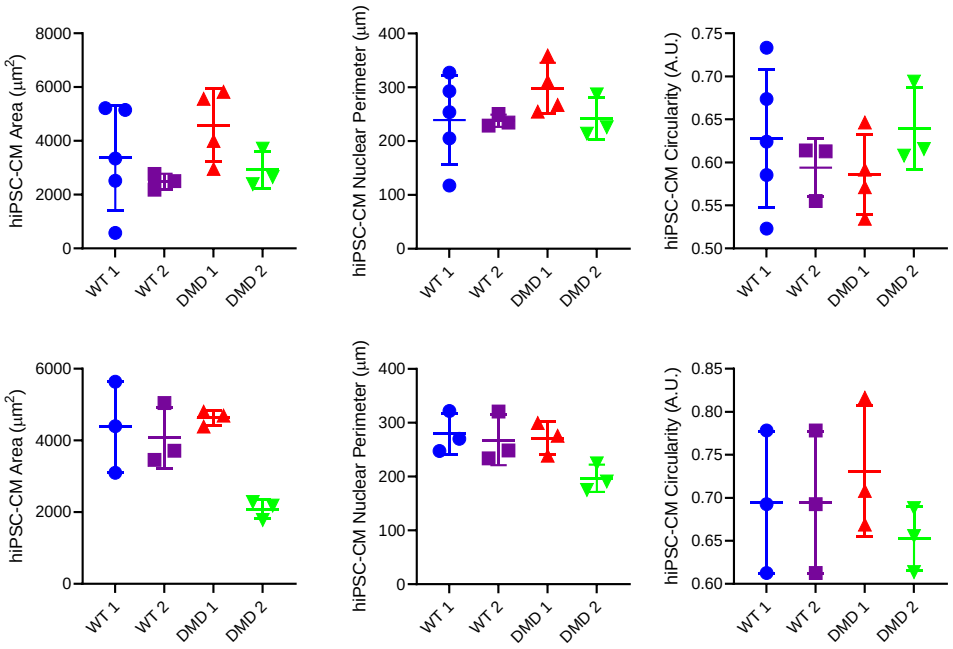

Figure A3.1: Cell Parameters. *Top Panels: 6kPa; Bottom panels: 130kPa. No sig diff between any cell lines.*

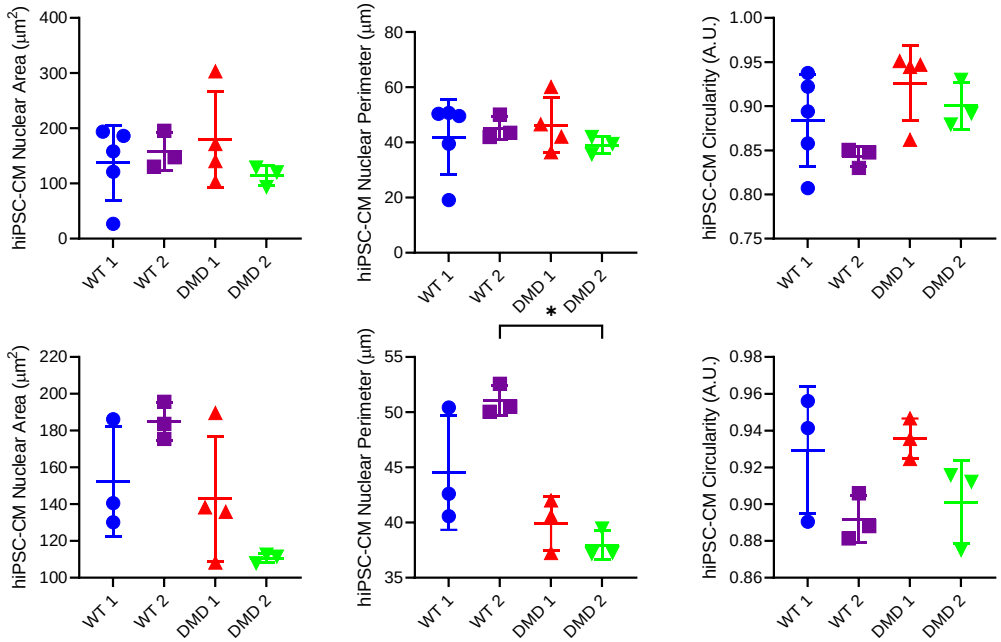

Figure A3.2: Nuclear Parameters. *Top panel: 6kPa; bottom panel: 130kPa. Only the perimeter on 130 kPa between WT2 and DMD 2 was significant.*

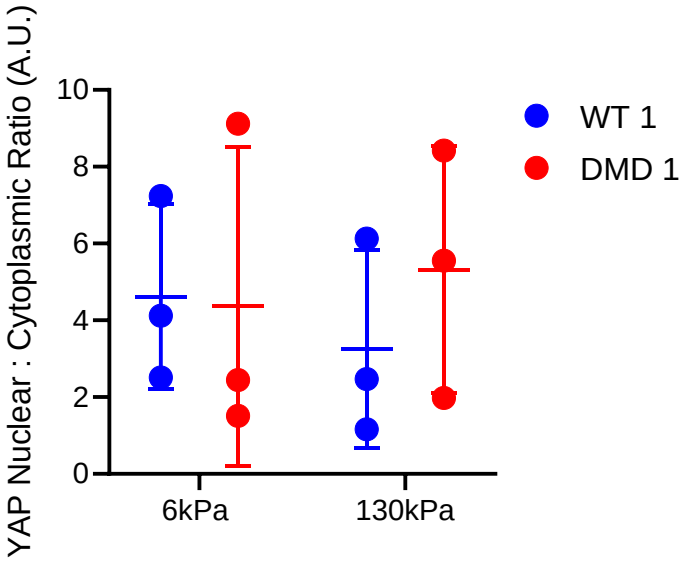

Figure A3.3: YAP nuclear: cytoplasmic ratio. *No significant differences.*

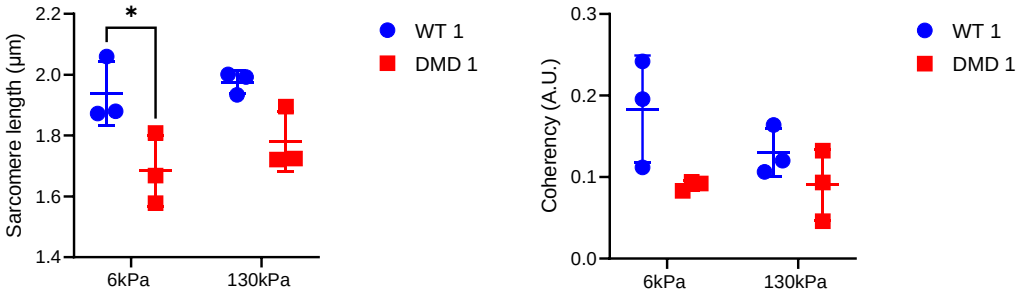

Figure A3.4: Sarcomere and Coherency at 6kPa and 130kPa. *No significant differences.*

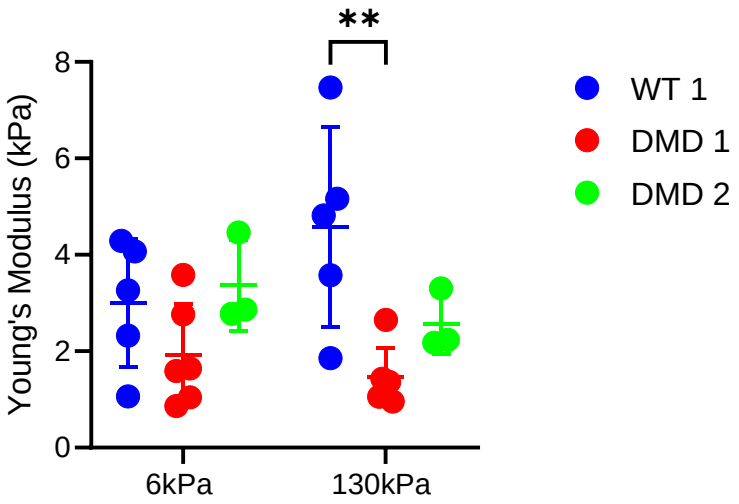

Figure A3.5: Young's Modulus on either 6kPa or 130kPa. *Significant difference observed between WT1 and DMD1.*

References

1. Iskratsch, T., Wolfenson, H. & Sheetz, M. P. Appreciating force and shape-the rise of mechanotransduction in cell biology. *Nature Reviews Molecular Cell Biology* vol. 15 825–833 Preprint at https://doi.org/10.1038/nrm3903 (2014).
2. Gao, Q. Q. & McNally, E. M. The Dystrophin Complex: structure, function and implications for therapy. *Compr Physiol* **5**, (2015).
3. Morikawa, Y., Heallen, T., Leach, J., Xiao, Y. & Martin, J. F. Dystrophin–glycoprotein complex sequesters Yap to inhibit cardiomyocyte proliferation. *Nature* **547**, 227–231 (2017).
4. Ward, M. & Iskratsch, T. Mix and (mis-)match – The mechanosensing machinery in the changing environment of the developing, healthy adult and diseased heart. *Biochimica et Biophysica Acta (BBA) - Molecular Cell Research* **1867**, 118436 (2019).
5. Hynes, R. O. Integrins: A family of cell surface receptors. *Cell* **48**, 549–554 (1987).
6. Campbell, K. P. & Kahl, S. D. Association of dystrophin and an integral membrane glycoprotein. *Nature* **338**, 259–262 (1989).
7. Petrof, B. J., Shrager, J. B., Stedman, H. H., Kelly, A. M. & Sweeney, H. L. Dystrophin protects the sarcolemma from stresses developed during muscle contraction. *Proc Natl Acad Sci U S A* **90**, 3710–3714 (1993).
8. Le, S. *et al.* Dystrophin As a Molecular Shock Absorber. *ACS Nano* **12**, 12140–12148 (2018).
9. Garbincius, J. F. & Michele, D. E. Dystrophin-glycoprotein complex regulates muscle nitric oxide production through mechanoregulation of AMPK signaling. *Proc Natl Acad Sci U S A* **112**, (2015).
10. McNally, E. M. *et al.* Caveolin-3 in muscular dystrophy. *Hum Mol Genet* **7**, 871–877 (1998).
11. Tadayoni, R., Rendon, A., Soria-Jasso, L. E. & Cisneros, B. Dystrophin Dp71: The smallest but multifunctional product of the duchenne muscular dystrophy gene. *Molecular Neurobiology* vol. 45 43–60 Preprint at https://doi.org/10.1007/s12035-011-8218-9 (2012).

12. Muntoni, F., Torelli, S. & Ferlini, A. Dystrophin and mutations: One gene, several proteins, multiple phenotypes. *Lancet Neurology* vol. 2 731–740 Preprint at https://doi.org/10.1016/S1474-4422(03)00585-4 (2003).
13. Millay, D. P. *et al.* Calcium influx is sufficient to induce muscular dystrophy through a TRPC-dependent mechanism. *Proc Natl Acad Sci U S A* **106**, 19023–19028 (2009).
14. Emery, A. E. H. The muscular dystrophies. *Lancet* **359**, 687–695 (2002).
15. Zhang, Q. *et al.* Nesprins: a novel family of spectrin-repeat-containing proteins that localize to the nuclear membrane in multiple tissues. *J Cell Sci* **114**, 4485–98 (2001).
16. Guo, C. *et al.* Absence of alpha 7 integrin in dystrophin-deficient mice causes a myopathy similar to Duchenne muscular dystrophy. *Hum Mol Genet* **15**, 989–998 (2006).
17. Rooney, J. E. *et al.* Severe muscular dystrophy in mice that lack dystrophin and alpha7 integrin. *J Cell Sci* **119**, 2185–2195 (2006).
18. Bonilla, E. *et al.* Duchenne Muscular Dystrophy: Deficiency of Dystrophin at the Muscle Cell Surface. *Cell* **54**, 447–452 (1988).
19. Muntoni, F. *et al.* Brief report: deletion of the dystrophin muscle-promoter region associated with X-linked dilated cardiomyopathy. *N Engl J Med* **329**, 921–925 (1993).
20. Yoshida, K. *et al.* Molecular analysis of the Duchenne muscular dystrophy gene in patients with Becker muscular dystrophy presenting with dilated cardiomyopathy. *Muscle Nerve* **16**, 1161–1166 (1993).
21. Zhang, Y. *et al.* A consolidated AAV system for single-cut CRISPR correction of a common Duchenne muscular dystrophy mutation. *Mol Ther Methods Clin Dev* **22**, 122 (2021).
22. Saotome, M., Yoshitomi, Y., Kojima, S. & Kuramochi, M. Dilated cardiomyopathy of Becker-type muscular dystrophy with exon 4 deletion--a case report. *Angiology* **52**, 343–347 (2001).
23. Gambetta, K. E. *et al.* Diversity of Dystrophin Gene Mutations and Disease Progression in a Contemporary Cohort of Duchenne Muscular Dystrophy. *Pediatr Cardiol* **43**, 855–867 (2022).
24. Walcher, T. *et al.* Cardiac involvement in a female carrier of Duchenne muscular dystrophy. *Int J Cardiol* **138**, 302–305 (2010).

25. Yilmaz, A. *et al.* Images in cardiovascular medicine. Cardiomyopathy in a Duchenne muscular dystrophy carrier and her diseased son: similar pattern revealed by cardiovascular MRI. *Circulation* **121**, (2010).
26. Ortiz-Lopez, R., Li, H., Su, J., Goytia, V. & Towbin, J. A. Evidence for a Dystrophin Missense Mutation as a Cause of X-Linked Dilated Cardiomyopathy. *Circulation* **95**, 2434–2440 (1997).
27. Duelen, R. *et al.* Human iPSC model reveals a central role for NOX4 and oxidative stress in Duchenne cardiomyopathy. *Stem Cell Reports* **17**, 352 (2022).
28. Bitetti, I., Mautone, C., Bertella, M., Manna, M. R. & Varone, A. Early treatment with Ataluren of a 2-year-old boy with nonsense mutation Duchenne dystrophy. *Acta Myologica* **40**, 184 (2021).
29. van Reeuwijk, J. *et al.* Intragenic deletion in the LARGE gene causes Walker-Warburg syndrome. *Hum Genet* **121**, 685 (2007).
30. Brockington, M. *et al.* Mutations in the fukutin-related protein gene (FKRP) cause a form of congenital muscular dystrophy with secondary laminin α2 deficiency and abnormal glycosylation of α-dystroglycan. *Am J Hum Genet* **69**, 1198–1209 (2001).
31. Poppe, M. *et al.* Cardiac and respiratory failure in limb-girdle muscular dystrophy 2I. *Ann Neurol* **56**, 738–741 (2004).
32. Kondo-Lida, E. *et al.* Novel Mutations and Genotype-Phenotype Relationships in 107 Families With Fukuyama-Type Congenital Muscular Dystrophy (FCMD). *Hum Mol Genet* **8**, 2303–2309 (1999).
33. Hara, Y. *et al.* A Dystroglycan Mutation Associated with Limb-Girdle Muscular Dystrophy. *New England Journal of Medicine* **364**, 939–946 (2011).
34. Bello, L. *et al.* Cardiomyopathy in patients with POMT1-related congenital and limb-girdle muscular dystrophy. *European Journal of Human Genetics* **20**, 1234 (2012).
35. Barresi, R. *et al.* Disruption of heart sarcoglycan complex and severe cardiomyopathy caused by sarcoglycan mutations. *J Med Genet* **37**, 102–107 (2000).
36. Lu, Y. *et al.* Identification of a novel SGCA missense mutation in a case of limb-girdle muscular dystrophy 2D with the absence of four sarcoglycan proteins. *Neuropathology* **39**, 207–211 (2019).

37. Xia, W. *et al.* Case Report: A Boy From a Consanguineous Family Diagnosed With Congenital Muscular Dystrophy Caused by Integrin Alpha 7 (ITGA7) Mutation. *Front Genet* **12**, 1538 (2021).
38. Hayashi, Y. K. *et al.* Mutations in the integrin α7 gene cause congenital myopathy. *Nat Genet* **19**, 94–97 (1998).
39. Voorhees, A. P. & Han, H. C. Biomechanics of Cardiac Function. *Compr Physiol* **5**, 1623 (2015).
40. Brady, A. J. Mechanical Properties of Isolated Cardiac Myocytes. *Physiol Rev* **71**, 413 (1991).
41. Pinto, A. R. *et al.* Revisiting Cardiac Cellular Composition. *Circ Res* **118**, 400 (2016).
42. Klaourakis, K., Vieira, J. M. & Riley, P. R. The evolving cardiac lymphatic vasculature in development, repair and regeneration. *Nat Rev Cardiol* **18**, 368 (2021).
43. Sweeney, H. L. & Hammers, D. W. Muscle Contraction. *Cold Spring Harb Perspect Biol* **10**, (2018).
44. Zhao, G., Qiu, Y., Zhang, H. M. & Yang, D. Intercalated discs: cellular adhesion and signaling in heart health and diseases. *Heart Fail Rev* **24**, 115–132 (2019).
45. Wilson, D. G. S., Tinker, A. & Iskratsch, T. The role of the dystrophin glycoprotein complex in muscle cell mechanotransduction. *Communications Biology 2022 5:1* **5**, 1–18 (2022).
46. Sun, Z., Guo, S. S. & Fässler, R. Integrin-mediated mechanotransduction. *J Cell Biol* **215**, 445–456 (2016).
47. Henderson, C. A., Gomez, C. G., Novak, S. M., Mi-Mi, L. & Gregorio, C. C. Overview of the Muscle Cytoskeleton. *Compr Physiol* **7**, 891 (2017).
48. Squire, J. M. Architecture and function in the muscle sarcomere. *Curr Opin Struct Biol* **7**, 247–257 (1997).
49. Crocini, C. & Gotthardt, M. Cardiac sarcomere mechanics in health and disease. *Biophys Rev* **13**, 637 (2021).
50. Ahmed, R. E., Tokuyama, T., Anzai, T., Chanthra, N. & Uosaki, H. Sarcomere maturation: function acquisition, molecular mechanism, and interplay with other organelles. *Philosophical Transactions of the Royal Society B* **377**, (2022).
51. Flashman, E., Redwood, C., Moolman-Smook, J. & Watkins, H. Cardiac myosin binding protein C: its role in physiology and disease. *Circ Res* **94**, 1279–1289 (2004).

52. Craig and Vibert. Troponin and tropomyosin regulate contraction via calcium binding | Learn Science at Scitable. *Nature* https://www.nature.com/scitable/content/troponin-and-tropomyosin-regulate-contraction-via-calcium-14723328 (1994).
53. Neagoe, C. *et al.* Titin Isoform Switch in Ischemic Human Heart Disease. *Circulation* **106**, 1333–1341 (2002).
54. Fletcher, D. A. & Mullins, R. D. Cell mechanics and the cytoskeleton. *Nature* **463**, 485 (2010).
55. Hohmann, T. & Dehghani, F. The Cytoskeleton—A Complex Interacting Meshwork. *Cells* **8**, (2019).
56. Ingber, D. E. *Tensegrity I. Cell Structure and Hierarchical Systems Biology*. *Journal of Cell Science* vol. 116 1157–1173 (2003).
57. Maruthamuthu, V., Aratyn-Schaus, Y. & Gardel, M. L. Conserved F-actin Dynamics and Force Transmission at Cell Adhesions. *Curr Opin Cell Biol* **22**, 583 (2010).
58. Caporizzo, M. A. & Prosser, B. L. The microtubule cytoskeleton in cardiac mechanics and heart failure. *Nat Rev Cardiol* **19**, 364 (2022).
59. Caporizzo, M. A., Chen, C. Y., Bedi, K., Margulies, K. B. & Prosser, B. L. Microtubules Increase Diastolic Stiffness in Failing Human Cardiomyocytes and Myocardium. *Circulation* **141**, 902–915 (2020).
60. Belmadani, S., Poüs, C., Ventura-Clapier, R., Fischmeister, R. & Méry, P. F. Post-translational modifications of cardiac tubulin during chronic heart failure in the rat. *Mol Cell Biochem* **237**, 39–46 (2002).
61. Vergarajauregui, S. *et al.* AKAP6 orchestrates the nuclear envelope microtubule-organizing center by linking golgi and nucleus via AKAP9. *Elife* **9**, 1–30 (2020).
62. Macquart, C. *et al.* Microtubule cytoskeleton regulates Connexin 43 localization and cardiac conduction in cardiomyopathy caused by mutation in A-type lamins gene. *Hum Mol Genet* (2018) doi:10.1093/hmg/ddy227.
63. Frangogiannis, N. G. The extracellular matrix in ischemic and nonischemic heart failure. *Circulation Research* vol. 125 117–146 Preprint at https://doi.org/10.1161/CIRCRESAHA.119.311148 (2019).
64. Silva, A. C., Pereira, C., Fonseca, A. C. R. G., Pinto-do-Ó, P. & Nascimento, D. S. Bearing My Heart: The Role of Extracellular Matrix on Cardiac Development,

Homeostasis, and Injury Response. *Frontiers in Cell and Developmental Biology* vol. 8 1705 Preprint at https://doi.org/10.3389/fcell.2020.621644 (2021).

65. Ffrench-Constant, C. Alternative Splicing of Fibronectin—Many Different Proteins but Few Different Functions. *Exp Cell Res* **221**, 261–271 (1995).
66. Lockhart, M., Wirrig, E., Phelps, A. & Wessels, A. Extracellular matrix and heart development. *Birth Defects Res A Clin Mol Teratol* **91**, (2011).
67. Mittal, A., Pulina, M., Hou, S.-Y. & Astrof, S. Fibronectin and integrin alpha 5 play requisite roles in cardiac morphogenesis. *Dev Biol* **381**, 73–82 (2013).
68. George, E., Georges-Labouesse, E., Patel-King, R., Rayburn, H. & Hynes, R. Defects in mesoderm, neural tube and vascular development in mouse embryos lacking fibronectin. *Development* **119**, 1079–1091 (1993).
69. Boyd, A., Montandon, M., Wood, A. J. & Currie, P. D. FKRP directed fibronectin glycosylation: A novel mechanism giving insights into muscular dystrophies? *Bioessays* **44**, e2100270 (2022).
70. Hamill, K. J., Kligys, K., Hopkinson, S. B. & Jones, J. C. R. Laminin deposition in the extracellular matrix: a complex picture emerges. *J Cell Sci* **122**, 4409–4417 (2009).
71. Jourdan-LeSaux, C., Zhang, J. & Lindsey, M. L. Extracellular Matrix Roles During Cardiac Repair. *Life Sci* **87**, 391 (2010).
72. Michele, D. E., Kabaeva, Z., Davis, S. L., Weiss, R. M. & Campbell, K. P. Dystroglycan matrix receptor function in cardiac myocytes is important for limiting activity-induced myocardial damage. *Circ Res* **105**, 984–993 (2009).
73. Libell, E. M. *et al.* Cardiomyopathy in limb girdle muscular dystrophy R9, FKRP related. *Muscle Nerve* **62**, 626–632 (2020).
74. Brancaccio, A. A molecular overview of the primary dystroglycanopathies. *J Cell Mol Med* **23**, 3058–3062 (2019).
75. Mayer, U. *et al.* Absence of integrin α7 causes a novel form of muscular dystrophy. *Nat Genet* **17**, 318–323 (1997).
76. Berry, M. F. *et al.* Mesenchymal stem cell injection after myocardial infarction improves myocardial compliance. *https://doi.org/10.1152/ajpheart.01017.2005* **290**, 2196–2203 (2006).
77. Bassat, E. *et al.* The extracellular matrix protein agrin promotes heart regeneration in mice. *Nature* **547**, 179–184 (2017).

78. Sato, S. *et al.* Pikachurin, a dystroglycan ligand, is essential for photoreceptor ribbon synapse formation. *Nat Neurosci* **11**, 923–931 (2008).
79. Clippinger, S. R. *et al.* Disrupted mechanobiology links the molecular and cellular phenotypes in familial dilated cardiomyopathy. *Proc Natl Acad Sci U S A* **116**, 17831 (2019).
80. Vardas, P., Maniadakis, N., Bardinet, I. & Pinto, F. The European Society of Cardiology Atlas of Cardiology: rational, objectives, and methods. *Eur Heart J Qual Care Clin Outcomes* **2**, 6–15 (2016).
81. Meyers, T. A. & Townsend, D. W. *Cardiac Pathophysiology and the Future of Cardiac Therapies in Duchenne Muscular Dystrophy.* vol. 20 (2019).
82. Chen, B. & Frangogiannis, N. G. Immune cells in repair of the infarcted myocardium. *Microcirculation* **24**, (2017).
83. Jacot, J. G., Mcculloch, A. D. & Omens, J. H. Substrate stiffness affects the functional maturation of neonatal rat ventricular myocytes. **95**, (2008).
84. Valiente-Alandi, I. *et al.* Inhibiting Fibronectin Attenuates Fibrosis and Improves Cardiac Function in a Model of Heart Failure. *Circulation* **138**, 1236–1252 (2018).
85. Bhana, B. *et al.* Influence of substrate stiffness on the phenotype of heart cells. *Biotechnol Bioeng* **105**, 1148–60 (2010).
86. Engler, A. J. *et al.* Embryonic cardiomyocytes beat best on a matrix with heart-like elasticity: scar-like rigidity inhibits beating. *J Cell Sci* **121**, (2008).
87. Chaturvedi, R. R. *et al.* Passive stiffness of myocardium from congenital heart disease and implications for diastole. *Circulation* **121**, 979–988 (2010).
88. Arani, A. *et al.* Cardiac MR elastography for quantitative assessment of elevated myocardial stiffness in cardiac amyloidosis. *Journal of Magnetic Resonance Imaging* **46**, 1361–1367 (2017).
89. Boothe, S. D. *et al.* The Effect of Substrate Stiffness on Cardiomyocyte Action Potentials. *Cell Biochem Biophys* **74**, 527–535 (2016).
90. Forte, G. *et al.* Substrate stiffness modulates gene expression and phenotype in neonatal cardiomyocytes in vitro. *Tissue Eng Part A* **18**, 1837–1848 (2012).
91. Kharraz, Y., Guerra, J., Pessina, P., Serrano, A. L. & Muñoz-Cánoves, P. Understanding the process of fibrosis in duchenne muscular dystrophy. *BioMed Research International* vol. 2014 Preprint at https://doi.org/10.1155/2014/965631 (2014).

92. Yuan, W. & Varga, J. Transforming Growth Factor-β Repression of Matrix Metalloproteinase-1 in Dermal Fibroblasts Involves Smad3. *Journal of Biological Chemistry* **276**, 38502–38510 (2001).
93. Ignotzs, R. A. & Massague, J. Transforming Growth Factor-beta Stimulates the Expression of Fibronectin and Collagen and Their Incorporation into the Extracellular Matrix. *Journal of Biological Chemistry* **261**, 4337–4345 (1986).
94. Khan, R. & Sheppard, R. Fibrosis in heart disease: understanding the role of transforming growth factor-β1 in cardiomyopathy, valvular disease and arrhythmia. *Immunology* **118**, 10 (2006).
95. Münch, J. & Abdelilah-Seyfried, S. Sensing and Responding of Cardiomyocytes to Changes of Tissue Stiffness in the Diseased Heart. *Front Cell Dev Biol* **9**, 642840 (2021).
96. Arslan, F. *et al.* Lack of fibronectin-EDA promotes survival and prevents adverse remodeling and heart function deterioration after myocardial infarction. *Circ Res* **108**, 582–592 (2011).
97. Mavrogeni, S. *et al.* Myocardial inflammation in Duchenne Muscular Dystrophy as a precipitating factor for heart failure: a prospective study. *BMC Neurol* **10**, (2010).
98. Arslan, F. *et al.* Lack of fibronectin-EDA promotes survival and prevents adverse remodeling and heart function deterioration after myocardial infarction. *Circ Res* **108**, 582–592 (2011).
99. Kerr, J. P. *et al.* Detyrosinated microtubules modulate mechanotransduction in heart and skeletal muscle. *Nat Commun* **6**, 1–14 (2015).
100. Luedde, M. *et al.* RIP3, a kinase promoting necroptotic cell death, mediates adverse remodelling after myocardial infarction. *Cardiovasc Res* **103**, 206–216 (2014).
101. Morgan, J. E. *et al.* Necroptosis mediates myofibre death in dystrophin-deficient mice. **9**, 1–10 (2018).
102. Qiao, S. *et al.* RIPK1-RIPK3 mediates myocardial fibrosis in type 2 diabetes mellitus by impairing autophagic flux of cardiac fibroblasts. *Cell Death Dis* **13**, (2022).
103. Chang, A. C. Y. *et al.* Increased tissue stiffness triggers contractile dysfunction and telomere shortening in dystrophic cardiomyocytes. *Stem Cell Reports* **16**, 2169 (2021).

104. Kamdar, F. & Garry, D. J. *Dystrophin-Deficient Cardiomyopathy*. *Journal of the American College of Cardiology* vol. 67 2533–2546 (2016).
105. Chen, C. Y. *et al.* Suppression of detyrosinated microtubules improves cardiomyocyte function in human heart failure. *Nature Medicine 2018 24:8* **24**, 1225–1233 (2018).
106. Robison, P. *et al.* Detyrosinated microtubules buckle and bear load in contracting cardiomyocytes. *Science* **352**, (2016).
107. Koenig, M. *et al.* Complete cloning of the Duchenne muscular dystrophy (DMD) cDNA and preliminary genomic organization of the DMD gene in normal and affected individuals. *Cell* **50**, 509–17 (1987).
108. Koenig, M., Monaco, A. P. & Kunkel, L. M. The complete sequence of dystrophin predicts a rod-shaped cytoskeletal protein. *Cell* **53**, 219–228 (1988).
109. Hoffman, E. P., Brown, R. H. & Kunkel, L. M. Dystrophin: the protein product of the Duchenne muscular dystrophy locus. *Cell* **51**, (1987).
110. Ervasti, J. M., Kahl, S. D. & Campbell, K. P. Purification of dystrophin from skeletal muscle. *Journal of Biological Chemistry* **266**, 9161–9165 (1991).
111. Roberds, S. L. *et al. Disruption of the Dystrophin-Glycoprotein Complex in the Cardiomyopathic Hamster*". *THE JOURNAL OF BIOLOGICAL CHEMISTRY* vol. 268 (1993).
112. Valera, I. C. *et al.* Essential roles of the dystrophin-glycoprotein complex in different cardiac pathologies. *Adv Med Sci* **66**, 52–71 (2021).
113. Anastasi, G. *et al.* Dystrophin-glycoprotein complex and vinculin-talin-integrin system in human adult cardiac muscle. *Int J Mol Med* **23**, 149–59 (2009).
114. Masubuchi, N., Shidoh, Y., Kondo, S., Takatoh, J. & Hanaoka, K. Subcellular localization of dystrophin isoforms in cardiomyocytes and Phenotypic analysis of dystrophin-deficient mice Reveal cardiac myopathy is predominantly caused by a deficiency in full-length dystrophin. *Exp Anim* **62**, 211–217 (2013).
115. Fabbrizio, E. *et al.* Characterization and localization of a 77 kDa protein related to the dystrophin gene family. *Biochemical Journal* **299**, 359–365 (1994).
116. Klietsch, R., Ervasti, J. M., Arnold, W., Campbell, K. P. & Jorgensen, A. O. Dystrophin-glycoprotein complex and laminin colocalize to the sarcolemma and transverse tubules of cardiac muscle. *Circ Res* **72**, 349–360 (1993).

117. Connors, N. C. & Kofuji, P. Dystrophin Dp71 is Critical for the Clustered Localization of Potassium Channels in Retinal Glial Cells. *Journal of Neuroscience* **22**, 4321–4327 (2002).

118. Schorling, D. C. *et al.* Impaired secretion of platelet granules in patients with Duchenne muscular dystrophy – results of a prospective diagnostic study. *Neuromuscular Disorders* **31**, 35–43 (2021).

119. Naidoo, M. & Anthony, K. Dystrophin Dp71 and the Neuropathophysiology of Duchenne Muscular Dystrophy. *Molecular Neurobiology* vol. 57 1748–1767 Preprint at https://doi.org/10.1007/s12035-019-01845-w (2020).

120. Karnam, S. & Ponugoti, V. R. The Role of Dystrophin (Dp71) in Membrane Organization and Mechanics of the Ocular Lens . *Investigative Opthamology and Visual Science* **60**, 5687 (2019).

121. Nico, B. *et al.* Altered blood–brain barrier development in dystrophic MDX mice. *Neuroscience* **125**, 921–935 (2004).

122. Hemmings, L., Kuhlman, P. A. & Critchley, D. R. Analysis of the actin-binding domain of α-actinin by mutagenesis and demonstration that dystrophin contains a functionally homologous domain. *Journal of Cell Biology* **116**, 1369–1380 (1992).

123. Rybakova, I. N., Patel, J. R. & Ervasti, J. M. The Dystrophin Complex Forms a Mechanically Strong Link Between the Sarcolemma and Costameric Actin. *J Cell Biol* **150**, 1209–1214 (2000).

124. Waugh, R. E. & Agre, P. Reductions of erythrocyte membrane viscoelastic coefficients reflect spectrin deficiencies in hereditary spherocytosis. *J Clin Invest* **81**, 133–141 (1988).

125. Pasternak, C., Wong, S. & Elson, E. L. *Mechanical Function of Dystrophin in Muscle Cells*. *The Journal of cell biology* vol. 128 355–361 (J Cell Biol, 1995).

126. Bhasin, N. *et al.* Molecular Extensibility of Mini-dystrophins and a Dystrophin Rod Construct. *J Mol Biol* **352**, 795–806 (2005).

127. DeWolf, C. *et al.* Interaction of dystrophin fragments with model membranes. *Biophys J* **72**, 2599–2604 (1997).

128. Le Rumeur, E. *et al.* Interaction of dystrophin rod domain with membrane phospholipids: Evidence of a close proximity between tryptophan residues and lipids. *Journal of Biological Chemistry* **278**, 5993–6001 (2003).

129. Zhao, J. *et al.* Dystrophin contains multiple independent membrane-binding domains. *Hum Mol Genet* **25**, 3647–3653 (2016).
130. Nelson, D. M. *et al.* Variable rescue of microtubule and physiological phenotypes in mdx muscle expressing different miniaturized dystrophins. *Hum Mol Genet* **27**, 2090–2100 (2018).
131. Ayalon, G., Davis, J. Q., Scotland, P. B. & Bennett, V. An ankyrin-based mechanism for functional organization of dystrophin and dystroglycan. *Cell* **135**, 1189–1200 (2008).
132. Belanto, J. J. *et al.* Microtubule binding distinguishes dystrophin from utrophin. *Proc Natl Acad Sci U S A* **111**, 5723–5728 (2014).
133. Constantin, B. Dystrophin complex functions as a scaffold for signalling proteins ☆. *Biochimica et Biophysica Acta (BBA) - Biomembranes* **1838**, 635–42 (2014).
134. Dwyer, T. M. & Froehner, S. C. Direct binding of Torpedo syntrophin to dystrophin and the 87 kDa dystrophin homologue. *FEBS Lett* **375**, 91–94 (1995).
135. Ervasti, J. M. Dystrophin, its interactions with other proteins, and implications for muscular dystrophy. *Biochimica et Biophysica Acta - Molecular Basis of Disease* vol. 1772 108–117 Preprint at https://doi.org/10.1016/j.bbadis.2006.05.010 (2007).
136. Sadoulet-Puccio, H. M., Rajala, M. & Kunkel, L. M. Dystrobrevin and dystrophin: an interaction through coiled-coil motifs. *Proc Natl Acad Sci U S A* **94**, 12413–12418 (1997).
137. Schofield, J., Houzelstein, D., Davies, K., Buckingham, M. & Edwards, Y. H. Expression of the dystrophin-related protein (utrophin) gene during mouse embryogenesis. *Dev Dyn* **198**, 254–264 (1993).
138. Love, D. R. *et al.* An autosomal transcript in skeletal muscle with homology to dystrophin. *Letters to Nature* **339**, 55 (1989).
139. Vulin, A. *et al.* The ZZ Domain of Dystrophin in DMD: Making Sense of Missense Mutations. *Hum Mutat* **35**, 257 (2014).
140. Ishikawa-Sakurai, M., Yoshida, M., Imamura, M., Davies, K. E. & Ozawa, E. ZZ domain is essentially required for the physiological binding of dystrophin and utrophin to β-dystroglycan. *Hum Mol Genet* **13**, 693–702 (2004).
141. Amann, K. J., Guo, A. W. X. & Ervasti, J. M. Utrophin lacks the rod domain actin binding activity of dystrophin. *J Biol Chem* **274**, 35375–35380 (1999).

142. Broderick, M. J. F., Bobkov, A. & Winder, S. J. Utrophin ABD binds to F-actin in an open conformation. *FEBS Open Bio* **2**, 6 (2012).
143. Rybakova, I. N., Humston, J. L., Sonnemann, K. J. & Ervasti, J. M. Dystrophin and Utrophin Bind Actin through Distinct Modes of Contact *. (2006) doi:10.1074/jbc.M513121200.
144. Rajaganapathy, S. *et al.* Distinct mechanical properties in homologous spectrin-like repeats of utrophin. *Sci Rep* **9**, (2019).
145. Song, M. H. *et al.* Matricellular Protein CCN5 Gene Transfer Ameliorates Cardiac and Skeletal Dysfunction in mdx/utrn (±) Haploinsufficient Mice by Reducing Fibrosis and Upregulating Utrophin Expression. *Front Cardiovasc Med* **9**, (2022).
146. Péladeau, C. *et al.* Identification of therapeutics that target eEF1A2 and upregulate utrophin A translation in dystrophic muscles. *Nat Commun* **11**, (2020).
147. Tinsley, J. *et al.* Expression of full-length utrophin prevents muscular dystrophy in mdx mice. *Nature Medicine 1998 4:12* **4**, 1441–1444 (1998).
148. Mizuno, Y., Nonaka, I., Hirai, S. & Ozawa, E. Reciprocal expression of dystrophin and utrophin in muscles of Duchenne muscular dystrophy patients, female DMD-carriers and control subjects. *J Neurol Sci* **119**, 43–52 (1993).
149. Barnabei, M. S. & Metzger, J. M. Ex Vivo Stretch Reveals Altered Mechanical Properties of Isolated Dystrophin-Deficient Hearts. *PLoS One* **7**, 32880 (2012).
150. Holt, K. H., Crosbie, R. H., Venzke, D. P. & Campbell, K. P. Biosynthesis of dystroglycan: Processing of a precursor propeptide. *FEBS Lett* **468**, 79–83 (2000).
151. Patthy, L. & Nikolics, K. Functions of agrin and agrin-related proteins. *Trends Neurosci* **16**, 76–81 (1993).
152. Klietsch, R., Ervasti, J. M., Arnold, W., Campbell, K. P. & Jorgensen, A. O. Dystrophin-glycoprotein complex and laminin colocalize to the sarcolemma and transverse tubules of cardiac muscle. *Circ Res* **72**, 349–360 (1993).
153. Jung, D., Yang, B., Meyer, J., Chamberlain, J. S. & Campbell, K. P. Identification and characterization of the dystrophin anchoring site on β-dystroglycan. *Journal of Biological Chemistry* **270**, 27305–27310 (1995).
154. Mercuri, E. *et al.* Congenital muscular dystrophy with secondary merosin deficiency and normal brain MRI: A novel entity? *Neuropediatrics* **31**, 186–189 (2000).

155. Endo, T. Dystroglycan glycosylation and its role in α-dystroglycanopathies. in *Acta Myologica* vol. 26 165–170 (XXVI, 2007).
156. Han, R. *et al.* Basal lamina strengthens cell membrane integrity via the laminin G domain-binding motif of α-dystroglycan. *Proc Natl Acad Sci U S A* **106**, 12573–12579 (2009).
157. Ilsley, J. L., Sudol, M. & Winder, S. J. The interaction of dystrophin with β-dystroglycan is regulated by tyrosine phosphorylation. *Cell Signal* **13**, 625–632 (2001).
158. Takawira, D., Budinger, G. R. S., Hopkinson, S. B. & Jones, J. C. R. A dystroglycan/plectin scaffold mediates mechanical pathway bifurcation in lung epithelial cells. *J Biol Chem* **286**, 6301–6310 (2011).
159. Ferry, A. *et al.* Desmin prevents muscle wasting, exaggerated weakness and fragility, and fatigue in dystrophic mdx mouse. *J Physiol* **598**, 3667–3689 (2020).
160. Carlier, M. F. *et al.* GRB2 links signaling to actin assembly by enhancing interaction of neural Wiskott-Aldrich syndrome protein (N-WASp) with actin-related protein (ARP2/3) complex. *J Biol Chem* **275**, 21946–21952 (2000).
161. Schlaepfer, D. D., Hanks, S. K., Hunter, T. & Geer, P. Van Der. Integrin-mediated signal transduction linked to Ras pathway by GRB2 binding to focal adhesion kinase. *Nature* **372**, 786–791 (1994).
162. Williamson, R. A. *et al.* Dystroglycan is essential for early embryonic development: disruption of Reichert's membrane in Dag1-null mice. *Hum Mol Genet* **6**, 831–841 (1997).
163. van Reeuwijk, J., Brunner, H. G. & van Bokhoven, H. Glyc-O-genetics of Walker-Warburg syndrome. *Clinical Genetics* vol. 67 281–289 Preprint at https://doi.org/10.1111/j.1399-0004.2004.00368.x (2005).
164. Beltran-Valero de Bernabé, D. *et al.* Mutations in the FKRP gene can cause muscle-eye-brain disease and Walker-Warburg syndrome. *J Med Genet* **41**, (2004).
165. Walter, M. C. *et al.* FKRP (826C>A) frequently causes limb-girdle muscular dystrophy in German patients. *J Med Genet* **41**, 50 (2004).
166. Holt, K. H. & Campbell, K. P. Assembly of the Sarcoglycan Complex Insights for Muscular Dystrophy. *Journal of Biological Chemistry* **273**, 34667–70 (1998).
167. Matsunari, H. *et al.* Pigs with δ-sarcoglycan deficiency exhibit traits of genetic cardiomyopathy. *Laboratory Investigation* **100**, 887–899 (2020).

168. Rutschow, D. *et al.* S151A δ-sarcoglycan mutation causes a mild phenotype of cardiomyopathy in mice. *European Journal of Human Genetics* **22**, 119–125 (2014).
169. Alonso-Pérez, J. *et al.* New genotype-phenotype correlations in a large European cohort of patients with sarcoglycanopathy. *Brain* **143**, 2696–2708 (2020).
170. Nigro, V. *et al.* Autosomal recessive limb-girdle muscular dystrophy, LGMD2F, is caused by a mutation in the delta-sarcoglycan gene. *Nat Genet* **14**, 195–198 (1996).
171. Tsubata, S. *et al.* Mutations in the human delta-sarcoglycan gene in familial and sporadic dilated cardiomyopathy. *J Clin Invest* **106**, 655–662 (2000).
172. Campbell, M. D., Witcher, M., Gopal, A. & Michele, D. E. Plasma Membrane Integrity in Cardiovascular Physiology and Pathology: Dilated cardiomyopathy mutations in δ-sarcoglycan exert a dominant-negative effect on cardiac myocyte mechanical stability. *Am J Physiol Heart Circ Physiol* **310**, H1140 (2016).
173. Shu, C. *et al.* High-throughput screening identifies modulators of sarcospan that stabilize muscle cells and exhibit activity in the mouse model of Duchenne muscular dystrophy. *Skeletal Muscle 2020 10:1* **10**, 1–17 (2020).
174. Miller, G., Wang, E. L., Nassar, K. L., Peter, A. K. & Crosbie, R. H. Structural and functional analysis of the sarcoglycan-sarcospan subcomplex. *Exp Cell Res* **313**, 639–651 (2007).
175. Mamsa, H., Stark, R. L., Shin, K. M., Beedle, A. M. & Crosbie, R. H. Sarcospan increases laminin-binding capacity of α-dystroglycan to ameliorate DMD independent of Galgt2. *Hum Mol Genet* **31**, 718–732 (2022).
176. Marshall, J. L. *et al.* Dystrophin and utrophin expression require sarcospan: loss of a7 integrin exacerbates a newly discovered muscle phenotype in sarcospan-null mice. (2012) doi:10.1093/hmg/dds271.
177. Brenman, J. E. *et al.* Interaction of nitric oxide synthase with the postsynaptic density protein PSD-95 and α1-syntrophin mediated by PDZ domains. *Cell* **84**, 757–767 (1996).
178. Bhat, S. S., Ali, R. & Khanday, F. A. Syntrophins entangled in cytoskeletal meshwork: Helping to hold it all together. *Cell Prolif* **52**, (2019).
179. Adams, M. E. *et al.* Two forms of mouse syntrophin, a 58 kd dystrophin-associated protein, differ in primary structure and tissue distribution. *Neuron* **11**, 531–540 (1993).

180. Adams, M. E., Odom, G. L., Kim, M. J., Chamberlain, J. S. & Froehner, S. C. Syntrophin binds directly to multiple spectrin-like repeats in dystrophin and mediates binding of nNOS to repeats 16–17. *Hum Mol Genet* **27**, 2978–2985 (2018).

181. Hillier, B. J., Christopherson, K. S., Prehoda, K. E., Bredt, D. S. & Lim, W. A. Unexpected modes of PDZ domain scaffolding revealed by structure of nNOS-syntrophin complex. *Science (1979)* **284**, 812–815 (1999).

182. Iwata, Y., Sampaolesi, M., Shigekawa, M. & Wakabayashi, S. Syntrophin is an actin-binding protein the cellular localization of which is regulated through cytoskeletal reorganization in skeletal muscle cells. *Eur J Cell Biol* **83**, 555–565 (2004).

183. Bhat, H. F., Baba, R. A., Adams, M. E. & Khanday, F. A. Role of SNTA1 in Rac1 activation, modulation of ROS generation, and migratory potential of human breast cancer cells. *Br J Cancer* **110**, 706–714 (2014).

184. Wang, H. *et al.* Proteomic analysis identifies key differences in the cardiac interactomes of dystrophin and micro-dystrophin. *Hum Mol Genet* **30**, 1321–1336 (2021).

185. Gavillet, B. *et al.* Cardiac sodium channel Nav1.5 is regulated by a multiprotein complex composed of syntrophins and dystrophin. *Circ Res* **99**, 407–414 (2006).

186. Seo, K. *et al.* Hyperactive adverse mechanical stress responses in dystrophic heart are coupled to transient receptor potential canonical 6 and blocked by cgmp-protein kinase g modulation. *Circ Res* **114**, 823–832 (2014).

187. Chung, H. S. *et al.* Transient receptor potential channel 6 regulates abnormal cardiac S-nitrosylation in Duchenne muscular dystrophy. *Proc Natl Acad Sci U S A* **114**, E10763–E10771 (2017).

188. Lopez, J. R., Uryash, A., Faury, G., Estève, E. & Adams, J. A. Contribution of TRPC Channels to Intracellular Ca2 + Dyshomeostasis in Smooth Muscle From mdx Mice. *Front Physiol* **11**, 126 (2020).

189. Ingber, D. E. Cellular mechanotransduction: putting all the pieces together again. *The FASEB Journal* **20**, 811–827 (2006).

190. Yao, M. *et al.* Force-dependent conformational switch of α-catenin controls vinculin binding. *Nat Commun* **5**, 4525 (2014).

191. Yao, M. *et al.* The mechanical response of talin. *Nature Communications 2016 7:1* **7**, 1–11 (2016).

192. Del Rio, A. *et al.* Stretching single talin rod molecules activates vinculin binding. *Science* **323**, 638–641 (2009).
193. Amann, K. J., Renley, B. A. & Ervasti, J. M. A cluster of basic repeats in the dystrophin rod domain binds F-actin through an electrostatic interaction. *Journal of Biological Chemistry* **273**, 28419–28423 (1998).
194. Wang, N., Tytell, J. D. & Ingber, D. E. Mechanotransduction at a distance: mechanically coupling the extracellular matrix with the nucleus. *Focus on Mechanotransduction* **10**, 75–82 (2009).
195. Miroshnikova, Y. A. & Wickström, S. A. Mechanical Forces in Nuclear Organization. *Cold Spring Harb Perspect Biol* **14**, a039685 (2021).
196. Na, S. *et al.* Rapid signal transduction in living cells is a unique feature of mechanotransduction. *Proc Natl Acad Sci U S A* **105**, 6626–6631 (2008).
197. Wilson, D. G. S. & Iskratsch, T. Factoring in the force: A novel role for eIF6. *J Cell Biol* **221**, (2022).
198. Keen, A. N. *et al.* Eukaryotic initiation factor 6 regulates mechanical responses in endothelial cells. *J Cell Biol* **221**, e202005213 (2022).
199. Prins, K. W. *et al.* Dystrophin is a microtubule-associated protein. *Journal of Cell Biology* **186**, 363–369 (2009).
200. Spreafico, M. *et al.* Targeting HDAC8 to ameliorate skeletal muscle differentiation in Duchenne muscular dystrophy. *Pharmacol Res* **170**, 105750 (2021).
201. Ono, H. *et al.* AMPK Complex Activation Promotes Sarcolemmal Repair in Dysferlinopathy. *Mol Ther* **28**, 1133–1153 (2020).
202. Campbell, I. D. & Humphries, M. J. Integrin Structure, Activation, and Interactions. *Cold Spring Harb Perspect Biol* **3**, a00494 (2002).
203. Hynes, R. O. Integrins: bidirectional, allosteric signaling machines. *Cell* **110**, 673–687 (2002).
204. Di Cio, S., Bøggild, T. M. L., Connelly, J., Sutherland, D. S. & Gautrot, J. E. Differential integrin expression regulates cell sensing of the matrix nanoscale geometry. *Acta Biomater* **50**, 280–292 (2017).
205. Yamada, M. & Sekiguchi, K. Molecular Basis of Laminin–Integrin Interactions. *Curr Top Membr* **76**, 197–229 (2015).
206. Sun, Y. *et al.* Matrix stiffness regulates myocardial differentiation of human umbilical cord mesenchymal stem cells. *Aging* **12**, (2020).

207. Zhang, S. J., Truskey, G. A. & Kraus, W. E. Effect of cyclic stretch on β1D-integrin expression and activation of FAK and RhoA. *Am J Physiol Cell Physiol* **292**, 2057–2069 (2007).

208. Ingber, D. E. Mechanical signaling and the cellular response to extracellular matrix in angiogenesis and cardiovascular physiology. *Circulation Research* vol. 91 877–887 Preprint at https://doi.org/10.1161/01.RES.0000039537.73816.E5 (2002).

209. Chen, C., Manso, A. M. & Ross, R. S. Talin and Kindlin as Integrin-Activating Proteins: Focus on the Heart. *Pediatr Cardiol* **40**, 1401–1409 (2019).

210. Castillo, E. A., Lane, K. V. & Pruitt, B. L. Micromechanobiology: Focusing on the Cardiac Cell–Substrate Interface. *https://doi.org/10.1146/annurev-bioeng-092019-034950* **22**, 257–284 (2020).

211. Roca-Cusachs, P., Iskratsch, T. & Sheetz, M. P. Finding the weakest link-exploring integrin-mediated mechanical molecular pathways. *Journal of Cell Science* vol. 125 3025–3038 Preprint at https://doi.org/10.1242/jcs.095794 (2012).

212. Sun, Z., Costell, M. & Fässler, R. Integrin activation by talin, kindlin and mechanical forces. *Nat Cell Biol* **21**, (2019).

213. Paul, R., Heil, P., Spatz, J. P. & Schwarz, U. S. Propagation of Mechanical Stress through the Actin Cytoskeleton toward Focal Adhesions: Model and Experiment. *Biophys J* **94**, (2008).

214. Jonas, O. & Duschl, C. Force propagation and force generation in cells. *Cytoskeleton* **67**, 555–563 (2010).

215. Anastasi, G. *et al.* Dystrophin-glycoprotein complex and vinculin-talin-integrin system in human adult cardiac muscle. *Int J Mol Med* **23**, 149–59 (2009).

216. Paul, A. C., Sheard, P. W., Kaufman, S. J. & Duxson, M. J. Localization of α7 integrins and dystrophin suggests potential for both lateral and longitudinal transmission of tension in large mammalian muscles. *Cell and Tissue Research 2002 308:2* **308**, 255–265 (2002).

217. Yoshida, T., Pan, Y., Hanada, H., Iwata, Y. & Shigekawa, M. Bidirectional Signaling between Sarcoglycans and the Integrin Adhesion System in Cultured L6 Myocytes *. *Journal of Biological Chemistry* **273**, 1583–1590 (1998).

218. Elsherif, L. *et al.* Combined deficiency of dystrophin and β1 integrin in the cardiac myocyte causes myocardial dysfunction, fibrosis and calcification. *Circ Res* **102**, 1109–1117 (2008).

219. Oliveira-Santos, A., Dagda, M. & Burkin, D. J. Sunitinib inhibits STAT3 phosphorylation in cardiac muscle and prevents cardiomyopathy in the mdx mouse model of Duchenne muscular dystrophy. *Hum Mol Genet* **ddac042**, 1–12 (2022).
220. Burkin, D. J. *et al.* Transgenic Expression of α7β1 Integrin Maintains Muscle Integrity, Increases Regenerative Capacity, Promotes Hypertrophy, and Reduces Cardiomyopathy in Dystrophic Mice. *Am J Pathol* **166**, 253 (2005).
221. Hodges, B. L. *et al.* Altered expression of the alpha7beta1 integrin in human and murine muscular dystrophies. *J Cell Sci* **110**, 2873–2881 (1997).
222. Heller, K. N. *et al.* AAV-mediated overexpression of human α7 integrin leads to histological and functional improvement in dystrophic mice. *Mol Ther* **21**, 520–525 (2013).
223. Sarathy, A. *et al.* SU9516 Increases α7β1 Integrin and Ameliorates Disease Progression in the mdx Mouse Model of Duchenne Muscular Dystrophy. *Molecular Therapy* **25**, 1395–1407 (2017).
224. Wuebbles, R. D., Sarathy, A., Kornegay, J. N. & Burkin, D. J. Levels of α7 integrin and laminin-α2 are increased following prednisone treatment in the mdx mouse and GRMD dog models of Duchenne muscular dystrophy. *DMM Disease Models and Mechanisms* **6**, 1175–1184 (2013).
225. Parvatiyar, M. S. *et al.* Stabilization of the cardiac sarcolemma by sarcospan rescues DMD-associated cardiomyopathy. *JCI Insight* **4**, (2019).
226. Côté, P. D., Moukhles, H. & Carbonetto, S. Dystroglycan is not required for localization of dystrophin, syntrophin, and neuronal nitric-oxide synthase at the sarcolemma but regulates integrin alpha 7B expression and caveolin-3 distribution. *J Biol Chem* **277**, 4672–4679 (2002).
227. Cerna, J. *et al.* Dystrophin Dp71f Associates with the β1-Integrin Adhesion Complex to Modulate PC12 Cell Adhesion. *J Mol Biol* **362**, 954–965 (2006).
228. García-Tovar, C. G. *et al.* Dystrophin isoform Dp71 is present in lamellipodia and focal complexes in human astrocytoma cells U-373 MG. *Acta Histochem* **104**, 245–254 (2002).
229. Park, J., Jia, S., Salter, D., Bagnaninchi, P. & Hansen, C. G. The Hippo pathway drives the cellular response to hydrostatic pressure. *EMBO J* **41**, (2022).

230. Cao, H. *et al.* Substrate stiffness regulates differentiation of induced pluripotent stem cells into heart valve endothelial cells. *Acta Biomater* **143**, 115–126 (2022).
231. Thievessen, I. *et al.* The focal adhesion protein β-parvin controls cardiomyocyte shape and sarcomere assembly in response to mechanical load. *Curr Biol* (2022) doi:10.1016/J.CUB.2022.05.047.
232. Chugh, P. *et al.* Actin cortex architecture regulates cell surface tension Europe PMC Funders Group. *Nat Cell Biol* **19**, 689–697 (2017).
233. Ramirez, M. P. *et al.* Dystrophin missense mutations alter focal adhesion tension and mechanotransduction. *Proc Natl Acad Sci U S A* **119**, (2022).
234. Huang, H. *et al.* Cell stiffness and receptors: Evidence for cytoskeletal subnetworks. *Am J Physiol Cell Physiol* **288**, 57–61 (2005).
235. McNally, E. M. *et al.* Contemporary cardiac issues in Duchenne muscular dystrophy. Working Group of the National Heart, Lung, and Blood Institute in collaboration with Parent Project Muscular Dystrophy. *Circulation* **131**, 1590–8 (2015).
236. Aartsma-Rus, A. *et al.* Exploring the frontiers of therapeutic exon skipping for Duchenne muscular dystrophy by double targeting within one or multiple exons. *Mol Ther* **14**, 401–407 (2006).
237. Yasuma, F., Konagaya, M., Sakai, M., Kuru, S. & Kawamura, T. A new lease on life for patients with Duchenne muscular dystrophy in Japan. *American Journal of Medicine* vol. 117 363 Preprint at https://doi.org/10.1016/j.amjmed.2004.03.028 (2004).
238. Broomfield, J., Hill, M., Guglieri, M., Crowther, M. & Abrams, K. Life Expectancy in Duchenne Muscular Dystrophy. *Neurology* **97**, e2304–e2314 (2021).
239. Ho, R., Nguyen, M.-L. & Mather, P. Cardiomyopathy in becker muscular dystrophy: Overview. *World J Cardiol* **8**, 356 (2016).
240. Dellefave, L. & Mcnally, E. M. The genetics of dilated cardiomyopathy Introduction: Incidence of inherited dilated cardiomyopathy. *Curr Opin Cardiol* **25**, 198–204 (2010).
241. Zhou, C. *et al.* Novel nesprin-1 mutations associated with dilated cardiomyopathy cause nuclear envelope disruption and defects in myogenesis. *Hum Mol Genet* **26**, (2017).

242. Vikhorev, P. G. *et al.* Titin-truncating mutations associated with dilated cardiomyopathy alter length-dependent activation and its modulation via phosphorylation. *Cardiovasc Res* **118**, 241–253 (2022).
243. Schultheiss, H. P. *et al.* Dilated cardiomyopathy. *Nat Rev Dis Primers* **5**, (2019).
244. Nigro, G., Politano, L., Nigro, V., Petretta, V. R. & Comi, L. I. Mutation of dystrophin gene and cardiomyopathy. *Neuromuscular Disorders* **4**, 371–379 (1994).
245. James, K. A. *et al.* Left ventricular dysfunction in Duchenne muscular dystrophy. *Cardiol Young* **30**, 171–176 (2020).
246. Townsend, D. W., Yasuda, S., Li, S., Chamberlain, J. S. & Metzger, J. M. Emergent Dilated Cardiomyopathy Caused by Targeted Repair of Dystrophic Skeletal Muscle. *Mol Ther* **16**, 832 (2008).
247. Chenard, A. A., Becane, H. M., Tertrain, F., de Kermadec, J. M. & Weiss, Y. A. Ventricular arrhythmia in Duchenne muscular dystrophy: Prevalence, significance and prognosis. *Neuromuscular Disorders* **3**, 201–206 (1993).
248. Groh, W. J. Arrhythmias in the muscular dystrophies. *Heart Rhythm* **9**, 1890–1895 (2012).
249. Ishizaki, M., Kobayashi, M., Adachi, K., Matsumura, T. & Kimura, E. Female dystrophinopathy: Review of current literature. *Neuromuscul Disord* **28**, 572–581 (2018).
250. Lee, S. H., Lee, J. H., Lee, K. A. & Choi, Y. C. Clinical and Genetic Characterization of Female Dystrophinopathy. *J Clin Neurol* **11**, 248 (2015).
251. Sarkozy, A. *et al.* 263rd ENMC International Workshop: Focus on female carriers of dystrophinopathy: refining recommendations for prevention, diagnosis, surveillance, and treatment. Hoofddorp, The Netherlands, 13-15 May 2022. *Neuromuscular Disorders* **33**, 274–284 (2023).
252. Takeshita, E. *et al.* Duchenne muscular dystrophy in a female with compound heterozygous contiguous exon deletions. *Neuromuscul Disord* **27**, 569–573 (2017).
253. Guglieri, M. *et al.* Effect of Different Corticosteroid Dosing Regimens on Clinical Outcomes in Boys With Duchenne Muscular Dystrophy: A Randomized Clinical Trial. *JAMA* **327**, 1456–68 (2022).
254. Aartsma-Rus, A., Ginjaar, I. B. & Bushby, K. The importance of genetic diagnosis for Duchenne muscular dystrophy. *J Med Genet* **53**, 145–51 (2016).

255. Birnkrant, D. J. *et al.* Cardiorespiratory management of Duchenne muscular dystrophy: emerging therapies, neuromuscular genetics, and new clinical challenges. *Lancet Respir Med* **10**, 403–420 (2022).
256. Birnkrant, D. J. *et al.* Cardiac and pulmonary function variability in Duchenne/Becker muscular dystrophy: an initial report. *J Child Neurol* **25**, 1110–1115 (2010).
257. Duboc, D. *et al.* Effect of perindopril on the onset and progression of left ventricular dysfunction in Duchenne muscular dystrophy. *J Am Coll Cardiol* **45**, 855–857 (2005).
258. Raman, S. V. *et al.* Stabilization of Early Duchenne Cardiomyopathy With Aldosterone Inhibition: Results of the Multicenter AIDMD Trial. *J Am Heart Assoc* **8**, (2019).
259. Raman, S. V. *et al.* Eplerenone for early cardiomyopathy in Duchenne muscular dystrophy: a randomised, double-blind, placebo-controlled trial. *Lancet Neurol* **14**, 153 (2015).
260. Allen, H. D. *et al.* A Randomized, Double-Blind Trial of Lisinopril and Losartan for the Treatment of Cardiomyopathy in Duchenne Muscular Dystrophy. *PLoS Curr* **5**, (2013).
261. Zhou, J., Xin, J., Niu, Y. & Wu, S. DMDtoolkit: a tool for visualizing the mutated dystrophin protein and predicting the clinical severity in DMD. *BMC Bioinformatics* **18**, (2017).
262. Lim, K. R. Q., Maruyama, R. & Yokota, T. Eteplirsen in the treatment of Duchenne muscular dystrophy. *Drug Design, Development and Therapy* vol. 11 533–545 Preprint at https://doi.org/10.2147/DDDT.S97635 (2017).
263. Frank, D. E. *et al.* Increased dystrophin production with golodirsen in patients with Duchenne muscular dystrophy. *Neurology* **94**, e2270–e2282 (2020).
264. Markati, T. *et al.* Emerging therapies for Duchenne muscular dystrophy. *Lancet Neurol* **21**, 814–829 (2022).
265. Chamberlain, J. *et al.* Micro-dystrophin expression as a surrogate endpoint for Duchenne muscular dystrophy clinical trials. *Hum Gene Ther* 1 (2023) doi:10.1089/HUM.2022.190.
266. Eser, G. & Topaloğlu, H. Current Outline of Exon Skipping Trials in Duchenne Muscular Dystrophy. *Genes (Basel)* **13**, (2022).

267. Bostick, B. *et al.* AAV micro-dystrophin gene therapy alleviates stress-induced cardiac death but not myocardial fibrosis in >21-m-old mdx mice, an end-stage model of Duchenne muscular dystrophy cardiomyopathy. *J Mol Cell Cardiol* **53**, 217 (2012).
268. Liang, L. C., Sulaiman, N. & Yazid, M. D. A Decade of Progress in Gene Targeted Therapeutic Strategies in Duchenne Muscular Dystrophy: A Systematic Review. *Front Bioeng Biotechnol* **10**, 833833 (2022).
269. Boehler, J. F. *et al.* Clinical potential of microdystrophin as a surrogate endpoint. *Neuromuscular Disorders* **33**, 40–49 (2023).
270. Chow, A. *et al.* Human Induced Pluripotent Stem Cell-Derived Cardiomyocyte Encapsulating Bioactive Hydrogels Improve Rat Heart Function Post Myocardial Infarction. *Stem Cell Reports* **9**, 1415 (2017).
271. Ingber, D. E. Tensegrity II. How structural networks influence cellular information processing networks. *J Cell Sci* **116**, 1397–408 (2003).
272. Mareedu, S., Million, E. D., Duan, D. & Babu, G. J. Abnormal Calcium Handling in Duchenne Muscular Dystrophy: Mechanisms and Potential Therapies. *Front Physiol* **12**, 355 (2021).
273. Millay, D. P. *et al.* Genetic and pharmacologic inhibition of mitochondrial-dependent necrosis attenuates muscular dystrophy. *Nat Med* **14**, 442–447 (2008).
274. Danialou, G. *et al.* Dystrophin-deficient cardiomyocytes are abnormally vulnerable to mechanical stress-induced contractile failure and injury. *The FASEB Journal* **15**, 1655–1657 (2001).
275. Dudley, R. W. R. *et al.* Sarcolemmal Damage in Dystrophin Deficiency Is Modulated by Synergistic Interactions between Mechanical and Oxidative/Nitrosative Stresses. *Am J Pathol* **168**, 1276 (2006).
276. Townsend, D. W. *et al.* Chronic administration of membrane sealant prevents severe cardiac injury and ventricular dilatation in dystrophic dogs. *Journal of Clinical Investigation* **120**, 1140–1150 (2010).
277. Yasuda, S. *et al.* Dystrophic heart failure blocked by membrane sealant poloxamer. *Nature* **436**, 1025–1029 (2005).
278. Spurney, C. F. *et al.* Membrane sealant Poloxamer P188 protects against isoproterenol induced cardiomyopathy in dystrophin deficient mice. *BMC Cardiovasc Disord* **11**, (2011).

279. Ryan, T. *Safety and Efficacy of P-188 NF in DMD Patients*. (2018). doi:NCT03558958.

280. Vila, M. C. *et al.* Mitochondria mediate cell membrane repair and contribute to Duchenne muscular dystrophy. *Cell Death & Differentiation 2017 24:2* **24**, 330–342 (2016).

281. Wallace, G. Q. & McNally, E. M. Mechanisms of muscle degeneration, regeneration, and repair in the muscular dystrophies. *Annu Rev Physiol* **71**, 37–57 (2009).

282. Sharma, N. *et al.* Use of Quantitative Membrane Proteomics Identifies a Novel Role of Mitochondria in Healing Injured Muscles. *J Biol Chem* **287**, 30455 (2012).

283. Altamirano, F. *et al.* Nifedipine treatment reduces resting calcium concentration, oxidative and apoptotic gene expression, and improves muscle function in dystrophic mdx mice. *PLoS One* **8**, (2013).

284. Mázala, D. A. G., Grange, R. W. & Chin, E. R. The role of proteases in excitation-contraction coupling failure in muscular dystrophy. *Am J Physiol Cell Physiol* **308**, C33–C40 (2015).

285. Hughes, M. C. *et al.* Early myopathy in Duchenne muscular dystrophy is associated with elevated mitochondrial H2O2 emission during impaired oxidative phosphorylation. *J Cachexia Sarcopenia Muscle* **10**, 643–661 (2019).

286. Dubinin, M. V. *et al.* Duchenne muscular dystrophy is associated with the inhibition of calcium uniport in mitochondria and an increased sensitivity of the organelles to the calcium-induced permeability transition. *Biochim Biophys Acta Mol Basis Dis* **1866**, (2020).

287. Williams, I. A. & Allen, D. G. The role of reactive oxygen species in the hearts of dystrophin-deficient mdx mice. *Am J Physiol Heart Circ Physiol* **293**, (2007).

288. Turner, P. R., Westwood, T., Regen, C. M. & Steinhardt, R. A. Increased protein degradation results from elevated free calcium levels found in muscle from mdx mice. *Nature* **335**, 735–738 (1988).

289. Fanchaouy, M. *et al.* Pathways of abnormal stress-induced Ca2+ influx into dystrophic mdx cardiomyocytes. *Cell Calcium* **46**, 114–121 (2009).

290. Mijares, A., Altamirano, F., Kolster, J., Adams, J. A. & López, J. R. Age-dependent changes in diastolic Ca2+ and Na+ concentrations in dystrophic cardiomyopathy: Role of Ca2+ entry and IP3. *Biochem Biophys Res Commun* **452**, 1054 (2014).

291. Law, M. L., Cohen, H., Martin, A. A., Angulski, A. B. B. & Metzger, J. M. Dysregulation of Calcium Handling in Duchenne Muscular Dystrophy-Associated Dilated Cardiomyopathy: Mechanisms and Experimental Therapeutic Strategies. *Journal of Clinical Medicine 2020, Vol. 9, Page 520* **9**, 520 (2020).
292. Bers, D. M. & Guo, T. Calcium signaling in cardiac ventricular myocytes. *Ann N Y Acad Sci* **1047**, 86–98 (2005).
293. Bellinger, A. M. *et al.* Hypernitrosylated ryanodine receptor calcium release channels are leaky in dystrophic muscle. *Nat Med* **15**, 325–330 (2009).
294. Fauconnier, J. *et al.* Leaky RyR2 trigger ventricular arrhythmias in Duchenne muscular dystrophy. *Proc Natl Acad Sci U S A* **107**, 1559–1564 (2010).
295. Lopez, J. R., Uryash, A., Faury, G., Estève, E. & Adams, J. A. Contribution of TRPC Channels to Intracellular Ca2 + Dyshomeostasis in Smooth Muscle From mdx Mice. *Front Physiol* **11**, 126 (2020).
296. Ward, C. W., Sachs, F., Bush, E. D. & Suchyna, T. M. GsMTx4-D provides protection to the D2.mdx mouse. *Neuromuscul Disord* **28**, 868 (2018).
297. Wang, J., Ma, Y., Sachs, F., Li, J. & Suchyna, T. M. GsMTx4-D is a cardioprotectant against myocardial infarction during ischemia and reperfusion. *J Mol Cell Cardiol* **98**, 83–94 (2016).
298. Iyer, S. R. *et al.* Altered nuclear dynamics in MDX myofibers. *J Appl Physiol* **122**, 470–481 (2017).
299. Khairallah, R. J. *et al.* Microtubules underlie dysfunction in duchenne muscular dystrophy. **5**, (2012).
300. Percival, J. M. *et al.* rAAV6-Microdystrophin rescues aberrant Golgi complex organization in mdx skeletal muscles. *Traffic* **8**, 1424–1439 (2007).
301. Stroud, M. J. Linker of nucleoskeleton and cytoskeleton complex proteins in cardiomyopathy. *Biophys Rev* **10**, 1033–1051 (2018).
302. Wang, S. *et al.* Mechanotransduction via the LINC complex regulates DNA replication in myonuclei. *J Cell Biol* **217**, 2005 (2018).
303. Lammerding, J. *et al.* Lamin A/C deficiency causes defective nuclear mechanics and mechanotransduction. *J Clin Invest* **113**, 370–8 (2004).
304. Kyrychenko, V. *et al.* Functional correction of dystrophin actin binding domain mutations by genome editing. *JCI Insight* **2**, (2017).

305. Vad, O. B. *et al.* Loss-of-Function Variants in Cytoskeletal Genes Are Associated with Early-Onset Atrial Fibrillation. *J Clin Med* **9**, 372 (2020).
306. Nielsen, J. B. *et al.* Biobank-driven genomic discovery yields new insight into atrial fibrillation biology. *Nature Genetics* vol. 50 1234–1239 Preprint at https://doi.org/10.1038/s41588-018-0171-3 (2018).
307. Hanft, L. M., Rybakova, I. N., Patel, J. R., Rafael-Fortney, J. A. & Ervasti, J. M. Cytoplasmic γ-actin contributes to a compensatory remodeling response in dystrophin-deficient muscle. *Proc Natl Acad Sci U S A* **103**, 5385–5390 (2006).
308. Nanni, S. *et al.* The nuclear pore protein Nup153 associates with chromatin and regulates cardiac gene expression in dystrophic mdx hearts. *Cardiovasc Res* **112**, 555–567 (2016).
309. Whitmore, C. & Morgan, J. What do mouse models of muscular dystrophy tell us about the DAPC and its components? *Int J Exp Pathol* **95**, 365 (2014).
310. Khouzami, L. *et al.* Delayed cardiomyopathy in dystrophin deficient mdx mice relies on intrinsic glutathione resource. *American Journal of Pathology* **177**, 1356–1364 (2010).
311. Birch, S. M. *et al.* Assessment of systemic AAV-microdystrophin gene therapy in the GRMD model of Duchenne muscular dystrophy. *Sci Transl Med* **15**, eabo1815 (2023).
312. Echigoya, Y. *et al.* A dystrophin exon-52 deleted miniature pig model of duchenne muscular dystrophy and evaluation of exon skipping. *Int J Mol Sci* **22**, (2021).
313. Min, Y.-L., Bassel-Duby, R. & Olson, E. N. CRISPR Correction of Duchenne Muscular Dystrophy. *Annu. Rev. Med. 2019* **70**, 239–255 (2018).
314. Wang, P. *et al.* Correction of DMD in human iPSC-derived cardiomyocytes by base-editing-induced exon skipping. *Mol Ther Methods Clin Dev* **28**, 40–50 (2022).
315. Pioner, J. M. *et al.* Calcium handling maturation and adaptation to increased substrate stiffness in human iPSC-derived cardiomyocytes: The impact of full-length dystrophin deficiency. *Front Physiol* **13**, (2022).
316. Pioner, J. M. *et al.* Advances in Stem Cell Modeling of Dystrophin-Associated Disease: Implications for the Wider World of Dilated Cardiomyopathy. *Frontiers in Physiology* vol. 11 368 Preprint at https://doi.org/10.3389/fphys.2020.00368 (2020).

317. Takahashi, K. & Yamanaka, S. Induction of Pluripotent Stem Cells from Mouse Embryonic and Adult Fibroblast Cultures by Defined Factors. *Cell* **126**, 663–676 (2006).
318. Takahashi, K. *et al.* Induction of Pluripotent Stem Cells from Adult Human Fibroblasts by Defined Factors. *Cell* **131**, 861–872 (2007).
319. Lian, X. *et al.* Robust cardiomyocyte differentiation from human pluripotent stem cells via temporal modulation of canonical Wnt signaling. **109**, (2012).
320. Burridge, P. W. *et al.* Chemically defined generation of human cardiomyocytes. *Nat Methods* **11**, 855–60 (2014).
321. Zhao, M., Tang, Y., Zhou, Y. & Zhang, J. Deciphering Role of Wnt Signalling in Cardiac Mesoderm and Cardiomyocyte Differentiation from Human iPSCs: Four-dimensional control of Wnt pathway for hiPSC-CMs differentiation. *Sci Rep* **9**, (2019).
322. Le, M. N. T., Takahi, M. & Ohnuma, K. Auto/paracrine factors and early Wnt inhibition promote cardiomyocyte differentiation from human induced pluripotent stem cells at initial low cell density. *Sci Rep* **11**, 21426 (2021).
323. Li, D., Sun, J. & Zhong, T. P. Wnt Signaling in Heart Development and Regeneration. *Curr Cardiol Rep* **24**, 1425–1438 (2022).
324. Liu, Y. *et al.* Mechanisms and inhibition of Porcupine-mediated Wnt acylation. *Nature 2022 607:7920* **607**, 816–822 (2022).
325. Nigro, G., Comi, L. I., Politano, L. & Bain, R. J. I. The incidence and evolution of cardiomyopathy in Duchenne muscular dystrophy. *Int J Cardiol* **26**, 271–277 (1990).
326. Mandegar, M. A. A. *et al.* CRISPR Interference Efficiently Induces Specific and Reversible Gene Silencing in Human iPSCs. *Cell Stem Cell* **18**, 541–553 (2016).
327. Parikh, S. S. *et al.* Thyroid and Glucocorticoid Hormones Promote Functional T-Tubule Development in Human-Induced Pluripotent Stem Cell–Derived Cardiomyocytes. *Circ Res* **121**, 1323–1330 (2017).
328. Palchesko, R. N., Zhang, L., Sun, Y. & Feinberg, A. W. Development of polydimethylsiloxane substrates with tunable elastic modulus to study cell mechanobiology in muscle and nerve. *PLoS One* **7**, (2012).
329. Tan, S. H., Nguyen, N. T., Chua, Y. C. & Kang, T. G. Oxygen plasma treatment for reducing hydrophobicity of a sealed polydimethylsiloxane microchannel. *Biomicrofluidics* **4**, (2010).

330. Nguyen, T. L., Polanco, E. R., Patananan, A. N., Zangle, T. A. & Teitell, M. A. Cell viscoelasticity is linked to fluctuations in cell biomass distributions. *Sci Rep* **10**, 1–11 (2020).

331. Swiatlowska, P. *et al.* Pressure and stiffness sensing together regulate vascular smooth muscle cell phenotype switching. *Sci Adv* **8**, 3471 (2022).

332. Gurdon, J. B. The Developmental Capacity of Nuclei taken from Intestinal Epithelium Cells of Feeding Tadpoles. *Development* **10**, 622–640 (1962).

333. Gurdon, J. B., Laskey, R. A. & Reeves, O. R. The developmental capacity of nuclei transplanted from keratinized skin cells of adult frogs. *Development* **34**, 93–112 (1975).

334. Chambers, I. *et al.* Functional expression cloning of Nanog, a pluripotency sustaining factor in embryonic stem cells. *Cell* **113**, 643–655 (2003).

335. Nichols, J. *et al.* Formation of pluripotent stem cells in the mammalian embryo depends on the POU transcription factor Oct4. *Cell* **95**, 379–391 (1998).

336. Holmes, Z. E. *et al.* The Sox2 transcription factor binds RNA. *Nature Communications 2020 11:1* **11**, 1–12 (2020).

337. Rizzino, A. & Wuebben, E. L. Sox2/Oct4: A delicately balanced partnership in pluripotent stem cells and embryogenesis. *Biochimica et Biophysica Acta (BBA) - Gene Regulatory Mechanisms* **1859**, 780–791 (2016).

338. Lanctot, P. M., Gage, F. H. & Varki, A. P. The Glycans of Stem Cells. *Curr Opin Chem Biol* **11**, 373 (2007).

339. Ehler, E. Cardiac cytoarchitecture — why the “hardware” is important for heart function! *Biochimica et Biophysica Acta (BBA) - Molecular Cell Research* **1863**, 1857–1863 (2016).

340. Keyt, L. K. *et al.* Thin filament cardiomyopathies: A review of genetics, disease mechanisms, and emerging therapeutics. *Front Cardiovasc Med* **9**, (2022).

341. Ahmed, R. E., Anzai, T., Chanthra, N. & Uosaki, H. A Brief Review of Current Maturation Methods for Human Induced Pluripotent Stem Cells-Derived Cardiomyocytes. *Front Cell Dev Biol* **0**, 178 (2020).

342. Megeney, L. A. *et al.* Severe cardiomyopathy in mice lacking dystrophin and MyoD. *Proc Natl Acad Sci U S A* **96**, 220–225 (1999).

343. Kalra, S., Montanaro, F. & Denning, C. Can Human Pluripotent Stem Cell-Derived Cardiomyocytes Advance Understanding of Muscular Dystrophies? *J Neuromuscul Dis* **3**, 309 (2016).

344. Miyaoka, Y. *et al.* Isolation of single-base genome-edited human iPS cells without antibiotic selection. *Nat Methods* **11**, 291–293 (2014).

345. Kilpinen, H. *et al.* Common genetic variation drives molecular heterogeneity in human iPSCs. *Nature* **546**, 370 (2017).

346. Du, D. T. M., Hellen, N., Kane, C. & Terracciano, C. M. N. Action potential morphology of human induced pluripotent stem cell-derived cardiomyocytes does not predict cardiac chamber specificity and is dependent on cell density. *Biophys J* **108**, 1–4 (2015).

347. Liu, Z., Yue, S., Chen, X., Kubin, T. & Braun, T. Regulation of Cardiomyocyte Polyploidy and Multinucleation by CyclinG1. *Circ Res* **106**, 1498–1506 (2010).

348. Lian, X. *et al.* Directed cardiomyocyte differentiation from human pluripotent stem cells by modulating Wnt/β-catenin signaling under fully defined conditions. *Nat Protoc* **8**, 162–75 (2013).

349. da Silva, T. D. *et al.* Heart Rate Variability and Cardiopulmonary Dysfunction in Patients with Duchenne Muscular Dystrophy: A Systematic Review. *Pediatr Cardiol* **39**, 869–883 (2018).

350. Eisen, B. *et al.* Electrophysiological abnormalities in induced pluripotent stem cell-derived cardiomyocytes generated from Duchenne muscular dystrophy patients. *J Cell Mol Med* **23**, (2019).

351. Guan, X. *et al.* Dystrophin-deficient cardiomyocytes derived from human urine: New biologic reagents for drug discovery. *Stem Cell Res* **12**, 467–480 (2014).

352. Scesa, G., Adami, R. & Bottai, D. iPSC Preparation and Epigenetic Memory: Does the Tissue Origin Matter? *Cells* **10**, (2021).

353. Pianezzi, E. *et al.* Role of somatic cell sources in the maturation degree of human induced pluripotent stem cell-derived cardiomyocytes. *Biochimica et Biophysica Acta (BBA) - Molecular Cell Research* **1867**, 118538 (2020).

354. Karamboulas, C. *et al.* HDAC activity regulates entry of mesoderm cells into the cardiac muscle lineage. *J Cell Sci* **119**, 4305–4314 (2006).

355. Jelinkova, S. *et al.* DMD Pluripotent Stem Cell Derived Cardiac Cells Recapitulate in vitro Human Cardiac Pathophysiology. *Front Bioeng Biotechnol* **8**, 535 (2020).

356. Laflamme, M. A. *et al.* Cardiomyocytes derived from human embryonic stem cells in pro-survival factors enhance function of infarcted rat hearts. *Nat Biotechnol* **25**, 1015–1024 (2007).

357. Canac, R. *et al.* Deciphering Transcriptional Networks during Human Cardiac Development. *Cells* **11**, (2022).

358. Gu, Y. *et al.* Multi-omics profiling visualizes dynamics of cardiac development and functions. *Cell Rep* **41**, (2022).

359. Pashmforoush, M. *et al.* Nkx2-5 Pathways and Congenital Heart Disease: Loss of Ventricular Myocyte Lineage Specification Leads to Progressive Cardiomyopathy and Complete Heart Block. *Cell* **117**, 373–386 (2004).

360. Israeli-Rosenberg, S., Manso, A. M., Okada, H. & Ross, R. S. Integrins and Integrin-Associated Proteins in the Cardiac Myocyte. *Circ Res* **114**, 572 (2014).

361. Hamad, S. *et al.* Generation of human induced pluripotent stem cell-derived cardiomyocytes in 2D monolayer and scalable 3D suspension bioreactor cultures with reduced batch-to-batch variations. *Theranostics* **9**, 7222 (2019).

362. De Sousa Lopes, S. M. C. *et al.* Patterning the heart, a template for human cardiomyocyte development. *Developmental Dynamics* **235**, 1994–2002 (2006).

363. Guo, Y. & Pu, W. T. Cardiomyocyte Maturation. *Circ Res* 1086–1106 (2020) doi:10.1161/CIRCRESAHA.119.315862.

364. Soonpaa, M. H., Kim, K. K., Pajak, L., Franklin, M. & Field, L. J. Cardiomyocyte DNA synthesis and binucleation during murine development. *https://doi.org/10.1152/ajpheart.1996.271.5.H2183* **271**, (1996).

365. Ali, S. R., Menendez-Montes, I., Warshaw, J., Xiao, F. & Sadek, H. A. Homotypic Fusion Generates Multinucleated Cardiomyocytes in the Murine Heart. *Circulation* **141**, 1940–1942 (2020).

366. Kamakura, T. *et al.* Ultrastructural Maturation of Human-Induced Pluripotent Stem Cell-Derived Cardiomyocytes in a Long-Term Culture. *Circulation Journal* **77**, 1307–1314 (2013).

367. Dias, T. P. *et al.* Biophysical study of human induced Pluripotent Stem Cell-Derived cardiomyocyte structural maturation during long-term culture. *Biochem Biophys Res Commun* **499**, 611–617 (2018).

368. Ronaldson-Bouchard, K. *et al.* Engineering of human cardiac muscle electromechanically matured to an adult-like phenotype. *Nat Protoc* (2018) doi:10.1038/s41596-019-0189-8.

369. Kim, C. *et al.* Non-cardiomyocytes influence the electrophysiological maturation of human embryonic stem cell-derived cardiomyocytes during differentiation. *Stem Cells Dev* **19**, 783–795 (2010).

370. Yang, X. *et al.* Fatty Acids Enhance the Maturation of Cardiomyocytes Derived from Human Pluripotent Stem Cells. *Stem Cell Reports* **13**, 657–668 (2019).

371. Janssen, R., Muller, A. & Simonides, W. S. Cardiac Thyroid Hormone Metabolism and Heart Failure. *Eur Thyroid J* **6**, 130 (2017).

372. Krüger, M. *et al.* Thyroid hormone regulates developmental titin isoform transitions via the phosphatidylinositol-3-kinase/ AKT pathway. *Circ Res* **102**, 439–447 (2008).

373. Yang, X. *et al.* Tri-iodo-L-thyronine Promotes the Maturation of Human Cardiomyocytes-Derived from Induced Pluripotent Stem Cells. *J Mol Cell Cardiol* **72**, 296 (2014).

374. Kosmidis, G. *et al.* Altered calcium handling and increased contraction force in human embryonic stem cell derived cardiomyocytes following short term dexamethasone exposure. *Biochem Biophys Res Commun* **467**, 998–1005 (2015).

375. Morkin, E. Control of Cardiac Myosin Heavy Chain Gene Expression. *Microsc. Res. Tech* **50**, 522–531 (2000).

376. Yasutake, H. *et al.* Decreased YAP activity reduces proliferative ability in human induced pluripotent stem cell of duchenne muscular dystrophy derived cardiomyocytes. *Scientific Reports 2021 11:1* **11**, 1–15 (2021).

377. Bansod, Y. D., Matsumoto, T., Nagayama, K. & Bursa, J. A Finite Element Bendo-Tensegrity Model of Eukaryotic Cell. *J Biomech Eng* **140**, (2018).

378. Wang, N., Butler, J. P. & Ingber, D. E. Mechanotransduction across the cell surface and through the cytoskeleton. *Science (1979)* **260**, 1124–1127 (1993).

379. Stamenović, D., Fredberg, J., Wang, N., Butler, J. & Ingber, D. A microstructural approach to cytoskeletal mechanics based on tensegrity. *J Theor Biol* **181**, 125–136 (1996).

380. Moeendarbary, E. & Harris, A. R. Cell mechanics: principles, practices, and prospects. *Wiley Interdiscip Rev Syst Biol Med* **6**, 371–388 (2014).

381. Haase, K. & Pelling, A. E. Investigating cell mechanics with atomic force microscopy. *J R Soc Interface* **12**, (2015).
382. Bao, G. & Suresh, S. Cell and molecular mechanics of biological materials. *Nature Materials 2003 2:11* **2**, 715–725 (2003).
383. Tajik, A. *et al.* Transcription upregulation via force-induced direct stretching of chromatin. *Nat Mater* **15**, 1287–1296 (2016).
384. Elosegui-Artola, A. *et al.* Force Triggers YAP Nuclear Entry by Regulating Transport across Nuclear Pores. *Cell* **171**, 1397-1410.e14 (2017).
385. Xin, M. *et al.* Hippo pathway effector Yap promotes cardiac regeneration. *Proc Natl Acad Sci U S A* **110**, 13839–13844 (2013).
386. Nardone, G. *et al.* YAP regulates cell mechanics by controlling focal adhesion assembly. *Nature Communications 2017 8:1* **8**, 1–13 (2017).
387. Morikawa, Y. *et al.* Actin cytoskeletal remodeling with protrusion formation is essential for heart regeneration in Hippo-deficient mice HHS Public Access. *Sci Signal* **8**, 41 (2015).
388. Bremner, S. B. *et al.* Full-length dystrophin deficiency leads to contractile and calcium transient defects in human engineered heart tissues. *J Tissue Eng* **13**, (2022).
389. Tariq, Z. *et al.* Lamin A and microtubules collaborate to maintain nuclear morphology. *Nucleus* **8**, 433–446 (2017).
390. Wang, X. P. *et al.* Live morphological analysis of taxol-induced cytoplasmic vacuoliazation in human lung adenocarcinoma cells. *Micron* **39**, 1216–1221 (2008).
391. Hoffman, B. D., Massiera, G., Van Citters, K. M. & Crocker, J. C. The consensus mechanics of cultured mammalian cells. *Proc Natl Acad Sci U S A* **103**, 10259 (2006).
392. Sultan, C., Stamenović, D. & Ingber, D. E. A computational tensegrity model predicts dynamic rheological behaviors in living cells. *Ann Biomed Eng* **32**, 520–530 (2004).
393. Körner, A., Mosqueira, M., Hecker, M. & Ullrich, N. D. Substrate Stiffness Influences Structural and Functional Remodeling in Induced Pluripotent Stem Cell-Derived Cardiomyocytes. *Front Physiol* **12**, (2021).
394. Yeung, T. *et al.* Effects of substrate stiffness on cell morphology, cytoskeletal structure, and adhesion. *Cell Motil Cytoskeleton* **60**, 24–34 (2005).

395. Depalma, S. J., Davidson, C. D., Stis, A. E., Helms, A. S. & Baker, B. M. Microenvironmental determinants of organized iPSC-cardiomyocyte tissues on synthetic fibrous matrices. *Biomater Sci* **9**, 93 (2021).

396. Doss, B. L. *et al.* Cell response to substrate rigidity is regulated by active and passive cytoskeletal stress. *Proc Natl Acad Sci U S A* **117**, 12817–12825 (2020).

397. Atmanli, A. *et al.* Cardiac Myoediting Attenuates Cardiac Abnormalities in Human and Mouse Models of Duchenne Muscular Dystrophy. *Circ Res* **129**, 602–616 (2021).

398. Wong, T. W. Y. *et al.* A novel mouse model of Duchenne muscular dystrophy carrying a multi-exonic DMD deletion exhibits progressive muscular dystrophy and early-onset cardiomyopathy. *DMM Disease Models and Mechanisms* **13**, (2020).

399. Macadangdang, J. *et al.* Nanopatterned Human iPSC-Based Model of a Dystrophin-Null Cardiomyopathic Phenotype. *Cell Mol Bioeng* **8**, 320–332 (2015).

400. Ramdas, N. M. & Shivashankar, G. V. Cytoskeletal Control of Nuclear Morphology and Chromatin Organization. *J Mol Biol* **427**, 695–706 (2015).

401. Lovett, D. B., Shekhar, N., Nickerson, J. A., Roux, K. J. & Lele, T. P. Modulation of Nuclear Shape by Substrate Rigidity. **6**, (2013).

402. Wallace, M. *et al.* Impaired lamin localization to the nuclear envelope is responsible for nuclear damage in LMNA-mutant iPSC-derived cardiomyocytes. *BioRxiv* (2021) doi:10.1101/2021.10.30.466591.

403. Suárez-Sánchez, R. *et al.* Nucleocytoplasmic shuttling of the Duchenne muscular dystrophy gene product dystrophin Dp71d is dependent on the importin α/β and CRM1 nuclear transporters and microtubule motor dynein. *Biochim Biophys Acta* **1843**, 985–1001 (2014).

404. Chamberlain, J. R. & Chamberlain, J. S. Progress toward Gene Therapy for Duchenne Muscular Dystrophy. *Molecular Therapy* vol. 25 1125–1131 Preprint at https://doi.org/10.1016/j.ymthe.2017.02.019 (2017).

405. Mosqueira, D. *et al.* Hippo pathway effectors control cardiac progenitor cell fate by acting as dynamic sensors of substrate mechanics and nanostructure. *ACS Nano* **8**, 2033–2047 (2014).

406. Hsiao, C. *et al.* Human pluripotent stem cell culture density modulates YAP signaling. *Biotechnol J* **11**, 662 (2016).

407. Pagliari, S. *et al.* YAP–TEAD1 control of cytoskeleton dynamics and intracellular tension guides human pluripotent stem cell mesoderm specification. *Cell Death Differ* **28**, 1193 (2021).

408. Carson, D. *et al.* Nanotopography-Induced Structural Anisotropy and Sarcomere Development in Human Cardiomyocytes Derived from Induced Pluripotent Stem Cells. *ACS Applied Materials and Interfaces* vol. 8 21923–21932 Preprint at https://doi.org/10.1021/acsami.5b11671 (2016).

409. Afzal, J. *et al.* Cardiac ultrastructure inspired matrix induces advanced metabolic and functional maturation of differentiated human cardiomyocytes. *Cell Rep* **40**, 111146–111146 (2022).

410. Eguchi, A. *et al.* TRF2 rescues telomere attrition and prolongs cell survival in Duchenne muscular dystrophy cardiomyocytes derived from human iPSCs. *Proc Natl Acad Sci U S A* **120**, (2023).

411. Hahn, D. *et al.* Rapid restitution of contractile dysfunction by synthetic copolymers in dystrophin-deficient single live skeletal muscle fibers. *Skelet Muscle* **13**, 1–14 (2023).

412. Hanft, L. M., Korte, F. S. & McDonald, K. S. Cardiac function and modulation of sarcomeric function by length. *Cardiovasc Res* **77**, 627–636 (2008).

413. Edman, K. A. The velocity of unloaded shortening and its relation to sarcomere length and isometric force in vertebrate muscle fibres. *J Physiol* **291**, 143 (1979).

414. Liu, J., Sun, N., Bruce, M. A., Wu, J. C. & Butte, M. J. Atomic Force Mechanobiology of Pluripotent Stem Cell-Derived Cardiomyocytes. *PLoS One* **7**, 37559 (2012).

415. Ingber, D. E. *et al. Tensegrity, Cellular Biophysics, and the Mechanics of Living Systems*. vol. 77 046603 (2014).

416. Stamenovic, D., Liang, Z., Chen, J. & Wang, N. Effect of the cytoskeletal prestress on the mechanical impedance of cultured airway smooth muscle cells. *J Appl Physiol* **92**, 1443–1450 (2002).

417. Xu, J., Wirtz, D. & Pollard, T. D. Dynamic cross-linking by alpha-actinin determines the mechanical properties of actin filament networks. *J Biol Chem* **273**, 9570–9576 (1998).

418. Grady, M. E., Composto, R. J. & Eckmann, D. M. Cell elasticity with altered cytoskeletal architectures across multiple cell types. *J Mech Behav Biomed Mater* **61**, 197–207 (2016).

419. Qiu, H. *et al.* Short Communication: Vascular Smooth Muscle Cell Stiffness As a Mechanism for Increased Aortic Stiffness With Aging. *Circ Res* **107**, 615–619 (2010).

420. Swiatlowska, P., Sanchez-Alonso, J. L., Wright, P. T., Novak, P. & Gorelik, J. Microtubules regulate cardiomyocyte transversal Young's modulus. *Proc Natl Acad Sci U S A* **117**, 2764–2766 (2020).

421. Bubb, M. R., Spector, I., Beyer, B. B. & Fosen, K. M. Effects of Jasplakinolide on the Kinetics of Actin Polymerization AN EXPLANATION FOR CERTAIN IN VIVO OBSERVATIONS*. *Journal of Biological Chemistry* **275**, 5163–5170 (2000).

422. Schweikart, K. *et al.* The Effects of Jaspamide on Human Cardiomyocyte Function and Cardiac Ion Channel Activity. *Toxicol In Vitro* **27**, 745 (2013).

423. Wang, J., Fan, Y., Dube, D. K., Sanger, J. M. & Sanger, J. W. Jasplakinolide reduces actin and tropomyosin dynamics during myofibrillogenesis. *Cytoskeleton (Hoboken)* **71**, 513 (2014).

424. Hawkes, W. *et al.* Regulation of cardiomyocyte adhesion and mechanosignalling through distinct nanoscale behaviour of integrin ligands mimicking healthy or fibrotic extracellular matrix. *Philosophical Transactions of the Royal Society B: Biological Sciences* **377**, (2022).

425. Park-Holohan, S. J. *et al.* Stress-dependent activation of myosin in the heart requires thin filament activation and thick filament mechanosensing. *Proc Natl Acad Sci U S A* **118**, (2021).

426. Adorisio, R. *et al.* Long-Term Outcome of LVAD in Duchenne Population with End Stage Cardiomyopathy. *The Journal of Heart and Lung Transplantation* **39**, S219–S220 (2020).

427. Pitoulis, F. G. & Terracciano, C. M. Heart Plasticity in Response to Pressure- and Volume-Overload: A Review of Findings in Compensated and Decompensated Phenotypes. *Front Physiol* **11**, 504088 (2020).

428. Zanotti, S. *et al.* Altered extracellular matrix transcript expression and protein modulation in primary Duchenne muscular dystrophy myotubes. *Matrix Biol* **26**, 615–624 (2007).

429. Zhang, W., Liu, Y. & Zhang, H. Extracellular matrix: an important regulator of cell functions and skeletal muscle development. *Cell & Bioscience 2021 11:1* **11**, 1–13 (2021).

430. Byun, J. *et al.* Yes-associated protein (YAP) mediates adaptive cardiac hypertrophy in response to pressure overload. *J Biol Chem* **294**, 3603–3617 (2019).
431. Khatau, S. B. *et al.* A perinuclear actin cap regulates nuclear shape. *Proc Natl Acad Sci U S A* **106**, 19017 (2009).
432. Wilson, R. G., Trogadis, J. E., Zimmerman, S. & Zimmerman, A. M. Hydrostatic pressure induced changes in the cytoarchitecture of pheochromocytoma (PC-12) cells. *Cell Biol Int* **25**, 649–666 (2001).
433. Okamoto, K. *et al.* Pressure-induced changes on the morphology and gene expression in mammalian cells. *Biol Open* **10**, (2021).
434. Bourns, B., Franklin, S., Cassimeris, L. & Salmon, E. D. High hydrostatic pressure effects in vivo: Changes in cell morphology, microtubule assembly, and actin organization. *Cell Motil Cytoskeleton* **10**, 380–390 (1988).
435. Yamaguchi, Y. *et al.* High hydrostatic pressure induces slow contraction in mouse cardiomyocytes. *Biophys J* **121**, 3286–3294 (2022).
436. Lombardi, M. L. *et al.* The Interaction between Nesprins and Sun Proteins at the Nuclear Envelope Is Critical for Force Transmission between the Nucleus and Cytoskeleton. *Journal of Biological Chemistry* **286**, 26743–26753 (2011).
437. Chancellory, T. J., Lee, J., Thodeti, C. K. & Lele, T. Actomyosin Tension Exerted on the Nucleus through Nesprin-1 Connections Influences Endothelial Cell Adhesion, Migration, and Cyclic Strain-Induced Reorientation. *Biophys J* **99**, 115 (2010).
438. Isermann, P. & Lammerding, J. Nuclear mechanics and mechanotransduction in health and disease. *Curr Biol* **23**, R1113-21 (2013).
439. Hsia, C.-R., Melters, D. P. & Dalal, Y. The Force is Strong with This Epigenome: Chromatin Structure and Mechanobiology. *J Mol Biol* **435**, 168019 (2023).
440. Zhou, C., Rao, L., Warren, D. T., Shanahan, C. M. & Zhang, Q. Mouse models of nesprin-related diseases. *Biochem Soc Trans* **46**, 669–681 (2018).
441. Bray, M. A., Sheehy, S. P. & Parker, K. K. Sarcomere alignment is regulated by myocyte shape. *Cell Motil Cytoskeleton* **65**, 641–651 (2008).
442. Raab, M. & Discher, D. E. Matrix rigidity regulates the microtubule network polarization in migration. *Cytoskeleton (Hoboken)* **74**, 114 (2017).
443. O'Connor, T. M., Houston, L. L. & Samson, F. Stability of neuronal microtubules to high pressure in vivo and in vitro. *Proc Natl Acad Sci U S A* **71**, 4198–4202 (1974).

444. Cooper IV, G. Cytoskeletal networks and the regulation of cardiac contractility: Microtubules, hypertrophy, and cardiac dysfunction. *Am J Physiol Heart Circ Physiol* **291**, 1003–1014 (2006).

445. Sequeira, V., Nijenkamp, L. L. A. M., Regan, J. A. & Van Der Velden, J. The physiological role of cardiac cytoskeleton and its alterations in heart failure. *Biochimica et Biophysica Acta - Biomembranes* vol. 1838 700–722 Preprint at https://doi.org/10.1016/j.bbamem.2013.07.011 (2014).

446. Driscoll, T. P., Cosgrove, B. D., Heo, S. J., Shurden, Z. E. & Mauck, R. L. Cytoskeletal to Nuclear Strain Transfer Regulates YAP Signaling in Mesenchymal Stem Cells. *Biophys J* **108**, 2783 (2015).

447. Park, J., Jia, S., Salter, D., Bagnaninchi, P. & Hansen, C. G. The Hippo pathway drives the cellular response to hydrostatic pressure. *EMBO J* **41**, (2022).

448. Yue, P. *et al.* Yap1 modulates cardiomyocyte hypertrophy via impaired mitochondrial biogenesis in response to chronic mechanical stress overload. *Theranostics* **12**, 7009 (2022).

449. Maul, T. M., Chew, D. W., Nieponice, A. & Vorp, D. A. Mechanical stimuli differentially control stem cell behavior: morphology, proliferation, and differentiation. *Biomech Model Mechanobiol* **10**, 939 (2011).

450. Ovchinnikova, E. *et al.* Modeling Human Cardiac Hypertrophy in Stem Cell-Derived Cardiomyocytes. *Stem Cell Reports* **10**, 794–807 (2018).

451. Cai, X., Wang, K. C. & Meng, Z. Mechanoregulation of YAP and TAZ in Cellular Homeostasis and Disease Progression. *Front Cell Dev Biol* **9**, 673599 (2021).

452. Quinlan, A. M., Sierad, L. N., Capulli, A. K., Firstenberg, L. E. & Billiar, K. L. Combining Dynamic Stretch and Tunable Stiffness to Probe Cell Mechanobiology In Vitro. *PLoS One* **6**, 23272 (2011).

453. Kreutzer, J. *et al.* Pneumatic unidirectional cell stretching device for mechanobiological studies of cardiomyocytes. **19**, 291–303 (2020).

454. Kreutzer, J. *et al.* Pneumatic cell stretching system for cardiac differentiation and culture. *Med Eng Phys* **36**, 496–501 (2014).

455. González-Ramírez, R., Morales-Lázaro, S. L., Tapia-Ramírez, V., Mornet, D. & Cisneros, B. Nuclear and nuclear envelope localization of dystrophin Dp71 and dystrophin-associated proteins (DAPs) in the C2C12 muscle cells: DAPs nuclear localization is modulated during myogenesis. *J Cell Biochem* **105**, 735–745 (2008).

456. Cerecedo, D. *et al.* Platelet adhesion: structural and functional diversity of short dystrophin and utrophins in the formation of dystrophin-associated-protein complexes related to actin dynamics. *Thromb Haemost* **94**, 1203–1212 (2005).
457. Codelia, V. A., Sun, G. & Irvine, K. D. Regulation of YAP by Mechanical Strain through Jnk and Hippo Signaling. *Curr Biol* **24**, 2012 (2014).
458. Ross, J. A. *et al.* Lem2 is essential for cardiac development by maintaining nuclear integrity. *Cardiovasc Res* **119**, 2074–2088 (2023).
459. Krause, M. *et al.* Cell migration through three-dimensional confining pores: speed accelerations by deformation and recoil of the nucleus. *Philos Trans R Soc Lond B Biol Sci* **374**, (2019).
460. Kaprielian, R. R. & Severs, N. J. *Dystrophin and the Cardiomyocyte Membrane Cytoskeleton in the Healthy and Failing Heart*. *Heart Failure Reviews* vol. 5 (2000).
461. Rybakova, I. N., Amann, K. J. & Ervasti, J. M. A new model for the interaction of dystrophin with F-actin. *J Cell Biol* **135**, 661–672 (1996).
462. Koenig, M. *et al.* The molecular basis for Duchenne versus Becker muscular dystrophy: Correlation of severity with type of deletion. *Am J Hum Genet* **45**, 498 (1989).
463. Cao, N. *et al.* Ascorbic acid enhances the cardiac differentiation of induced pluripotent stem cells through promoting the proliferation of cardiac progenitor cells. *Cell Res* **22**, 219–36 (2012).
464. Bizy, A. *et al.* Myosin light chain 2-based selection of human iPSC-derived early ventricular cardiac myocytes. *Stem Cell Res* **11**, 1335 (2013).
465. Feaster, T. K. *et al.* Matrigel Mattress: A Method for the Generation of Single Contracting Human-Induced Pluripotent Stem Cell-Derived Cardiomyocytes. *Circ Res* **117**, 995 (2015).
466. Dostanić, M. *et al.* A Miniaturized EHT Platform for Accurate Measurements of Tissue Contractile Properties. *Journal of Microelectromechanical Systems* **29**, 881–887 (2020).
467. Querdel, E. *et al.* Human Engineered Heart Tissue Patches Remuscularize the Injured Heart in a Dose-Dependent Manner. *Circulation* **143**, 1991 (2021).
468. Jacot, J. G., Martin, J. C. & Hunt, D. L. Mechanobiology of cardiomyocyte development. *J Biomech* **43**, 93–98 (2010).

469. Pandey, P. *et al.* Cardiomyocytes Sense Matrix Rigidity through a Combination of Muscle and Non-muscle Myosin Contractions. *Dev Cell* **44**, 326-336.e3 (2018).
470. Tallawi, M., Rai, R., Boccaccini, A. R. & Aifantis, K. E. Effect of Substrate Mechanics on Cardiomyocyte Maturation and Growth. *Tissue Eng Part B Rev* **21**, 157 (2015).
471. Kumar, S. *et al.* Viscoelastic Retraction of Single Living Stress Fibers and Its Impact on Cell Shape, Cytoskeletal Organization, and Extracellular Matrix Mechanics. *Biophys J* **90**, 3762 (2006).
472. Bajaj, P., Tang, X., Saif, T. A. & Bashir, R. Stiffness of the substrate influences the phenotype of embryonic chicken cardiac myocytes. *J Biomed Mater Res A* **95A**, 1261–1269 (2010).
473. Nukuda, A. *et al.* Stiff substrates increase YAP-signaling-mediated matrix metalloproteinase-7 expression. *Oncogenesis* **4**, 165 (2015).
474. Caporizzo, M. A., Chen, C. Y. & Prosser, B. L. Cardiac microtubules in health and heart disease. *https://doi.org/10.1177/1535370219868960* **244**, 1255–1272 (2019).